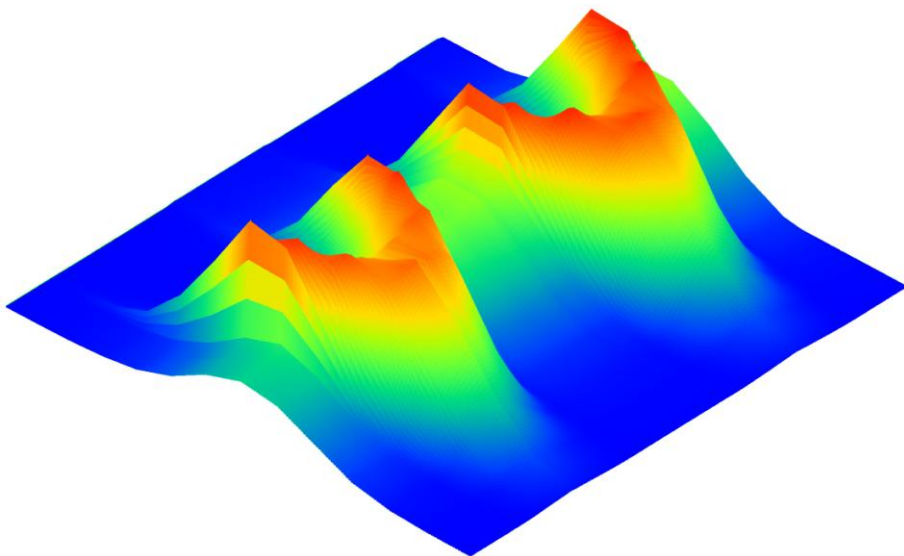


**Solid-supported lipid membranes
and their response to varied
environmental conditions**

Dissertation

by Martin Kreuzer



Inaugural-Dissertation

**zur Erlangung der Doktorwürde der
Naturwissenschaftlich – Mathematischen Gesamtfakultät der
Ruprecht-Karls-Universität Heidelberg**

vorgelegt durch

Diplom-Physiker Martin Kreuzer

aus Obernburg (Hessen)

Tag der mündlichen Prüfung: 3. Februar 2012

**Solid-supported lipid membranes
and their response to varied
environmental conditions**

Gutachter:

Prof. (apl.) Dr. Reiner Dahint

Prof. Dr. Motomu Tanaka

**Physikalisch-Chemisches Institut,
Ruprecht-Karls-Universität Heidelberg**

Summary

Biological membranes are a main component of living organisms. They separate the inside of cells from their surrounding and act as selective permeable barriers. Those membranes are build up by lipid molecules by self-organization processes. Model membranes of that type can not only be used for improved understanding of fundamental structural principles like phase transition behaviour, but also for the investigation of biological phenomena such as joint lubrication. For both purposes, the response of substrate-supported lipid membranes were studied at the solid-liquid interface at varied external parameters and membrane interactions with organic molecules.

The spin-coating and air-brush technique were applied as straightforward and reliable preparation methods for these model membranes. The structure of the prepared membranes was characterized in X-ray (XR) and neutron reflectometry (NR) experiments. Fourier transform infrared spectroscopy (FTIR) was employed in the surface sensitive attenuated total reflectance (ATR) geometry to characterize the vibrational modes of the investigated systems in contact with liquids. The unrestricted comparability of ATR-FTIR and NR results was ensured by unified experiments on the same sample at the same time. This required the design of an external ATR-FTIR beam line, which was combined with a neutron reflectometer, resulting in the BioRef instrument at the BER II neutron source at the Helmholtz-Zentrum Berlin. Differential scanning calorimetry (DSC) was applied as a complementary method in order to study the phase transitional behaviour of the corresponding bulk systems. Besides varied environmental conditions including temperature and pressure changes, different solutions were used as incubating liquid phases. Furthermore, the effects of applied shear load on the prepared model membranes were studied.

The performed NR experiments revealed the limits of stability of the prepared DMPC lipid coatings incubated in pure water (D_2O): The coatings are stable in the ripple phase $P_{\beta'}$ of the lipid molecules. That could be shown for various combinations of applied temperature and hydrostatic pressure up to physiologically relevant temperatures and approximately 100 MPa, upon exposure to an external shear force and for lipid layers on both silicon and titanium-coated surfaces. However, in the fluid-like L_{α} phase of the lipid molecules, the oligolamellar DMPC coatings detached irreversibly from the substrates.

The strong impact of the main phase transition on the structure of the coating was further seen in a multi-layered lipid system. In the $P_{\beta'}$ phase, the lipid chains were in all-trans conformation, resulting in an increased lipid membrane thickness. In comparison, in the L_{α} phase with molten lipid chains, a decreased lipid membrane thickness was found. In addition, structural changes of the coating (as seen by NR) were observed, which could not be correlated to the lipid chain melting alone (as seen by ATR-FTIR): An anomalous swelling of the lipid stack of 1-2 Å occurred upon approaching the main phase transition temperature.

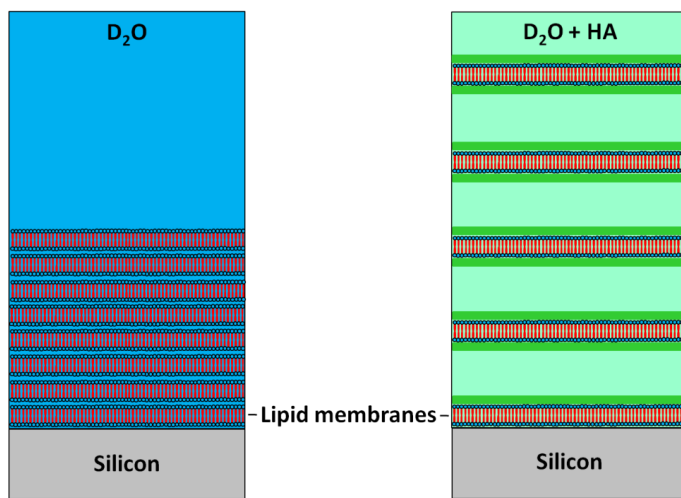


Figure 1: Model for oligolamellar lipid coatings in pure D_2O (left) and after incubation in a solution of HA in D_2O (right).

Further to measurements performed in pure water, solid-supported lipid membrane systems were also studied in solutions of hyaluronic acid (HA) in water. These systems were used as a more elaborate model for mammalian joints. It was found that HA provokes pronounced effects on the lipid model membranes: At room temperature and ambient pressure a new lamellar phase developed in which the lipid stack drastically increased in thickness by 380% with the lamellar order of the lipid molecules preserved (Figure 1). A detailed analysis of the scattering curves revealed an agglomeration of HA molecules outside the individual lipid lamellae, close to the head group regions. Crossing the main phase transition from $P_{\beta'}$ to the L_{α} phase of the lipid molecules within the coating did not result in unbinding of the lipid membranes: they remained stable on the substrate. Furthermore, the lipid coating increased in thickness (as seen by NR) with the lipid chains in their molten state (as seen with ATR-FTIR). It was shown that the swelling of the lipid coating could be suppressed by screening the electrostatic interactions of the system by adding salt to the incubating solution of HA in water. The effects on the solid-supported lipid membranes induced by HA could qualitatively be understood on the bases of the DLVO theory taking into account additional steric interactions.

Zusammenfassung

Biologische Membranen sind ein Hauptbestandteil von lebenden Organismen. Sie trennen das Zellinnere von dessen Umgebung und wirken als selektiv permeable Barrieren. Solche Membranen können durch Selbstaggregation von Lipiden gebildet werden. Modell-Membranen dieses Typs können verwendet werden um grundlegende strukturelle Prinzipien im Nahbereich von Phasenübergängen zu verstehen und um biologische Phänomene wie die Gelenkschmierung zu untersuchen. Zu diesem Zweck wurden Lipidbeschichtungen an der Fest-Flüssig-Grenzfläche präpariert und vermessen. Dabei wurden die Reaktionen der Membranen auf unterschiedliche äußere Parameter und die Wechselwirkung mit organischen Molekülen in den Mittelpunkt der Untersuchungen gestellt.

Die Rotationsbeschichtung (spin-coating) und die Luftdruckbeschichtung (air-brush) wurden als einfache und zuverlässige Herstellungsverfahren für Modellmembranen eingesetzt. Die Struktur der hergestellten Membranen wurde in Röntgen- (XR) und Neutronenreflektometrie (NR) Experimenten verifiziert. Die Fourier-Transformations-Infrarotspektroskopie (FTIR) wurde in der oberflächenempfindlichen, abgeschwächten Totalreflexions (ATR) Geometrie eingesetzt, um die Schwingungsmodi der untersuchten Systeme in Kontakt mit Flüssigkeiten zu charakterisieren. Die uneingeschränkte Vergleichbarkeit zwischen ATR-FTIR- und NR-Ergebnissen wurde durch gleichzeitige Messungen an derselben Probe gewährleistet. Dies erforderte die Konstruktion einer externen ATR-FTIR Strahlführung, welche am BioRef-Neutronenreflektometer der BER II Neutronenquelle am Helmholtz-Zentrum Berlin realisiert wurde. Die dynamische Differenzkalorimetrie (DSC) wurde als eine ergänzende Methode angewandt, um das Verhalten von Membranen in Lösung am Phasenübergang zu untersuchen. Neben vielfältigen Umgebungsbedingungen wie Temperatur- und Druckänderungen, wurden die Beschichtungen in unterschiedlichen Lösungen inkubiert. Darüber hinaus wurde der Einfluss von äußerer Scherung auf die Modellmembranen getestet.

Die Stabilität der präparierten DMPC-Lipidbeschichtungen wurde zuerst in reinem Wasser (D_2O) verifiziert: Die Beschichtungen sind stabil in der Rippel-Phase $P_{\beta'}$ der Lipiddoppelschichten. Dies konnte für verschiedene Druck- und Temperaturbedingungen bis hin zu physiologisch relevanten Temperaturen und etwa 100 MPa gezeigt werden. Zudem reagierten die Beschichtungen stabil auf äußere Scherkräfte und hafteten sowohl auf reinen Silizium-Oberflächen als auch auf Oberflächen mit Titanbeschichtung.

In der flüssigen Phase L_α der Lipide hingegen lösten sich die oligolamellaren Beschichtungen irreversibel vom Substrat. Der Einfluss des Hauptphasenübergangs auf die Struktur der Beschichtungen wurde mittels einer multilamellaren Lipidbeschichtung gemessen. In der P_β -Phase sind die Lipidketten in all-trans Konformation, was zu einer erhöhten Schichtdicke der Lipidmembranen beiträgt. Im Vergleich dazu wurde in der L_α -Phase mit geschmolzenen Lipidketten eine verminderte Schichtdicke gemessen. Darüber hinaus wurden strukturelle Veränderungen der Beschichtung mittels NR beobachtet, die nicht auf das Schmelzen der Lipidketten (gemessen durch ATR-FTIR) zurückgeführt werden können: ein anomales Quellverhalten der Lipiddoppelschichten bei Annäherung an den Hauptphasenübergang.

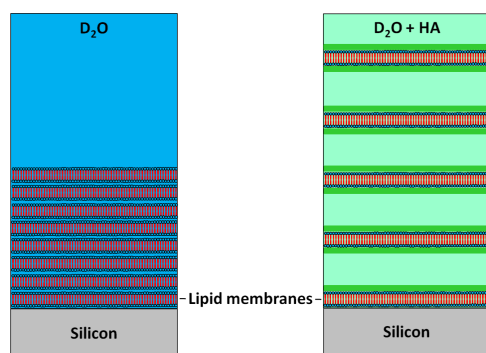


Abbildung 1: Modell von Lipidbeschichtungen auf Silizium in reinem D_2O (links) und in einer Lösung aus HA in D_2O (rechts).

Neben den Messungen in reinem Wasser wurden Lipidbeschichtungen auch in Lösungen aus Hyaluronsäure (HA) in Wasser (D_2O) untersucht. Dieses System wurde als ein Modell für Säugetiergelenke verwendet. Es wurde festgestellt, dass HA tiefgreifende Veränderungen der Lipidmembranen verursacht: Bei Raumtemperatur und Umgebungsdruck entstand eine neue lamellare Phase, in der die Lipiddoppelschichten drastisch an Dicke zugenommen haben (Abbildung 1). Eine detaillierte Analyse der Streukurven ergab, dass sich HA-Moleküle außerhalb der einzelnen Lipidlamellen in der Nähe der Kopfgruppen anlagern. Das Überschreiten des Hauptphasenübergangs von P_β -Phase in die L_α -Phase der Lipidmoleküle führte nicht zum Ablösen der Lipidbeschichtung. Darüber hinaus wurde nachgewiesen, dass die Lipiddoppelschichten mit Lipidketten in geschmolzenem Zustand (gemessen mit ATR-FTIR) an Dicke zunehmen (gemessen mit NR). Es konnte gezeigt werden, dass das Quellen der Lipidbeschichtung durch Zugabe von 1 M Kochsalz in die HA-Wasser-Lösung unterdrückt werden kann. Hiermit verbunden ist die Abschirmung der elektrostatischen Wechselwirkungen im System. Der Einfluss von HA auf die Lipidmembranen wurde qualitativ auf der Basis der DLVO-Theorie unter Berücksichtigung zusätzlicher sterischer Wechselwirkungen diskutiert.

Acknowledgements

The presented project was based on a cooperation between the University of Heidelberg and the Helmholtz-Zentrum Berlin. It has been funded by the German Ministry for Education and Science (BMBF) through contract no. 05KN7VH1. In practice it was realized and filled with life by day to day collaborations and activities of many people.

I would like to thank...

...Dr. Roland Steitz for being a great mentor. I gained not only from his guidance through the project, but from several discussions around everything. In addition, I enjoyed learning from his skills as an experimenter on several beam times around Europe.

...Prof. Dr. Reiner Dahint for giving me the opportunity to write this thesis at the University of Heidelberg and for day and night support during several beam times.

...Prof. Dr. Motomu Tanaka for refereeing the thesis on short notice.

...Dr. Markus Strobl for introducing me to the reflectivity group at HZB. Furthermore he was the guiding hand regarding the activities around the BioRef beam line.

...Robby Kischnik and Werner Graf for helping me out with their technical skills.

...Michael Rose and his team of the HZB engineering department.

...Holger Herrlich for the preparation of the BioRef software package, which made the BioRef data analysis enjoyable.

...Jan-Ekkehard Hoffmann and Andreas Stellmacher for titanium coated silicon substrates and for keeping the X-ray reflectometer in shape.

...Dr. Thomas Hauß for fruitful discussions about lipid systems and access to the well organized bio-lab at HZB.

...Matthias Reinhardt and Charlotte Hemmer for their help during several beam times and other lab work.

...Dr. Jochen Stahn, Prof. Regine Willumeit and Maksym Golub for their help concerning AMOR.

...Dr. Robert Wimpory, Dr. Marcus Trapp, Hristina Karastaneva and Dr. Beate-Annette Brüning for proof reading.

...Prof. Dr. Matthias Ballauff and the department of Soft Matter and Functional Materials at HZB for the enjoyable working atmosphere.

...Prof. Gerald Brezesinski and Dr. Matthias Dittrich for access to the dynamic scanning calorimeter at the Max-Planck-Institute (Golm, Germany).

Furthermore many people were involved in giving me reality checks on a regular base:

Laura Urrea Garcia and the WeserWG with Sibylle (Bille) Braungardt, Kristin (Krissi) Nicolaus, Lutz (Lutzifer) Kreische, Kai Lehmann, Jana Werner, Markus Stephan, Elise Bournizien, Lisa Li and Alexander (Alex) Valentin.

Gerti (Mama) and Manfred (Papa) Kreuzer I would like to thank for their everlasting support.

Contents

Summary	6
Zusammenfassung	8
Acknowledgements	10
Contents	12
1. Introduction	14
2. Theory and status quo of joint components	17
2.1 Phospholipids.....	17
2.2 Hyaluronic acid.....	22
3. Experimental section	23
3.1 Used Chemicals and substrates	23
3.2 Sample characterization	24
3.2.1 Differential scanning calorimetry.....	24
3.2.2 Infrared spectroscopy	26
3.2.3 The general laws of wave optics	31
3.2.4 Reflectometry	33
3.2.5 Two ways to build a neutron reflectometer	42
3.2.6 Shear setup employed at AMOR.....	50
3.2.7 High pressure cell.....	51
3.2.8 X-Ray reflectometer	51
3.3 Preparation of lamellar lipid coatings.....	52
3.3.1 Spin coating.....	52
3.3.2 Air brush.....	54
4. Instrument Development at BioRef	56
4.1 Substrates	57
4.2 Sample cell	58
4.3 External FTIR setup	60
4.4 Resulting IR intensities.....	63
5. Lipid membranes in pure aqueous solutions	66
5.1 A simulated neutron reflectometry experiment	67

5.2	Stability of oligolamellar lipid coatings	71
5.2.1	Effect of temperature	71
5.2.2	Effect of pressure	80
5.2.3	Effect of shear	84
5.2.4	Effect of substrate.....	88
5.2.5	Discussion on the stability of lipid coatings	93
5.3	Phase transition of multilamellar lipid coatings	97
5.3.1	Infrared absorption of a multilamellar lipid coating.....	98
5.3.2	Neutron reflectivity of a multilamellar lipid coating.....	102
5.3.3	Phase transition in the light of IR and NR – a comparative discussion.....	107
5.4	Summary of chapter 5.....	110
6.	Lipid membranes at physiological conditions.....	112
6.1	Vibrational modes of DMPC and HA	113
6.2	Differential scanning calorimetry on multilamellar lipid vesicles	117
6.3	Effect of hyaluronic acid on the lamellar structure of surface bound lipid films	118
6.4	Effect of time and temperature	123
6.5	Effect of HA and salt.....	134
6.6	Effect of shear	136
6.7	Effect of pressure	140
6.8	Phase transition of multilamellar lipid systems	148
6.8.1	Infrared absorption of a multilamellar lipid coating.....	149
6.8.2	Neutron reflectivity of a multilamellar lipid coating.....	152
6.8.3	Discussion.....	154
6.9	Summary of chapter 6.....	156
7.	Conclusions and Outlook	158
	Appendix A: Summary of the measured samples.....	160
	Appendix B: Mechanical test of the pressure cell	161
	Appendix C: List of selected publications	162
	Table of Figures	164
	References.....	173
	Abbreviations	189

1. Introduction

The most disabling disease of the western world is osteoarthritis [1]. It affects around 66% of the population older than 65 years [2]. Osteoarthritis is a degenerative joint disease, which can affect any joint of the body. It mostly occurs on the heavy weight bearing joints like hips and knees [3]. In natural joints the two opposing surfaces are covered with cartilage to which lipids are adsorbed in a graphite-like oligolamellar structure [4]. The two opposing surfaces are separated by a liquid phase, the synovial fluid (Figure 2) [5]. A main component of synovial fluid is hyaluronic acid (HA), a high molecular weight polysaccharide [6]. HA is known to be also involved in other processes in the human body, such as wound healing [7] and tumour progression [8] further to its unique role in joints [9]. In particular the combination of phospholipids and HA is claimed to play an important role in joint lubrication [10-12]. Recent investigations show that injected mixtures of phospholipids and HA reduce friction in animal joints [11] and in human systems [13].

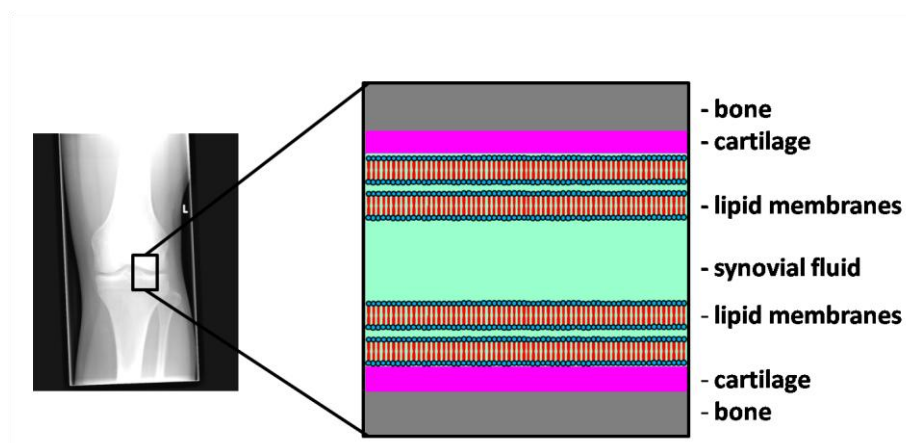


Figure 2: Radiograph of a human knee joint (left) [14]. Schematic diagram (right), showing a close up of the opposing bones, covered with cartilage and lipid layers, separated by synovial fluid.

Even though the interaction of phospholipids and hyaluronic acid is essential for the understanding of joint lubrication, little is known about these interactions on a molecular scale. Investigations on the behaviour of lipids and HA would further be beneficial for an improved medical treatment of arthritis or for the design of artificial joints [15]. Lipid membrane coatings are in addition proposed as biomimetic interfaces for long lasting body implants [16]. Based on above motivations, molecular organization between solid-supported lipid membranes and HA solutions on a molecular scale have been investigated in the present work.

The successful preparation of oligolamellar lipid coatings on silicon substrates was the starting point for the present investigations. Due to physiological relevance, measurements were performed *in-situ*, first against pure water for reference and second against solutions of HA in water (Figure 3). Neutron reflectivity and infrared spectroscopy were applied as the main methods for surface sensitive and complementary *in-situ* measurements. The stability of the lipid coatings with increasing temperature was investigated, particularly in the vicinity of the main phase transition temperature of the lipid molecules. In independent experiments, the main phase transition was induced by changing hydrostatic pressure at a fixed temperature. Samples incubated in solutions of HA in water were examined in long term studies and the importance of system intrinsic electrostatic contributions to the interaction of lipids and HA crosschecked. Structural changes of the lipid coating were investigated under external shear, in order to mimic the forces acting on lipid membranes in human joints. In addition, the influence of the underlying substrate on the lipid coating was analyzed. As titanium is a promising material for artificial body implants, the stability of lipid membranes on titanium-coated silicon substrates was studied at various temperatures and external shear load.

In their dried state against air the prepared lipid coatings on solid silicon support were characterized by X-ray reflectivity in order to verify coating thicknesses and orientation, and tuning the number of substrate-bound membranes by applying different coating parameters. Fourier transform infrared spectroscopy (FTIR) was applied to identify the main molecular groups of the adsorbate as well as conformational changes in the films. For the required surface sensitivity, FTIR was performed in attenuated total reflection (ATR) mode. With differential scanning calorimetry (DSC) measurements, the main phase transition temperature was measured in the bulk systems, i.e. lipid molecules dispersed in D₂O and lipid molecules dispersed in a solution of HA in D₂O, respectively.

The main focus of the present work is on substrate-bound coatings, incubated in corresponding liquid phases. Neutron reflectivity (NR) is a powerful method for the investigation of support-solution interfaces. Detailed membrane profiles along the z direction are obtained due to the different neutron scattering length densities (SLD's) of the individual components (lipids, HA and liquid phase). D₂O was used instead of H₂O as a liquid phase to enhance the neutron scattering contrast between protonated lipid molecules and liquid phase. NR experiments have been performed at different reflectometers, hosted at different neutron sources.

NR is sensitive to structure and the molecular organization of the lipid ensembles, while FTIR is probing local environment and conformation of the lipid molecules. In that respect the two techniques probe different aspects of the molecular systems under study here and complement each other. Therefore, a substantial part of the present work was to construct and implement a specialized ATR-FTIR facility into the BioRef neutron reflectometer at the Helmholtz-Zentrum Berlin. That instrumental development made it possible to perform *in-situ* NR and ATR-FTIR experiments on the same sample at the same time. Thus, structural changes of the investigated lipid coatings, as measured by NR, could be directly correlated to changes in the vibrational states of the participating components, as measured by ATR-FTIR. In particular, the main phase transition of the lipid molecules and potential interactions between lipids and HA were subject of these investigations.

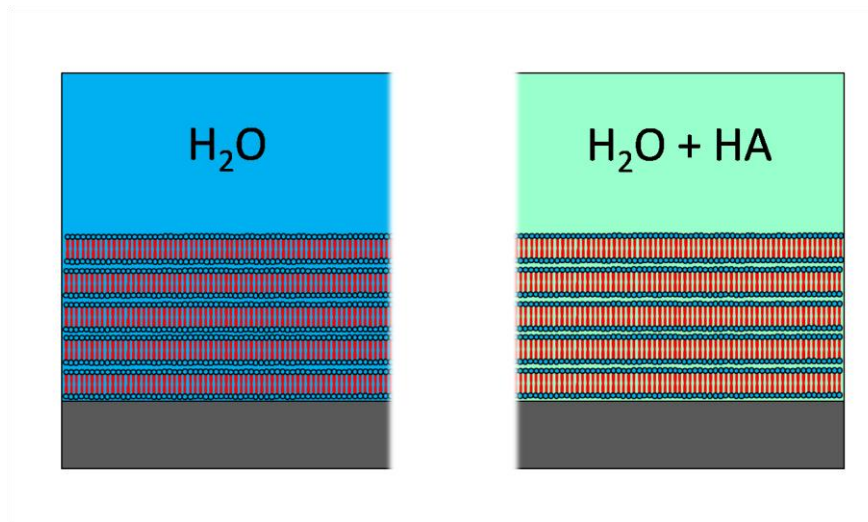


Figure 3: Model systems: Lamellar lipid membranes as coatings on a silicon substrate, incubated in pure water as a reference (left) or incubated in a model synovial fluid, consisting of a solution of hyaluronic acid (HA) in water (right).

2. Theory and status quo of joint components

The main characteristics of the investigated joint components are given in this chapter: phospholipids (chapter 2.1) and hyaluronic acid (chapter 2.2).

2.1 Phospholipids

Phospholipids are naturally occurring molecules with an amphiphilic character: They consist of a hydrophilic (water-loving) head group and a hydrophobic (water-fearing) tail group. When exposed to water, the molecules tend to form clusters in order to shield of the tail groups from the water phase, with the head groups aligned towards the polar water molecules, known as the hydrophobic effect [17]. With increasing lipid concentration the formation of larger aggregates becomes more favourable, resulting in extended bilayers. Lipid bilayers form the basis of biological membranes found in any life form. A bilayer consists of two opposing monolayers, where the hydrophobic lipid tails face each other. The repeat distance d in a stack of lipid bilayers can be described by a simplified model based on the thickness of a bilayer and a separating inter solution layer with thickness d_{solution} (Figure 4). The lipid bilayer thickness is defined by the thickness of the hydrophobic chain groups d_{chains} with hydrophilic head groups of thickness d_{heads} on either side. The measured repeat distance d is the sum of all contributions:

$$d = \underbrace{(2 \cdot d_{\text{heads}} + d_{\text{chains}})}_{\text{bilayer}} + d_{\text{solution}} \quad \text{Equation 2.1}$$

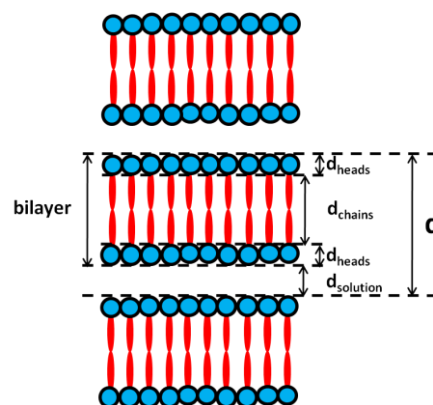


Figure 4: Sketch of a stack of lipid membranes (bilayers). A bilayer consists of hydrophobic lipid chains (d_{chains}) with hydrophilic lipid heads (d_{heads}) on either side. Neighbouring membranes are separated by an inter water layer (d_{solution}). The repeat distance (d) is measured by scattering experiments. The figure is inspired by [18].

Katherine Burr Blodgett developed (together with Irving Langmuir) the Langmuir-Blodgett technique which enables one to coat solid substrates with lipid monolayer, bilayer or even multibilayer systems [19]. Irving Langmuir's work in surface chemistry was well recognized and awarded the Nobel Prize in 1932. Multi-bilayers, or simply multilayers, consist of a stack of bilayers. For a multilayer system at least two different forces must be taken into account to describe the interactions between the individual lipid membranes according to the DLVO theory [20, 21]:

- The hydration forces due to the repulsion of the opposing hydrated head group layers decays as $e^{-d_{\text{solution}}/\lambda_0}$, with d_{solution} being the width of the interstitial water layer between the membranes and a decay length λ_0 of about 2 Å [22, 23]. Its contribution is purely short ranged [24].
- The attractive Van der Waals forces are due to dipole-dipole attraction of opposing membranes. The force scales with d_{solution}^{-3} [23].

In addition, thermodynamic fluctuations result in a repulsive force:

- The repulsive undulation force is generated by undulations in the membranes and scales with the inverse of the bending rigidity κ [25].

Furthermore, the adsorption of charged molecules at the former neutral lipid membrane leads to an additional repulsive contribution between individual lipid membranes [24]:

- Electrostatic repulsions between charged molecules, adsorbed at opposing membranes have to be taken into account.

Above contributions have been confirmed by X-ray diffraction experiments on dipalmitoylphosphatidylcholine (DPPC) membrane systems [26]. In pure water without any further additions the membranes have a thickness of 65 Å [26]. After incubation of DPPC lipid membranes in a solution of 10 mM MgCl₂ in water a lamellar swelling of around 150 Å

was observed [26]. Here, the adsorption of Mg^{2+} ions on opposing membranes increased the electrostatic repulsion. It could also be shown in theoretical studies that the combination of attractive van der Waals forces with repulsive electrostatic interactions can even yield a static repeat distance of around 250 Å [24, 27].

Lamellar phases

Lipid bilayers (membranes) occur in different lamellar phases, depending on water content, temperature and pressure (Figure 5). The phase transitions are connected to hydrocarbon chain-melting. In general it can be stated, that with increasing temperature the probability for rotations in the hydrocarbon chains increases, resulting in decreasing order of the lipid chains and increasing lateral diffusion [28]. This transitional behaviour is typical of second order phase transitions [29]. However, at critical points in the phase diagram first order phase transitions occur, accompanied with sharp changes of the system entropy and ordering [18, 30, 31]. In the following some of the main lamellar phases with their common nomenclature are listed in order of their appearance with increasing temperature [32, 33]. The Latin letters describe the type of long range order: L stands for one-dimensional lamellar and P for two-dimensional inclined. The lower case Greek letters describe the conformation of the chains: α stands for disordered (fluid) and β' for ordered and tilted (gel).

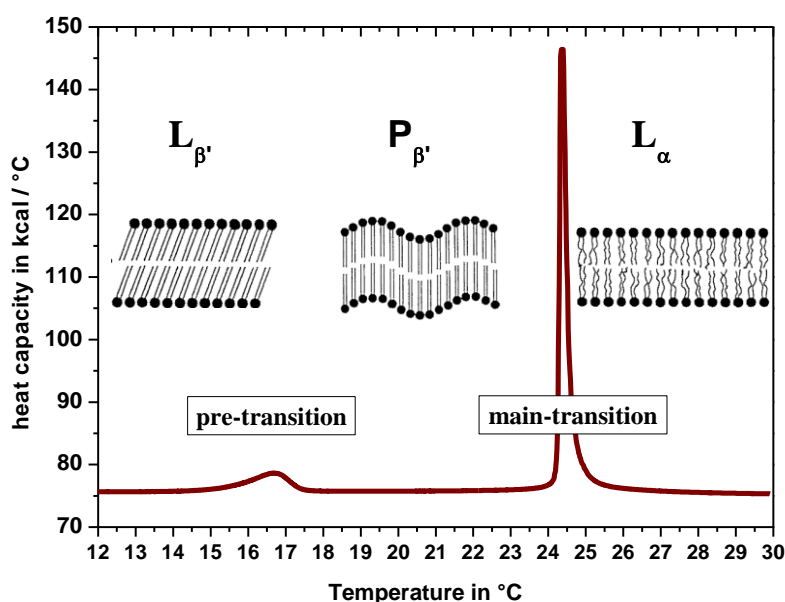


Figure 5: Calorimetric melting profile of 1,2-dimyristoyl-*sn*-glycero-3-phosphocholine (DMPC) lipid vesicles in pure D_2O . The used calorimetric setup is described in chapter 3.2.1 (on page 24) and the measurement itself in chapter 6.2 on page 117. Inserted sketches, displaying the membrane structure, are from [34].

- $L_{\beta'}$ phase: In the gel phase the bilayers appear almost flat, with a long-range in plane order. The lipid chains are mostly ordered in an all-trans configuration and tilted with respect to the membrane normal.
- $P_{\beta'}$ phase: This phase, the ripple phase, is characterized by periodic undulations in the membrane surface [35], the long-range order is lost. The origin of the ripples is probably due to the coexistence of lipid patches in the $L_{\beta'}$ phase and patches in the L_{α} phase [35].
- L_{α} phase: This is the fluid phase or liquid-disordered phase with chain disorder. The chains show kink conformations, resulting in a shortened chain layer thickness by 1.27 Å and an increased cross-sectional area per lipid molecule [31, 36]. Here, the average bilayer thickness decreases, accompanied by the appearance of *free* volume in the bilayer, thus the diffusion of individual lipids or small molecules through the bilayer increases. However, the membrane appears almost flat.

The first order phase transition from the $L_{\beta'}$ to $P_{\beta'}$ phase is a pre-transition, which transfers the planar bilayer to the ripple phase [37]. In the present work we shall only be concerned with the main phase transition from $P_{\beta'}$ to L_{α} phase, which occurs at a critical temperature T_m .

Anomalous swelling

Concerning the bilayer structure, a swelling behaviour around the phase transition takes place. Interestingly, the swelling cannot be explained by changes in the hydrocarbon chains alone [38]. As the origins of the additional swelling by 1 to 2 Å (for DMPC) [18, 39] and a nonlinear swelling behaviour [40] are not fully understood, a challenging puzzle remains, which is discussed widely in the literature and is referred to as anomalous swelling [38, 39, 41-43]. Many studies emphasize that the anomalous swelling results from an increase of the water layer thickness d_{solution} [44, 45]. It is reported that undulations or fluctuations in the bilayer membrane around the phase transition increase [43, 44]. Consequently, the steric repulsion between two bilayers is enhanced when approaching the phase transition temperature, resulting in a swelling of the water layer [41]. In contrast, other groups report, that the swelling is caused by a critical straightening of the hydrocarbon chains. Furthermore, it is reported that only little change of membrane undulations takes place [46]. The discussion about the origins of the anomalous swelling is still ongoing and controversially held [43].

Unbinding

One would expect a bilayer to unbind irreversibly from its neighbouring membranes once the attractive van der Waals interaction is overcome by the repulsive undulation force (compare DLVO theory on page 18), resulting from a softening of the bilayer with increasing temperature [20, 21]. Although the term “unbinding” is used frequently in literature, it often also refers to the swelling of lipid bilayers [47]. However, here the term is used to describe the irreversible process, which provokes freely dispersed bilayers and reduces the number of substrate-bound membranes.

DMPC

The present study is focused on the phospholipid 1,2-dimyristoyl-*sn*-glycero-3-phosphocholine (DMPC). The polar head group contains a phosphate and a choline group. The tail group consists of two aliphatic hydrocarbon chains, each having 14 saturated carbon atoms (Figure 6). DMPC lipid molecules undergo a first order phase transition from the ripple phase P_{β} to a liquid-like phase L_{α} between 21.5 °C and 24.2 °C [29, 48-50]. The manufacturer quotes a transition temperature of 23 °C for the material used in this work [51]. The main phase transition temperature increases when lipids are dissolved in heavy water (D_2O) to a value of 24.5 °C [46, 50]. The authors suggest, that this observation is an indicator of water present close to the hydrocarbon chain groups of the lipids: An increase in enthalpy and therefore in the transition temperature is caused by melting of structured water around the lipid chain groups.

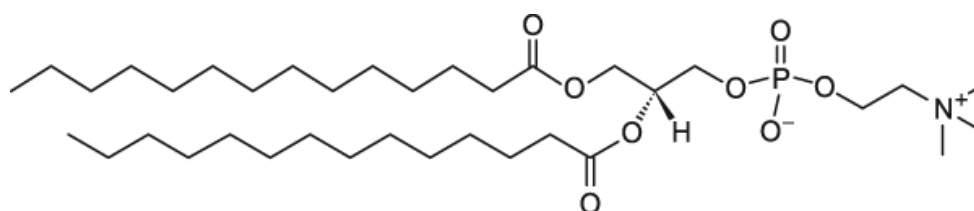


Figure 6: Schematic structure of 1,2-dimyristoyl-*sn*-glycero-3-phosphocholine (DMPC) taken from [51].

2.2 Hyaluronic acid

In 1934 Karl Meyer and John W. Palmer reported about a substance “unique in higher animals, and may be best compared with some of the specific polysaccharides of bacteria.” They discovered an acid from the vitreous humour of a “fresh cattle” for which they proposed, “for convenience, the name ‘hyaluronic acid’, from hyaloid (vitreous) + uronic acid.” [52]

Hyaluronic acid (HA), also called hyaluronan, is found in the extracellular matrix of mammals as soft connective tissue. In 1954, 20 years after its announcement, Meyer published an article with the chemical structure of HA [53]: Altering units of glucuronic acid and N-acetylglucosamine, linked with glycosidic bonds, make up this high molecular weight polysaccharide (Figure 7). The disaccharide has an average length of ≈ 1 nm. The molecular weight can range from 6000 – 8000 kDa [54], with an approximated end-to-end length of 15 μ m [55]. In solution, at pH = 6.0, HA is negatively charged, because 90% of the carboxyl groups are ionized [56]. A HA molecule forms random coil structures, counterbalancing the electrostatic repulsion of hydrogen bonds and hydrophobic interactions [57]. At higher concentrations, HA molecules can form network-like structures through interactions of hydrophobic patches of different molecules [58].

HA is a major component of the synovial fluid in natural joints, with a concentration of 2 to 4 mg/mL [59]. As a natural occurring molecule synthesized by cultured streptococci, HA is used in a number of medical applications. For example, HA is injected in the knees of patients for the treatment of osteoarthritis [60] and for a variety of applications in ophthalmic medicine [61].

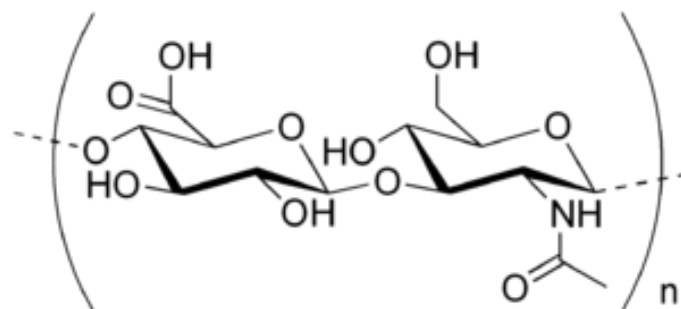


Figure 7: Schematic structure of hyaluronic acid (HA) from [62].

3. Experimental section

The technical aspects of the performed experiments are presented in this chapter. First, a list of the used chemicals is given (chapter 3.1). Second, the theoretical framework and the experimental setups are described (chapter 3.2). In the third part, different preparation methods for lamellar lipid coatings are introduced (chapter 3.3).

3.1 Used Chemicals and substrates

Lipids

1,2-dimyristoyl-*sn*-glycero-3-phosphocholine (DMPC) lipid was purchased from Avanti Polar Lipids [51] and used without further purification.

Hyaluronic Acid

Hyaluronic acid (HA, sodium salt, streptococcus sp.) within a molecular weight range of $M_w = 769000$ was purchased from Merck [63] and used without further purification. Liquid phases were either pure D_2O or solutions of 3 mg/mL hyaluronic acid (HA) in D_2O . HA was dissolved in D_2O by stirring for 20 minutes with a magnetic stirrer.

Solvents

Ultrapure Water (H_2O) was obtained by using a Milli-Q purification system (resistance > 18.2 MOhm·cm) [64]. Deuterium dioxide (D_2O , purity ≥ 99.9 atom % D) and ethanol (absolute puriss. p.a.) was purchased from Sigma-Aldrich [65]. Chloroform (Uvasol grade) was purchased from Merck [66].

Substrates

Disc-shaped silicon substrates (60 mm in diameter and 10 mm thickness) were used for measurements in a pressure cell. For measurements in a shear setup, disc-shaped silicon substrates with a diameter of 100 mm and a thickness of 10 mm have been employed. In addition, for temperature dependent measurements, block-shaped silicon wafers (80 mm length x 50 mm width x 15 mm thickness) were used. Special substrates for combined measurements on the neutron reflectometer V18 are described in chapter 4.1 on page 57. All substrates were supplied by Siliziumbearbeitung Andrea Holm (Tann/Ndb., Germany, [67]). Before use, all substrates were cleaned for one hour in an ethanol bath and subsequently rinsed for 10 min in ultrapure water, resulting in a purely hydrophobic surface.

3.2 Sample characterization

As a straightforward method to study the interrelation of the selected joint components DMPC and HA, differential scanning calorimetry was used and is described in chapter 3.2.1. Infrared spectroscopy was employed to obtain a more detailed picture. Here, interactions of HA and DMPC and the impact of HA on the phase transition of DMPC can be probed on a molecular scale (chapter 3.2.2). In the present work the samples were mainly characterized by the use of X-rays and neutrons. Both kinds of probes obey the general laws of wave optics, which will be described in chapter 3.2.3. On the basis of these general laws, the reflectometry technique will be introduced in chapter 3.2.4. Here, X-rays and neutrons are introduced as the probing “waves”. Furthermore, the instruments utilized for neutron reflectometry measurements are described in chapter 3.2.5. In addition, different sample environments for neutron reflectivity measurements have been provided by the use of a shear setup (chapter 3.2.6) and a high pressure cell (chapter 3.2.7). The utilized X-ray reflectometer is introduced in chapter 3.2.8.

3.2.1 Differential scanning calorimetry

Differential scanning calorimetry (DSC) is a technique for studying the thermotropic phase behaviour of hydrated lipid dispersions [68]. The measurements are performed by simultaneously heating a sample and a reference. The reference should be of comparable heat capacity without thermotropic events in the temperature range of interest. Sample and reference cells are equipped with independent heating units and thermo elements (Figure 8). Upon simultaneously heating, the temperature of sample and reference is equal, if far from any thermotropic events of the sample. In the case of a thermotropic event, a temperature difference between sample and reference appears. In order to compensate the different rates in heat flow the instrument actively changes the power input for the sample cell to approach a zero temperature difference between the two cells. The difference in heat output ΔP is the DSC measuring signal, displayed as the difference in heat capacity Δc_p as a function of temperature or time:

$$\Delta c_p = \frac{\Delta P}{r} \qquad \text{Equation 3.1}$$

using the heating rate r . In case of non-thermotropic events a straight, horizontal baseline is

seen. An endothermic event is reflected by a positive peak, while an exothermic event by a negative peak.

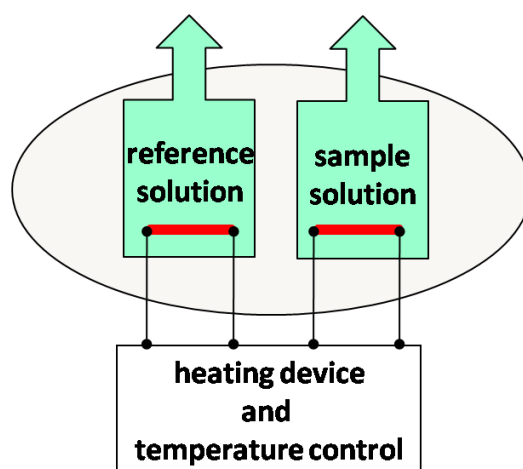


Figure 8: Schematic diagram of a differential scanning calorimetry (DSC) instrument.

Differential scanning experiments were performed on a microcalorimetry system (MicroCal Inc., Northampton, MA) at the Max Planck Institute of Colloids and Interfaces (Golm/Germany) [69]. The reference cell and the sample cell had a volume of 1.2 mL. The lipid sample solutions were prepared by dissolving DMPC in chloroform in a glass beaker. Afterwards the solvent was evaporated under vacuum, leaving behind a thin film of lipids at the glass wall. In the following step the lipids were diluted again to a final concentration of 2.5 mg/mL, either in pure D₂O or in a solution of 3 mg/mL HA in D₂O. After hydration the lipid solutions were mixed for 5 min using a vortex mixer. The lipid solutions were prepared one day before the measurements and stored at room temperature. Reference solutions were either pure D₂O or a solution of 3 mg/mL HA in D₂O. Shortly before the measurement, reference and sample solutions were degassed for 10 min by slow stirring under vacuum. The heating rate r for the measurements was set to 1 °C per minute.

3.2.2 Infrared spectroscopy

In infrared (IR) spectroscopy the interaction of electromagnetic waves with molecules is utilized as a tool for structural analysis. In general, molecules can absorb energy of an electromagnetic wave in the infrared region. The amount of absorbed energy is specific for the vibrational modes of a molecule. Therefore, the type of bonds and atoms involved can be identified. Furthermore, infrared spectroscopy makes it possible not only to identify certain molecules, but to obtain knowledge about deformation of its bonds. A detailed description of the technique can be found elsewhere [70, 71].

Vibrational modes

A vibrational mode can be compared to the motion of two bodies, with masses m_1 and m_2 , connected with a spring, as described by the theory of harmonic oscillators. While in the spring-mass system the resonance frequencies depend on the reduced mass and the spring constant, the vibrational modes in a molecule can be qualitatively described by the reduced mass and the strength of the atomic bonds. In general, the resonance frequency of the oscillation is higher for stronger bonds or lighter masses. As a molecule lies within the boundaries of quantum mechanics, a more realistic description of the possible resonant states of a molecule can be obtained by the quantum mechanical description of a harmonic oscillator. Here, a harmonic oscillator can only take up discrete energy levels. A solution for Schrödinger's equation for the vibrational energy levels of a molecule in the harmonic approximation is:

$$E_n = h \cdot \nu \cdot \left(n + \frac{1}{2} \right) \quad \text{Equation 3.2}$$

with n being the vibrational quantum number ($n = 0, 1, 2, \dots$), ν the frequency and h Planck's constant. Within this description the resonance condition is only fulfilled, if the energy of a light quantum E_{ph} (photon) matches the energy difference ΔE_{vib} of two discrete energy levels of a molecule ($\Delta n = \pm 1$):

$$E_{ph} = h \cdot \nu \quad \text{Equation 3.3}$$

$$\Delta E_{vib} = E_{n+1} - E_n = h \cdot \nu \quad \text{Equation 3.4}$$

The vibration frequency ν of a molecule depends on the reduced mass μ of the system and

the strength of the bond k :

$$v = \frac{1}{2\pi} \sqrt{\frac{k}{\mu}}; \quad \mu = \frac{m_1 \cdot m_2}{m_1 + m_2} \quad \text{Equation 3.5}$$

Furthermore, six different types of vibrational modes in a molecule with more than two atoms are known: Scissoring, δ_s , rocking, ν_{ro} , wagging, ν_{wa} , twisting, ν_{tw} , and symmetric, ν_s and asymmetric, ν_{as} stretching. An animated overview can be found in [72].

FTIR

Fourier transform infrared spectroscopy (FTIR) enables probing a sample simultaneously with a whole spectrum of frequencies. A main component of an FTIR spectrometer is a Michelson interferometer, which was introduced by Albert Michelson in 1887 [73]. In a Michelson interferometer an electromagnetic wave is guided to a beam splitter, which transmits part of the wave and reflects the other (Figure 9). The transmitted part will then be reflected from a static mirror, while the reflected part will be reflected from a mirror moving with a constant velocity. Afterwards both parts will be superimposed again at the beam splitter. Depending on the path difference, g , set by the position of the moving mirror, electromagnetic waves can interfere in a constructive or destructive way. The measured intensity S as a function of path difference g is called an interferogram, described by the following relation [71]:

$$S(g) = \int_0^{\infty} I(\nu) \cos(2\pi\nu g) d\nu \quad \text{Equation 3.6}$$

with $I(\nu)$ being the intensity of the infrared spectrum as a function of the frequency ν .

According to Jean Baptiste Joseph Fourier (1768 – 1830) it is possible to describe every mathematical function with the superposition of sine and cosine functions, also known as Fourier analysis [74]. An interferogram is a superposition of the cosine functions of the original wavelength spectrum $I(\nu)$, which can be obtained by applying a Fourier transformation:

$$I(\nu) = \int_{-\infty}^{+\infty} S(g) \cos(2\pi\nu g) dg \quad \text{Equation 3.7}$$

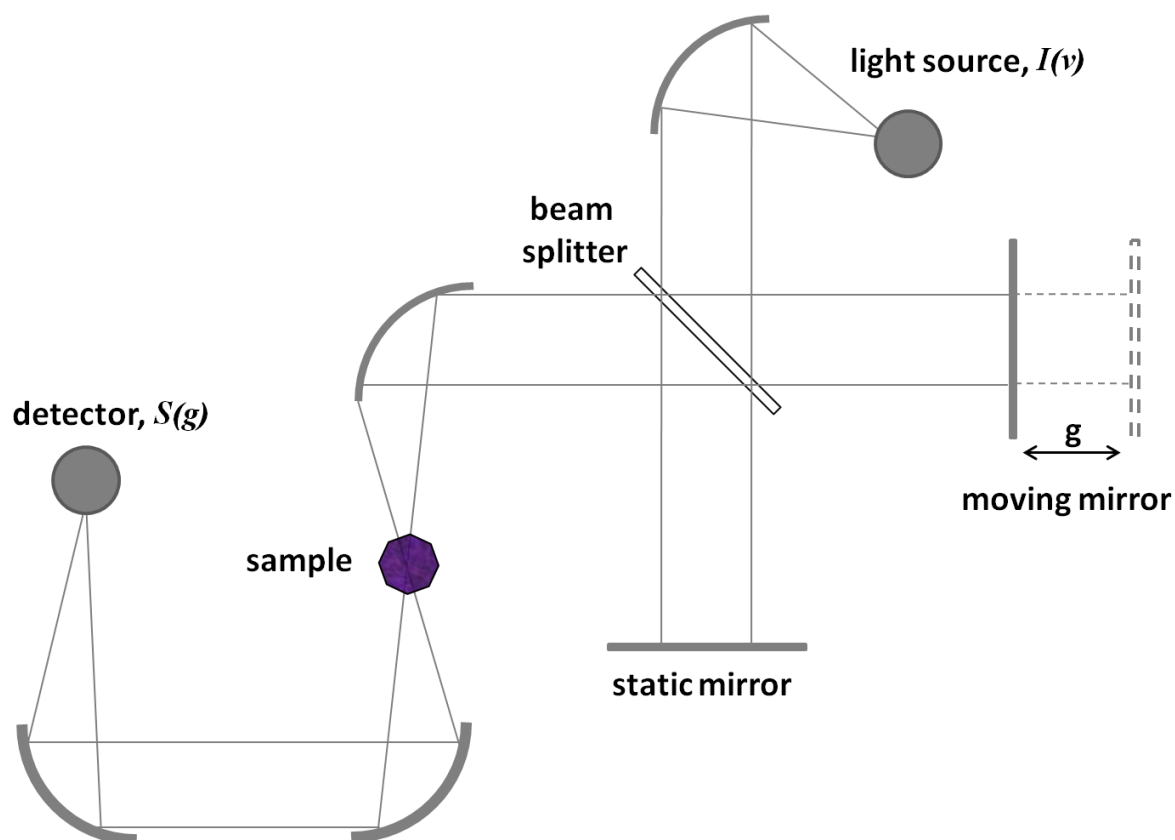


Figure 9: Schematic diagram of a FTIR setup with a Michelson interferometer.

In order to verify the interaction of the sample with the infrared light its absorbance is determined, defined by the Beer-Lambert law [75, 76]:

$$\text{absorbance}(\nu) = -\ln\left(\frac{I(\nu)}{I_0(\nu)}\right) \quad \text{Equation 3.8}$$

with the initial intensity I_0 of the incoming wave. It is common to display the absorbance as a function of the wavenumber $\tilde{\nu}$, as it is proportional to the energy E of the electromagnetic wave [75]:

$$\tilde{\nu} = \frac{E}{h \cdot c} = \frac{\nu}{c} \quad \text{Equation 3.9}$$

with c being the speed of light in vacuum and h Planck's constant. $\tilde{\nu}$ is given in units of cm^{-1} .

ATR

For surface sensitive measurements at a solid–liquid interface the attenuated total reflectance (ATR) sampling technique is widely used. It was introduced by N.J. Harrick in 1960 [77]. Here, the existence of an evanescent electric field in total reflection geometry is used in order to analyze the penetrated medium. Even if a wave is totally reflected at an interface between two media, the reflected wave penetrates the adjacent medium. Upon penetration the wave interacts with the medium and energy can be absorbed according to the resonance conditions (Equation 3.3 - Equation 3.4). The ATR technique is sensitive to an interface within the penetration depth d_p , which is defined as the depth at which the amplitude of the evanescent wave has only $\frac{1}{e}$ (~ 37%) of its initial amplitude [77]

$$d_p = \frac{\lambda_{n_1}}{2\pi \sqrt{\sin^2 \alpha_{in} - \left(\frac{n_2}{n_1}\right)^2}} \quad \text{Equation 3.10}$$

(cf. Figure 11 on page 32). Here, λ_{n_1} is the wavelength of the reflected wave in the initial medium with a refractive index of n_1 . The refractive index of the opposing medium is n_2 and α_{in} is the angle of incidence. As a rule of thumb, a totally reflected electromagnetic wave penetrates the interfacial region of the opposing medium by about one tenth of its wavelength. For example, if an electromagnetic wave with a wavelength of $\lambda = 6.45 \mu\text{m}$ travels through silicon ($n_1 = 3.4$) and is reflected at a water interface ($n_2 = 1.3$) at an angle of $\theta = 45^\circ$, the wave penetrates $d_p = 0.51 \mu\text{m}$ into the water.

Used lab setup

ATR-FTIR experiments were in part performed with a commercially available in situ unit (BioATR II, Bruker Optik GmbH, Germany), as shown in Figure 10. Here, a special mirror setup guides the infrared wave through a silicon internal reflection crystal. After 11 internal reflections and a total path length of 6-8 μm in the liquid phase, the beam leaves the crystal at the inclined exit surface (45°) to the detector. The crystal has a circular sampling area of 2 mm and is the bottom part of a sample chamber. For in situ measurements the sample chamber can be filled with up to 30 μl of liquid phase. The sample cell can be tempered by using an independent closed water circuit, which is connected to an external water bath. The ATR unit was integrated in the measurement chamber of a Tensor 27 FTIR spectrometer from Bruker Optik GmbH, Germany. ATR-FTIR spectra were recorded with a liquid nitrogen

3. EXPERIMENTAL SECTION

cooled mercury cadmium telluride (MCT) detector using a spectral resolution of 4 cm^{-1} and 128 scans per spectrum. Data processing was carried out with the Opus 6.5 software package (Bruker Optik GmbH, Germany). For coating the silicon crystal with lipids, the sample chamber was filled with $20\text{ }\mu\text{L}$ of a 10 mg/mL solution of DMPC in chloroform, with the chloroform evaporating overnight. This resulted in a lipid multilayer film. For in situ measurements the sample chamber was afterwards filled with $30\text{ }\mu\text{L}$ of liquid phase and closed.

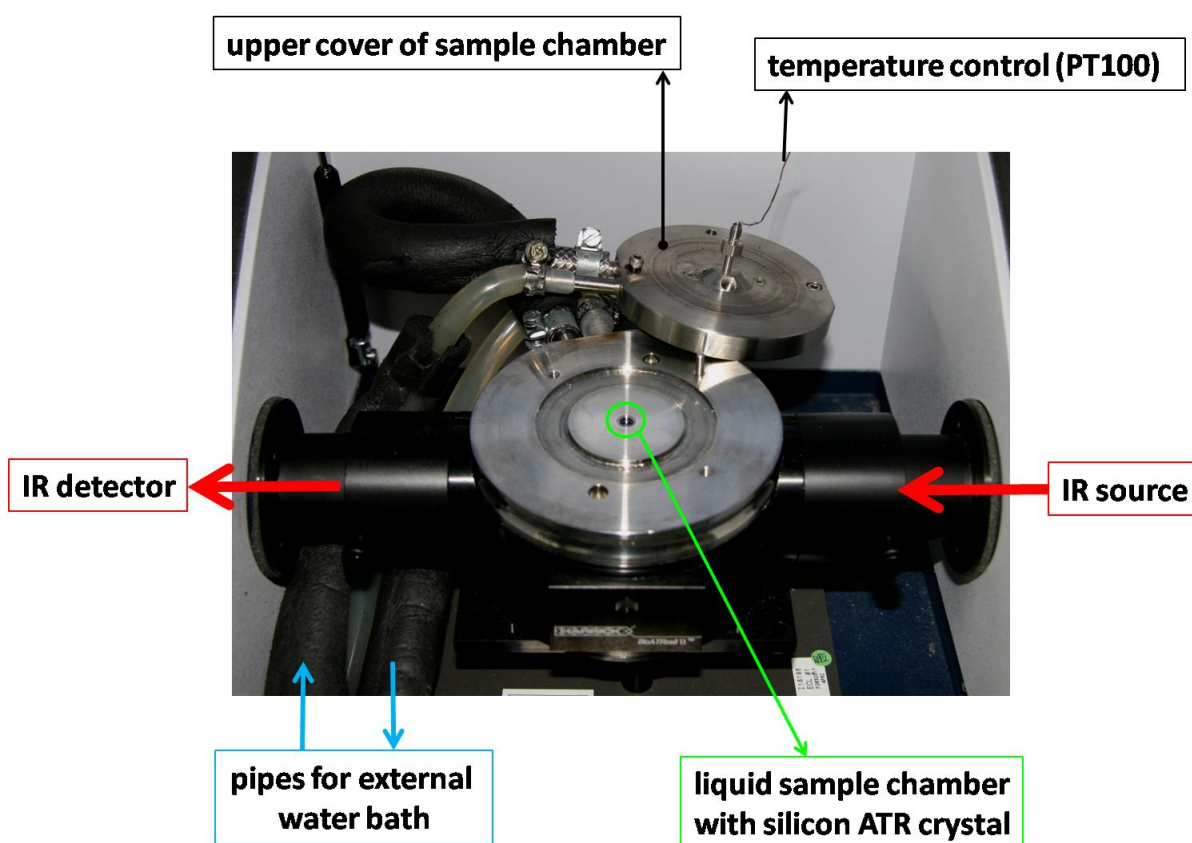


Figure 10: Photograph of BioATR II setup for ATR-FTIR measurements.

3.2.3 The general laws of wave optics

When an electromagnetic wave hits an interface it can be absorbed, reflected or refracted [75]. The angle between incident wave and interface, α_{in} , equals the angle between reflected wave and interface, α_r (Figure 11):

$$\alpha_{in} = \alpha_r \quad \text{Equation 3.11}$$

The scattering geometry for the refracted wave is described by Snell-Descartes' law:

$$n_1 \cos(\alpha_{in}) = n_2 \cos(\alpha_t) \quad \text{Equation 3.12}$$

with n_1 and n_2 being the refractive indices of the initial and traversed medium, respectively, α_t the angle between transmitted wave and surface. Equation 3.12 implies the existence of a critical angle α_c :

$$\alpha_c = \sin^{-1} \left(\frac{n_2}{n_1} \cdot \sin(90^\circ) \right) = \sin^{-1} \left(\frac{n_2}{n_1} \right) \quad \text{Equation 3.13}$$

In this case, the transmitted wave propagates parallel to the surface ($\alpha_t = 0^\circ$). The refractive index n describes in general the ratio between the phase velocity of a wave in vacuum c (speed of light for electromagnetic waves) and the velocity in the transmitted medium v :

$$n(\lambda) = \frac{c}{v(\lambda)} \quad \text{Equation 3.14}$$

with λ being the wavelength of the wave. As v is wavelength dependent, dispersion occurs for the refracted wave.

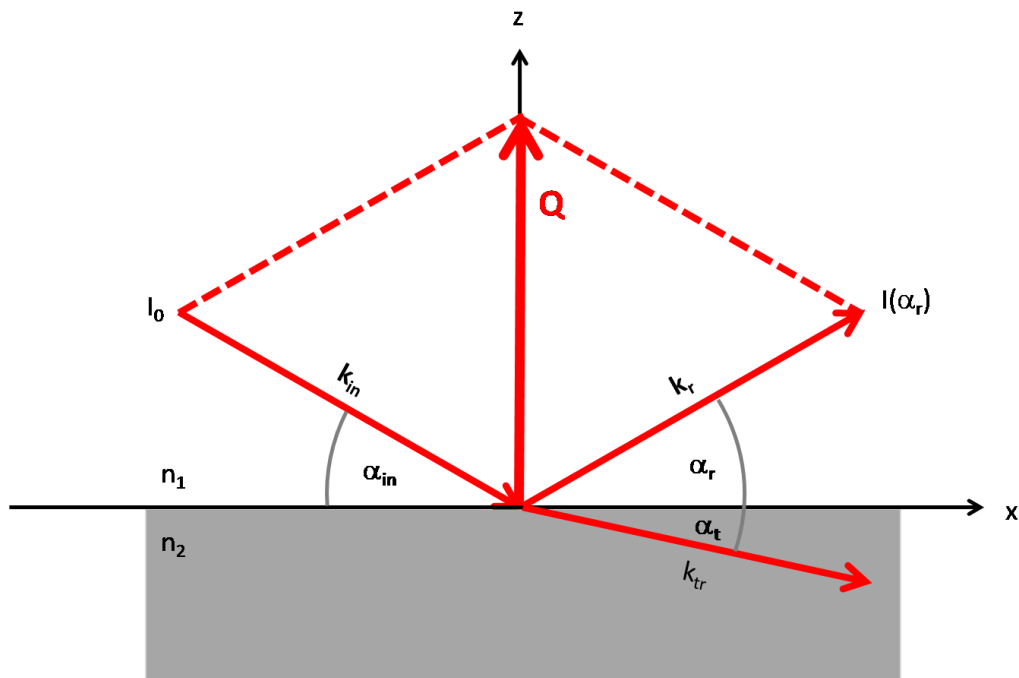


Figure 11: Scattering geometry at a smooth surface for $n_1 < n_2$.

Scattering at a smooth surface

The amplitude of the reflected wave R at a smooth surface is given by Fresnel's equations, which Fresnel derived by applying the wave theory of light at an interface between air ($n_1 = 1$) and a reflecting medium ($n_2 > 1$) [78]:

$$R(\alpha_{in}) = \frac{I(\alpha_r)}{I_0} = |r^{fr}|^2 \quad \text{Equation 3.15}$$

using Fresnel's reflectivity coefficient, which is for small grazing angles of incident independent of the electric field polarization of the wave [78] and given by

$$r^{fr} = \frac{\sin \alpha_{in} - n_2 \sin \alpha_t}{\sin \alpha_{in} + n_2 \sin \alpha_t} \quad \text{Equation 3.16}$$

As the angle of incident α_{in} is usually the experimental parameter, Equation 3.16 can be written as

$$r^{\text{fr}} = \frac{\sin \alpha_{\text{in}} - \sqrt{n_2^2 \cos^2 \alpha_{\text{in}}}}{\sin \alpha_{\text{in}} + \sqrt{n_2^2 \cos^2 \alpha_{\text{in}}}} \quad \text{Equation 3.17}$$

by applying Snell-Descartes' law (Equation 3.12). If no absorption occurs, the transmittance satisfies the relation

$$T = 1 - R \quad \text{Equation 3.18}$$

3.2.4 Reflectometry

In 1895 W.C. Röntgen published an article about a new kind of rays. The rays seemed not to be useful for scattering experiments, since he could “not conclude any regular reflection or refraction of the X-rays” [79, 80]. This was not questioned until Compton pointed out in 1924, that the refractive index n of a medium for X-rays can be less than unity [81]. According to the laws of optics it should be therefore possible to reflect X-rays at a surface between two media in a predictable way. X-ray reflectometry (XR) at a smooth surface was first demonstrated in 1927 by J.A. Prins [82].

“The one to one correspondence between reflection of electromagnetic waves and particle waves is well known” [83]. Following this approach, the laws of optics as described in chapter 3.2.3 are adaptive for X-rays and neutrons. Here, neutrons can be described by the Compton wavelength λ of a quantum mechanical particle:

$$\lambda_n = \frac{h}{m_n \cdot c} \quad \text{Equation 3.19}$$

with λ_n the wavelength of a neutron with mass m_n . If no magnetization occurs, the refractive index n for X-rays and neutrons can be written as:

$$n = 1 - \delta - i\beta \quad \text{Equation 3.20}$$

with δ describing the dispersion and β being the absorption coefficient. The latter is neglected in the present work, as it is small for the samples investigated. The relation for δ is

different for X-rays and neutrons, which is not surprising, since X-rays interact with the electron shell of an atom and neutrons with the core of an atom.

$$\begin{array}{cc} \delta \text{ for X-rays:} & \delta \text{ for neutrons:} \\ \hline \delta_x = \frac{\lambda_x^2}{2\pi} r_e \rho_e & \delta_n = \frac{\lambda_n^2}{2\pi} b \rho_n \end{array} \quad \text{Equation 3.21}$$

with r_e the electron radius, ρ_e the electron density, b the coherent scattering length for neutrons and ρ_n the atomic density [78]. In vacuum and approximately in air $n = 1$ for X-rays and neutrons. For X-rays the values for ρ_e increase linearly with the atomic number of an atom in its non-ionized state and are always smaller than one in a medium. For neutrons on the other hand such a trend for b does not exist, since the neutrons interact with the nuclear potential of the atoms. This has the effect, that b varies for different isotopes, which is used as an advantage for probing biological samples: The large difference in b for hydrogen (H) and deuterium (D) allows contrast variation measurements [84]. Here, the contrast of different parts of a sample can be enhanced by changing specific H atoms against D atoms.

Scattering length density

Equation 3.21 fully characterizes δ for layers of a pure material, if b is known (for measurements using neutrons). However, in the case of liquids and polymers, $b\rho_n$ can be replaced by an averaged coherent scattering length, the scattering length density (SLD):

$$SLD = \frac{\sum_{i=1}^n b_i}{V} \quad \text{Equation 3.22}$$

with b_i being the coherent scattering length of the i^{th} atom, n the total number of atoms and V the volume for a unit cell or molecule [85, 86]. For X-rays, $r_e\rho_e$ can be replaced by SLD calculated with $Z_i \cdot r_e$ instead of b_i with Z_i being the atomic number of the i^{th} atom. SLD is given in units of [\AA^{-2}].

Furthermore, the SLD of a layer or colloid, consisting only of substance A with a volume fraction φ_A and substance B with a volume fraction φ_B , can be calculated:

$$SLD(layer) = \varphi_A \cdot SLD(A) + (1 - \varphi_A) \cdot SLD(B) \quad \text{Equation 3.23}$$

with $\varphi_A + \varphi_B = 1$. Typically, SLD(A) and SLD(B) are calculated by using Equation 3.22 and SLD(layer) is measured in a scattering experiment, in order to obtain φ_A and φ_B .

Momentum transfer Q

Since X-rays and neutrons can be described by the theory of quantum mechanics, in the following the formalism introduced 1926 by E. Schrödinger will be used [87]. This has the advantage of being able to describe all reflectivity measurements independent of wavelength and angle as a function of the wavevector transfer Q (Figure 11). In quantum mechanics X-rays and neutrons are described by wave functions:

$$\Psi(\vec{r}) = I \cdot e^{\vec{k} \cdot \vec{r}} \quad \text{Equation 3.24}$$

with \vec{r} being the position in three dimensional space at time t and the amplitude I . The wavevector \vec{k} has an absolute value of:

$$|\vec{k}| = \frac{2\pi}{\lambda} \quad \text{Equation 3.25}$$

The momentum of a wave is defined by:

$$\vec{p} = \frac{h}{2\pi} \vec{k} \quad \text{Equation 3.26}$$

using Planck's constant h . Reflection at an interface results in a change of the propagation direction and therefore in a momentum transfer \vec{Q} :

$$\vec{Q} = \vec{k}_r - \vec{k}_{in} \quad \text{Equation 3.27}$$

with \vec{k}_{in} and \vec{k}_r being the wavevector of the incident wave and reflected wave, respectively.

For the elastic specular reflectivity, i.e. in the plane of incidence with $\alpha_{in} = \alpha_r$, \vec{Q} simplifies to [78]:

$$Q_z = \frac{4\pi}{\lambda} \sin \alpha_r \quad \text{Equation 3.28}$$

which is the projection of the momentum transfer on the z-axis (Figure 11). In the following Q_z is denoted Q .

For completeness, the reflectivity R for $\alpha_{in} > \alpha_c$ can be written as a function of Q :

$$R(Q) = \left(\frac{Q - \sqrt{Q^2 - Q_c^2}}{Q + \sqrt{Q^2 - Q_c^2}} \right)^2 \quad \text{Equation 3.29}$$

using the critical momentum transfer Q_c :

$$Q_c = \frac{4\pi}{\lambda} \sin \alpha_c \quad \text{Equation 3.30}$$

which can be approximated by [88]:

$$Q_c \cong \sqrt{16\pi (SLD_{n_2} - SLD_{n_1})} \quad \text{Equation 3.31}$$

The reflectivity for neutrons with $\lambda = 4.66 \text{ \AA}$ at a smooth air / silicon surface is shown as an example in lab space (angle dependent) and Q-space (Q-dependent) in Figure 12. Here, the angle dependent reflectivity curve can be divided into two parts:

1. For $\alpha_{\text{in}} \leq \alpha_c$ total reflection ($R=1$) occurs. The critical angle α_c is defined by Equation 3.13. If $\left(\frac{n_2}{n_1}\right)$ is greater than one, then total reflection does not occur.
2. At $\alpha_{\text{in}} > \alpha_c$, the reflectivity drops drastically. Therefore, the ordinate is usually shown on a logarithmic scale. An asymptotic behaviour is observed, known as Fresnel reflectivity.

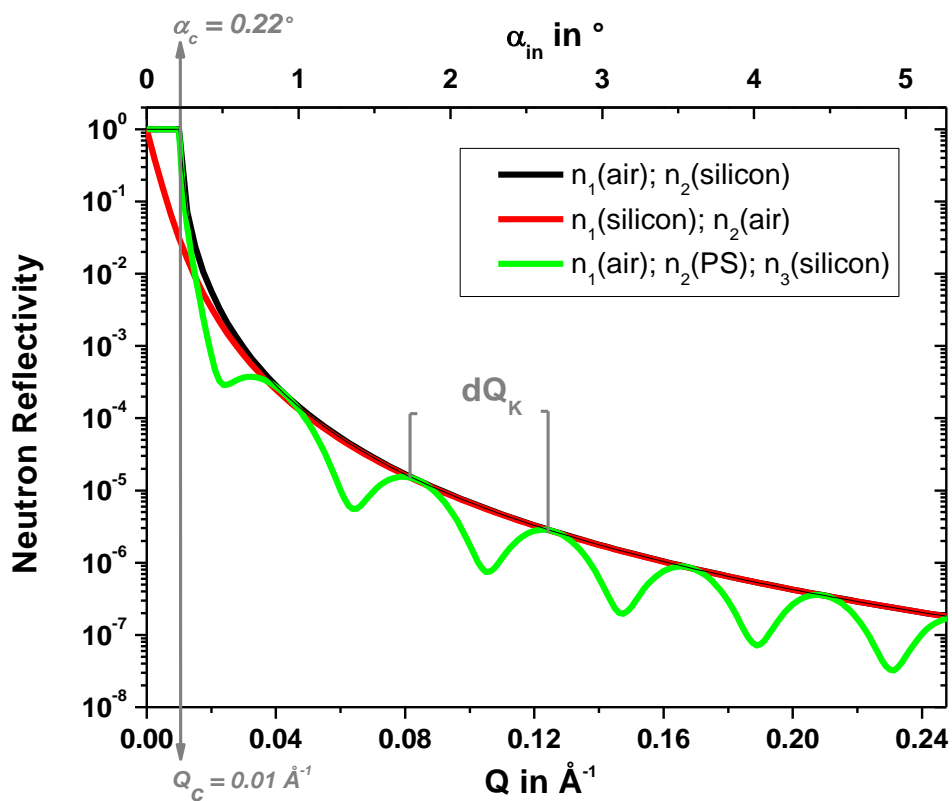


Figure 12: Theoretically calculated neutron reflectivity curves from a smooth interface between air ($SLD = 0$) and silicon ($SLD = 2.07 \times 10^{-6} \text{ \AA}^{-1}$) as a function of Q (bottom abscissa) and in addition as a function of incident angle α_{in} with a neutron wavelength of $\lambda = 4.66 \text{ \AA}$ (top abscissa). The curve in black results from a scattering geometry where the neutron hit the surface from the air-side of the sample and in red from the silicon side. The green curve results from the reflectivity of a 150 \AA thick polystyrene ($SLD = 1.42 \times 10^{-6} \text{ \AA}^{-1}$) coating on a silicon substrate, illuminated from the silicon side. The scattering geometry is displayed in Figure 13.

Reflectivity of thin films

The reflectivity of a surface can change drastically, if a thin layer is adsorbed. Figure 12 shows an example of a reflectivity curve for a 150 Å thick polystyrene (PS) layer on a silicon wafer measured with neutrons of a wavelength of 4.66 Å. Here, additional features due to interference of detected waves appear in the reflectivity curve: Kiessig oscillations (K). The frequency of the oscillations depends on the total layer thickness. In the case of a thin adsorbed layer, e.g. PS, one has to take the reflectivity of an additional interface into account: First, the interface between air and PS, and second, that between PS and silicon. Waves which get transmitted through the first interface can get reflected at the second interface (Figure 13). The reflected waves interfere with each other and an interference pattern is observed at the detector.

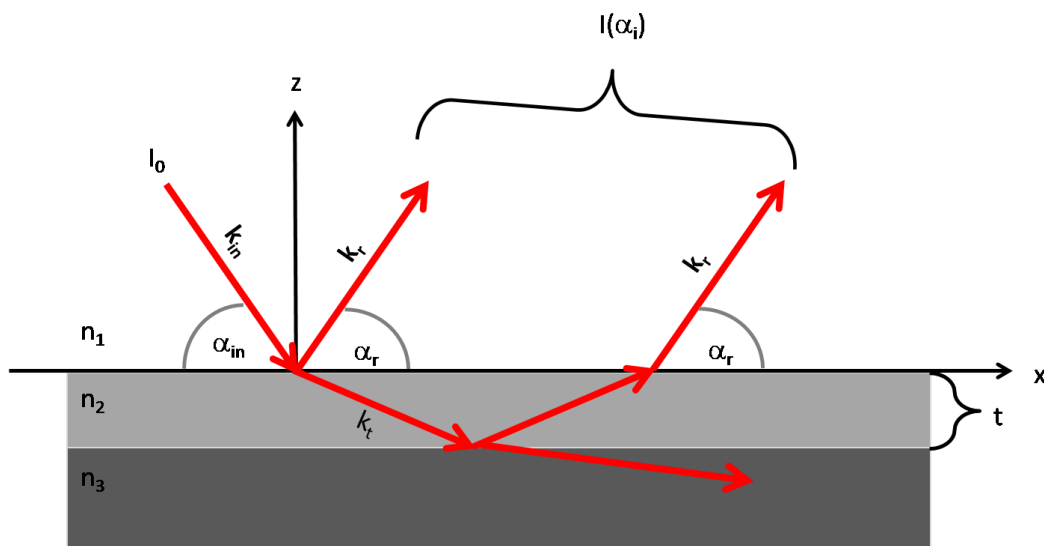


Figure 13: Scattering geometry for thin films with $n_1 < n_2 < n_3$.

Bragg analysis

According to Bragg's law the total film thickness t can be calculated by:

$$t = \frac{2\pi}{\Delta Q_K} \quad \text{Equation 3.32}$$

with the distance ΔQ_K between adjacent Kiessig maxima or minima (Figure 12).

For multilayer coatings, in addition to Kiessig oscillations, a Bragg peak (B) can appear at Q_B . While the total film thickness t is still described by Equation 3.32, the lamellar spacing d can be extracted from Q_B by applying Bragg's law:

$$d = \frac{2\pi}{Q_B} \quad \text{Equation 3.33}$$

In the case where higher order Bragg peaks $Q_{B,h}$ are visible, the following equation is used:

$$d = \frac{2\pi}{m} \quad \text{Equation 3.34}$$

with m being the slope of a plot of $Q_{B,h}$ versus the diffraction order h :

$$Q_{B,h} = m \cdot h \quad \text{Equation 3.35}$$

The number N of repeated units, making up a stack of layers, can now be calculated by:

$$N = \frac{t}{d} \quad \text{Equation 3.36}$$

Peak shape

It is not only the Bragg peak position Q_B that contains information about the multilayer coating, but also width and amplitude of the Bragg peak. Following a relation introduced by Paul Scherrer and initially used for diffraction experiments on single crystals, the full width at half maximum (FWHM) is related to the number of coherent scattering domains N within the sample [89]:

$$FWHM = \frac{K \cdot 2\pi}{d \cdot N} \quad \text{Equation 3.37}$$

with $K = 0.88$ being a shape factor for crystalline systems and d the lattice constant [90]. For reflectivity measurements ($d \cdot N$) can be understood as the correlation length perpendicular to the sample surface with a number of N layers. The amplitude of the Bragg peak is proportional to N^2 with a constant o :

$$\text{amplitude} = o \cdot (N)^2 \quad \text{Equation 3.38}$$

From Equation 3.37 and Equation 3.38 follows, that the integrated area of a Bragg peak is

directly proportional to N:

$$area = \frac{o \cdot K \cdot 2\pi}{d} \cdot N \quad \text{Equation 3.39}$$

In the following, the number of coherent scattering domains N is indexed, depending on the relation used in order to calculate N, namely as N_{BK} (Equation 3.36), N_{FWHM} (Equation 3.37), N_{amp} (Equation 3.38) and N_{area} (Equation 3.39). An illustrated example for the above relations is given in chapter 5.1 on page 67. These relations are derived for purely crystalline systems. For samples with a weak crystalline order, due to roughness or undulations within the scattering domains, additional influences on the Bragg peak shape have to be considered [91].

Optical matrix method

In 1954 Parratt introduced a description for calculating the reflectivity of a multilayer system [92]. He proposed to describe each layer i with a certain thickness d_i and refractive index n_i . Having a number of $i = N$ layers, $i = 0$ is defined as the medium of the incoming wave with infinite thickness and layer $i = N+1$ represents the substrate. For each layer the reflectivity coefficient of the interface between layers i and $i+1$ can be calculated by using Fresnel's equation (Equation 3.15). Please note, that in the following Fresnel coefficient no multiple reflection is implied:

$$r_{i,i+1}^{fr} = \frac{Q_i - Q_{i+1}}{Q_i + Q_{i+1}} \quad \text{Equation 3.40}$$

with Q_i , according to Equation 3.27 on page 35 being

$$Q_i = k_{i,r} - k_{i,in} \quad \text{Equation 3.41}$$

using the wavevector $k_{i,in}$ and $k_{i,r}$ of the incoming (in) and reflected (r) wave in the i^{th} layer, respectively. Starting from the interface between substrate ($i=N+1$) and the attached layer ($i=N$) the reflectivity coefficient $r_{N,N+1}$ can be calculated simply by applying:

$$r_{N,N+1} = r_{N,N+1}^{fr} = \frac{Q_N - Q_{N+1}}{Q_N + Q_{N+1}} \quad \text{Equation 3.42}$$

For the following interface between layer $i=N$ and $i=N-1$ multiple reflections have to be taken into account, as here the reflected waves from both interfaces interfere:

$$r_{N-1,N} = \frac{r_{N-1,N}^{\text{fr}} - r_{N,N+1} \cdot a_N^2}{r_{N-1,N}^{\text{fr}} \cdot r_{N,N+1} + 1} \quad \text{Equation 3.43}$$

With a phase difference of:

$$a_i = \exp(-iQ_i d_i). \quad \text{Equation 3.44}$$

By following this recurrence relation the reflectivity coefficients of each layer have to be calculated. Finally the reflectivity of the multilayer system is given:

$$R(\alpha_{in}) = |r_{0,1}|^2 \quad \text{Equation 3.45}$$

Parratt's approach was implemented by C. Braun in the software package *Parratt32* which enables to analyze reflectivity curves for X-ray and neutron measurements [93]. In the presented work Version 1.6.0 of the software package was used to obtain density profiles of the measured sample.

Fourier analysis

Reflectivity curves containing higher order Bragg peaks can be further evaluated by classical Fourier analysis, known from diffraction experiments [94]. That way it is possible to obtain a scattering length density profile of a single unit cell, $S_{\text{exp}}(z)$, independently from the box-model fitting:

$$S_{\text{exp}}(z) = \frac{2}{d_l} \sum_{n=1}^{n_{\text{max}}} F_n \cos\left(\frac{2\pi n z}{d_l}\right) \quad \text{Equation 3.46}$$

with $z = 0$ being the centre position of a layer and n_{max} the number of appearing Bragg peaks. The scaled structure factor F_n was calculated by using the Lorentz corrected integral intensity of a single Bragg peak of order n [94].

3.2.5 Two ways to build a neutron reflectometer

In general the aim of a reflectometer is to measure the reflectivity $R(Q)$ of a given surface. Since Q (Equation 3.28) is not only depending on the neutron wavelength λ , but also on the incident angle α , different instrumental setups are realized. While the angles can be set by the use of rotation tables with an accuracy of up to 0.001° , the selection of a well-defined neutron wavelength is more sophisticated. Two approaches are used to select neutrons with a known wavelength from the polychromatic neutron beam coming from a neutron source:

1. A beam of monochromatic neutrons can be obtained by using a single crystal as a monochromator, as realized at the V6 instrument. Only neutrons with a certain wavelength λ are reflected under a certain take-off angle θ with respect to the crystal lattice of the monochromator (mc) as defined by Bragg's law, with d_{MC} denoting the lattice spacing:

$$\lambda = 2d_{mc} \cdot \sin \theta \quad \text{Equation 3.47}$$

2. A pulsed white beam approach can be used in a time-of-flight (TOF) instrument as realized at the V18 instrument (BioRef). By measuring the TOF of the neutrons over the distance L from the pulsed source to the detector, the wavelength λ can be determined for every detected neutron through the following relation [95]:

$$\lambda = \frac{TOF \cdot h}{m \cdot L} \quad \text{Equation 3.48}$$

with h being Planck's constant and m the mass of a neutron.

The V6 and V18 instruments are located at the reactor neutron source BER II of the Helmholtz-Zentrum Berlin (Germany).

The V6 neutron reflectometer

A detailed description of the V6 instrument is given elsewhere [88, 96]. In summary, a monochromatic beam with a wavelength $\lambda = 4.66 \text{ \AA}$, selected by a graphite monochromator, is used to measure the reflectivity $R(Q)$ (Figure 14). In addition, the instrument is equipped with a spin polarizer and analyzing setup in order to enable investigations of magnetic interfaces, which was not used for studies presented here. The instrumental resolution is on the one hand limited by the monochromatisation provided by the monochromator and was on the other hand set by a slit system on the incident side to 0.001 \AA^{-1} for $Q < 0.0518 \text{ \AA}^{-1}$ and 0.002 \AA^{-1} , otherwise. The reflectivity curves were recorded step by step (sample rotation) by a ^3He -detector with a complete run from 0.0047 \AA^{-1} to 0.1646 \AA^{-1} consuming typically 7 hours of beam time. The measured intensities were footprint corrected and normalized to the primary intensities [97]. A photograph of the instrument is shown in Figure 15.

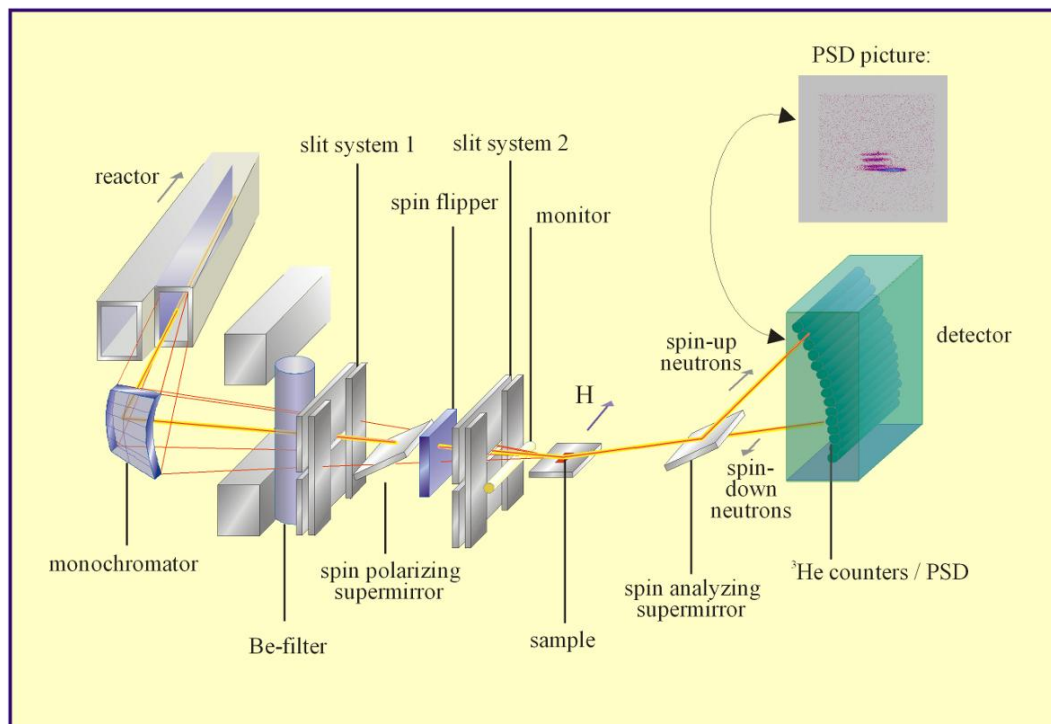


Figure 14: Schematic diagram of the V6 instrument. A graphite monochromator is used to select a wavelength of $\lambda = 4.66 \text{ \AA}$. The angular resolution can be set by the slit system. The neutrons can be detected with several single counters or with a position sensitive detector (PSD).



Figure 15: Photograph with beam line scientists at the V6 instrument.

The V18 neutron reflectometer (BioRef)

At the V18 instrument (Figure 16 on page 47), measurements were performed by using pulses of a polychromatic neutron beam, created by a TOF setup [98, 99]. The heart of the instrument is a chopper system (FZJ, Jülich, Germany), consisting of three discs, which cut the continuous neutron beam coming from the cold neutron source into pulses (Figure 17). All three chopper discs are made of aluminium with a boron carbide ($^{10}\text{B}_4\text{C}$) coating, having a diameter of 600 mm and rotating around an axis parallel to the neutron beam. Windows in the chopper discs allow the neutrons to pass. The first chopper, the master chopper (MC), chops the continuous neutron beam into pulses and defines the beginning of the time measurements.

Here, each pulse still contains the whole wavelength spectrum transmitted from the cold neutron source. In general, the wavelength resolution for a specific wavelength and a certain distance from the pulse source to the detector is determined by the burst time τ of one pulse:

$$\frac{\Delta\lambda}{\lambda} = \frac{\tau}{\text{TOF}(\lambda)} \quad \text{Equation 3.49}$$

In order to achieve a fixed λ resolution, which enhances the efficiency of the instrument, a

λ -dependent burst time $\tau(\lambda)$ is required that fulfils the condition that $\frac{\tau(\lambda)}{\text{TOF}(\lambda)}$ is constant for all λ , i.e. $\tau \sim \lambda$. For this reason a second chopper, slave chopper 1 (SC1), is used. SC1 is mounted downstream on a linear translation stage with a variable distance z_0 to MC. These choppers are operated in such a way, that MC closes exactly when SC1 opens [95]. In such an optical blind mode the burst time τ and the transmission for neutrons increases linearly with λ up to a maximum wavelength of λ_0 which is defined by (Figure 18 on page 48):

$$\lambda_0 = \frac{h}{m \cdot v_0} = \frac{h \cdot w}{m \cdot 360 \cdot z_0 \cdot f} \quad \text{Equation 3.50}$$

with v_0 being the velocity of passing neutrons with the wavelength λ_0 , w the window width in degrees, z_0 the distance between MC and SC1 and f the chopper frequency. The result is a burst time depending on wavelength, yielding a constant wavelength resolution up to λ_0 , calculated by:

$$\frac{\Delta\lambda}{\lambda} = \frac{\tau(\lambda)}{\text{TOF}(\lambda)} = \frac{z_0}{L} = \text{constant} \quad \text{Equation 3.51}$$

with L being the flight path from the point half way between the choppers MC and SC1 to the detector. Different resolutions can now be obtained by changing the position of SC1 and hence the distance z_0 between the choppers: Typically, the SC1-MC distance is set to values between $z_0 = 80$ mm and $z_0 = 400$ mm, corresponding to wavelength resolutions of 1% and 5%, respectively. For optimum performance, the slit system is set to corresponding values of angular resolution [95, 99]. MC and SC1 have a real single window of $w = 26^\circ$. An increase in chopper frequency for MC and SC1 does not influence the wavelength resolution, but decreases the passing wavelength bandwidth. In addition, the neutron flux per time increases for the shorter wavelengths, which compensates the shorter wavelength bandwidth. To cover the whole Q -range up to $Q \leq 0.4 \text{ \AA}^{-1}$, a different number of angular sample positions have to be used, depending on the selected chopper frequency. An overview of the instrumental parameters is given in Table 3.1. A more detailed description of parameters is given in [99].

chopper frequency	wavelength bandwidth	Number of angular settings for $Q \leq 0.4 \text{ \AA}^{-1}$	z_0 for a λ resolution		
			of 1%	of 3%	of 5%
90 Hz	3.9 – 7.9	12	80 mm	240 mm	400 mm
45 Hz	3.9 – 11.9	6	80 mm	240 mm	400 mm
25 Hz	3.9 – 18.3	3	80 mm	240 mm	400 mm

Table 3.1: Overview of instrumental parameters for different operational settings at V18. [99]

A third chopper (SC2), a so-called bandwidth chopper, is installed 3200 mm downstream from MC with a real single window of 126° . SC2 is installed for mainly three reasons (Figure 18 on page 48): first, a wavelength band is chosen such that the passing wavelengths do not exceed λ_0 and therefore only neutrons with a constant wavelength resolution are transmitted, second, to prevent neighbouring pulses to overlap at the detector and third, to choose a range of the spectrum with maximum neutron flux (i.e. to cut the wavelength band at a minimum wavelength of about 4 \AA). In addition, an optional frame overlap mirror (not shown) is mounted in between SC1 and SC2, in order to filter out wavelengths longer than 12 \AA . A more detailed description of the setup is given elsewhere [95, 98, 99].

In the work presented here, the following instrumental parameters were used in the performed experiments: With the selected chopper speed of 45 Hz, a sample was measured at 5 different angular positions to cover a full Q-range from 0.0050 \AA^{-1} to 0.3563 \AA^{-1} consuming typically 1 h of beam time. The relative Q-resolution was selected by the chopper position and the slit system to be 7% over the whole Q-range probed. The scattered neutrons were recorded with a position sensitive area detector (PSD) using a ^3He filled wire chamber.

In addition, the V18 instrument is equipped with an infrared spectrometer. The implementation of this feature was an essential part of the present thesis. This additional FTIR option opens the unique possibility to measure the infrared absorption at total reflection (ATR) and the neutron reflectivity of one sample at the same time. A detailed description of the setup and its implications are given in chapter 4 on page 56.

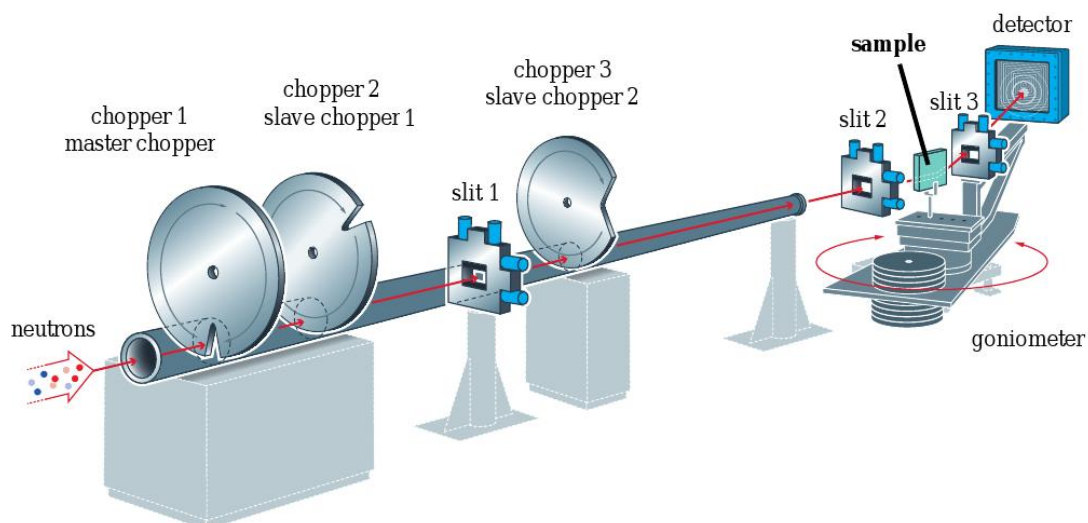


Figure 16: Schematic diagram of the V18 instrument (BioRef). A chopper system enables time-of-flight (TOF) measurements with variable wavelength resolutions. The slit system is set to corresponding values of angular resolutions. A wide range of angular sample positions can be obtained by using a goniometer, in order to cover a Q -range up to 0.4 \AA^{-1} in our case. Finally, the neutrons are detected with a position sensitive detector (PSD).
[100]

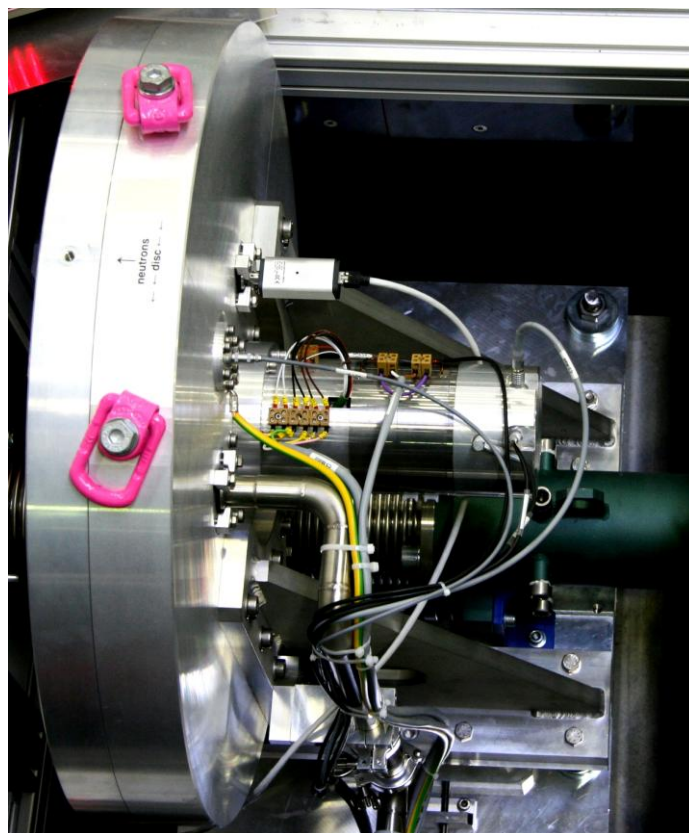


Figure 17: Top view of chopper SC2 at the V18 neutron beam line. On the left side is the chopper housing. The neutrons are incident from the right side through a neutron guide (dark green).

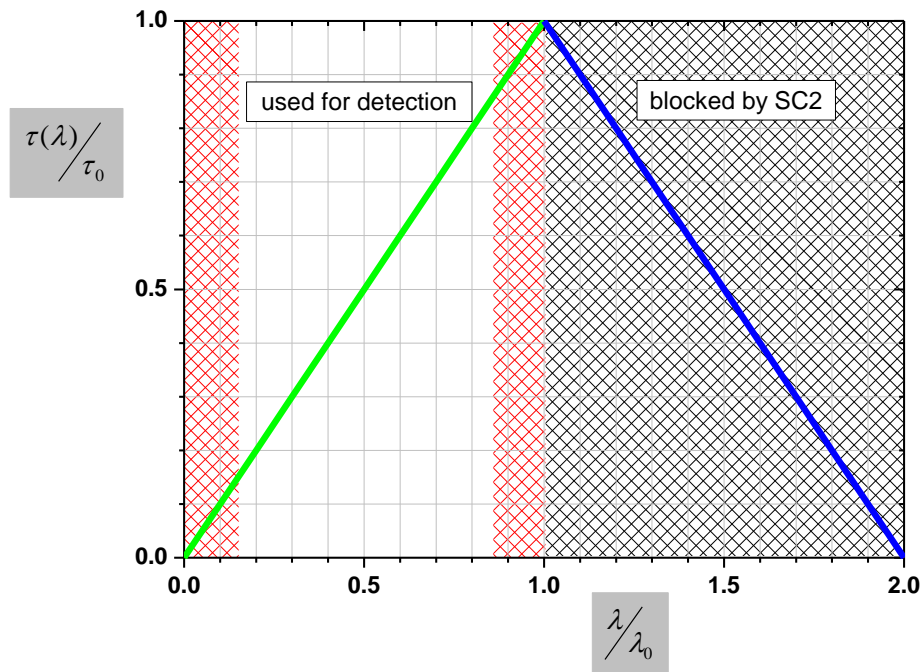


Figure 18: Transmission of SC1: Wavelength dependent burst time $\tau(\lambda)$, normalized by the maximum burst time $\tau_0(\lambda_0)$, as a function of passing wavelength λ , normalized to λ_0 . Only for $\lambda \leq \lambda_0$ the wavelength resolution is constant (green line), while it is changing for $\lambda > \lambda_0$ (blue line). The third chopper, SC2, blocks wavelengths longer than λ_0 (black pattern) and in addition prevents overlapping of neutrons with very short and long wavelengths from neighbouring pulses (red pattern). The diagram is inspired by [95].

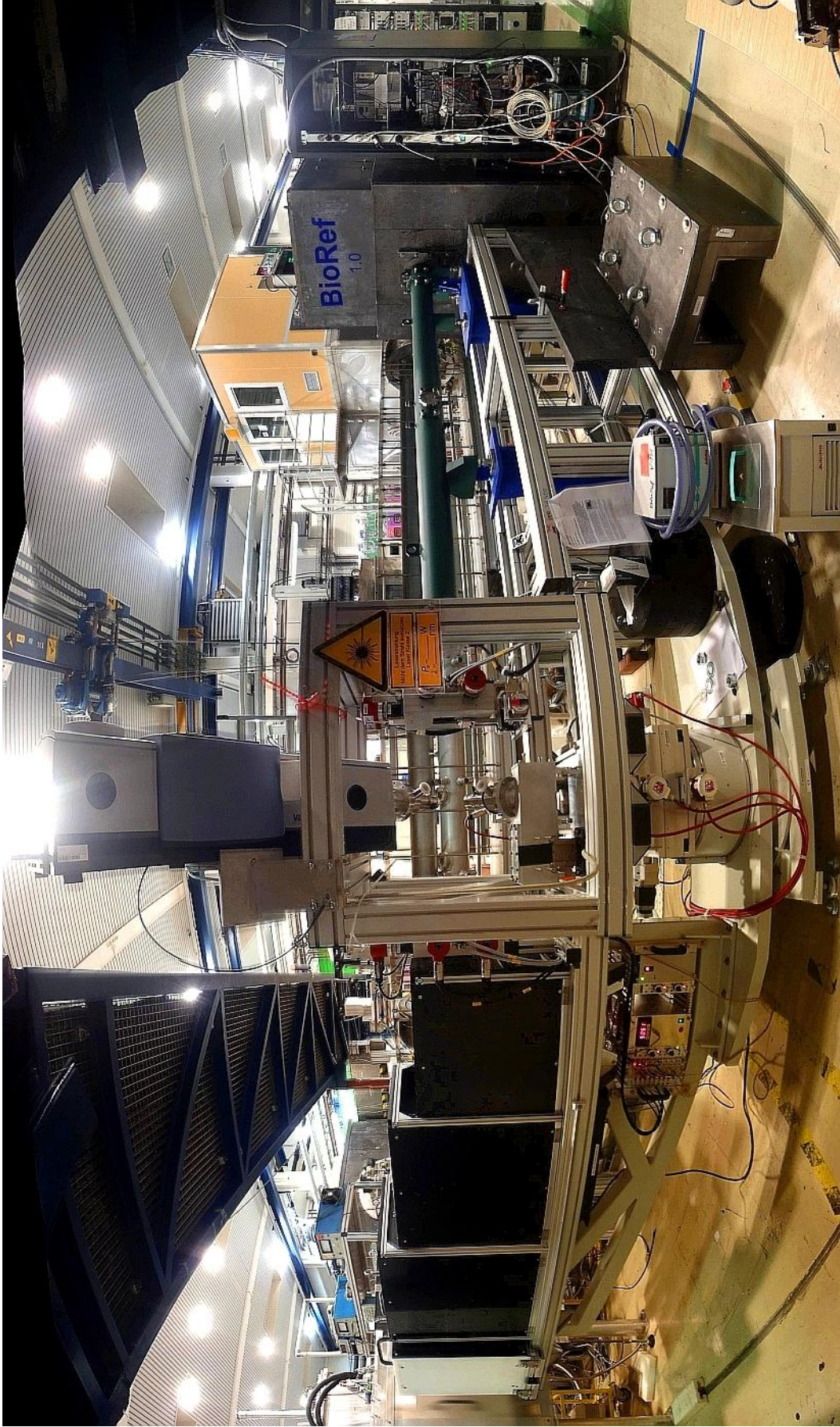


Figure 19: Fisheye perspective of the V18 instrument in the neutron guide hall I of BER II at the Helmholtz-Zentrum Berlin with the sample position in the centre. The neutrons are incident through the chopper system from the right side and are recorded at the neutron detector on the left side. The IR setup is on the sample stage in the centre of the picture, with the IR spectrometer on top. [101]

3.2.6 Shear setup employed at AMOR

In order to study the mechanisms of joint lubrication using the above model surfaces a shear setup for neutron reflectivity measurements was used. The setup enables one to apply an external force to a coated silicon substrate by applying a variable shear force on a solution in contact with the sample surface. The construction and the design of the setup was part of the dissertation submitted to the University of Heidelberg by Thomas Kaltofen [102].

The setup is illustrated in Figure 20: A coated silicon substrate is pressed against an incubating solution. As substrates, polished silicon discs with a diameter of 100 mm and a thickness of 10 mm were used. A lipid coating was either prepared by spin coating or by the air brush technique as described in chapter 3.3 on page 52. In order to apply a shear force on the sample surface, the solution can be sheared by a rotator. To achieve a constant shear flow at the sample surface, the used rotator has a conical shape in such a way, that the distance to the sample increases linearly with the radius. Rotation frequencies of up to 20 Hz can be applied. In addition, the solution housing and the substrate can be temperature controlled by an external water bath. A more detailed description can be found elsewhere [102].

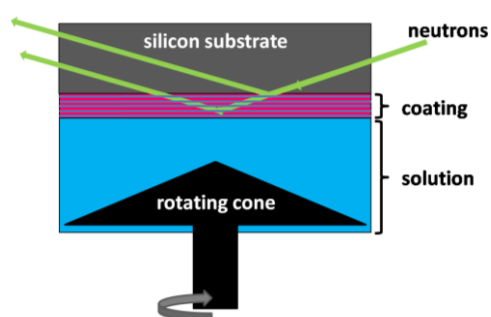


Figure 20: Schematic diagram of the shear setup for neutron reflectivity measurements.

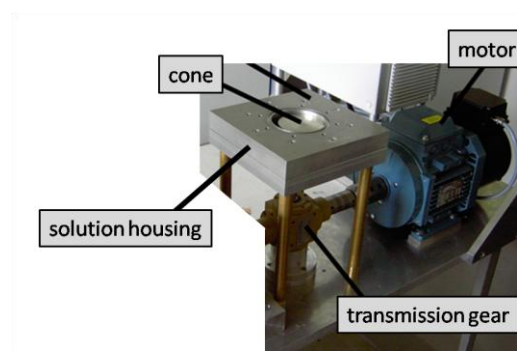


Figure 21: Photograph of the shear setup.[102]

Neutron reflectivity measurements with the shear setup were performed at the time-of-flight reflectometer AMOR at the Swiss spallation neutron source (SINQ) hosted at the Paul-Scherrer Institute (PSI), Villigen [103, 104]. The instrument is designed to perform measurements in horizontal sample geometry using a pulsed cold neutron beam produced by a chopper system. Measurements were performed with a chopper frequency of 33 Hz, choosing a wavelength band from 2 Å to 8 Å, with a Q-resolution of $\delta Q = 10\%$.

3.2.7 High pressure cell

Experiments under high hydrostatic pressure conditions were performed in a pressure cell, designed for in situ neutron reflectivity measurements [96]. Hydrostatic pressure between 0.1 MPa and 100 MPa in the temperature range from 5 °C to 60 °C can be applied to a substrate with a sample area of 28 cm². The reflectivity of disc shaped silicon, graphite or sapphire substrates with a maximum diameter of 60 mm can be probed against noncorrosive sample solutions. In the present work, silicon substrates with a diameter of 60 mm and a height of 10 mm were used. The sample compartment with 55 mL of sample solution is separated from an independent compartment hosting a hydraulic fluid (H₂O). Using a manual syringe pump, pressure can be built up upon the hydraulic fluid, which is directly conveyed to the sample solution, as the two compartments are connected by a movable piston (Figure 22). A detailed description of the pressure setup has already been published [96].

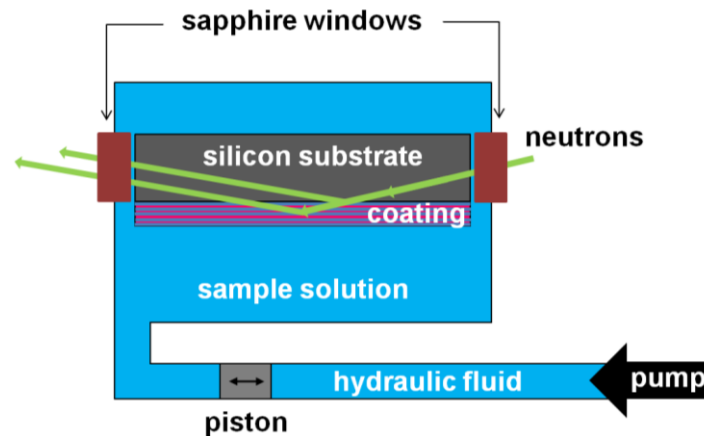


Figure 22: Schematic diagram of the pressure cell for neutron reflectivity measurements. A piston separates the sample solution from the hydraulic fluid.

3.2.8 X-Ray reflectometer

X-ray reflectometry measurements were performed with an in-house made reflectometer at Helmholtz-Zentrum Berlin [105]. The polychromatic beam from a copper (Cu) anode was monochromatized with a graphite crystal monochromator. The wavelength of $\lambda = 1.541 \text{ \AA}$ of the Cu K _{α} doublet was chosen as the probing X-ray wavelength. The beam geometry was defined by a (0.004 x 8.000) mm slit in front of the sample, followed by a (2 x 10) mm slit after the sample position, resulting in an experimental resolution of $\delta Q = 0.003 \text{ \AA}^{-1}$. The low Q-range region up to $Q = 0.143 \text{ \AA}^{-1}$ was measured by attenuating the beam with a nickel (Ni) absorber in order to protect the detector. If not noted otherwise, all data are footprint corrected and normalized to the primary intensities [97].

3.3 Preparation of lamellar lipid coatings

For reflectivity measurements of solid-supported lipid coatings, two different preparation techniques were used. The spin-coating technique (chapter 3.3.1) results in oligolamellar lipid coatings and the air brush technique (chapter 3.3.2) produces multilamellar lipid coatings.

3.3.1 Spin coating

Oligolamellar lipid coatings were prepared on pre-cleaned substrates by spin-coating (Figure 23). Before coating, the substrates were cleaned three times with pure chloroform: after covering the surface with chloroform, the substrates were rotated for 10 sec with 4000 rpm in order to spin-off the chloroform. Subsequently the lipid coatings were generated by covering the substrate surface with lipid solution in chloroform: the surface was completely covered with lipid solution in chloroform (1-2 mL) with different concentrations $c(\text{DMPC})$. By rotating the substrate afterwards at a speed of 4000 rpm for 60 sec, the solution spins off leaving behind a dry substrate surface. A spin-coater (Model 6708D, SCS, US) was used, following a procedure described by Mennicke and Salditt [106].

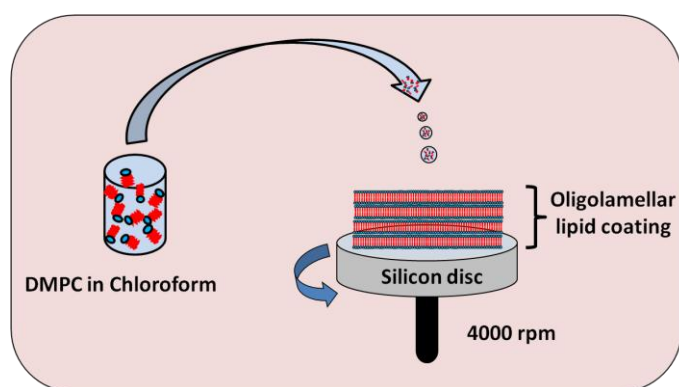


Figure 23: Schematic diagram of the spin-coating technique.

The technique has the great advantage of being able to produce oligolamellar lipid coatings with a tuneable number of bilayers: The use of coating solutions with different lipid concentrations results in a predictable number of bilayers. In order to calibrate the procedure, a series of silicon wafers with an area of $25 \times 25 \text{ mm}^2$ were spin-coated with different solutions. Solutions of DMPC solved in chloroform with concentrations between 0 mg/mL and 50 mg/mL were used. The resulting number of substrate bound bilayers N was determined by X-ray reflectometry (Figure 24). Applying Equation 3.38 (on page 39) reveals the number of bilayer N_{BK} (Figure 25), taking the Bragg peak (B) and the Kiessig oscillations (K) into account. The bilayer spacing could be read out best from the sharpest Bragg peak,

measured with $c(\text{DMPC}) = 50 \text{ mg/mL}$, yielding $Q_B = (0.1205 \pm 0.0002) \text{ \AA}^{-1}$ with a d-spacing of $d = (52.1 \pm 0.4) \text{ \AA}$. Interestingly, N_{BK} shows a parabolic behaviour as a function of the used concentration $c(\text{DMPC})$ (Figure 25).

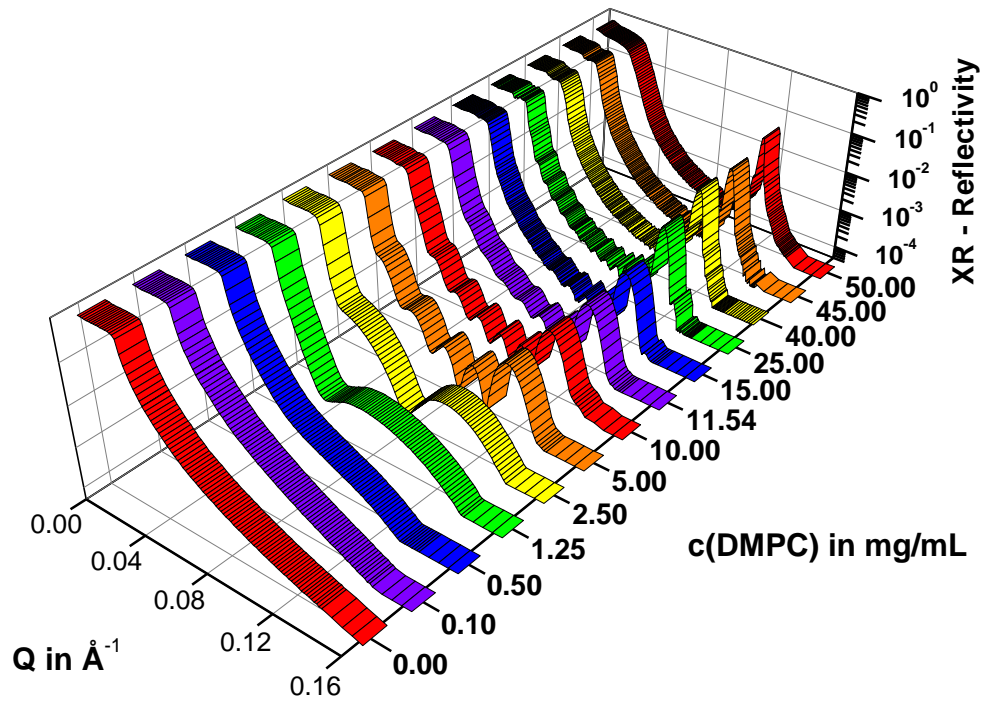


Figure 24: X-ray (XR) reflectivity of spin-coated silicon wafers, measured in air. As a coating solution the lipid molecule DMPC was solved in chloroform in different concentrations $c(\text{DMPC})$.

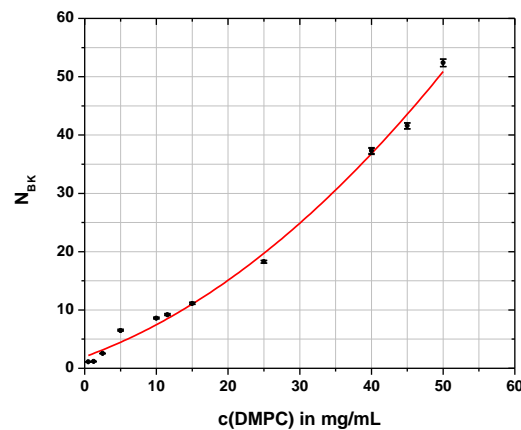


Figure 25: Resulting number of lipid bilayers N_{BK} on a spin-coated silicon wafer. N_{BK} was calculated by using the values of the Bragg peak position (B) and the Kiessig oscillations (K). Solutions with different DMPC concentrations $c(\text{DMPC})$ in chloroform were used as coating solution. The red line represents a fit of a second order polynomial function to the data points.

3.3.2 Air brush

Multilamellar lipid coatings were prepared by the air brush technique (Figure 26). Here, 10 mL of a 10 mg/mL lipid solution in chloroform were sprayed at a constant flow (0.1 bar) of nitrogen onto the pre-cleaned substrates. By keeping a distance of around 400 mm from air brush to sample surface at constant flow rate, generated by only 1 bar of nitrogen pressure, an optically homogeneous film was obtained.

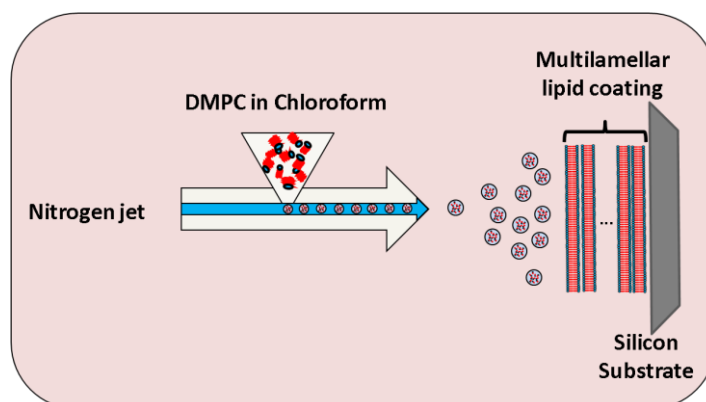


Figure 26: Schematic diagram of the air-brush technique.

An example for a reflectivity curve from an air-brushed sample is shown in comparison to a spin-coated sample in Figure 27. The appearance of a Bragg peak at $Q_B = 0.1198 \pm 0.0003 \text{ \AA}^{-1}$ clearly shows the presence of a multilamellar lipid stack, with a bilayer repeat thickness of $d = 54.5 \pm 0.4 \text{ \AA}$. The total thickness t of the stack cannot be determined in this case, since no Kiessig oscillations appear. This is due to the limited resolution of the experiment. However, the minimum at $Q = 0.02 \text{ \AA}^{-1}$ belongs to a second critical momentum transfer Q_c (cf. chapter 3.2.4 on page 35), due to the micrometer thick lipid coating. In addition, the absence of total reflection for $Q < 0.03 \text{ \AA}^{-1}$ and the less pronounced higher order Bragg peaks, indicate a high surface roughness of the multilamellar coating. The high surface roughness could also be shown by an increase of the off-specular scattering [107], measured around the Bragg peak position: A comparison of so-called sample angle (α_{in}) scans (or rocking scans) around the first Bragg peak position ($0^\circ \leq \alpha_{in} \leq 2^\circ$) at fixed detector position ($\alpha_{det} = \text{const.}$) is displayed in Figure 28. For the air-brushed sample, the background is more than one order of magnitude higher than that of the spin-coated sample. In contrast, the Bragg peak amplitude is more than one order of magnitude lower for the air-brushed sample than that of the spin-coated sample. Background level and Bragg peak amplitude indicate a better layer alignment and reduced roughness of the spin-coated oligolamellar lipid coating, as compared to the air-brushed multilamellar lipid coating.

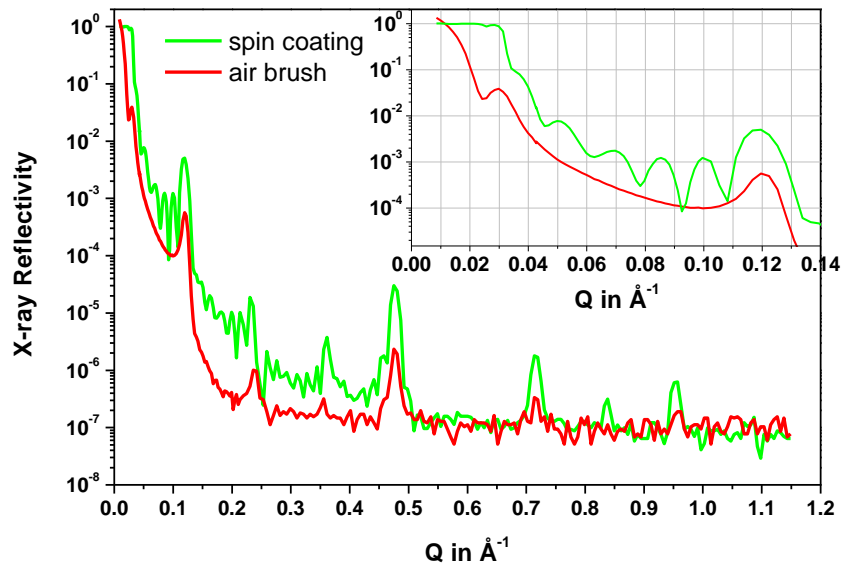


Figure 27: X-ray reflectivity of DMPC lipid coated silicon wafers. The coatings were achieved by two different techniques: Spin-coating a solution of 10 mg/mL DMPC in chloroform (green) or by the air-brush technique. The inset shows a magnification of the low Q -region.

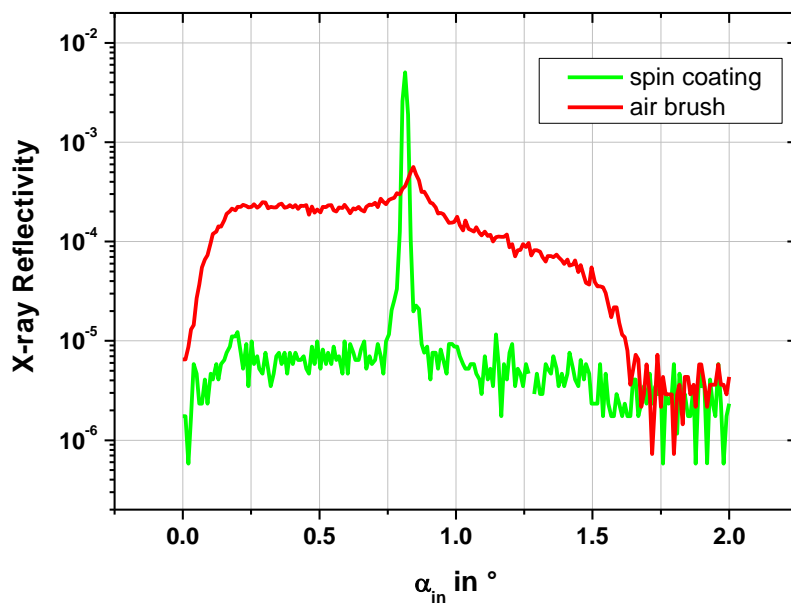


Figure 28: Scans around the first Bragg peak position with a fixed detector position (rocking scan). Both curves are normalized to measurement time (40 sec/point) and to incident intensity I_0 . The minor differences in maximum positions are probably due to differences in temperature and humidity during the measurements.

4. Instrument Development at BioRef

A major part of the present thesis was the design and implementation of an infrared beam line at the V18 neutron beam line. The challenge was to design a substrate, a sample cell and an external infrared beam line which enables combined neutron reflectivity (NR) and ATR-FTIR measurements at the same time on the same sample. In addition, the setup should facilitate temperature dependent measurements. Furthermore, the option of *in-situ* measurements and measurements against vapours were realized. The setup was designed in collaboration with the HZB engineering department. A summary of the setup has already been published [98].

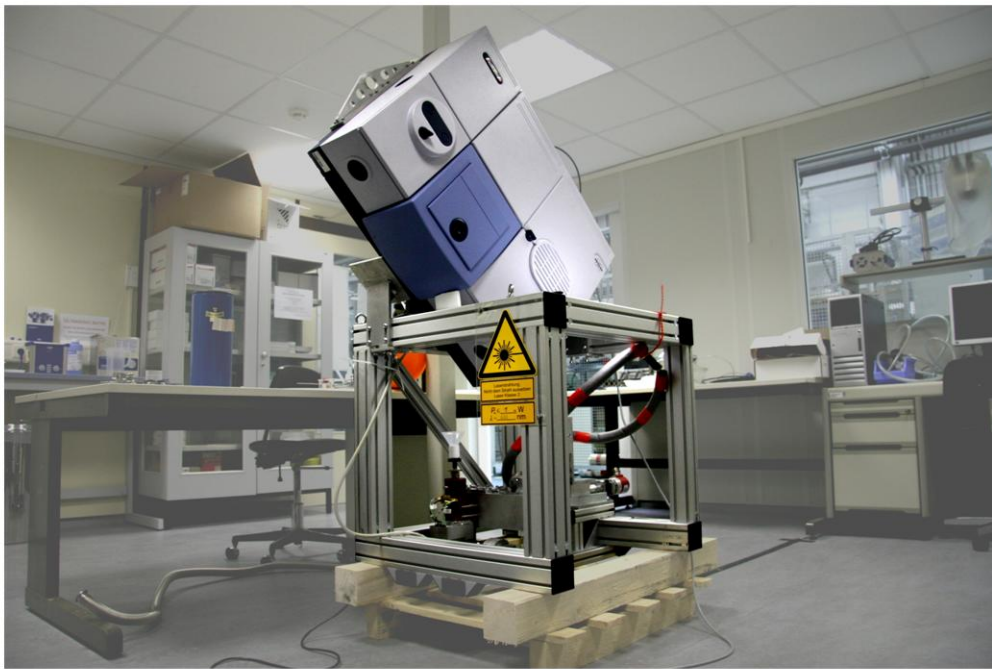


Figure 29: Picture with an overview of the infrared setup: A spectrometer mounted to an item holder (item Industrietechnik GmbH, Germany) above the sample position.

4.1 Substrates

For combined NR and ATR-FTIR measurements it is necessary to use substrates which are especially designed for this purpose (Figure 30). As for both techniques different constraints have to be considered, the BioRef substrates are designed accordingly to be able to employ both techniques simultaneously and to exploit their full potentials. Silicon was the material of choice for all integrative substrates, as it is transparent for both neutrons and infrared light in the desired range of the spectra [108]. Silicon blocks with 100 mm length and 80 mm width were fabricated, resulting in a sample surface of 8000 mm². In order to have IR entrance and exit windows perpendicular to the infrared beam forward direction, the two opposing long sides of the crystal were inclined under an angle of 45° without affecting the probed sample surface (Figure 30).

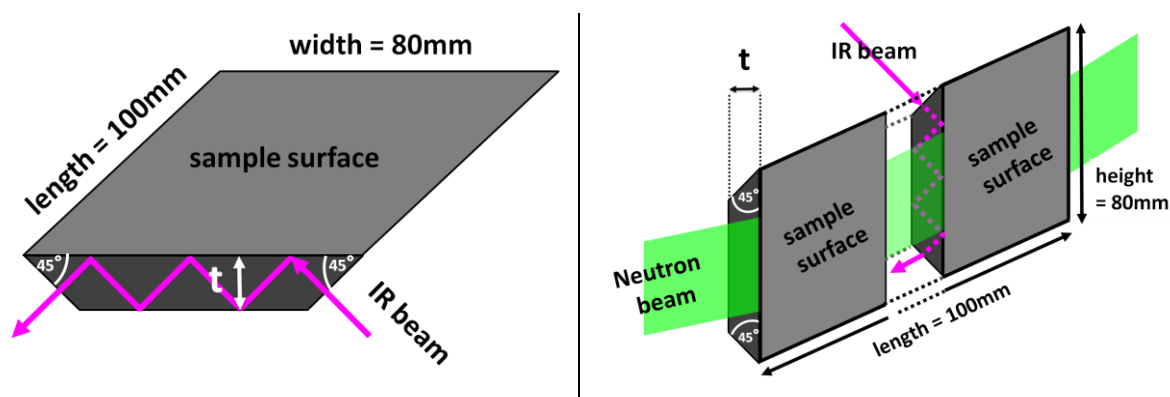


Figure 30: Sketches of the integrative silicon substrate ATR13 for combined infrared (IR) spectroscopy and neutron reflectivity measurements at BioRef. Left: ATR13 in the horizontal position with a sketched IR beam in magenta. Right: ATR13 in a vertical position with the IR beam shown in the realistic position for a combined measurement, passing through the centre of the substrate. The neutron beam is sketched in green.

A critical parameter for an integrative substrate is its thickness t . For ATR-FTIR decreasing t increases the number of internal reflections M at the sample surface, which is proportional to the IR absorbance of the probed surface. In order to obtain a high IR absorbance signal t should be minimized. On the contrary a decreased t limits the Q -range which can be probed in NR as t defines the maximum height of the entrance window for the NR beam. The entrance window has to be high enough to let the whole NR beam enter, even at high incident angles α_i . As Q is proportional to α_i , the accessible Q -range is confined by t .

substrate notation	t [mm]	Q_{\max} [\AA^{-1}]	M
ATR13	13.3	0.36	3
ATR8	8.0	0.20	5
ATR5	5.0	0.13	8

Table 4.1: Summary of available silicon samples for combined measurements at V18 with thickness (t), maximum accessible Q -range for neutrons (Q_{\max}) and number of internal reflections at the sample surface for infrared light (M).

In order to cover a variety of experimental situations, three different integrative substrates were fabricated (Table 4.1). A first substrate, ATR13, with $t = 13.3$ mm allows to probe a large Q -range up to $Q_{\max} = 0.36 \text{ \AA}^{-1}$. Q_{\max} was calculated according to Equation 3.47 for a neutron wavelength of 4.66 \AA . Basic geometrical considerations reveal that for ATR13 the IR beam reflects only $M = 3$ times at the sample surface. A second substrate, ATR8, with $t = 8$ mm allows to probe only up to $Q_{\max} = 0.22 \text{ \AA}^{-1}$ with $M = 5$. And the third one, ATR5, with $t = 5$ mm reduces Q_{\max} to a minimum value ($Q_{\max} = 0.13 \text{ \AA}^{-1}$) with a maximum in M ($M = 8$).

4.2 Sample cell

A fixed substrate height and length made it possible to use one sample cell for all substrates described before (Figure 31). The sample area of the silicon substrate was pressed against a Teflon trough, which was sealed with flat sealing material made of Viton. The substrate and the Teflon trough were then sandwiched between two temperature adjustable aluminium plates connected to an external water bath (Figure 32). To measure the temperature closest to the silicon-solution interface a thermometer (PT100) was placed inside the Teflon slab. Through tubes connected to the top and bottom of the Teflon trough it is possible to inject and change a liquid phase for *in-situ* measurements. The trough has a depth of 3 mm and can be filled with a total volume of 10 mL liquid phase, including excess solution in the inlet and outlet tubes. The shape of the trough makes it possible to avoid air bubble formation when filled.

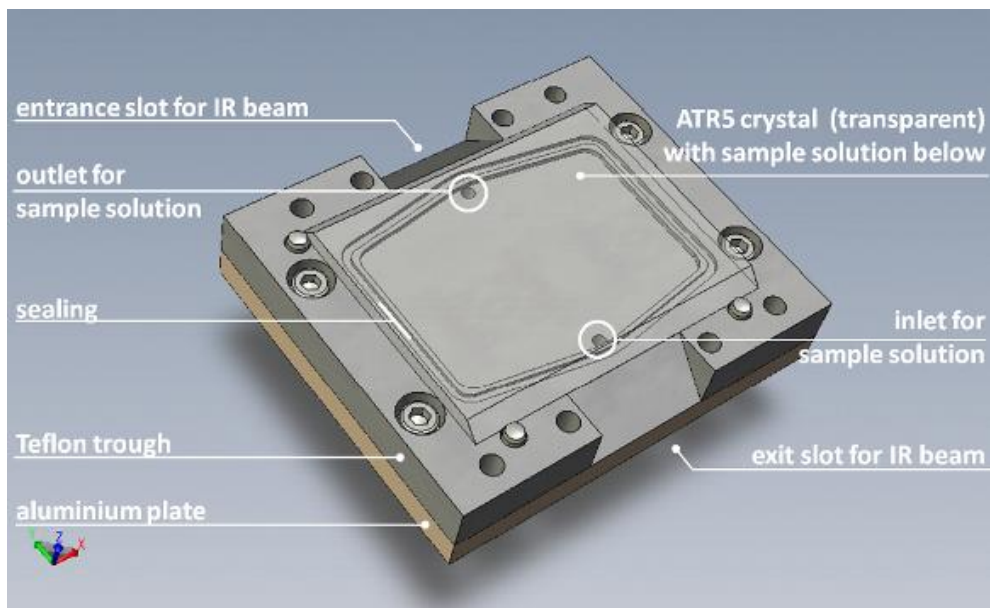


Figure 31: Design drawing of the sample cell for combined infrared and neutron reflectivity measurements at a solid-liquid interface. The top aluminium plate is not shown. The silicon ATR substrate is marked transparent.

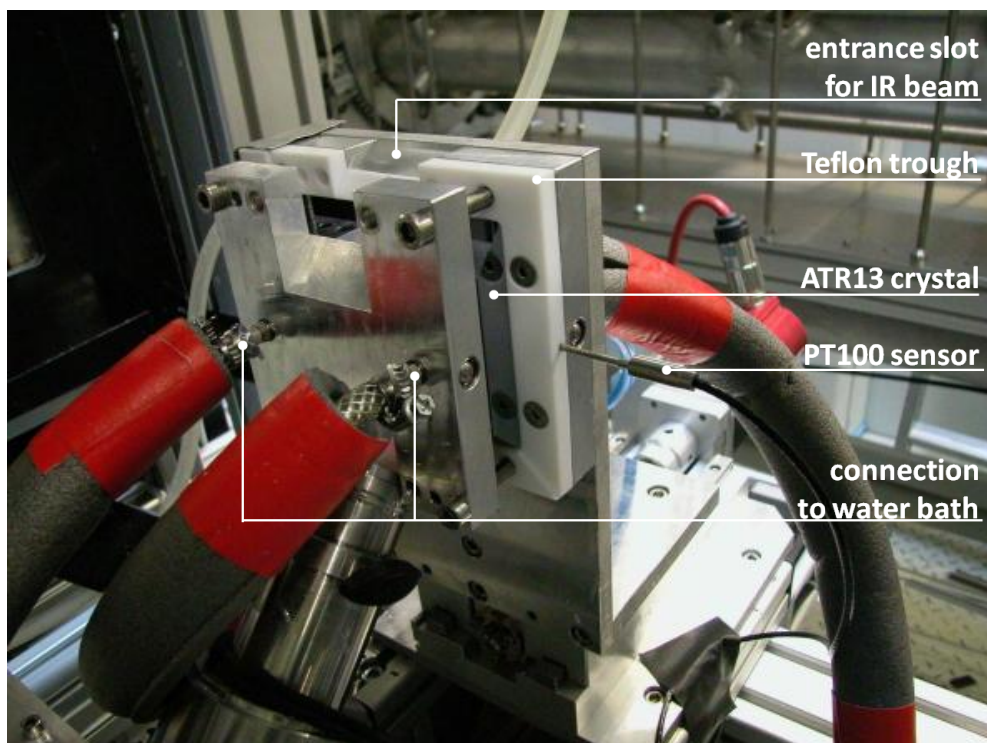


Figure 32: Photograph of the sample cell connected to an external water bath.

4.3 External FTIR setup

An infrared spectrometer (Vertex70, Bruker Optik GmbH, Germany) was installed above the sample position to provide the FTIR signal. The spectrometer was advantageously mounted in a vertical position in order to bring the IR source closest to the sample position, between the slits of the neutron pathway (Figure 35). The spectrometer has an exit window to enable IR analysis in external beam geometry. In order to guide the IR beam through the sample, such external pathway had to be designed (Figure 33).

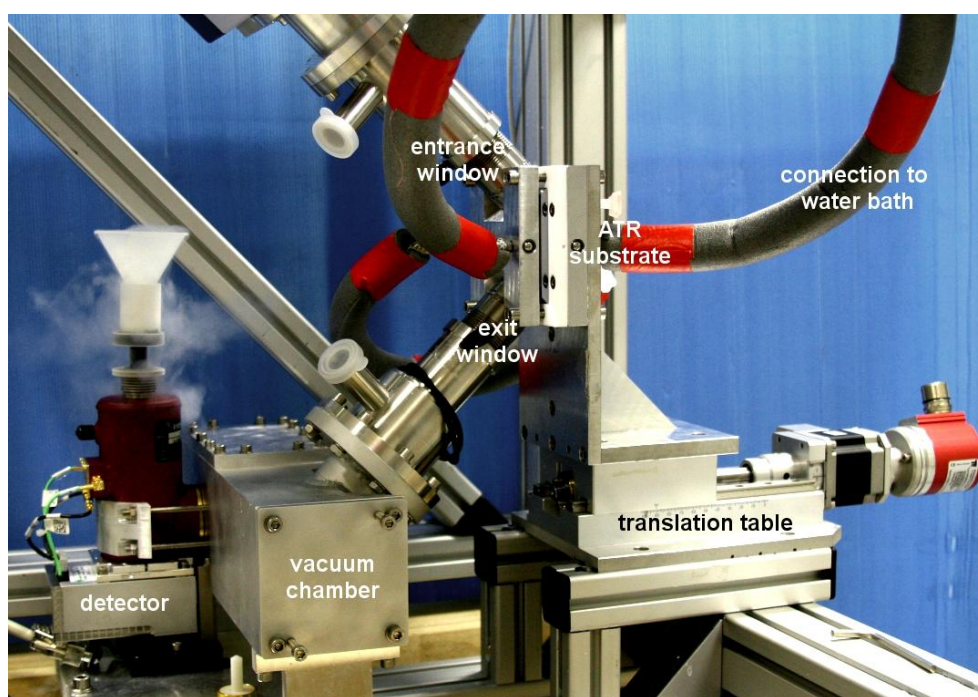


Figure 33: External beam pathway with sample cell (centre) on a translation table (right side) and a nitrogen cooled mercury cadmium telluride detector in dark red (left side)

The IR beam, coming in parallel rays from the spectrometer, is focused via a lens f_1 with a focal length of $f_1 = 400$ mm to the centre of the sample position (Figure 34). The focusing lens with $f_1 = 400$ mm diminishes the cross section of the IR beam at the substrate and makes it possible to pass the whole beam through the inclined entrance window of the substrate. After the IR beam is reflected several times inside the ATR substrate, the beam leaves the sample at the inclined exit window of the substrate. A second lens with $f_2 = 400$ mm reconstitutes a parallel beam geometry. The now parallel beam is focused with an $f_3 = 43$ mm lens into the detector window. The detector is connected with a data cable to the spectrometer. The detector can either be a liquid nitrogen cooled mercury cadmium telluride (MCT) or a deuterated triglycine sulphate (DTGS) detector, depending on the experimental

needs. All lenses used have a gold-coated surface.

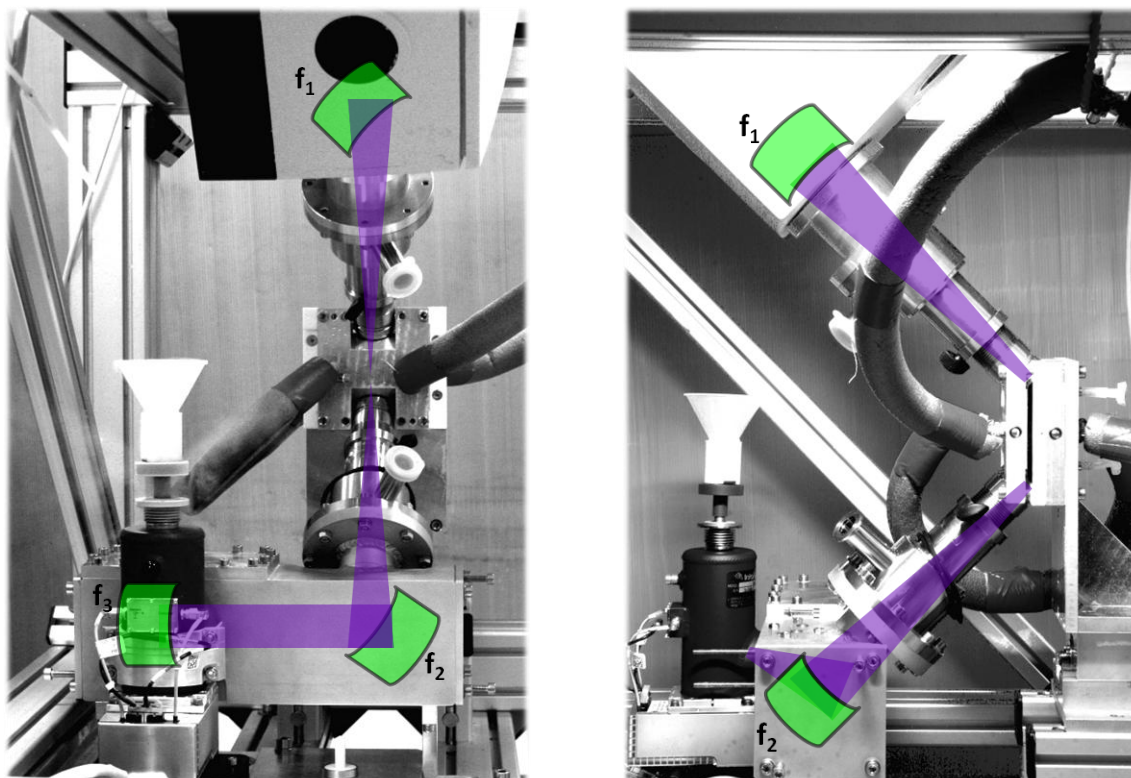


Figure 34: Side view (left picture) and front view (right picture) of IR guide system, with the IR beam in violet. The lenses (green) are gold-coated and have focal lengths of $f_1 = f_2 = 400$ mm and $f_3 = 43$ mm, respectively. The lens f_1 focuses the beam on the sample and f_2 reconstitutes a parallel beam after being transmitted through the sample. The lens f_3 focuses the beam on the detector plate.

The sample cell equipped with one of the silicon substrates is mounted on a linear translation stage in order to be able to correctly position substrates of different thickness in the IR beam (Figure 33). By only changing the z-position of the translation table all three types of substrates (ATR5, ATR8 and ATR13) can be positioned in the fixed IR beam geometry without further alignment.

A beam path cover, of flexible length mounted to the spectrometer can be adjusted such that only a gap of a few millimetres remains between the cover and the inclined top entrance window of the substrate. At the inclined beam exit window at the bottom a similar beam path is mounted, which leads to an external detector. In order to eliminate water vapour, it is possible to flush the top beam path and the spectrometer with a stream of dry nitrogen. In addition, the bottom beam path can be evacuated. Potassium bromide (KBr) is used as window material.

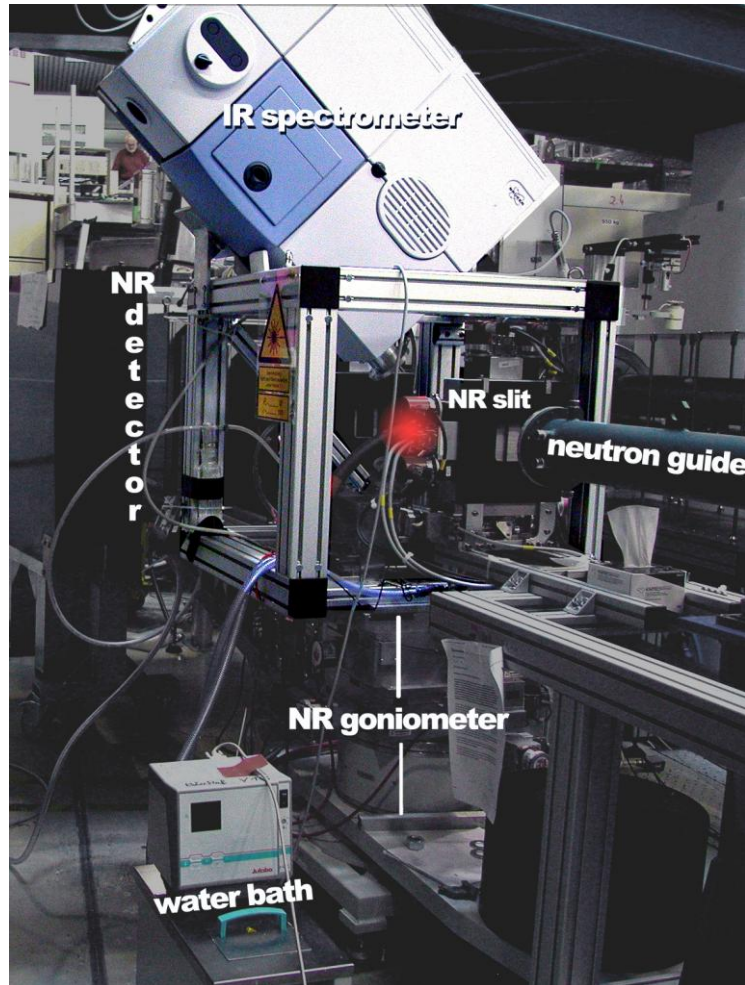


Figure 35: Infrared (IR) setup on the neutron reflectivity (NR) sample stage at the V18 beam line at Helmholtz-Zentrum Berlin. The red spot marks the sample position.

The V18 instrument has been designed with a horizontal neutron scattering geometry. Therefore, the sample has to be mounted vertically, such that grazing incidence of the neutron beam can be achieved. In addition, the whole IR setup including spectrometer, lenses, sample holder with sample cell and substrate, linear translation stage and detector are mounted on a static *item* (*item Industrietechnik GmbH, Germany*) frame. For NR measurements, the *item* frame is mounted on a second linear translation stage on the V18 goniometer to adjust the sample surface with respect to the neutron beam (Figure 35). This setup has the great advantage that changes in the sample surface position with respect to the neutron beam do not alter the IR beam alignment.

4.4 Resulting IR intensities

As a first test of the designed infrared beam line, the absorbance of an integrative silicon sample (ATR8) was measured. ATR-FTIR spectra were recorded with a DTGS detector using a spectral resolution of 2 cm^{-1} and 5 scans per spectrum. Data processing was carried out with the Opus 6.5 software package (Bruker Optik GmbH, Germany).

First, a polished silicon wafer was installed at the sample position, in order to guide the incoming IR beam with a single reflection along the external beam line (Figure 36). This setup allowed recording the reference signal I_0 (see Equation 3.8 on page 28). In the following the sample signal I was recorded with substrate ATR8 in the beam path, instead of the silicon wafer. By aligning the z -position of the ATR crystal the fixed infrared beam geometry could be kept. Here, the IR beam is guided through the sample, following 5 internal reflections at the sample surfaces. The measurements were performed in ambient humidity, without evacuation of the beam path. Therefore, both signals, I and I_0 , show pronounced water vapour bands between 3500 cm^{-1} and 4000 cm^{-1} and between 1500 cm^{-1} and 2000 cm^{-1} (Figure 37). Also a pronounced absorption of carbon dioxide (CO_2) at 2340 cm^{-1} appeared.

The changes in water and CO_2 absorption band intensities are due to stochastic changes in humidity along the not-evacuated beam path.

The multiple reflection setup with the ATR crystal yields a higher signal intensity than the single reflection setup, which is due to further alignment of the infrared beam geometry in order to obtain a maximum in intensity. Measurements with the liquid nitrogen cooled mercury cadmium telluride (MCT) detector showed in addition the good transmission for infrared light through the ATR crystals with the designed beam geometry: A beam aperture of 2 mm has to be used, in order to prevent saturation of the detector. For wavenumbers smaller than 1500 cm^{-1} the intensity drops drastically due to the high photon absorption cross section of silicon in this wavenumber range [108]. However, even the region between 1500 cm^{-1} and 900 cm^{-1} is accessible for ATR-FTIR measurements.

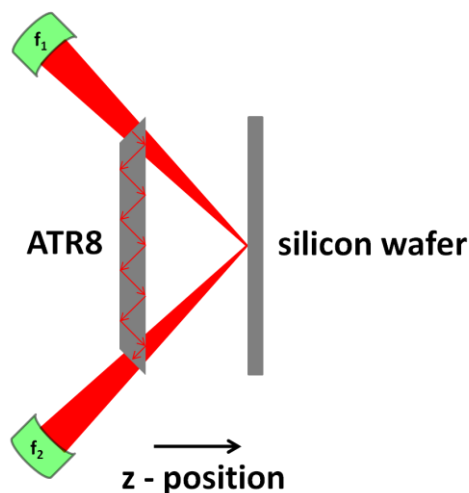


Figure 36: Schematic diagram of the used infrared beam geometry (red), with the two focusing lenses f_1 and f_2 , in order to measure an absorbance spectrum of the silicon ATR crystal (ATR8). For the reference signal I_0 , a polished silicon wafer was used to provoke a single “external” reflection, without ATR crystal in the beam path, followed by a measurement of the sample signal intensity I in ATR geometry. Here, all infrared light is guided through the ATR crystal, resulting in nine internal reflections.

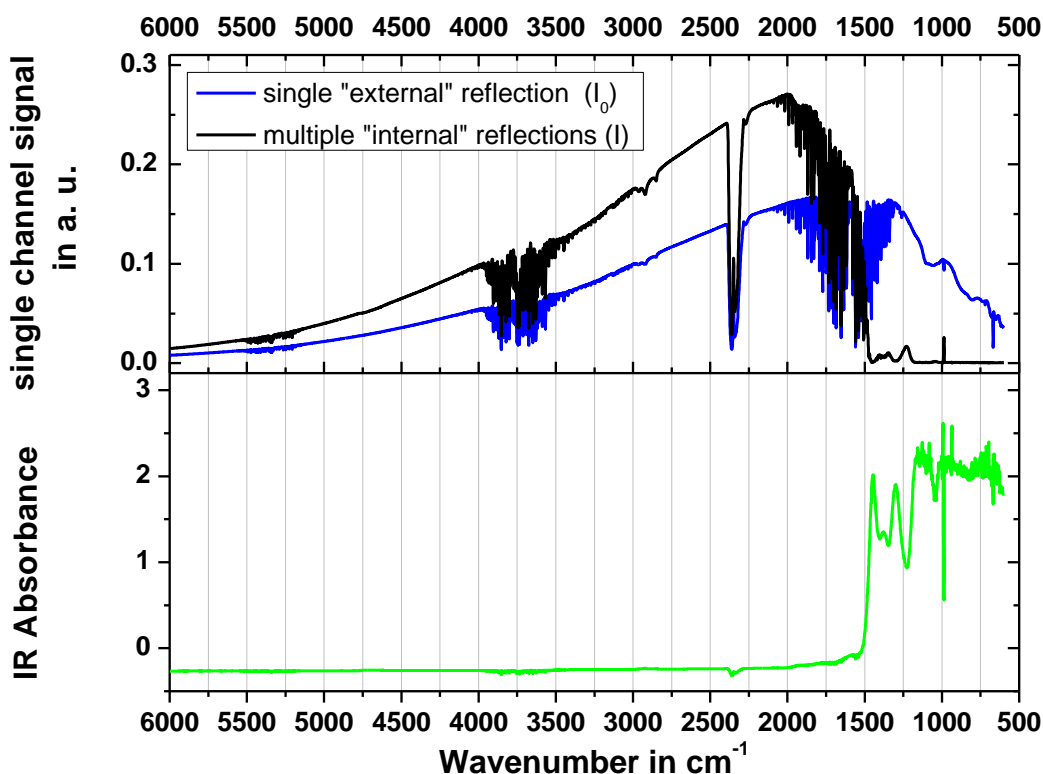


Figure 37: Infrared signals measured at the BioRef setup: First, by using a polished silicon wafer to provoke a single “external” reflection (blue line) yielding a reference signal I_0 , and second, by guiding the infrared beam through a silicon ATR crystal (black line), as a sample measurement I . The resulting absorbance spectrum of the silicon ATR crystal, calculated by Equation 3.8 (on page 28), is shown in the bottom graph (green line).

The silicon crystal does not absorb between 6000 cm^{-1} and 1500 cm^{-1} . For wavenumbers smaller than 1500 cm^{-1} , the intensity drops drastically due to the high photon absorption cross section of silicon in this wavenumber range. The infrared beam geometries are illustrated in Figure 36 and described in the text.

5. Lipid membranes in pure aqueous solutions

Lipid membranes show characteristic properties, depending on the surrounding environment (e. g. humidity, pH, temperature, pressure). As the liquid phase is the natural environment for lipid membranes, the investigations were started in purely aqueous solutions. First, a box model for an oligolamellar lipid coating was introduced and a reflectivity experiment simulated (chapter 5.1). The stability of the prepared oligolamellar lipid coatings was studied under the influence of different parameters (e.g. temperature, pressure, shear and substrate) as described in chapter 5.2. Second, the phase transition of multilamellar lipid coatings was investigated using the BioRef instrument for combined infrared spectroscopy and neutron reflectivity measurements (chapter 5.3). All studied lipid membrane systems are solid-supported interfacial coatings, measured against pure liquid D_2O .

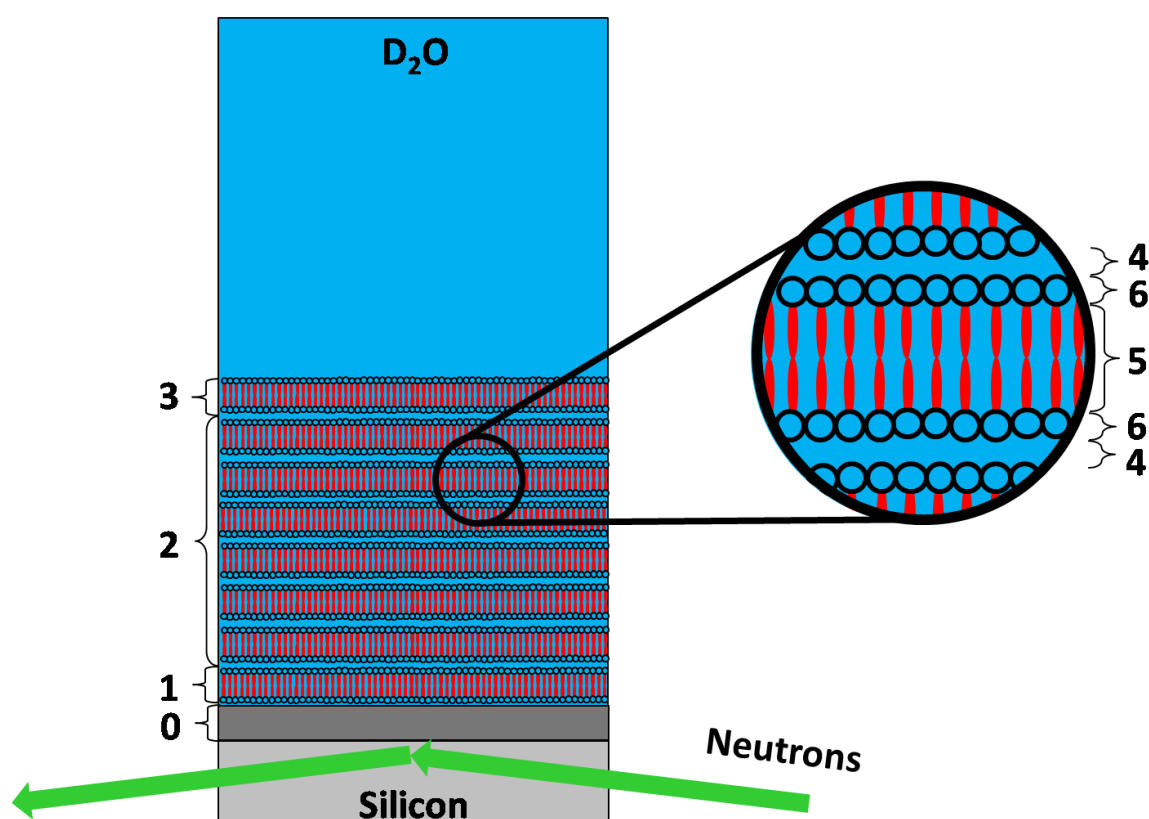


Figure 38: Model for an oligolamellar lipid coating in excess D_2O on a silicon substrate. The individual layers are described in the text on page 67. [109]

5.1 A simulated neutron reflectometry experiment

In order to demonstrate the viability and the constraints of a reflectometry experiment, neutron reflectivity curves have been simulated with the *Parratt32* software package. For this purpose a model for an oligolamellar lipid coating on a silicon substrate in excess D₂O was introduced (Figure 38 on page 66). The model was the basis of the simulated curves and is furthermore used for the analysis of measured reflectivity curves, as shown in the subsequent chapters. In addition, the simulated curves have been analyzed by the Bragg peak analysis as described before (on page 38). The extracted values are compared to the input values in the simulations.

The model

The analysis of a measured reflectivity with the optical matrix approach for a lipid coating on a silicon substrate is based on a box model displayed in Figure 38. The reliability of the model was already demonstrated in earlier studies [96, 110]. Silicon was used as a solid support, covered with a layer of silicon oxide (0). An oligolamellar lipid coating was modelled by subdividing the system into three parts: First, an inner lamella (1) is directly attached to the silicon oxide layer. The inner lamella is followed by several core lamellae (2), which have the same thickness d and SLD. Finally, this stack of layers is covered by a terminal lamella, the outer lamella (3). Each lipid lamella is represented by a bilayer of hydrophobic lipid chains or tail groups (5) with a hydrophilic head group layer at each side (6). Two neighbouring lamellae are separated by a solution inter-layer (4). Thickness and SLD of each layer were subject to fitting. Roughness of the different interfaces was set to zero: This turned out to be a reasonable approach for the Q-range addressed within the experiments and further cut down the number of variable parameters.

Since SLD's of head group layers and solution inter-layers differ only slightly, a simplified model was used when appropriate [96]. Here, the head group layer and solution inter-layer of the core part were represented in a unified layer, the interlayer. This simplified approach additionally reduces the number of variable parameters. All used parameters for d and SLD are listed in Table 5.2 on page 77 (first column).

Peak shape analysis of simulated reflectivity curves

A number of up to $N = 65$ bilayers on the substrate were simulated. For comparison with experiments, the resolution δQ of the simulations was set to a value typical for measurements at the V6 neutron reflectometer (chapter 3.2.5): constant resolutions of $\Delta Q = 0.0001 \text{ \AA}^{-1}$ from $Q = 0 \text{ \AA}^{-1}$ to $Q = 0.0520 \text{ \AA}^{-1}$ and $\Delta Q = 0.0002 \text{ \AA}^{-1}$ from $Q = 0.0520 \text{ \AA}^{-1}$ to the probed Q value of $Q_{\text{max}} = 0.1600 \text{ \AA}^{-1}$ were used. In addition, the background was set to a constant value of 3×10^{-5} .

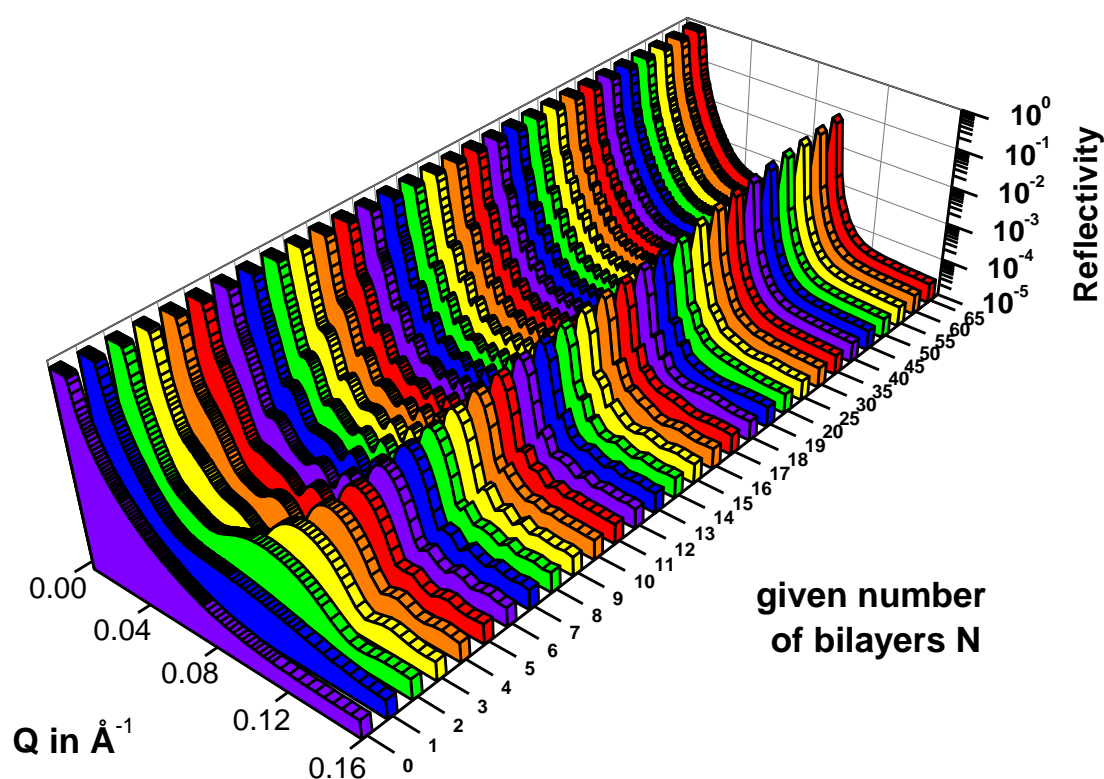


Figure 39: Simulated neutron reflectivity curves according to the model of a multi-layered lipid coating on a silicon substrate in excess D_2O . The first curve in the very front with a number of $N = 0$ bilayers represents the Fresnel reflectivity of the uncoated silicon substrate.

For $N = 0$, the Fresnel reflectivity of an uncoated silicon substrate simply shows a decaying reflectivity. For $N = 2$, already a broad maximum appears at $Q = 0.1 \text{ \AA}^{-1}$. With an additional bilayer ($N = 3$) an additional maximum appears at a lower Q value. The frequency of these Kiessig oscillations increases, indicating an increase of the total coating thickness t , according to Equation 3.32. Additionally, the maximum of the Kiessig oscillation at

$Q = 0.1 \text{ \AA}^{-1}$ emerges into a Bragg peak. The fixed position corresponds to the thickness of the repeating bilayer with $d = 64 \text{ \AA}$, according to Equation 3.33. The peak shape also changes with increasing N : the full width at half maximum (FWHM) decreases and its maximum intensity increases.

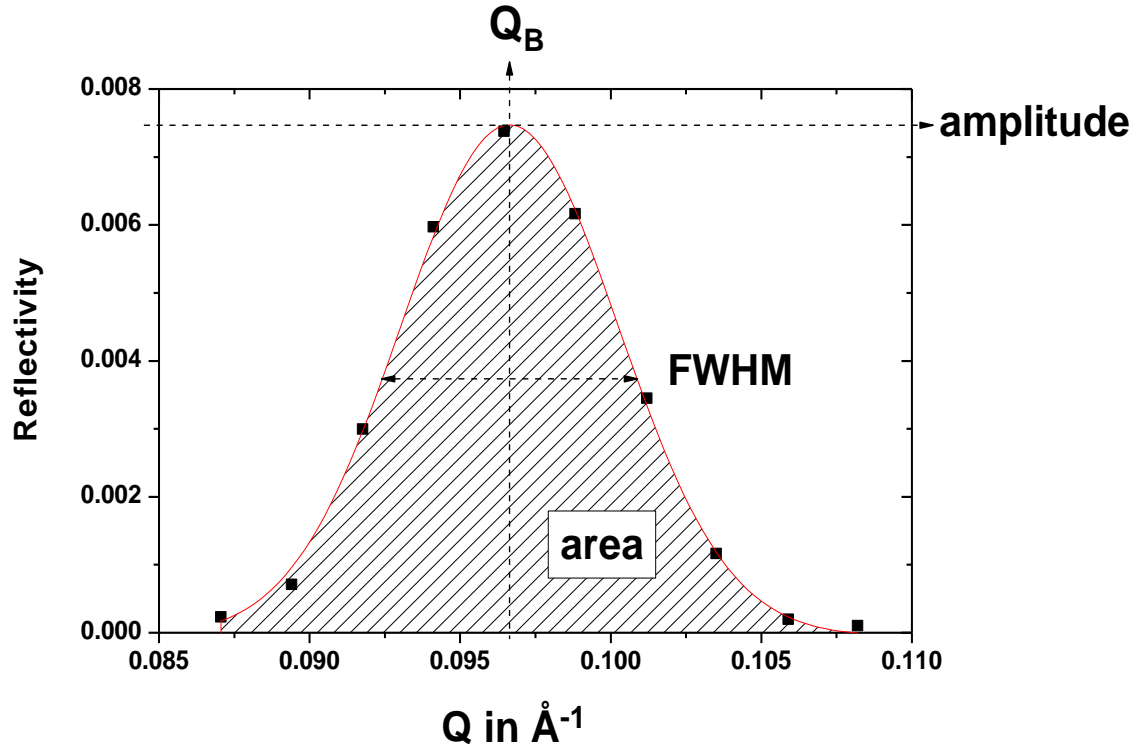


Figure 40: Exemplary Gaussian fit (red line) to the Bragg peak (black squares) simulated with $N = 10$ bilayers at $Q_B = (0.0966 \pm 0.0001) \text{ \AA}^{-1}$ with $\text{FWHM} = (0.0080 \pm 0.0003) \text{ \AA}^{-1}$ and an area of $(0.60 \pm 0.03) \times 10^{-4} \text{ \AA}^{-1}$.

In order to analyze the Bragg peak quantitatively, a Gaussian curve was fitted to the data (Figure 40). As seen in Figure 41 the full width at half maximum (FWHM) decreases up to $N = 20$. The fitted values follow the predictions according to Equation 3.37 almost within the error. A different behaviour is observed for values for $N \geq 25$: here, the fitted values reach a constant value of $\text{FWHM} \approx 0.003 \text{ \AA}^{-1}$ and differ severely from the predictions. In this range the Bragg peak width is dominated by the limited resolution of the simulations. This assumption does not count for the peak area: Here, the effect of restricted resolution is compensated by the significant increase of the amplitude, according to Equation 3.38. Therefore, the area of the fitted Gaussian profiles increases linearly with increasing N up to $N = 50$ (Figure 42).

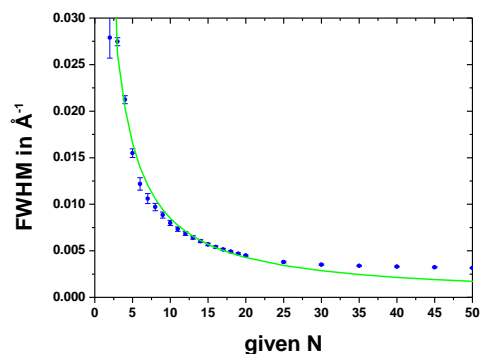


Figure 41: Blue points indicate the FWHM derived from a Gaussian fit to the Bragg peak at $Q = 0.1 \text{ \AA}^{-1}$. The green line is guide to the eye calculated by $y = K*(Q/N)$ according to Equation 3.37.

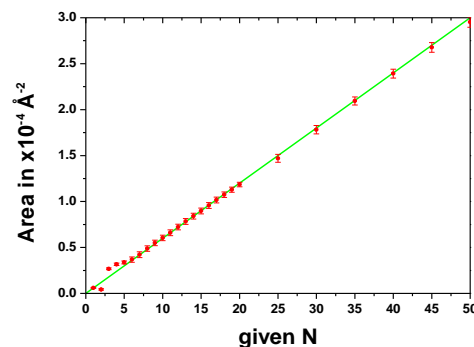


Figure 42: Red points represent the area of a Gaussian fit to the Bragg peak at $Q = 0.1 \text{ \AA}^{-1}$. The green line is guide to the eye.

Using the fitted values for FWHM and peak area, the values for N were calculated according to Equation 3.37 and Equation 3.38, respectively, and displayed as a function of given N , which was implemented in the simulations (Figure 43). While for $N < 25$ the given N could be reproduced by the calculations, for $N > 25$ the calculated N_{FWHM} values disagree, when using the FWHM. However, the calculated N_{area} using the peak area reproduces the given N within the error.

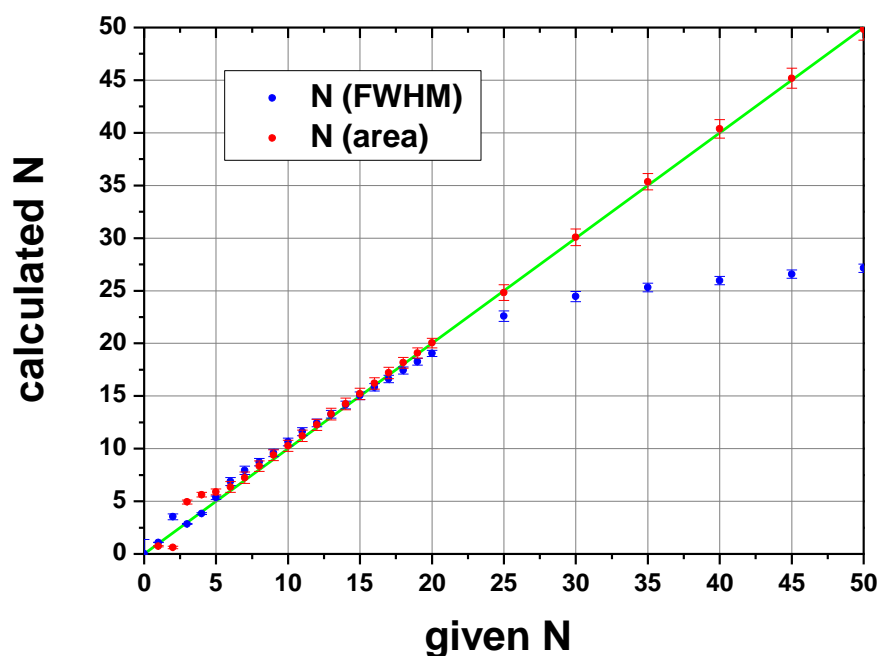


Figure 43: Calculated number of bilayers N_{FWHM} according to Equation 3.37 for the blue points and according N_{area} according to Equation 3.39 for the red points with the constant $o = 6.9 \times 10^{-5}$. The green line is guide to the eye with calculated $N = \text{given } N$.

5.2 Stability of oligolamellar lipid coatings

Once we succeeded in the preparation of oligolamellar lipid films on solid substrates, the question arose, whether these films maintain their structure when incubated in aqueous solution. The stability of lipid coatings was essential for further experiments and is also an important prerequisite for a successful application of lipid coated implants [16]. Neutron reflectivity measurements were performed with oligolamellar and multilamellar lipid coatings against pure excess D₂O in the vicinity of the main phase transition, first by a temperature dependent approach (chapter 5.2.1) and second, by a pressure dependent approach (chapter 5.2.2). In addition, the influence of an external shear force was investigated (chapter 5.2.3). Due to the importance of titanium for body implants, the stability of lipid coatings on titanium was investigated (chapter 5.2.4). A discussion is given in chapter 5.2.5.

5.2.1 Effect of temperature

Disc shaped silicon substrates (samples *A*, *B*, *C* and *D*) with a diameter of 60 mm were coated with lipid layers. Samples *A*, *B* and *C* were prepared with an oligolamellar coating by using the spin-coating technique with different concentrations. For sample *A* a concentration of 5 mg/mL and for sample *B* and *C* of 10 mg/mL DMPC in chloroform was used. Sample *D* was coated with a multilamellar coating using the air brush technique. Here, 10 mL of a 10 mg/mL solution of DMPC in chloroform was used. The samples were mounted in a liquid cell and exposed to pure liquid D₂O at 21 °C for neutron reflectivity measurements. Subsequently the temperature was increased to 24 °C, followed by further increase of the temperature in steps of 2 °C up to 30 °C. For every temperature the neutron reflectivity was measured two times. All measurements were performed at the V6 instrument as described in chapter 3.2.5 (on page 43). Parts of this chapter have already been published in [109].

Bragg peak analysis

All samples were first measured at 21 °C after incubation in pure D₂O and revealed a Bragg peak (B) around 0.1 Å⁻¹ (Figure 44). Differences in the Bragg peak positions might be due to differences in the alignment of the lipid lamellae, as the samples have not been annealed before the measurements. The spin-coated samples revealed in addition Kiessig oscillations (K), which allowed calculating the number of bilayers N_{BK} on the substrate, according to Equation 3.38 (on page 39). Sample *A* consisted of $N_{BK} = 5.0 \pm 0.3$ bilayers. As samples *B*

and *C* were coated with a higher concentrated lipid solution in CHCl_3 , they were consequently coated with a higher number of bilayers: $N_{\text{BK}} = 8.2 \pm 0.9$ for sample *B* and $N_{\text{BK}} = 7.6 \pm 0.7$ for sample *C*. For sample *D* the number of bilayers N_{BK} could not be extracted, as any Kiessig oscillations appeared. The results are summarized in Table 5.1.

Sample	d in \AA	t in \AA	N_{BK}	N_{FWHM}
A	66.89 ± 0.04	334 ± 20	5.0 ± 0.3	6.12 ± 0.27
B	73.36 ± 0.11	600 ± 65	8.2 ± 0.9	7.38 ± 0.34
C	65.48 ± 0.05	495 ± 45	7.6 ± 0.7	8.07 ± 0.26
D	65.31 ± 0.25	-- --	-- --	8.52 ± 4.10

Table 5.1: Results from measurements at 21 °C with repeat distance (d), total coating thickness (t), and number of bilayers calculated from the Bragg peak position and the Kiessig oscillations (N_{BK}), and by using FWHM (N_{FWHM}).

Changes of the first order Bragg peak were subsequently traced, raising the temperature in 2 °C steps for sample *A*, *B* and *D* (Figure 47), starting from 24 °C. Sample *C* was heated in 1 °C steps starting at 21 °C (Figure 48 on page 75). For each temperature the neutron reflectivity was measured two times around the Bragg peak position from $Q = 0.075 \text{ \AA}^{-1}$ to $Q = 0.110 \text{ \AA}^{-1}$. As a result of heating, the Bragg peaks decreased drastically for the spin-coated samples *A*, *B* and *C* after passing the main phase transition at 26 °C. In contrast, the Bragg peaks intensity increased drastically at elevated temperature for the air-brushed sample *D*. The resulting reflectivity profiles are shown in Figure 45. In order to quantify these results, a Gaussian profile was fitted to each Bragg peak. The numbers of bilayers N , which contribute to the Bragg peak signal, were calculated by using the resulting FWHM (Equation 3.37, page 39). A comparison between N_{BK} and N_{FWHM} is shown in Table 5.1 for the measurements at 21 °C. N_{BK} and N_{FWHM} for sample *A* differ by one layer. For samples *B* and *C* the values agree within the experimental uncertainty. All calculated values for N_{FWHM} are displayed in Figure 46. After heating to 26 °C, i.e. above the main phase transition temperature all samples show a drastic change in the number of layers contributing to the Bragg peak signal. The Bragg peaks vanish completely for the oligolamellar coatings with increasing temperature. When the reflectivity curves were too flat to be fitted with any Gaussian profile, N_{FWHM} was set to zero and no error bar was attached in the figure (Figure 46). These findings are in strong contrast to the development of N_{FWHM} for sample *D*: With

increasing temperature N_{FWHM} increases until a plateau of $N_{FWHM} \approx 26$ is reached. The increase is due to a better alignment of the coherent scattering domains upon heating, as discussed in more detail in chapter 5.3. That maximum value of N_{FWHM} is limited by the resolution of the experimental setup. A combined discussion of the results is given in chapter 5.2.5 on page 93.

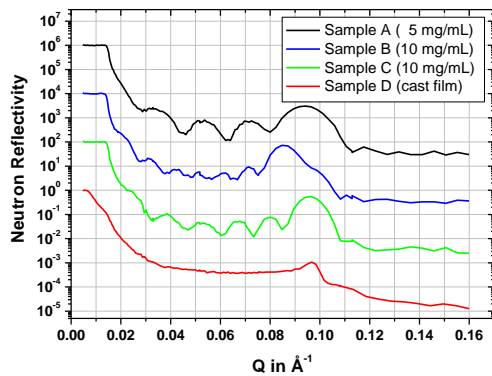


Figure 44: Neutron reflectivity of lipid-coated silicon substrates incubated in pure D_2O at 21 °C. The curves are shifted along the vertical axis for clarity.

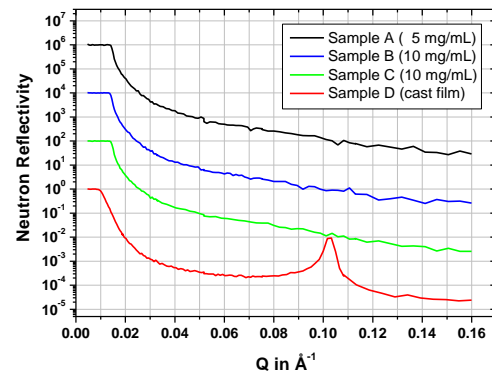


Figure 45: Neutron reflectivity after crossing the phase transition. The curves are shifted along the vertical axis for clarity.

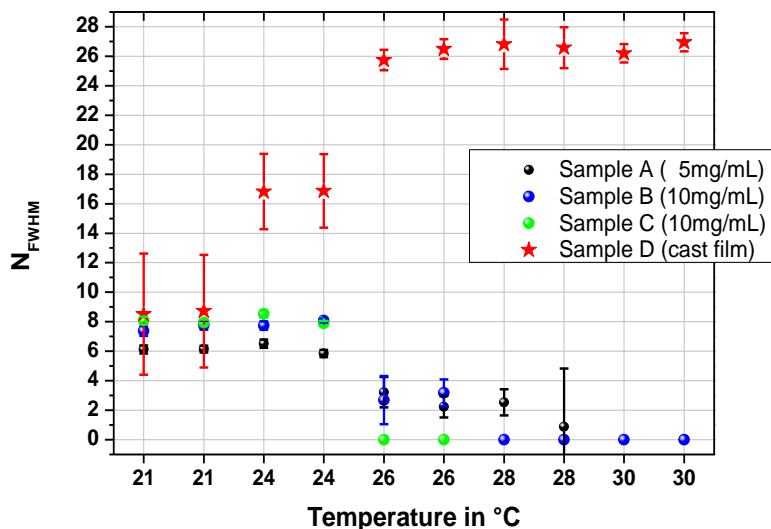


Figure 46: Number of bilayers (N_{FWHM}) as a function of temperature. For each temperature two measurements were performed. While for the oligolamellar coatings (sample A, B and C) an unbinding process starts for $T > 24$ °C, the number of coherent scattering domains increases for the multilamellar cast film (sample D).

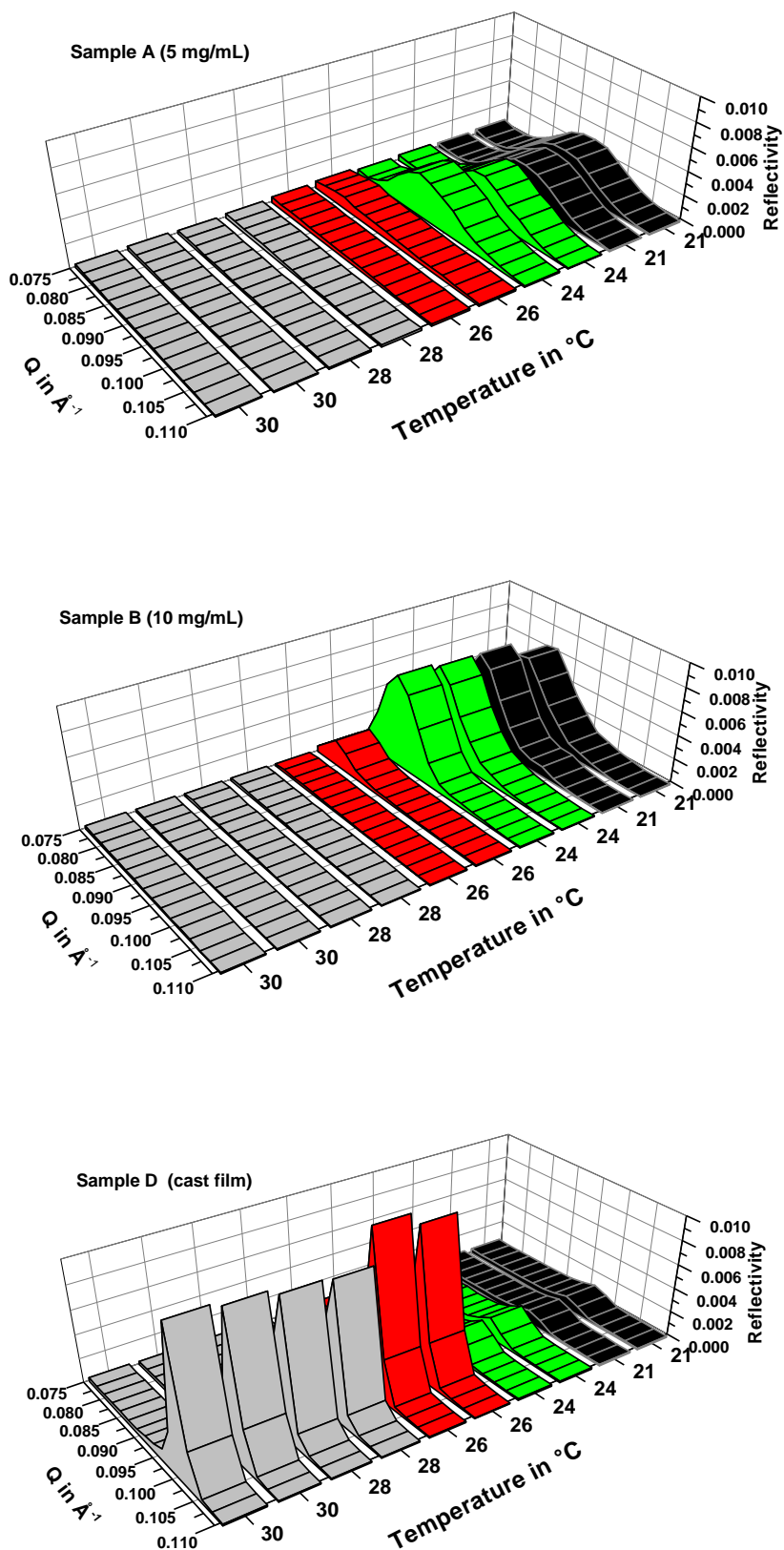


Figure 47: Neutron reflectivity profiles at different temperatures for sample A, B and D incubated in pure D₂O. At each temperature two measurements were performed.

Analysis by the optical matrix approach

In order to study the behaviour close to the phase transition, sample *C* was measured in 1 °C temperature steps between 21 °C and 26 °C (Figure 48). Here, in addition to the Bragg analysis, an analysis by the optical matrix approach was performed for several reflectivity curves (Figure 49), utilizing the model for an oligolamellar lipid coating (Figure 38 on page 66), which was therefore implemented in the *Parratt* software package. First, the reflectivity curve of the freshly prepared sample at 21 °C was fitted. Implementing a total number of 8 lamellae and varying the thickness *d* and SLD of the individual layers resulted in a calculated reflectivity curve which was in good agreement with the measured reflectivity curve (Figure 49). The corresponding SLD profiles are displayed in Figure 50 (on page 76) and the fitting parameters are summarized in Table 5.2 (on page 77).

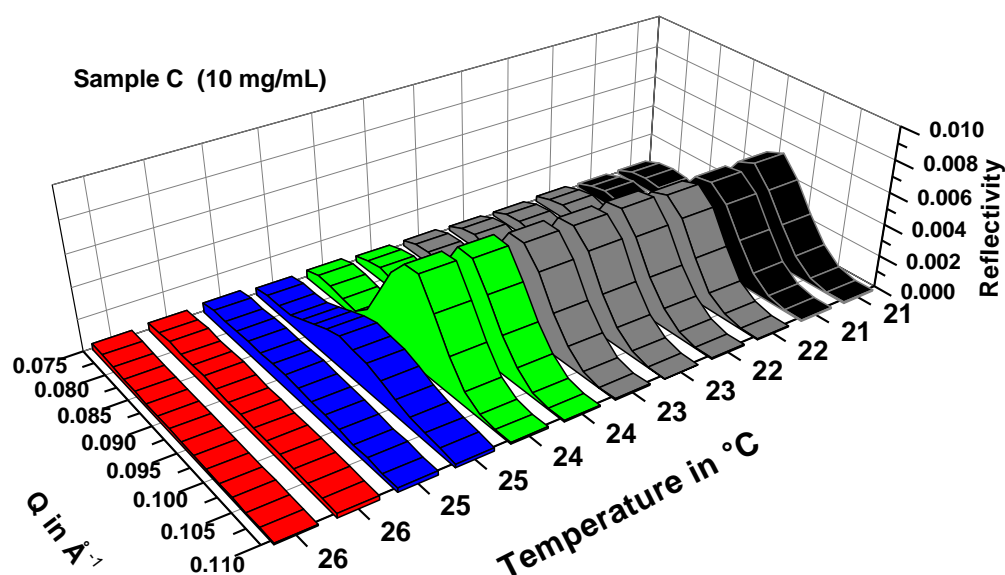


Figure 48: Neutron reflectivity profiles at different temperatures of Sample *C*, incubated in pure D_2O . At each temperature step two measurements were performed.

At 25 °C (meas. 1) a drastic change in reflectivity was observed (Figure 49). The measured reflectivity curve could be described by the original model, only reducing the number of the core lipid membranes from 6 to 3, resulting in a total number of 5 bilayers. In order to minimize the free fitting parameters, changes in *d*-spacing and SLD were not considered. The second measurement at 25 °C (meas. 2) showed an even more smeared-out Bragg peak profile. That profile was represented by the model profile when further reducing the number of core lipid membranes from 3 to 1, resulting in a total number of 3 bilayers. A full reflectivity profile over the whole *Q*-range was measured again at 26 °C. Here, the profile

shows a continuous decay. The intensities between 0.03 \AA^{-1} and 0.14 \AA^{-1} are higher than the Fresnel reflectivity of an uncoated silicon surface, indicating that not all lipid membranes underwent the unbinding process. The whole profile could be fitted with the model profile by assuming only one single lipid membrane on top of the silicon substrate. A combined discussion of the results is given in chapter 5.2.5 on page 93.

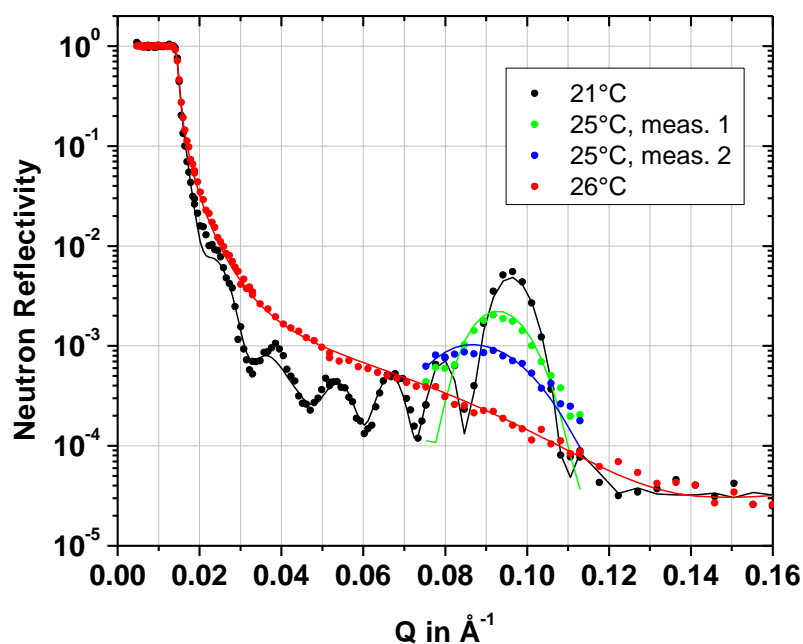


Figure 49: Neutron reflectivity of a lipid coated silicon substrate (sample C) against excess D_2O . [109]

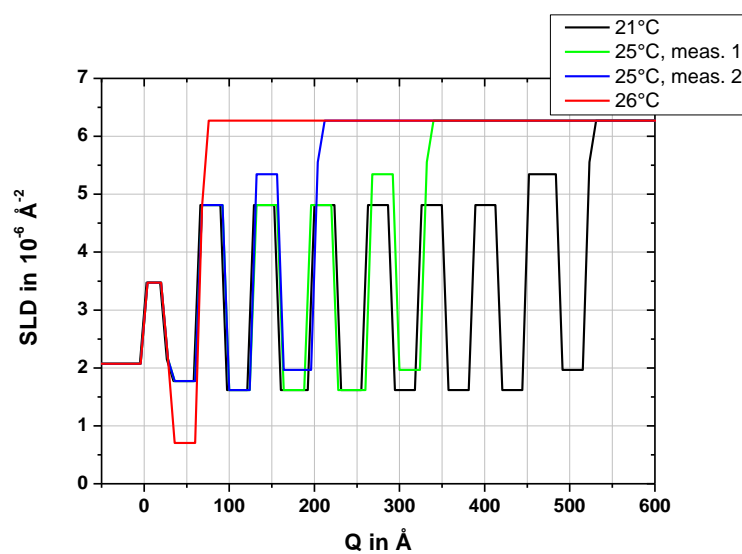


Figure 50: Scattering length density profiles across the solid-liquid interface of a lipid coated silicon substrate (sample C) against excess D_2O corresponding to the fits in Figure 49. Upon increasing temperature the lipid bilayer unbind from the solid support. All values are listed in Table 5.2 on page 77.

Temp.:		21 °C		25 °C		25 °C		26 °C	
		meas. 1		meas. 1		meas. 2		meas. 1	
param.:		d	SLD	d	SLD	d	SLD	d	SLD
[param.]:		[Å]	[Å ⁻²]						
substrate	Silicon	N/A	2.07	N/A	2.07	N/A	2.07	N/A	2.07
	SiO _x	24	3.48	24	3.48	24	3.48	24	3.48
inner lamella	Heads	7	1.90	7	1.90	7	1.90	7	1.90
	Tails	32	1.73	32	1.73	32	1.73	33	0.73
core lamellae	..								
	Interlayer	32	4.77	x3	x1	x0			
	Tails	32	1.56						
outer lamella	..								
	Interlayer	36	5.24	36	5.24	36	5.24	-	-
	Tails	32	1.89	32	1.89	32	1.89	-	-
solution	Heads	6	5.12	6	5.12	6	5.12	6	3.46
	D ₂ O	N/A	6.27	N/A	6.27	N/A	6.27	N/A	6.27
goodness of fit	χ^2	3.10 x10 ⁻²		1.74 x10 ⁻¹		2.85 x10 ⁻²		1.28 x10 ⁻²	

Table 5.2: Fitting parameters for sample C, according to the fits in Figure 49. The “Interlayer” represents a combined layer of lipid head groups and solution, as described in chapter 5.1 on page 67. [109]

Comparison of Bragg peak analysis and optical matrix approach

Up to 25 °C (meas. 1) each Bragg peak was fitted by a Gaussian function. The resulting d-spacings, FWHMs and amplitudes are displayed in Figure 51 (on page 78). During increase of the temperature for $T \leq 24$ °C, an increase in amplitude was observed, while FWHM and d-spacing was constant within error for $T \leq 24$ °C. Between 24 °C and 25 °C a drastic change in all parameters can be seen. The increase in d is a widely discussed phenomenon called the anomalous swelling (introduced in chapter 2.1 on page 20). This effect was further investigated by complementary FTIR measurements, presented in chapter 5.3 (on page 97). In Figure 52 (on page 79) the resulting values for N are displayed in comparison to the fitting results by the more elaborated optical matrix approach. The analysis shows that the number

of contributing bilayers N can be calculated by the use of FWHM and amplitude. The values gained from the different methods are in good agreement within $\Delta N = \pm 1.5$ bilayers.

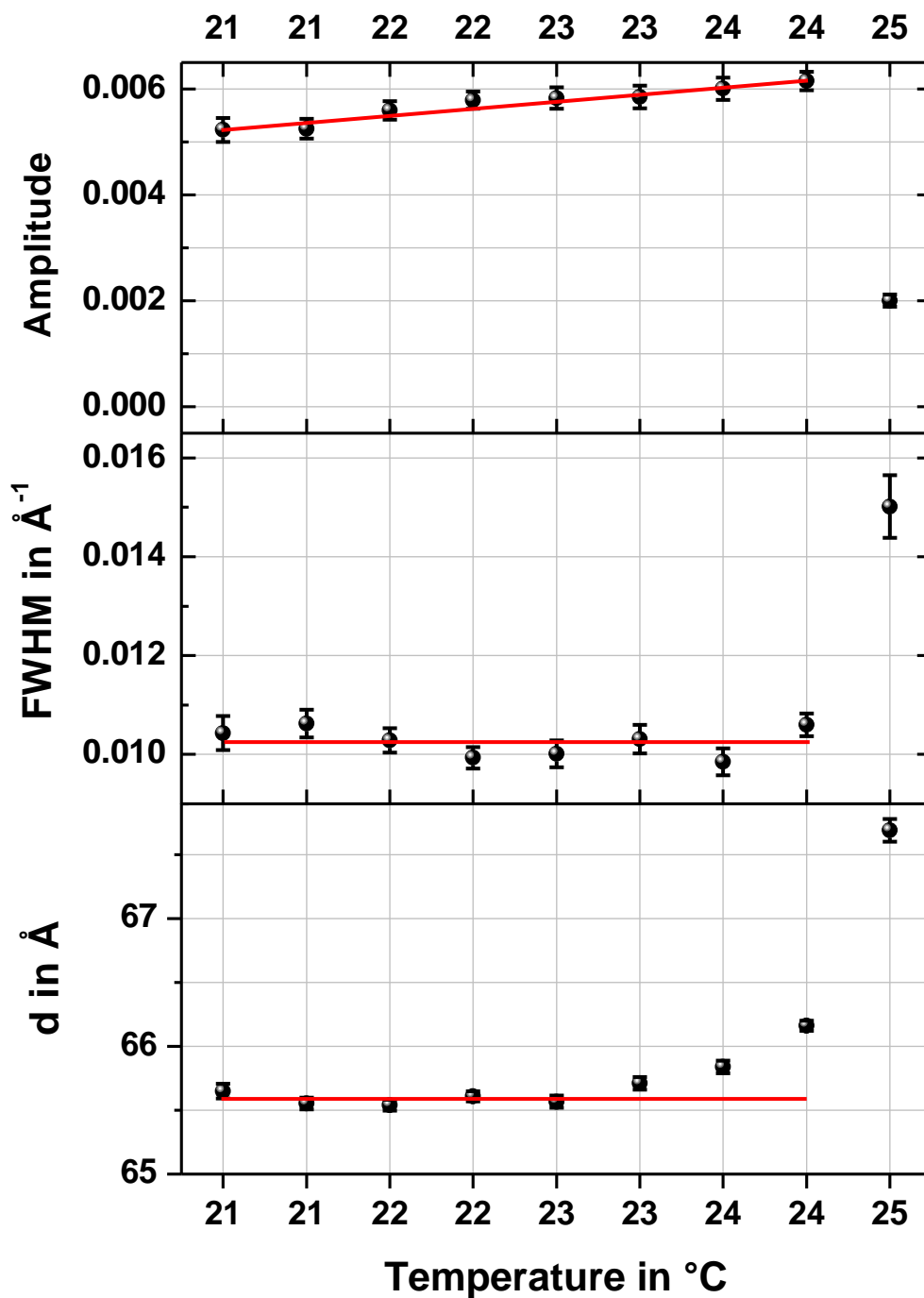


Figure 51: Bragg peak analysis for sample C. The red lines are guides to the eye, showing the average slope for the amplitude and the average values for FWHM and d , for the temperature range between 21°C and 23°C. At 25°C a drastic change in all three parameters is clearly visible.

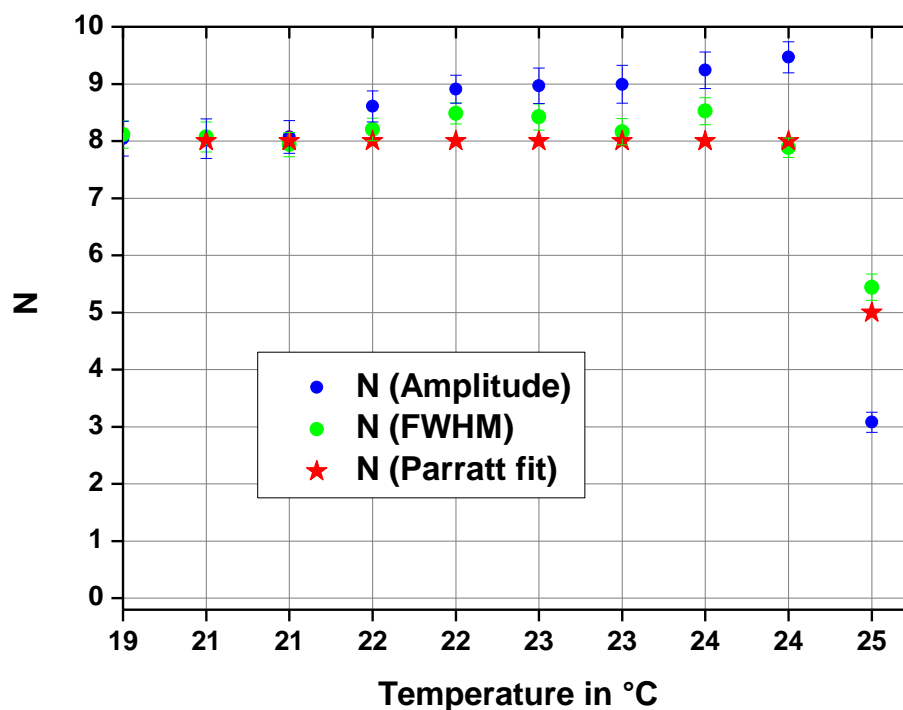


Figure 52: Calculated number of lipid bilayers N by using amplitude (blue points) or FWHM (green points) of Gaussian fits to the first Bragg peak. The red stars show values for a best fit by using the optical matrix approach and the Parratt software package

5.2.2 Effect of pressure

Introduction

The stability of oligolamellar lipid coatings in excess solution was further investigated with respect to changes in hydrostatic pressure. Lipids have been shown to respond to changes in hydrostatic pressure with phase transitions similar to phase transitions induced by temperature changes [34, 111] providing the opportunity to study lamellar phase transitions at fixed temperatures [112, 113]. In addition, there are pressure-induced phase transitions that could not be seen by temperature changes [114, 115]. Furthermore, lamellar phases are non-congruent for different pressure and temperature regions. For example, the main phase transition of DMPC from the ripple phase $P_{\beta'}$ to the fluid phase L_{α} increases by a rate of ≈ 0.2 °C/MPa [116]. In contrast to the effect of pressure on the bulk lipid system, very little is known about solid supported, oligolamellar lipid coatings. For that reason NR measurements were performed at the V6 instrument in a high pressure cell [96] in excess D_2O . The experiments covered a temperature range between 21 °C and 38 °C and a pressure range from 0.1 MPa (ambient pressure) to 90 MPa. The aim of the experiment was to cross the main phase transition from a high pressure region (90 MPa) to a low pressure region (45 MPa) at a fixed temperature of 38 °C. Some of the results have already been published in [96]. The experimental cycle was performed with a freshly prepared sample (sample *E*) with a diameter of 60 mm using the spin-coating technique as described previously. Here, a 10 mg/mL solution of DMPC in chloroform was used.

Results

A first reflectivity curve of sample *E* was collected at 21 °C and 0.1 MPa (Figure 53). It features the typical reflectivity of an oligolamellar lipid coating on silicon in excess D_2O : A first Bragg peak at 0.0963 \AA^{-1} and well-resolved Kiessig oscillations with a spacing of 0.0107 \AA^{-1} were observed. The Bragg analysis revealed a lamellar spacing of $d = (65.2 \pm 0.3) \text{ \AA}$ with a total film thickness of $t = (587 \pm 5) \text{ \AA}$, resulting in a number of NBK = 9 lamellae making up the whole oligolamellar stack. In addition, optical matrix fitting of the measured reflectivity curves with the model of an oligolamellar lipid coating revealed a detailed picture of the scattering length density profile of the lipid coating (Figure 54). Using a number of 7 core lamellae and varying the thickness d and SLD of the individual layers resulted in a calculated reflectivity curve which was in good agreement with the measured reflectivity curve at 0.1 MPa and 21 °C.

The fitting parameters are summarized in Table 5.3 (on page 83). Raising the pressure to 90.0 MPa resulted in an immediate decrease in Bragg peak amplitude by 40%, which could be reproduced in a second measurement of the Bragg peak 7 h later. However, the peak position as well as the Kiessig oscillations did not alter. Increasing the temperature to 38 °C, while keeping the pressure at 90.0 MPa, revoked the intensity loss from the Bragg peak. Again, the same Bragg peak position and Kiessig oscillations were measured. The reflectivity of the substrate changed drastically after a pressure release to 45.0 MPa, keeping the temperature constant at 38 °C: The Bragg peak and the pronounced Kiessig oscillations vanished. As already described in the previous chapter, also here the reflectivity curve could be fitted with a model of one remaining lipid lamella on the silicon substrate. A summary of the performed experimental cycle is given in Figure 55 (on page 82). Further discussion of the results is given in chapter 5.2.5 on page 93.

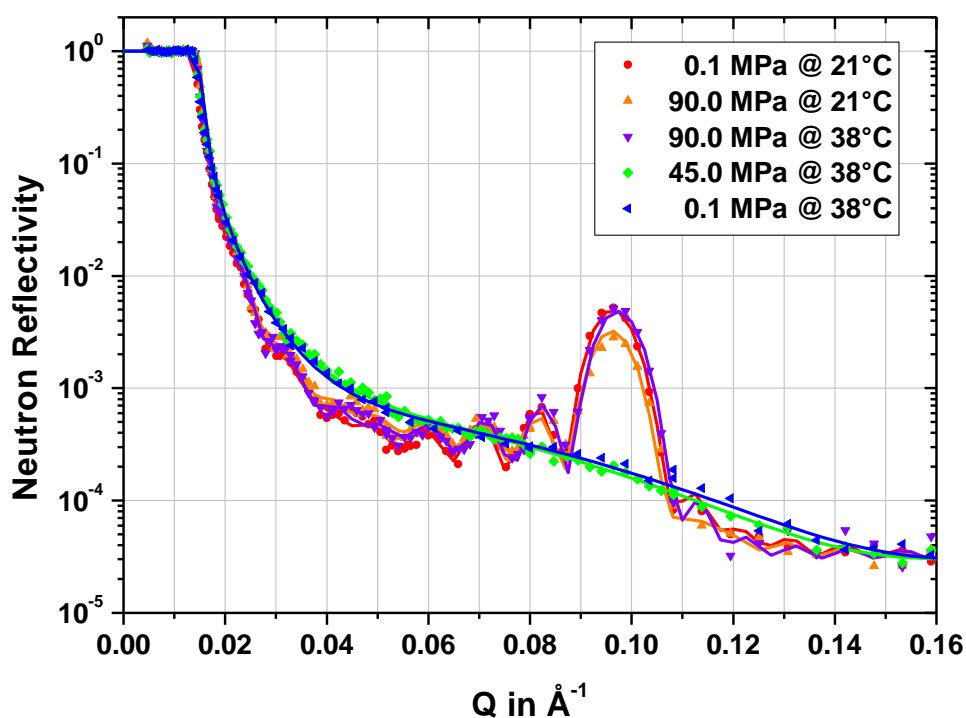


Figure 53: Neutron reflectivity curves (symbols) of an oligolamellar lipid coating on silicon (sample E), measured against pure D₂O. Solid lines are Parratt fits to the data, with corresponding SLD profiles shown in Figure 54. [96]

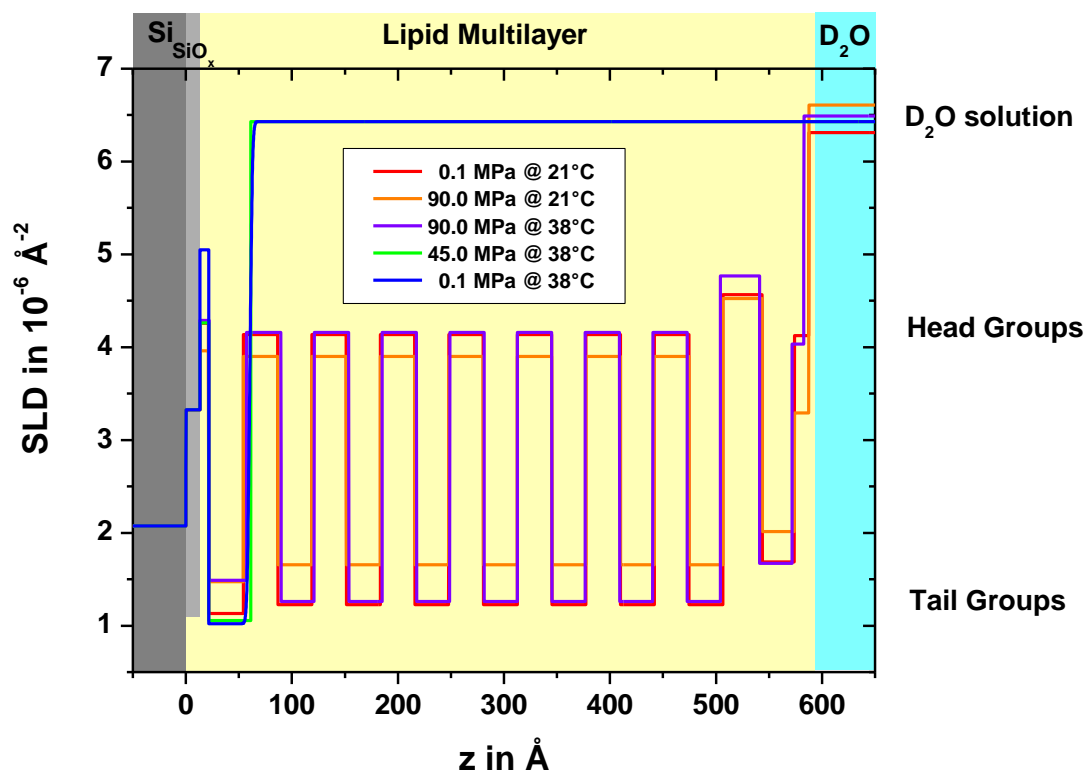


Figure 54: Scattering length density (SLD) profiles perpendicular to the solid-liquid interface, corresponding to the fits in Figure 53. [96]

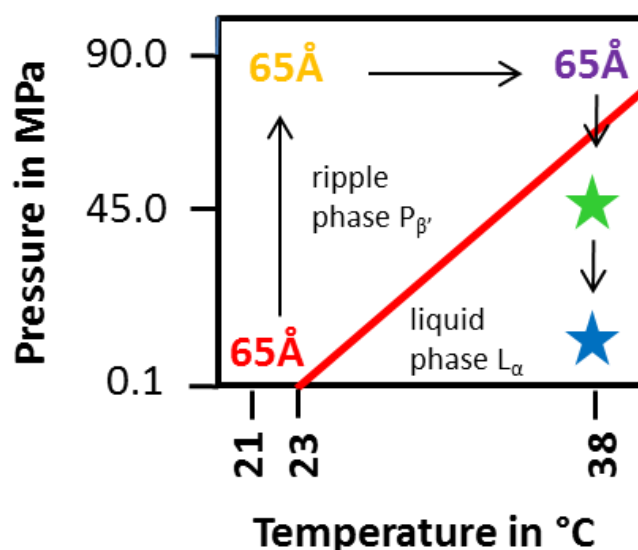


Figure 55: Phase diagram of DMPC with a summary of the experimental findings. The red line indicates the main phase transition for the bulk system, taken from [111]. One experimental cycle was performed along the arrows starting at 0.1 MPa and 20 °C. All three measurements in the ripple phase $P_{\beta'}$ revealed a repeat distance of 65 Å. After crossing the phase transition at 38 °C unbinding of lipids occurred (stars). [96]

		0.1 MPa		90.0 MPa		90.0 MPa		45.0 MPa		0.1 MPa	
		21 °C		21 °C		38 °C		38 °C		38 °C	
Nr.	param. [param.]	d	SLD	d	SLD	d	SLD	d	SLD	d	SLD
		[Å]	[Å ⁻²]	[Å]	[Å ⁻²]	[Å]	[Å ⁻²]	[Å]	[Å ⁻²]	[Å]	[Å ⁻²]
0	Si	N/A	2.07	N/A	2.07	N/A	2.07	N/A	2.07	N/A	2.07
	SiO _x	13	3.34	13	3.33	13	3.34	13	3.34	13	3.34
1	Heads	8	3.47	8	3.34	8	4.04	8	4.00	8	4.50
	Tails	32	1.13	32	1.45	32	1.29	32	0.60	32	0.48
	...										
2 (x7)	Interlayer	32	3.93	32	3.69	32	4.02	-	-	-	-
	Tails	32	1.05	32	1.45	32	1.24	-	-	-	-
	...										
3	Interlayer	38	4.32	38	4.30	38	4.55	-	-	-	-
	Tails	30	1.36	30	1.52	30	1.23	-	-	-	-
	Heads	11	3.92	11	3.30	11	4.65	12	4.00	12	4-50
4	D ₂ O	N/A	6.13	N/A	6.38	N/A	6.28	N/A	6.25	N/A	6.16
	D ₂ O _{th}		6.36		6.60		6.57		6.45		6.33

Table 5.3: Table of parameters (param.) extracted from model fits measured with sample E. The coloured columns correspond each to one measurement shown in Figure 53, respectively. The numbers in the left column correspond to the nomenclature according to the model of an oligolamellar lipid coating (Figure 38). The “Interlayer” represents a combined layer of lipid head groups and solution, as described in chapter 5.1 on page 67. The core membranes (Nr. 2) are repeated 7 times in the fitting routine in order to give the best fit. A theoretical SLD of D₂O (D₂O_{th}) for the measured temperature and pressure was calculated according to [117]. All data have already been published in [96].

The position of the critical momentum transfer Q_c can be used as an indicator for the pressure change inside the sample cell [117]. For a thin organic coating, the reflectivity in the low Q -range is exclusively determined by the scattering length densities (SLD) of the bulk materials, i.e. silicon substrate, and the liquid fronting phase, i.e. D₂O. As the density of the silicon does not alter significantly within the probed pressure range [118], a shift in Q_c directly corresponds to a density change of the D₂O liquid phase. The position of Q_c was read out at

$R = 0.5$ to avoid the influence of surface roughness, when plotted on a linear scale (Figure 56). With increasing pressure at 21 °C a pronounced shift to higher Q -values from 0.0146 Å⁻¹ (0.1 MPa) to 0.0151 Å⁻¹ (90 MPa) was observed. By increasing the temperature to 38 °C, Q_c shifted back to 0.0149 Å⁻¹ (90 MPa). Upon full pressure release at 38 °C, Q_c shifted back to 0.0148 Å⁻¹. After every change of pressure the sample was newly aligned, which underlines the significance of the measured shifts in Q_c . The value of Q_c can be determined with an accuracy of 0.0001 Å⁻¹, taking into account the accuracy in angular movements of α_i of 0.002° for angular dispersion at V6. Hence, the shifts of Q_c are above the experimental error. In addition, the relative shifts of SLD for the D₂O bulk phase upon pressure changes, resulting from the analysis of Q_c by the *Parratt* software package, correspond well to theoretical values from the literature [117]. A comparison of calculated SLD values for D₂O (D_2O_{th}) and values extracted from the experiment (D_2O) is shown in Table 5.3.

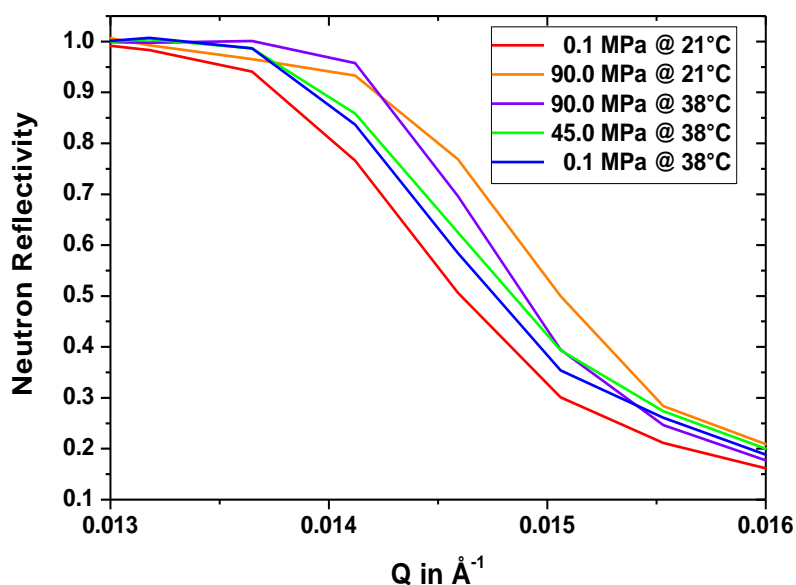


Figure 56: Close-up region of the critical momentum transfer Q_c on a linear scale. The total reflection edge shifts to higher Q -values with increasing pressure. [96]

5.2.3 Effect of shear

Introduction

Keeping in mind the potential use of lipid layers as a biocompatible coating for movable and mechanically stressed implants such as artificial joints [16], the stability of the lipid coatings under external shear forces is a key parameter for a successful application. Therefore, oligolamellar lipid coatings were investigated under applied load using a shear setup. In order

to study the stability of the coating in excess solution, neutron reflectivity measurements have been performed at the AMOR reflectometer at the Paul-Scherrer-Institute (PSI, Villigen, Switzerland). The investigated sample was an oligolamellar lipid coating on silicon (sample F), prepared by spin-coating a solution of 10 mg/mL DMPC in chloroform. The temperature range between 21 °C and 30 °C was subject of the investigation. The coating was incubated and measured against D₂O solution. In order to mimic the shear force on a knee joint for a rather pronounced strain, for example resulting from a short distance sprint of a person, a frequency of 5 Hz was estimated and applied. Starting at 21 °C, the temperature was increased to 24 °C and subsequently increased in steps of 2 °C up to 30 °C. For each temperature step two reflectivity curves were recorded in order to distinguish between temperature and time effects. All measurements are displayed in Figure 57. Each first order Bragg peak was fitted with a Gaussian profile. The resulting values (amplitude, FWHM and d-spacing) are shown in Figure 58 on page 87, including the uncertainties of the Gaussian fits.

Results

The first measurements at 21 °C with no shear force applied showed the already well-known reflectivity of an oligolamellar lipid coating with a d-spacing of $d = (65.21 \pm 0.02) \text{ \AA}$. A second measurement showed an identical result. After a shear force was applied, using a frequency of 5 Hz, the d-spacing increased slightly to $d = (65.35 \pm 0.01) \text{ \AA}$. Furthermore, up to 24 °C the reflectivity of the sample did not show any variations beyond the experimental uncertainties. For $T \leq 24 \text{ °C}$ only a slight increase in amplitude by 0.0012 was recorded from 0.0087 ± 0.0001 to 0.0099 ± 0.0001 . Above 24 °C the d-spacing dropped to $d = (64.49 \pm 0.02) \text{ \AA}$, the FWHM increased from $(0.0089 \pm 0.0001) \text{ \AA}^{-1}$ to $(0.0093 \pm 0.0001) \text{ \AA}^{-1}$, and the amplitude reached its maximum at 0.0111 ± 0.0001 . For $T > 26 \text{ °C}$ the amplitude decreased continuously to 0.0014 ± 0.0001 . In addition, FWHM increased, until a maximum of $\text{FWHM} = (0.0110 \pm 0.0002) \text{ \AA}^{-1}$ was reached for the first measurement at 28 °C. In subsequent measurements FWHM decreased to $\text{FWHM} = (0.0105 \pm 0.0005) \text{ \AA}^{-1}$, reached at the second measurement at 30 °C. The d-spacing directly scaled with the temperature for $T > 24 \text{ °C}$: for every 2 °C the d-spacing dropped by around 1 Å to a final value of $d = (63.07 \pm 0.11) \text{ \AA}$. A combined discussion of the results is given in chapter 5.2.5 on page 93.

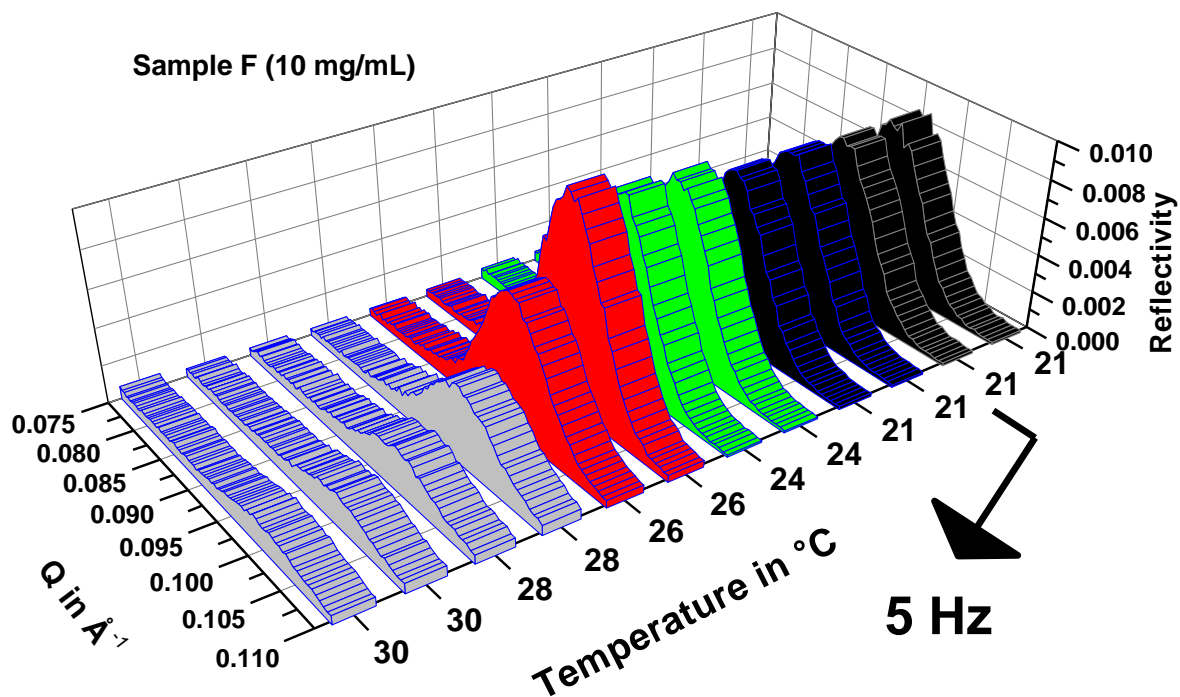


Figure 57: Neutron reflectivity curves of an oligolamellar lipid coating on silicon (sample F) in excess D_2O . After the first two measurements at 21°C a shear force was applied with a frequency of 5 Hz. Subsequently the temperature was increased up to 30°C . At each temperature step two reflectivity measurements were made.

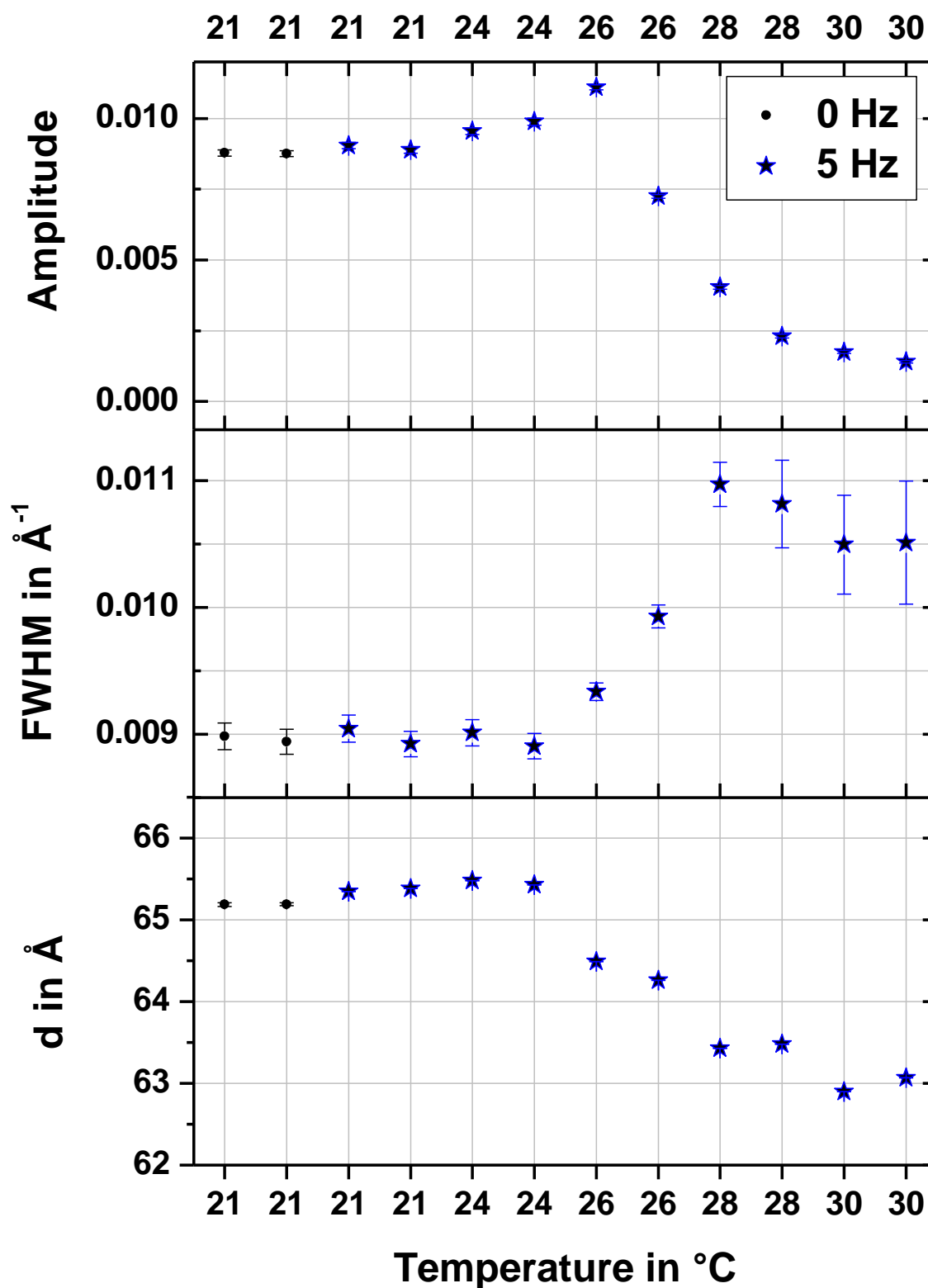


Figure 58: Results of the Bragg peak analysis of the first order Bragg peaks, displayed in Figure 57.

5.2.4 Effect of substrate

Introduction

In the last decade, the search for biocompatible materials has become a major topic in medical research. While the durability of implants has been improved significantly, the need for permanent and long-lasting implants is steadily growing [119]. For biomedical applications, titanium-based alloys are most suitable [120]. The combination of suitable metallic implant surfaces with lipid coverage is most promising for forthcoming implant modifications [16]. Here, one of the fundamental requirements is the reliable preparation of stable lipid coatings on the implant surfaces. In the following, the stability of oligolamellar lipid coatings on silicon substrates with titanium cover is quantified. Measurements were performed against excess D₂O in the temperature range between 20 °C and 30 °C (sample TiA). Starting at 21 °C, the temperature was increased to 24 °C and consequently increased in steps of 2 °C up to 30 °C. For each temperature step two successive reflectivity curves were recorded in order to distinguish between temperature and time effects. In addition, the stability under load was studied (sample TiB) using the shear setup as described in chapter 3.2.6.

For sample preparation, three silicon substrates (TiA, TiB and TiC) were first covered with a 90 Å thick titanium coating by the sputtering technique [121]. X-ray reflectivity measurements of the samples revealed identical titanium layer thicknesses within the experimental resolution, calculated by the appearing Kiessig oscillations (Figure 59): for sample TiA $t = (148 \pm 4) \text{ \AA}$ and for sample TiB $t = (149 \pm 4) \text{ \AA}$. In addition, Bragg peaks measured for TiA and TiB at $Q_B = (1.0241 \pm 0.0002) \text{ \AA}^{-1}$ with a lattice parameter of $6.13 \pm 0.04 \text{ \AA}$ are measured. For sample TiC the Bragg peak was not observed. The origin of these additional Bragg peak is not clear, as they do not appear for sample TiC and do not result from the titanium lattice parameters ($a = 2.96 \text{ \AA}$, $c = 4.71 \text{ \AA}$) [122]. Subsequently the samples TiA and TiB were coated with an oligolamellar stack of lipid layers, by spin-coating a solution of 10 mg/mL DMPC in chloroform.

Results of the effect of temperature

After the incubation of sample TiA in pure D₂O, the sample was measured at the V6 neutron reflectometer in a solid-liquid cell (Figure 60). The first order Bragg peak, resulting from the oligolamellar lipid coating of the first measurement at 21 °C, revealed a d-spacing of $d = (66.10 \pm 0.77) \text{ \AA}$. The Kiessig oscillations revealed a total coating thickness of

$t = (525 \pm 50) \text{ \AA}$. With a measured titanium layer thickness of 149 \AA , a number of $N = (6 \pm 1)$ lipid bilayers was extracted. Already the second measurement at $21 \text{ }^\circ\text{C}$ revealed a decreasing Bragg peak amplitude. In the following the Bragg peak amplitudes decreased further. At $30 \text{ }^\circ\text{C}$, a total coating thickness of $t = (162 \pm 5) \text{ \AA}$ remained, calculated by the minimum positions of the first Kiessig oscillation. All measured reflectivity curves are shown in Figure 61. The fitted Bragg peak amplitudes are shown in Figure 66 on page 96 and discussed on the same page.

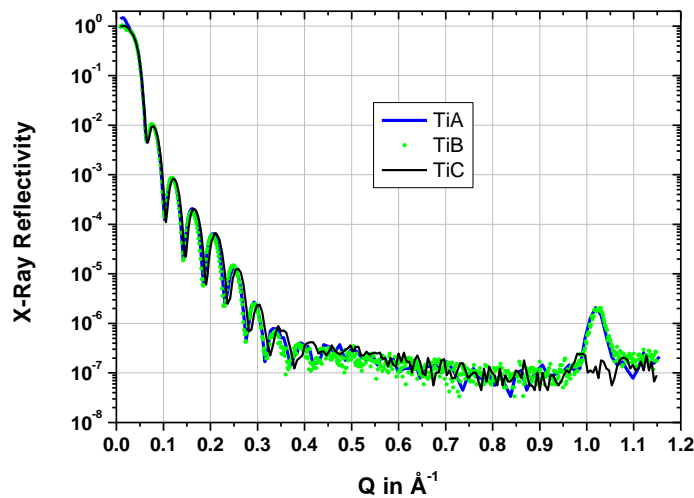


Figure 59: X-ray reflectivity measurement of sample TiA, TiB and TiC, *before* lipid coating, in order to characterize the titanium layers on the silicon substrates. The Kiessig oscillations revealed a d -spacing of $t = (148 \pm 4) \text{ \AA}$. The Bragg peaks with unknown origin at $Q_B = (1.0241 \pm 0.0002) \text{ \AA}^{-1}$ appeared only for TiA and TiB, but not for TiC.

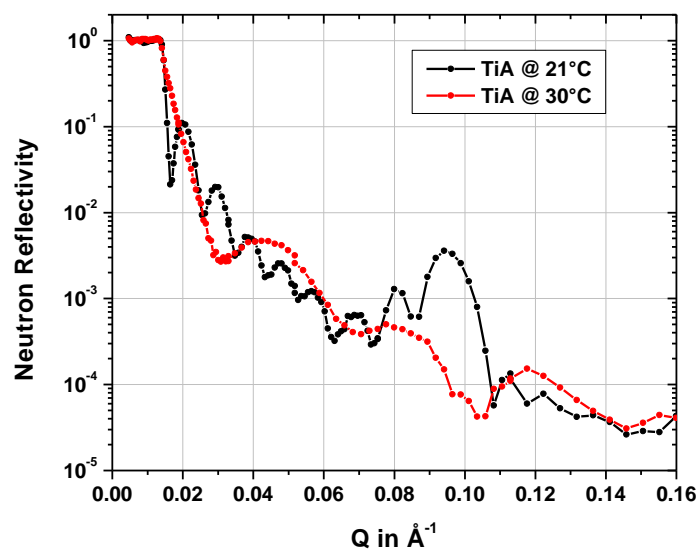


Figure 60: Neutron reflectivity of sample TiA in excess D_2O at elevated temperatures.

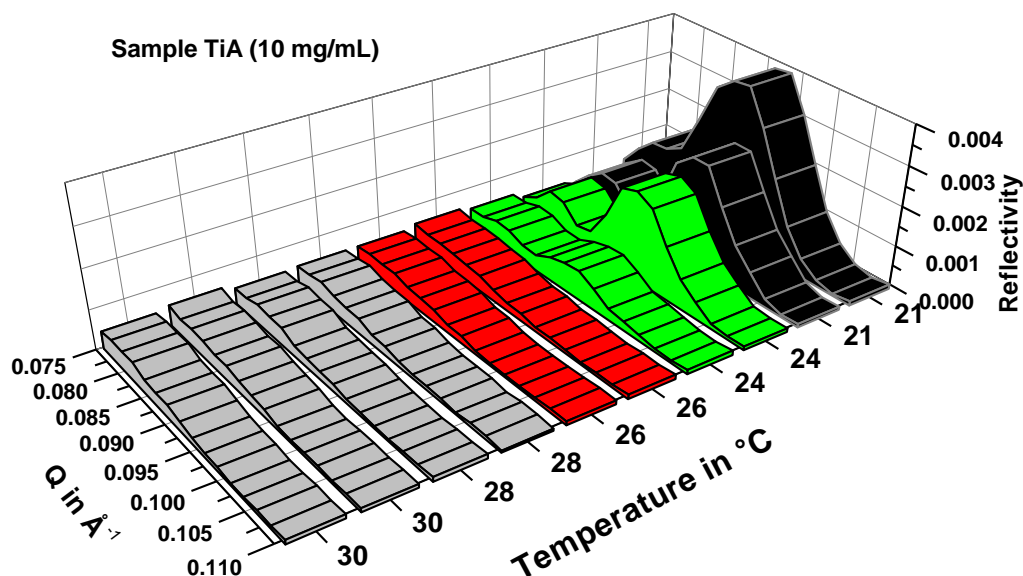


Figure 61: Neutron reflectivity profiles of sample TiA in excess D_2O , measured in the temperature range between 20 °C and 30 °C. At each temperature step two measurements were performed.

Results of the effect of temperature and shear

Sample TiB was measured following the same protocol as described before for sample F (Figure 57 on page 86). The lipid-coated sample was incubated in pure D_2O and measured in the shear setup at the neutron reflectometer AMOR at PSI in Switzerland at elevated temperatures between 21 °C and 30 °C. A first measurement at 21 °C revealed a d-spacing of $d = (68.03 \pm 0.13) \text{ \AA}$. The poorly resolved Kiessig oscillations are probably due to a less homogeneous coating and do not allow for the calculation of the total coating thickness (Figure 62). All measured reflectivity curves are shown in Figure 63 on page 91. A complete analysis of the first order Bragg peak is shown in Figure 64 on page 92. Upon employing the shear force with a frequency of 5 Hz, an increase of the d-spacing by 1.26 Å to $d = (69.29 \pm 0.13) \text{ \AA}$ was measured. The FWHM, seen from the following analysis, does not show a clear trend beyond the uncertainties of the measurement. Also the d-spacing did not change further until temperature was increased to 26°C. Here, the d-spacing decreased by 3 Å to $d = (66.10 \pm 0.04) \text{ \AA}$, accompanied by an increase in Bragg peak amplitude from 0.0041 ± 0.0001 at 24°C to 0.00633 ± 0.0001 at 26°C. With increasing temperature to 28°C the amplitude started to drop, accompanied by a further decrease in d-spacing to $d = (64.47 \pm 0.05) \text{ \AA}$. For the second measurement at 28°C, the Bragg peak was already so weak, that it was not possible to distinguish between the Bragg peak, resulting from the lipid

coating, and the Kiessig oscillations, resulting from the titanium coating. A final measurement of the whole reflectivity curve after an additional increase in temperature to 40°C is shown in Figure 62. The remaining Kiessig oscillations revealed a total coating thickness of $t = (169 \pm 5) \text{ \AA}$. A combined discussion of the results is given in chapter 5.2.5 on page 93.

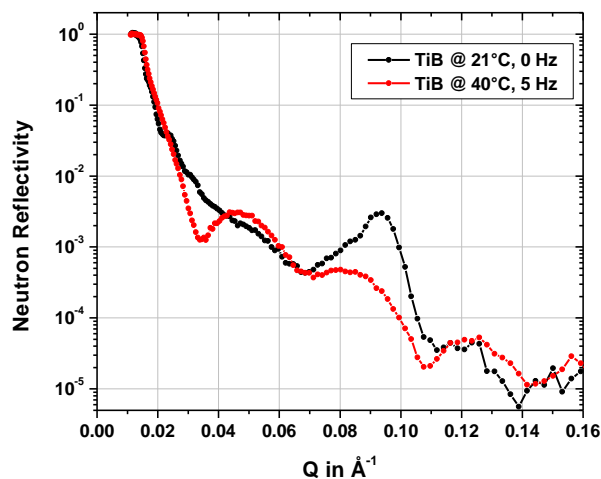


Figure 62: Neutron reflectivity of sample TiB at elevated temperatures, measured with the shear setup. As opposed to sample TiA, sample TiB was sheared at 5 Hz during the increase in temperature.

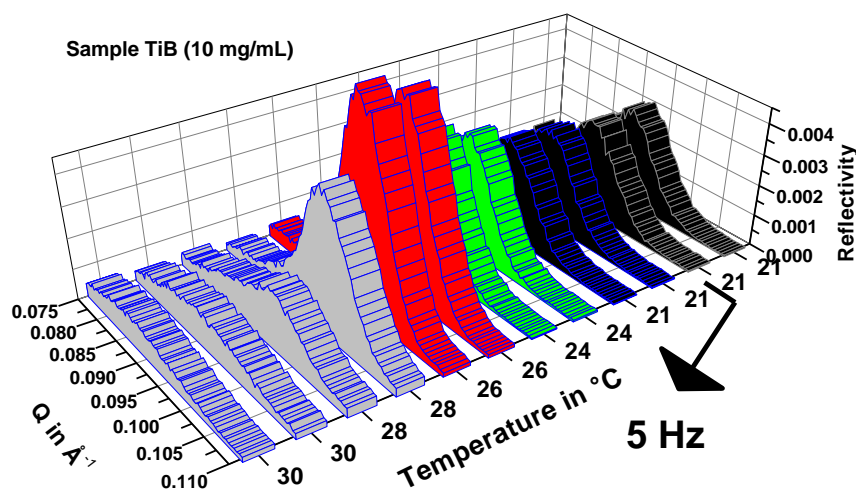


Figure 63: Neutron reflectivity curves of sample TiB, measured in the shear setup at elevated temperatures. All plots illustrated with a blue border are measured under a constant shear force at a frequency of 5 Hz.

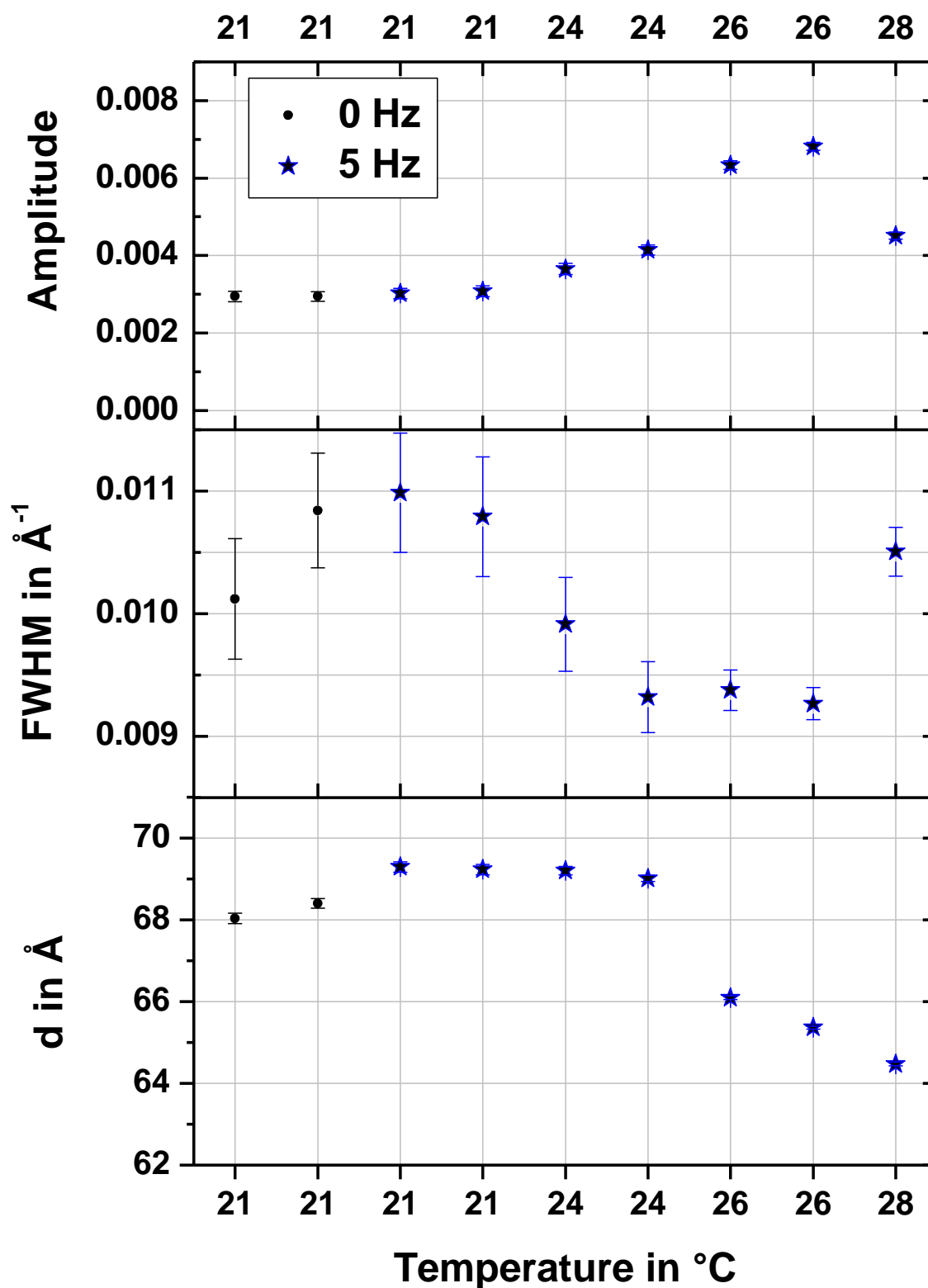


Figure 64: Bragg peak analysis of sample TiB.

5.2.5 Discussion on the stability of lipid coatings

An overview on the samples measured in this section is given in Table 5.4.

Sample	coating technique	used solution	coating	d-spacing at 21°C in Å	investigated parameter
A	spin coating	5 mg/mL	oligolamellar	66.89 ± 0.04	temperature
B	spin coating	10 mg/mL	oligolamellar	73.36 ± 0.11	temperature
C	spin coating	10 mg/mL	oligolamellar	65.48 ± 0.05	temperature
D	air brush	10 x 10mg/mL	multilamellar	65.31 ± 0.25	temperature
E	spin coating	10 mg/mL	oligolamellar	65.20 ± 0.30	pressure
F	spin coating	10 mg/mL	oligolamellar	65.19 ± 0.02	shear
TiA	spin coating	10 mg/mL	oligolamellar	66.10 ± 0.77	substrate
TiB	spin coating	10 mg/mL	oligolamellar	68.03 ± 0.13	substrate/shear
TiC	-	-	-	-	titanium coating

Table 5.4: Overview of investigated samples of chapter 5. The d-spacings are results of measurements on the DMPC lipid coatings, when incubated in a pure D_2O liquid phase at 21 °C.

As proved by the above listed samples, the spin-coating technique yields reproducible and highly ordered lipid coatings: Beside the appearing Bragg peaks, the measured reflectivity curves showed in addition Kiessig oscillations. The lamellar spacing between 65 Å and 68 Å found at 21 °C for the samples *A*, *C*, *D*, *E*, *F*, *TiB* and *TiB* correspond well with the d-spacing reported for the ripple-like phase $P_{\beta'}$ of fully hydrated DPMC multilayers at 21 °C [29, 112]. Sample *B*, in contrast, with $d = (73.36 \pm 0.11)$ Å at 21 °C deviates significantly in d-spacing. Differences in the structure of the lipid coating might be due to differences in the alignment of the lipid lamellae, as the samples have not been annealed before the measurements. It is reported in literature, that lipid multilayer were annealed before the measurements, in order to obtain well oriented samples [123]. In addition, other groups report of variations in the d-spacings for nominally equally prepared samples [124]. The analysis of samples *C* and *E* by the optical matrix approach revealed a more detailed picture of the oligolamellar lipid coatings (Figure 50 on page 76, Figure 54 on page 82). Samples *C* and *E* were fitted by the model of an oligolamellar lipid coating. The differences seen for inner lamella, core lamellae and outer lamella are due to the fact, that these lamellae are restricted by different physical

conditions: The inner head groups, directly attached to the substrate, are confined by the silicon support, while the outer head groups do not experience this confinement. In addition, inner and outer lamellae miss one opposing lamella.

A major change in the structure of the lipid coating was observed with increasing temperature for samples *A*, *B*, *C* and *D* and decreasing pressure for sample *E*, namely, when heated to 26°C or upon pressure release at 38°C from 90 MPa to 45.0 MPa. The oligolamellar lipid coatings follow an unbinding process, leaving only one lipid membrane attached to the silicon substrate. While the temperature-induced unbinding process was followed with intermediate temperature steps, pressure-induced unbinding was only measured for its final state. The unbinding from the samples observed for all oligolamellar lipid coatings (sample *A*, *B*, *C* and *E*) occurred after crossing the main phase transition to the liquid-like L_α phase. We associate the present unbinding process of the lipid films from its solid support with the phase transition from P_β to L_α .

In many experiments only a swelling process was observed experimentally in the vicinity of T_m measured by neutron and X-ray diffraction [29, 125] and nuclear magnetic resonance measurements [18, 125]. A total unbinding of a multilamellar thick DMPC coating was observed by X-ray reflectivity measurements at a critical temperature of 95°C [126]. All these studies focused on thick multilamellar bulk systems and did not show an unbinding transition around T_m . The stability of a multilayered lipid system around T_m was also confirmed by measurements with a multilayered coating (sample *D*) in this work. Here, the presence of at least 26 bilayers on the sample surface was measured up to 30°C. Due to the restricted resolution of the experiment, a higher number of bilayers could not be resolved.

In contrast, the measurements on the oligolamellar lipid coatings show that an unbinding process is initiated with the phase transition into the fluid-like L_α phase. The described unbinding transition has already been proposed in 1986 by a theoretical work of Lipowsky and Leibler [47]. After initiation of the process by increasing temperature, all investigated oligolamellar samples showed an unbinding transition with intermediate steps, until finally only one bilayer remained on the substrates (compare Figure 52 on page 79 and Table 5.2 on page 77). The high sensitivity of neutron reflectometry for the outer membranes of a lipid stack was achieved by preparing only a thin oligolamellar lipid coating. In 2006 Lecuyer and Charitat studied a multilamellar thick lipid coating by fluorescence microscopy [127]. The applied technique allowed in particular studying the behaviour of the outer membranes of the

lipid stack. By approaching the main phase transition, the authors followed an unbinding of these outer layers. These results are in good agreement with the measurements on oligolamellar lipid coatings by neutron reflectometry. They show an unbinding transition, starting at the main phase transition, which proceeds layer by layer (compare Figure 52 on page 79 and Table 5.2 on page 77). It is assumed that the sharp decrease in the bending rigidity κ , when approaching the main phase transition, is followed by the formation of lipid vesicles (Figure 65) [127]. The decrease in κ has been shown in independent studies [29, 44, 45]. Once the lipid vesicles are built, they disperse irreversibly in the surrounding solution.

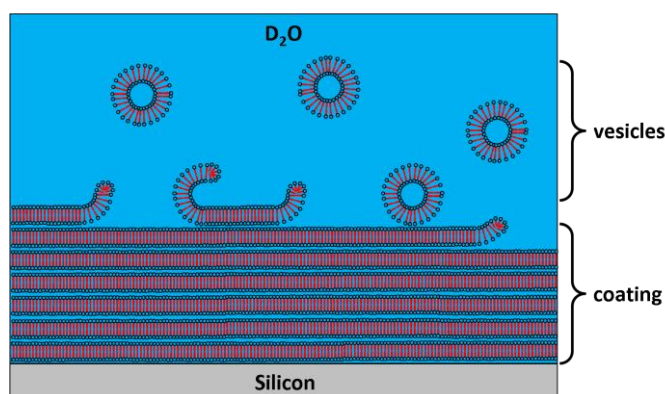


Figure 65: Sketch of the unbinding process of a lipid coating from a silicon substrate in excess D_2O by vesicle formation.

About the effect of substrate and shear

For sample *TiA* the reflectivity changed within the first two measurements already at 21°C. The second sample on titanium support, sample *TiB*, did not show these changes in reflectivity at 21°C. As these two samples show contradictory results, further measurements are necessary in order to verify the stability of oligolamellar lipid coatings on titanium support. In addition, up to 24°C, shear force and titanium sub-layer did not alter the reflectivity of the lipid coatings *F* and *TiB*. The resulting reflectivity curves (Figure 57 on page 86, Figure 61 on page 90 and Figure 63 on page 91) are almost identical to curves measured without shear, but with identical temperature steps, as described before (Figure 47 on page 74 and Figure 48 on page 75). Interestingly, even when exposed to an external force, the coating *TiB* showed a stable lamellar structure up to 26°C, i.e. for T 2°C higher than T_m , the main phase transition temperature of bulk DMPC. Only at 28 °C the structure started to change. For the non-metalized sample *F*, structural changes were already observed for the second measurement at 26 °C, i.e. somewhat earlier. From the decrease in d -spacing, observed for both samples, *F* and *TiB*, starting at 24°C, it is clear, that the main phase

transition occurred at 24°C, as the decrease in d-spacing is due to the chain melting of the lipid tail groups [36].

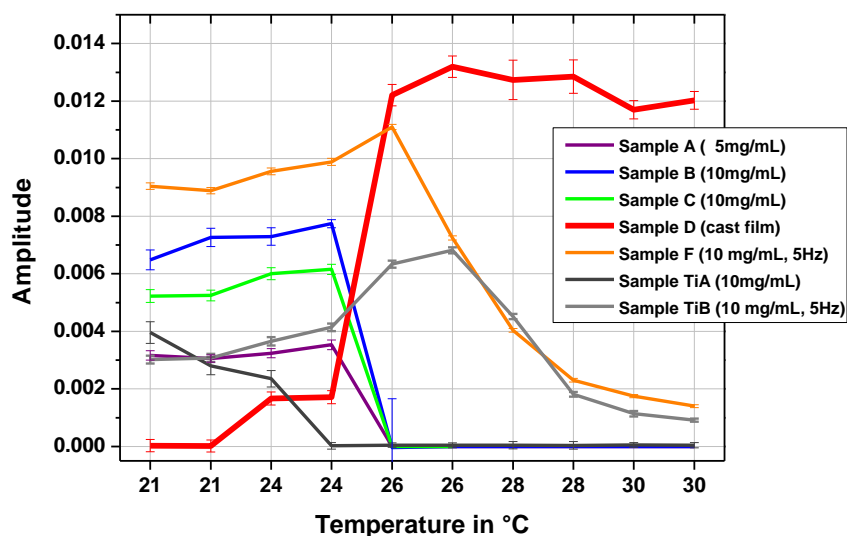
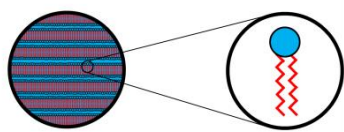


Figure 66: Comparison of all measured first order Bragg peak amplitudes as a function of temperature. Taking the amplitude as a measure for the number of solid-bound lipid layers, the graph shows clearly that all oligolamellar lipid coatings unbind from the substrate: Without shear between 24 °C and 26 °C (Sample A, B, C), with shear between 26 °C and 28 °C (Sample F and TiB). The oligolamellar coating of sample TiA was not stable, in strong contrast to sample D, for which the multilamellar coating remained bound to the substrate over the measured temperature and time range.

In the following the Bragg peak amplitude of the lipid coatings is taken as a parameter to describe the number of substrate bound bilayers; a comparison is shown in Figure 66. The decreasing amplitudes of oligolamellar samples measured without shear (A, B and C) for $T > 26$ °C indicate the trend for the oligolamellar lipid lamellae to unbind from the solid support after crossing the main phase transition of DMPC in D_2O at $T_m = 24.5$ °C. In contrast, for the multilamellar lipid coating (sample D) a pronounced increase in amplitude for $T > 24$ °C without shear is observed, due to an increase of coherent scattering domains upon further alignment of the lipid lamellae (compare detailed discussion in chapter 5.3). Therefore, within the resolution of the experiment, i.e. 26 lipid membranes, no unbinding could be observed for a multilamellar lipid coating. For the oligolamellar lipid coatings, measured at 5 Hz (sample F and TiB), an increase in amplitude could be observed for $T > 24$ °C, which might be due to a better alignment of the lipid membranes. The applied shear force stabilizes the oligolamellar lamellar system above the main phase transition for 24 °C $< T < 28$ °C, which was not reported before. The following decrease in amplitude for $T > 28$ °C is the result of the unbinding of the lipid membranes. The instant decrease of amplitude of sample TiA is an exception.

5.3 Phase transition of multilamellar lipid coatings



As described previously (chapter 2.1 on page 17), DMPC lipid molecules undergo a first order phase transition from the ripple phase $P_{\beta'}$ to a liquid-like phase L_{α} between 21.5 °C and 24.5 °C [29, 48-50]. Reported main phase transition temperatures T_m for bulk systems as measured by different techniques disagree concerning the value of the phase transition temperature [128]. Crossing the main phase transition temperature has a pronounced impact on the conformation of the hydrocarbon chains (for more details see chapter 2.1): While in the ripple phase the hydrocarbon chains are more extended and ordered, a chain melting induces conformationally disordered chains in the liquid-like state for $T > T_m$ [34]. The chain melting has an impact on the vibrational modes of the hydrocarbon groups of the individual lipids as can be seen by ATR-FTIR. On a larger scale the chain melting influences the structural state of a lipid bilayer: Due to the chain melting the bilayer thickness decreases. Consequently, a change of the lamellar structure can be probed by NR.

With the tools of BioRef at hand, we were able to address the question on the correlation between chain melting of individual lipid molecules and the impact on a solid-supported lipid multilayer coating. Consequently, temperature dependent combined ATR-FTIR and NR studies were performed simultaneously on the same sample. The temperature range around the main phase transition between 20°C and 30°C of DMPC multilayer system against excess D_2O liquid phase was probed. A silicon ATR crystal (ATR5) was used as integrative support (introduced in chapter 4.1 on page 57). A lipid multilayer coating was prepared with the air brush technique. After evaporation of chloroform the sample was incubated in pure D_2O in the sample cell. The experimental cycle covered four scans in the respective temperature range from 20°C to 30 °C: First, the sample was heated from 20°C to 30°; second, the sample was directly cooled again to 20°C. The described cycle of heating and cooling was repeated one more time. In the following the four scans are referred to as *heating1*, *cooling1*, *heating2*, *cooling2*. Temperature was changed every 100 minutes in 0.5 °C steps. At each temperature two subsequent NR measurements were performed and 5-6 IR absorbance spectra recorded.

5.3.1 Infrared absorption of a multilamellar lipid coating

The conformational changes of lipid molecules were studied by ATR-FTIR using the setup described in chapter 4. A measurement consisting of 124 full scans was performed every 20 minutes, resulting in 5-6 absorbance spectra per temperature step.

Results

The most pronounced temperature induced changes on infrared absorption are changes seen in the absorption bands of the hydrocarbon groups (CH_2). The asymmetric $\nu_{\text{as}}(\text{CH}_2)$ and symmetric $\nu_{\text{s}}(\text{CH}_2)$ stretching bands show high peak amplitudes and sharp peak shapes (Figure 67). The following analysis is focused on the $\nu_{\text{s}}(\text{CH}_2)$ band, since it is less altered by neighbouring vibrational modes of methyl groups [129]. In the gel-like phase at 20°C the $\nu_{\text{s}}(\text{CH}_2)$ band absorbs at 2851 cm^{-1} . When heated to 30°C the band shifts 2 cm^{-1} to 2853 cm^{-1} . In addition, its full width at half maximum (FWHM) increases, while the amplitude decreases. Cooling the system again to 20°C reproduces the original absorption band position and FWHM.

The absorption bands $\nu_{\text{s}}(\text{CH}_2)$ after 80 minutes of equilibration time were fitted for all four temperature cycles. The fitting results (wavenumber, FWHM and amplitude) are shown in Figure 68 on page 100. The maximum uncertainties are $\delta\text{wavenumber} = 0.01\text{ cm}^{-1}$, $\delta\text{FWHM} = 0.12\text{ cm}^{-1}$ and $\delta\text{amplitude} = 0.011$, given from the Gaussian fitting profiles. For legibility reasons they are mentioned only at the beginning of the following paragraph. The values for wavenumber, FWHM and amplitude are almost identical at each temperature, regardless of the type (heating or cooling) of the cycles. Pronounced *jumps* in wavenumber, FWHM and amplitude between 24.0°C and 24.5°C are clearly visible and reproducible. These *jumps* are characterized by drastic changes in wavenumber ($\Delta\tilde{\nu} = (0.98 \pm 0.01)\text{ cm}^{-1}$), FWHM ($\Delta\text{FWHM} = (0.47 \pm 0.12)\text{ cm}^{-1}$) and amplitude ($\Delta\text{amplitude} = 0.029 \pm 0.011$) and are a clear sign for a first order phase transition. Here, it is the phase transition from the ripple phase $\text{P}_{\beta'}$ to the fluid-like phase L_{α} upon heating of the sample.

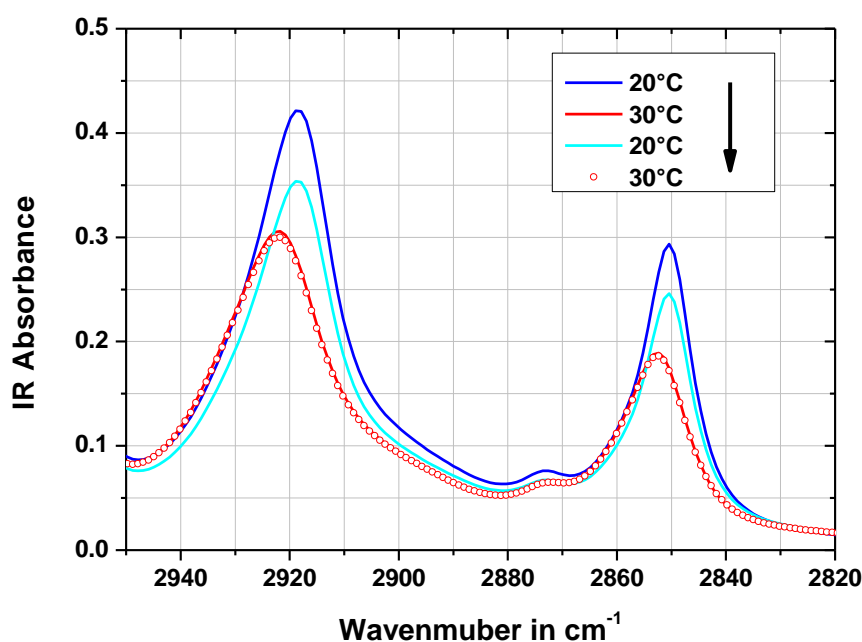


Figure 67: Infrared absorption of a multilamellar lipid coating on a silicon substrate (ATR5) against pure D_2O . Shown is the absorbance of the CH_2 groups, measured after 80 minutes of equilibration time. Temperature was cycled from 20 °C to 30 °C to 20 °C and back to 30 °C.

Discussion on IR results

In general, for increasing (decreasing) temperature the values for wavenumber and FWHM are increasing (decreasing), while the values for amplitude are decreasing (increasing) (Figure 68 on page 100). This is due to the fact, that upon administering of thermal energy to the lipid system the chain mobility increases, resulting in a broadening of the absorption bands, as well as in a decrease of the absorption amplitudes [129]. Only recently it was proposed, that the $\nu(CH_2)$ bands of the hydrocarbon groups can be divided in two components by singular value decomposition analysis [30, 130]: One component refers to vibrations of the trans segments (lower wavenumber) and the other to vibrations of the gauche segments (higher wavenumber). Within this approach a change of the maximum position of the absorption band, FWHM and amplitude is due to a change in the relative intensity of the two components. The chain melting results in a higher number of gauche segments, resulting in a bigger intensity of the gauche-component of the absorption band. Since this component has a higher wavenumber than the trans-component, the maximum position shifts to higher wavenumbers, the FWHM increases and the overall amplitude decreases. The chain melting is most pronounced at a critical temperature between 24.0 °C and 24.5 °C, which corresponds to the main phase transition of fully hydrated DMPC in D_2O , reported to be at $T_m = 24.5$ °C [50].

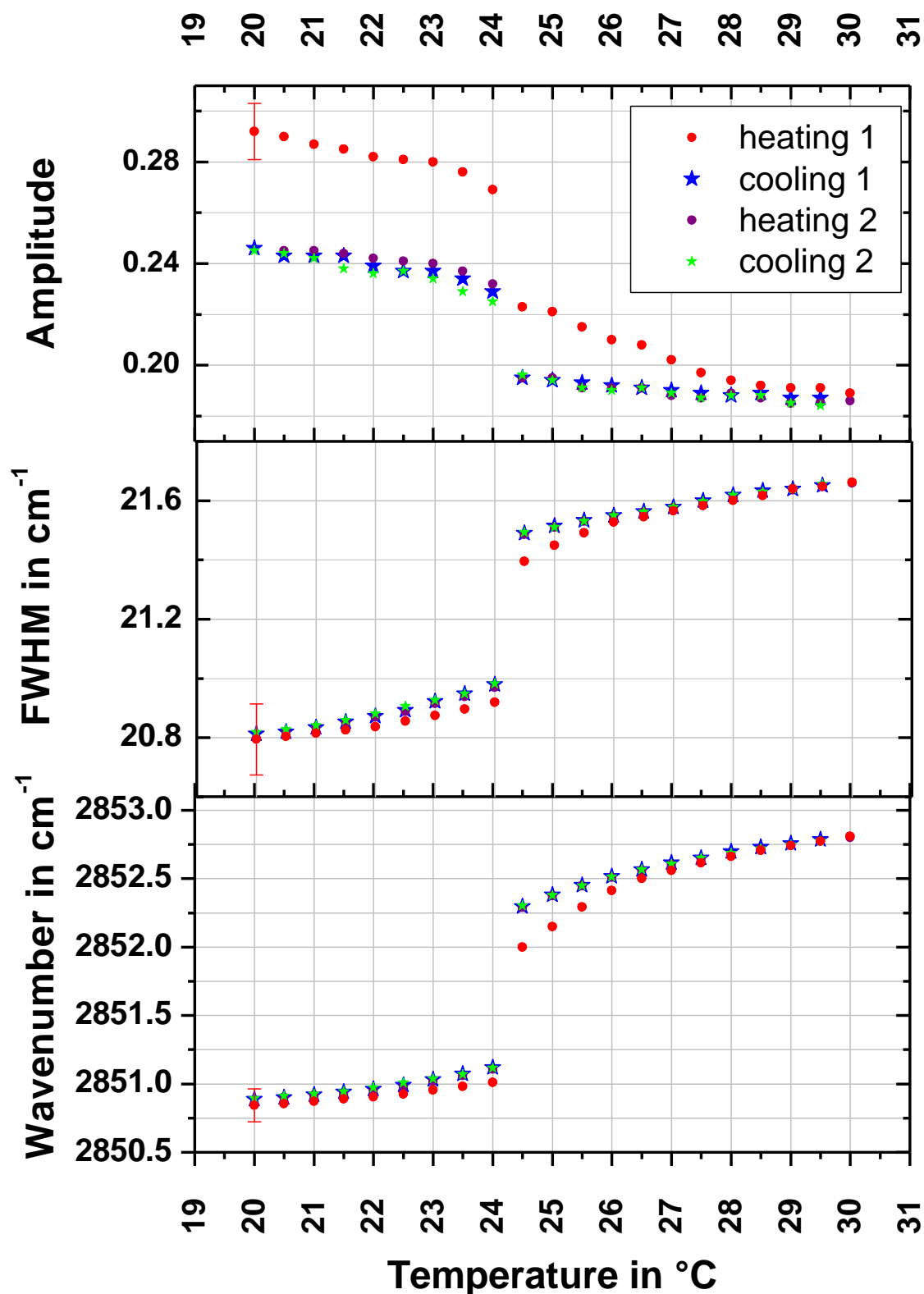


Figure 68: Infrared absorption band analysis by fitting Gaussian profiles to the $\nu_s(\text{CH}_2)$ absorption band. Shown are the results of measurements, performed after 80 minutes of equilibration time. For legibility, error bars are displayed only for the first data point taken at 20 $^{\circ}\text{C}$ ($\delta\text{wavenumber} = 0.12 \text{ cm}^{-1}$, $\delta\text{FWHM} = 0.12 \text{ cm}^{-1}$ and $\delta\text{amplitude} = 0.011$).

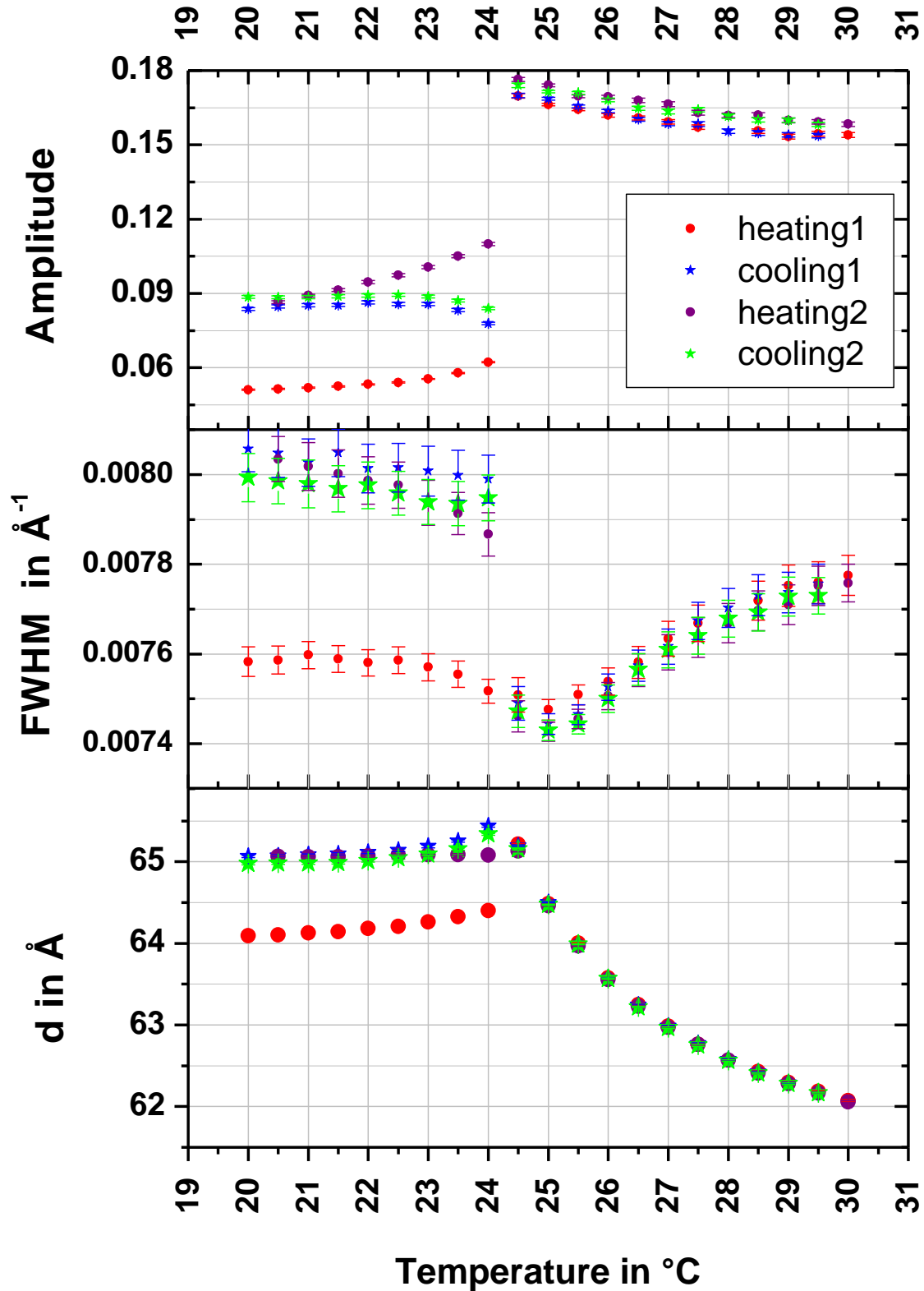


Figure 69: Neutron reflectivity results (meas. 2) of the Bragg peak analysis of the first order Bragg peak at $Q \approx 0.1 \text{ \AA}^{-1}$. Error bars are not shown, if smaller than the symbols.

5.3.2 Neutron reflectivity of a multilamellar lipid coating

In order to follow temperature-induced changes in the lamellar structure of the multilayer system, the neutron reflectivity of the solid-liquid interface was measured. With a selected chopper frequency of 45 Hz at BioRef the sample was measured at 5 different angular positions α_i to cover a Q-range from 0.005 \AA^{-1} to 0.227 \AA^{-1} in total. The resolution was set to a constant value of 7% over the Q-range probed. At each temperature step two complete reflectivity curves (meas. 1 and meas. 2) were recorded. The second measurement (meas. 2) was conducted in order to distinguish between changes due to time dependent and temperature dependent effects. One measurement took 50 minutes of measurement time. Temperature was changed every 100 minutes.

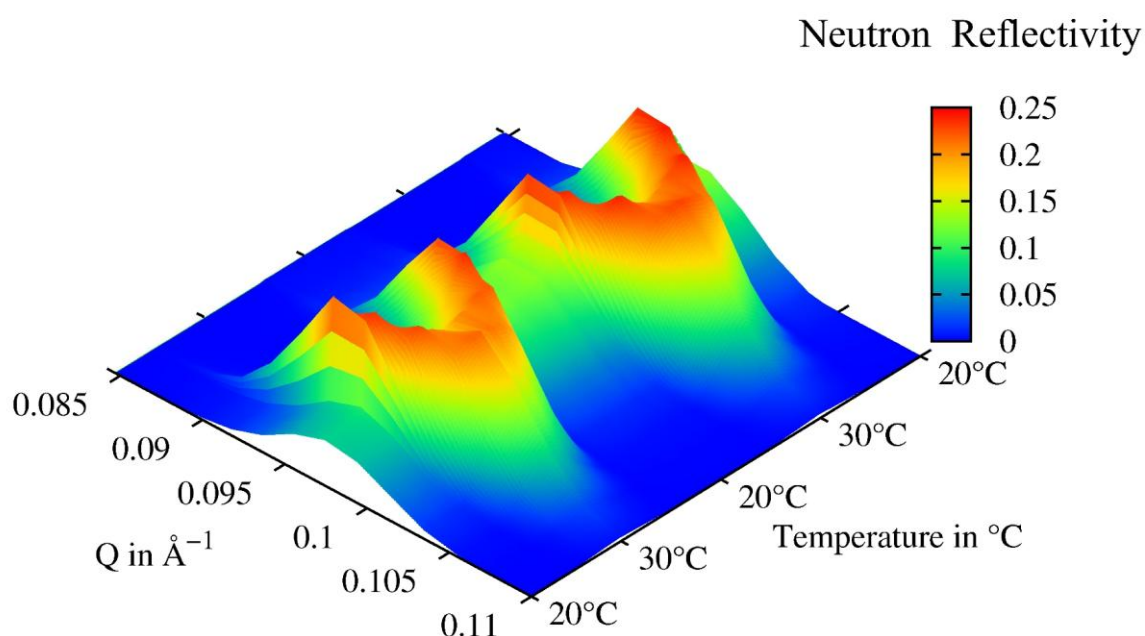


Figure 70: Neutron reflectivity resulting from a multilamellar lipid coating in excess D_2O . Shown are the first order Bragg peaks of the second measurements of all four temperature cycles between $20 \text{ }^\circ\text{C}$ and $30 \text{ }^\circ\text{C}$.

Results

In each reflectivity curve two Bragg peaks are clearly visible in the probed Q-range, which are the first and second order peaks of a lamellar phase. At $20 \text{ }^\circ\text{C}$ the peaks at $Q_1 = 0.0980 \text{ \AA}^{-1}$ and $Q_2 = 0.1967 \text{ \AA}^{-1}$ belong to a repeat distance of $d = 64.11 \text{ \AA}$ (Figure 71). The analysis was focused on the first order Bragg peak, since position, height and width of the peak reveal the desired information about the lamellar structure of the multilayer system. Each peak was fitted by a Gaussian function. The maximum uncertainties are $\delta d = 0.01 \text{ \AA}$, $\delta \text{amplitude} = 0.0009$ and $\delta \text{FWHM} = 0.00004 \text{ \AA}^{-1}$, as a result from the Gaussian profile fits.

For legibility reasons they are only mentioned at the beginning of the following paragraph. The resulting repeat distances, FWHM and amplitudes are displayed in Figure 69 on page 101.

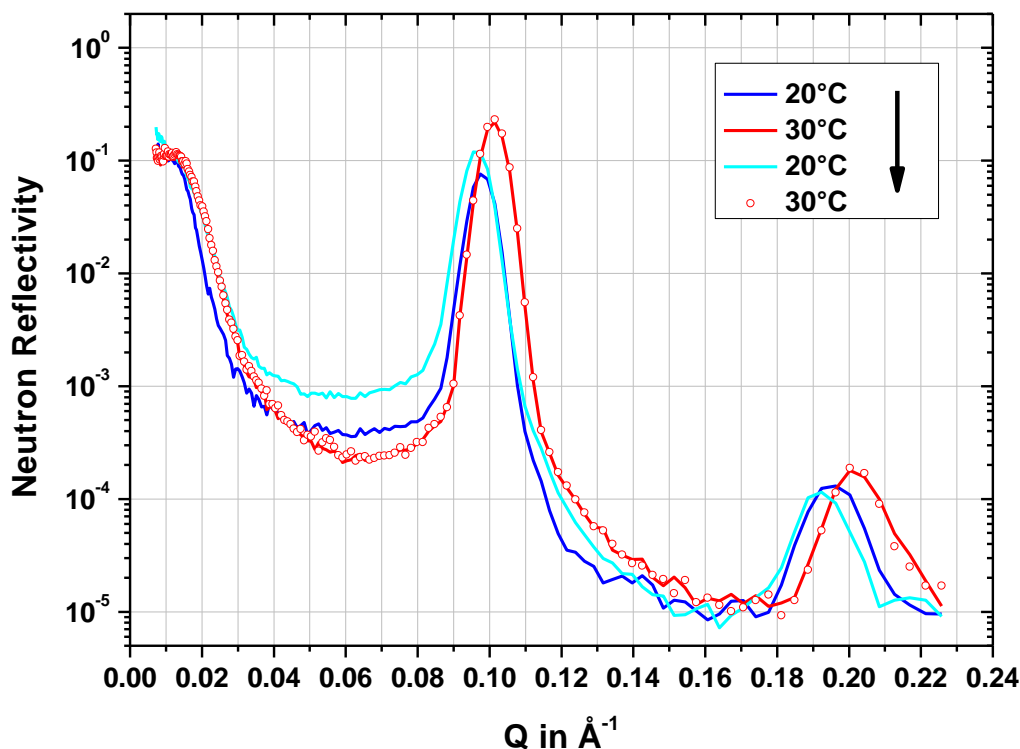


Figure 71: Neutron reflectivity (meas.2) of a multilamellar lipid coating on a silicon substrate (ATR5) against pure D_2O . Temperature was cycled from 20 °C to 30 °C to 20 °C and back to 30 °C.

Heating the first time from 20 °C to 30 °C (**heating1**) showed three distinctive regions: First, between 20 °C and 24 °C the repeat distances increased slowly from $d = (64.10 \pm 0.01) \text{ \AA}$ to $d = (64.40 \pm 0.01) \text{ \AA}$, accompanied with an increase of amplitude from 0.0509 ± 0.0009 to 0.0620 ± 0.0009 and a decrease of FWHM from $(0.00758 \pm 0.00004) \text{ \AA}^{-1}$ to $(0.00752 \pm 0.00004) \text{ \AA}^{-1}$. Second, at 24.5 °C a *jump* in repeat distance to 65.15 Å and in amplitude to 0.1643 was clearly visible. The third region between 25 °C and 30 °C was characterized by a decrease in repeat distance to a minimum of 62.07 Å. The amplitude decreased slowly to 0.1540, while the FWHM increased to a value of 0.0078 \AA^{-1} . Upon cooling (**cooling1**) the system passed through all three regions in reverse order: First, in the region between 30 °C and 24.5 °C, the d-spacing, FWHM and amplitude returned to the initial values. Second, at 24.5 °C the d-spacing reached a maximum of 65.63 Å, accompanied with a maximum in FWHM of 0.0081 \AA^{-1} and a minimum in amplitude of 0.0697. Third,

upon cooling the system to 20 °C, the d-spacing reached a constant value of 65.06 Å with a FWHM of 0.0081 Å⁻¹ and an amplitude of 0.0837. In **heating2** the measured values started off at different starting points. However, for T > 24 °C the cycle is identical to heating1. Furthermore, **cooling2** was identical to cooling1. After the sample was heated for the first time to 24.5 °C, the structure of the membrane system could be reproduced, depending on temperature and type of cycle (heating or cooling). For a graphical summary of the effects described see Figure 69 on page 101.

It shall be highlighted, that between 24.5 °C and 30 °C all measured values were identical for a given temperature, not depending on type of cycle or measurement number. Time dependent effects could only be measured at 24 °C in the cooling cycles (Figure 73 on page 106). Here, the d-spacing for measurement 1 reached a maximum. For the subsequent measurement 2, on the contrary, the d-spacing was lower. For both measurements in both cooling cycles, the d-spacings at 24 °C are *anomaly* large, compared to the values of the heating cycles.

Discussion on NR results

The Bragg peak amplitude is an excellent parameter to follow the main phase transition between P_{β'} and L_α phase. Most pronounced changes are visible at a critical temperature between 24.0 °C and 24.5 °C (Figure 69 on page 101). Here, the main phase transition between the P_{β'} phase and L_α phase appears, as also confirmed by other groups [38, 50]. The rapidly changing slope of the d-spacing and its peak behaviour upon approaching the phase transition temperature T_m show the anomalous swelling as reported earlier [18, 37] and described in chapter 2.1. (on page 20). After heating, a pronounced change is also visible in FWHM. As described in chapter 3.2.4 (on page 38) amplitude and FWHM of the Bragg peaks are linked to the correlation length of the lipid bilayers of the system: The number of correlated bilayers is proportional to $\sqrt{\text{amplitude}}$ and $\frac{1}{\text{FWHM}}$ (Equation 3.37 and Equation 3.38 on page 39). These relations are derived for crystalline systems, with stacks of perfectly flat layers and identical d-spacing. In the multilayer system investigated here, stacking disorder and bending fluctuations are present, which result in variations of the Bragg peak shape. A review on such effects is given in [91]. Small variations in d-spacing or stacking disorder are described within the paracrystalline theory (PT). The long-range order is lost, resulting in decreasing Bragg peak amplitudes and increasing FWHM. In a second theory, bending fluctuations of the layers are considered, described by the modified Caillé theory

(MCT). Here, the decrease in Bragg peak amplitude and increase in FWHM are less pronounced (cf. Figure 5 in [131]). In the $P_{\beta'}$ phase, the substrate-bound lipid layers exhibit a high bending rigidity κ , resulting in a static stacking disorder in their gel state and the PT theory should be applicable for $T < T_m$. As the bending fluctuations increase with temperature and become prominent in the L_{α} phase, the MCT theory should be applied for $T > T_m$. In order to display the different effects on the Bragg peak shape, the ratio between $\sqrt{\text{amplitude}}$ and $\frac{1}{FWHM}$ was calculated and is displayed in Figure 72.

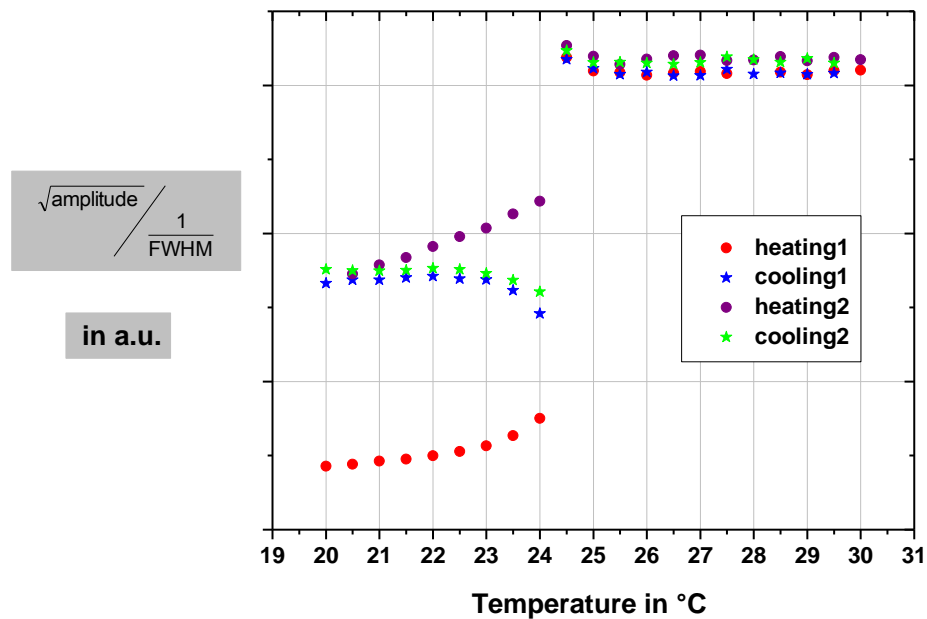


Figure 72: Ratio between $\sqrt{\text{amplitude}}$ and $\frac{1}{FWHM}$ as a function of temperature.

In the $P_{\beta'}$ phase between 20.0 °C and 24.0 °C the ratio $\frac{\sqrt{\text{amplitude}}}{\frac{1}{FWHM}}$ does not show a constant value. Hence, there is stacking disorder in the lipid multilayer stack, and the long range crystalline order is lost [91]. Upon approaching the main phase transition from below, the long range order increases with the increase of the domain size, i.e. the number of coherently scattering individual lipid layers, resulting in increasing Bragg peak amplitudes. The main phase transition from $P_{\beta'}$ to L_{α} between 24.0 °C to 24.5 °C induces a chain melting with an increasing mobility of the individual lipid molecules within the lipid layers, that allows the system to correct for stacking disorder. The constant value between 24.5 °C and 30.0 °C is a result of the good alignment of the lipid stack with respect to the interface [38]. Here, an increase in amplitude, accompanied with a decrease in FWHM, has its origins in an

increasing correlation between the lipid bilayers, hence an increasing coherence length perpendicular to the sample surface.

In addition, the chain melting at the transition from 24.0 °C to 24.5 °C is accompanied with an increase in gauche conformations [31], which results in a decrease of bilayer thickness along the bilayer normal [36]. Also the reverse, the transition from gauche back to trans conformers, resulting in an increasing repeat distance, can be followed by cooling the system. At a critical temperature of 24.0 °C a time dependent effect was observed upon cooling. Here, the first of two subsequent measurements at 24 °C revealed a different d-spacing ($d = (65.63 \pm 0.02) \text{ \AA}$) as compared to the second measurement at the same temperature ($d = (65.44 \pm 0.02) \text{ \AA}$). Even though the difference of 0.2 Å is small, it is beyond the experimental uncertainty.

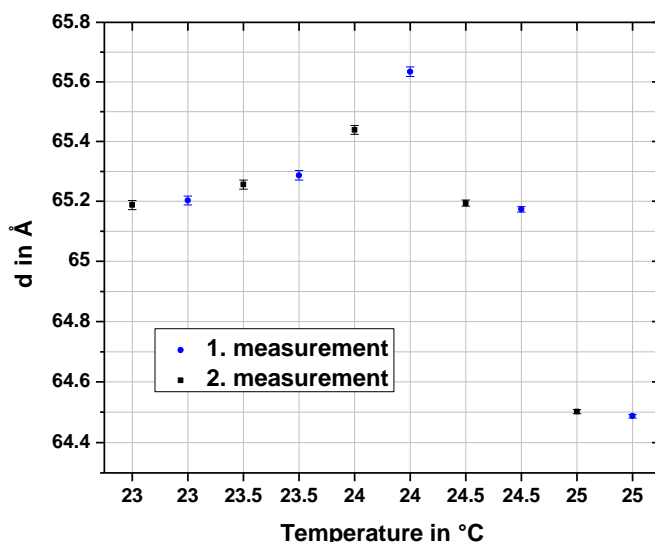


Figure 73: The d-spacings for the cycle cooling1. Displayed are the values for both measurements (meas. 1 and meas. 2) measured with a time difference of 50 min.

Furthermore, this time dependent effect was measured for both cooling cycles (*cooling1* and *cooling2*). In addition, for all other temperatures, the measured values for first and second measurement are identical within the error. The d-spacings for cycle *cooling1*, the first and second measurement, are shown in Figure 73. The d-spacings around the critical temperature are reported with differing values in the literature. In addition, the variations of the d-spacings with temperature upon approaching the critical temperature are reported with different slopes. A summary of literature data is given in [18]. The discrepancies reported might have their origin in the partly long equilibration time ($> 50 \text{ min}$) of the investigated systems, as seen in the present work (Figure 73).

5.3.3 Phase transition in the light of IR and NR – a comparative discussion

The performed experiment gave the unique possibility to correlate the lipid phase behaviour on different length scales. The combined IR and NR experiment at BioRef showed clearly the relation between the order of the individual lipid chains and the resulting order of the lipid layers (Figure 74).

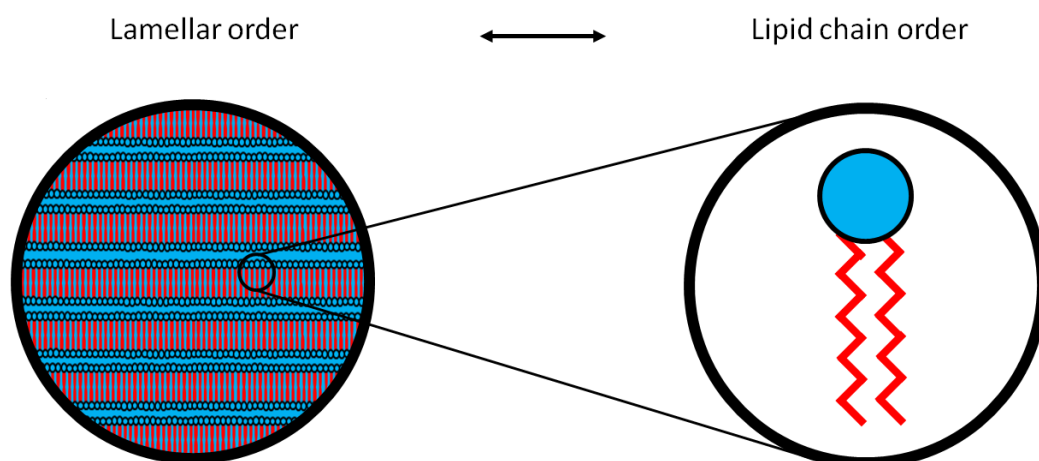


Figure 74: Measurements at BioRef comprise structural orders on different length scales. While the lamellar lipid order on the mesoscopic scale is probed by neutron reflectivity, the lipid chain order on the molecular length scale is probed by infrared spectroscopy.

Both techniques, IR and NR, revealed a drastic change in the corresponding signals between 24.0 °C and 24.5 °C, that corresponds to the main phase transition between the ripple phase $P_{\beta'}$ and the liquid phase L_{α} of DMPC fully hydrated in D_2O [132]. Taking the peak amplitudes of each technique as an order parameter, an inverse behaviour is observed (Figure 75 on page 109). While the IR amplitude of the $\nu_s(\text{CH}_2)$ absorption band is correlated with the order of the lipid chains, the Bragg peak amplitude from NR is correlated with the order of the layered system. A direct comparison of the amplitudes upon heating shows that a decreasing order of the individual lipid chains results in an increasing order of the layered system when crossing the phase transition temperature between 24.0 °C and 24.5 °C. Upon cooling the inverse effect can be seen: the order of the individual lipid chains increases, while the order of the layered system decreases when the phase transition is crossed.

In addition, the combined measurements assist the ongoing discussion about the origins of the swelling behaviour of the multilayered system in the vicinity of the main phase transition [39,

42-44]. In line with literature observations the present measurements show (Figure 76 on page 109), that changes (*anomalies*) in the repeat distance arise (as seen by NR), which cannot be explained by changes in the chain conformation of the lipid molecules (as seen by IR): For $T < 24\text{ }^{\circ}\text{C}$ an increase in wavenumber upon approaching the main phase transition temperature indicates additional gauche conformers in the lipid bilayers, which result in an decreasing bilayer thickness [36]. In contrast, the total d-spacing increased in the same temperature range. These discrepancies are most pronounced between 24.0° and $24.5\text{ }^{\circ}\text{C}$: The drastic increase in gauche conformers, upon heating, does not result in a decrease in total d-spacing. Quite the contrary effect was measured in the first heating cycle (heating1): An increase in total d-spacing was observed. In addition, these discrepancies are visible upon cooling the system. As the change in repeat distance cannot be explained by a change in the conformation of the hydrocarbon chains, an additional effect must be taken into account. Keeping the model for fully hydrated lipid bilayers in mind (Figure 4 on page 17), it is assumed, that the increase in total d-spacing is a result of an increase in water layer thickness (d_{solution}) in between two neighbouring lipid membranes [44, 45]. A decrease in the bending rigidity κ upon approaching the main phase transition temperature at $T_m = 24.46\text{ }^{\circ}\text{C}$, induces an increase in steric repulsions between two bilayers and hence results in the observed increase of d_{solution} [43].

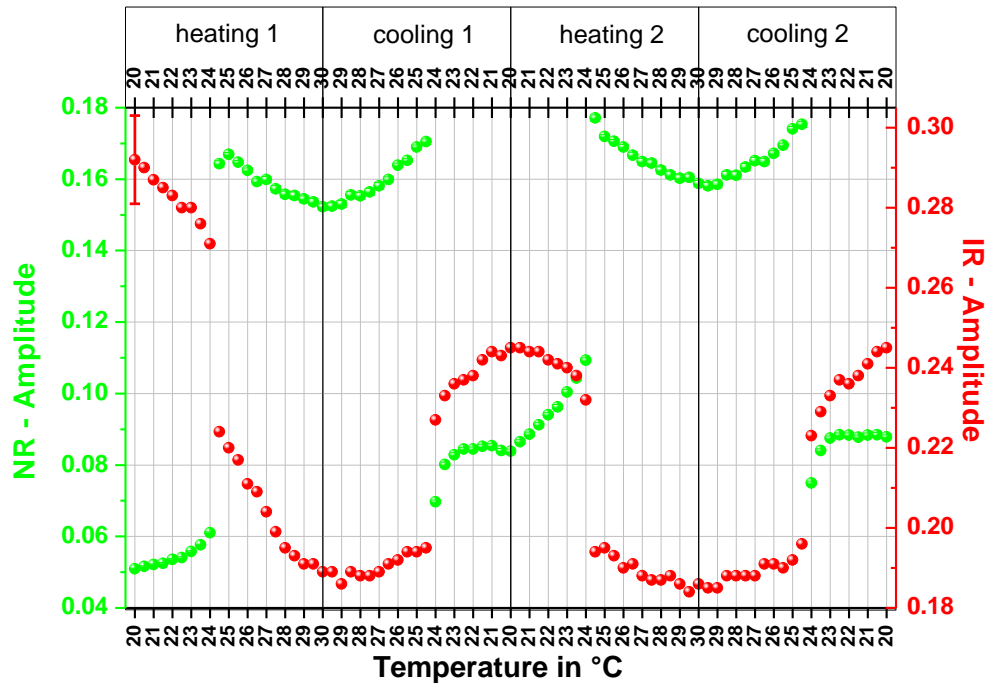


Figure 75: Comparison between neutron reflectivity (NR) and infrared absorption (IR) data. Shown are the Bragg peak amplitude from NR (green) and the absorption amplitude from IR (red). While the NR amplitude is proportional to the lipid bilayer order, the IR amplitude is proportional to the chain order of the individual lipid molecules. The signals show inverse behaviour. The values for the IR amplitude are within an uncertainty of ± 0.011 , as is illustrated for the first point only. The uncertainties of the NR amplitudes are smaller than the symbols.

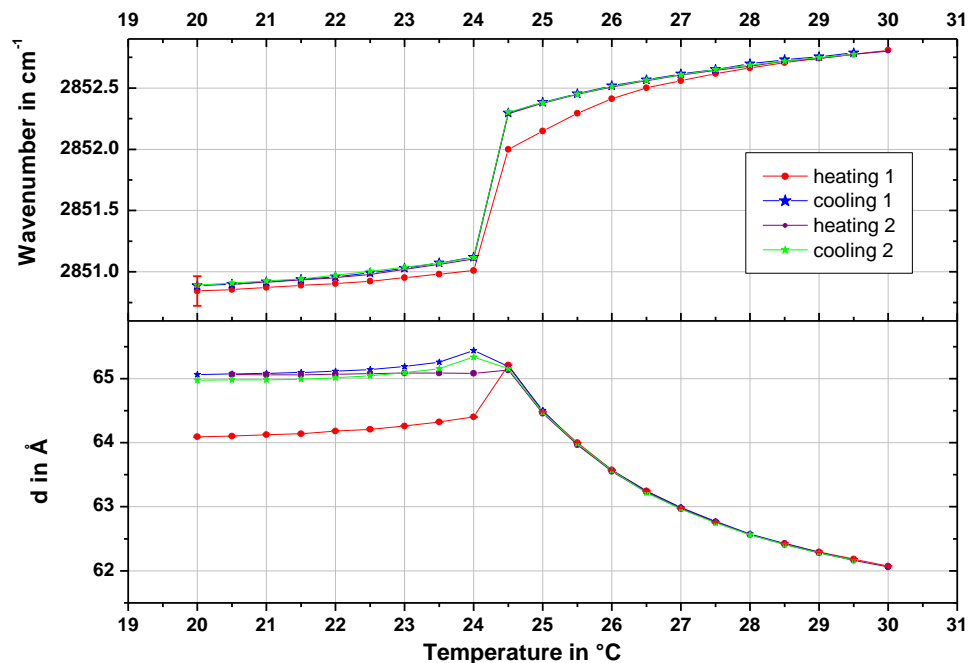


Figure 76: Comparison between neutron reflectivity (bottom) and infrared spectroscopy (top) data. Shown are the d -spacings (bottom) of a multilamellar lipid coating on silicon support and the corresponding wavenumbers (top) of the $\nu_s(\text{CH}_2)$ absorption band. The temperature range between 20 °C and 30 °C was investigated in four successive temperature cycles. The values for the wavenumbers are within an uncertainty of $\pm 0.12 \text{ cm}^{-1}$, as is illustrated for the first point only. The uncertainties of the d -spacings are smaller than the symbols.

5.4 Summary of chapter 5

This chapter addressed the structure of solid-supported lipid membranes incubated in pure D_2O . At first, the expected neutron reflectivity (NR) of the systems was simulated as a function of the number of lipid bilayers. Subsequently, the stability of the experimental systems was examined under varied environmental parameters such as temperature (T), pressure (p), shear rate and substrate chemistry. At third, the main phase transition of the experimental lipid systems was investigated simultaneously on different length scales by combined NR and ATR-FTIR measurements.

A box model of an oligolamellar lipid coating in D_2O was developed and the viability and constraints of a single Bragg peak analysis were verified by the analysis of simulated NR experiments.

Experimentally it was found, that the measured DMPC lipid coatings at the solid- D_2O interface were stable in their ripple phase, P_{β} , both on Si/SiO₂ and Ti surfaces, also upon application of external shear forces. In their L_{α} phase (at higher T or elevated p at higher T) unbinding of the lipids from support occurred layer-by-layer.

The main phase transition of multilamellar lipid coatings incubated in pure D_2O , monitored as a function of temperature and time, was accompanied by drastic changes in both neutron reflectivity and infrared absorption signals. An anomalous swelling was found in the vicinity of the main phase transition that could not be explained by the concurrent lipid chain melting. It is suggested that a decrease in bending rigidity κ of the lipid membranes is the origin of the observed effects.

6. Lipid membranes at physiological conditions

After completion of all necessary reference measurements against pure D₂O, we now turn to measurements in a more natural environment. Important in the contexts of lipid membranes under load and joint lubrication is the combination of phospholipids with hyaluronic acid (HA). In mammal joints HA is one of the most abundant components [133]. In a first approach, infrared absorption spectra of HA, DMPC and mixtures of both were analyzed (chapter 6.1). Next, the influence of HA on DMPC phase transitions was investigated by calorimetry (chapter 6.2). Subsequently, the impact of HA on supported lipid membranes at the solid-liquid interface was examined by neutron reflectivity measurements (chapter 6.3). In order to approach physiological conditions, the influence of HA on a lipid membrane system was further studied at 39 °C (chapter 6.4). In addition, the stability of the interfacial lipid coatings under load was investigated by using a shear setup (chapter 6.5) and a pressure cell (chapter 6.7) for neutron reflectometry measurements. The studies were extended to a multilamellar lipid coating in order to study the phase transition of the system around the main phase transition of DMPC by infrared spectroscopy and neutron reflectivity simultaneously (chapter 6.8).

6.1 Vibrational modes of DMPC and HA

Introduction

Infrared spectroscopy is a well-developed tool to study chemical bonds of various molecules. Furthermore, molecular interactions can be detected. In order to study interactions between lipid molecules (DMPC) and HA on a molecular scale, the infrared absorbance of mixtures with three different DMPC:HA weight ratios (1:1, 1:0.1 and 1:0.01) were recorded. The absorbance spectra of the DMPC and HA mixtures were compared to absorbance spectra of the pure components.

Pure DMPC

To get an insight in the chemical structure of the lipid molecule DMPC in the lamellar phase, ATR-FTIR measurements were performed. For this purpose 30 μL of a solution of 10 mg/mL DMPC in chloroform were injected in the BioATR II sample cell. A detailed description of the setup used is given in chapter 3.2.2 (on page 29). After the chloroform was evaporated overnight an infrared spectrum of the resulting multilamellar lipid coating was measured at room temperature in ambient humidity. A spectrum of the clean sample cell was used as a reference spectrum. The resulting absorbance spectrum shows a number of characteristic absorption peaks of DMPC (Figure 77). The most pronounced peaks with corresponding wavenumbers $\tilde{\nu}_{\text{DMPC}}$ are summarized in Table 6.1 on page 116 including vibrational modes of the respective functional groups and references from literature ($\tilde{\nu}_{\text{lit}}$). The characteristic absorption bands of the lipid head groups are clearly visible: the asymmetric and symmetric stretching mode of the phosphate groups (PO_2) at 1233 cm^{-1} and 1089 cm^{-1} as well as the absorption of the nitrogen groups ($\text{N}^+(\text{CH}_3)_3$) at 970 cm^{-1} . The carbonyl groups ($\text{C}=\text{O}$) absorb at 1736 cm^{-1} . The strongest bands result from the lipid chain groups: The methylene groups (CH_2) have prominent absorption bands at 2917 cm^{-1} , 2849 cm^{-1} and 1468 cm^{-1} corresponding to the asymmetric and symmetric stretching, and the scissoring mode, respectively.

Pure HA

With the same protocol the infrared absorption of a thick coating of hyaluronic acid (HA) was measured: For this purpose, 20 μL of a solution of 3 mg/mL HA in D_2O was injected in the clean BioATR II sample cell. After evaporation of the solution, a spectrum was measured the next day at room temperature in ambient humidity, using a spectrum of the clean sample cell as a reference spectrum (Figure 77). The most pronounced infrared absorption results from the carboxyl groups at 1035 cm^{-1} and the amide groups at 1604 cm^{-1} . The absorption

bands at 946 cm^{-1} , 1149 cm^{-1} and 1074 cm^{-1} show the existence of CO-O-C bonds. In addition, typical absorption bands of HA are at 1645 cm^{-1} ($\nu(\text{C}=\text{O})$), 1407 cm^{-1} ($\nu(\text{C}-\text{N})$, $\delta(\text{N}-\text{H})$) and 1375 cm^{-1} ($\nu(\text{C}=\text{O})$) [134, 135].

Mixtures of DMPC and HA

Finally, the infrared absorption of a three mixtures of DMPC and HA were measured. For this purpose, three different glass beakers were each filled with 3 mg DMPC dissolved in chloroform. In the following the solvent was evaporated under vacuum. The resulting thin films of DMPC were dissolved in 1 mL of different HA solutions, using a vortex mixer. The different concentrations were 3 mg/mL, 0.3 mg/mL and 0.03 mg/mL HA in D_2O . This procedure resulted in different DMPC to HA weight ratios of 1:1, 1:0.1 and 1:0.01. For ATR-FTIR measurements, 20 μL of a mixed solution was filled in the BioATR II sample cell. Afterwards the sample chamber was left open for 7 h, in order to let the D_2O solvent evaporate. This resulted in strong absorption bands of the composite films. A spectrum of the clean sample cell was used as a reference spectrum. An analysis of the 1:1 mixture showed, that the resulting absorption bands consist of a superposition of the individual absorption bands of DMPC and HA (Figure 78). The amplitudes of the HA absorption bands are in general higher than the amplitudes of the absorption bands of DMPC for the 1:1 mixture. A change in spectral position of the infrared absorption of any quasi molecular group could not be detected, as compared to the absorption of the pure components. Keeping the reproducibility of the individual absorption bands in mind, an interaction between DMPC molecules and HA molecules in terms of HA binding to the head group or tail group region of the lipid molecules could not be. The spectra of mixtures with lower HA fraction, showed decreasing HA absorption bands. This can be best followed at the strongest absorption bands of HA for $\nu(\text{C}-\text{N}, \text{N}-\text{H})$ at 1604 cm^{-1} and $\nu(\text{C}-\text{O})$ at 1035 cm^{-1} , labelled 4 and 9, respectively, and marked with a green line in Figure 78. For the 1:0.01 mixture, the absorption of HA is not recognizable anymore. In addition, when the dried mixtures got re-hydrated with 20 μL D_2O , the influence of HA on the absorption spectra vanished, even though the infrared absorption of DMPC is still clearly visible. HA might have dissolved into the solution and was therefore outside the penetration depth of the IR beam.

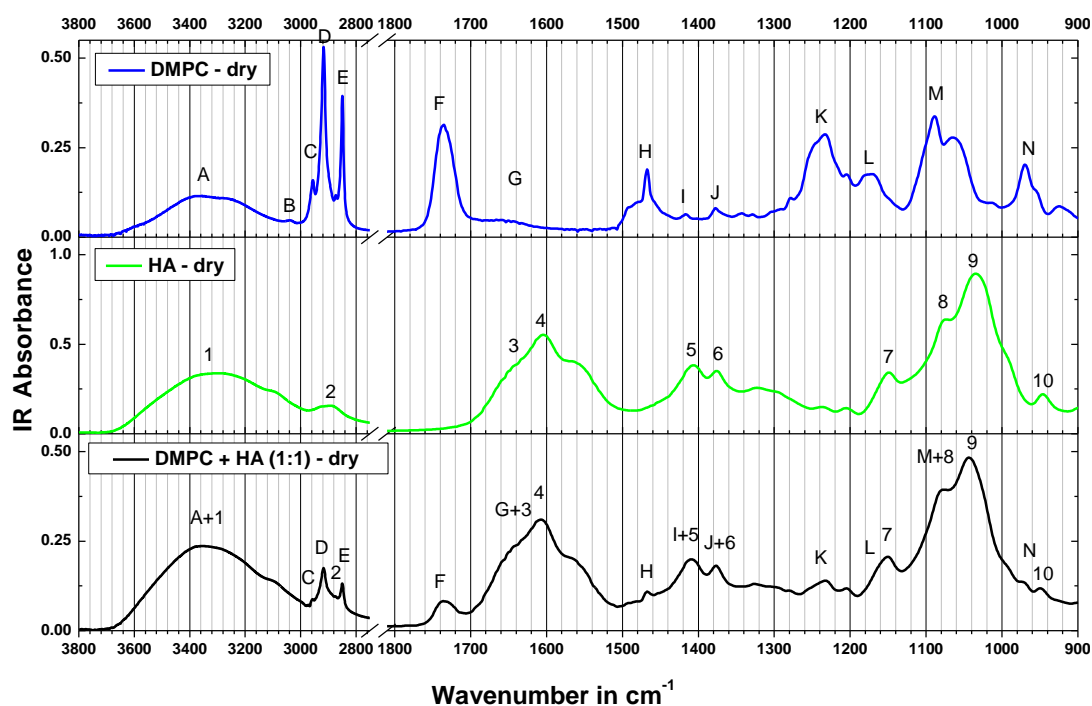


Figure 77: Infrared absorbance spectra of DMPC (top), HA (middle) and a mixture (bottom) of DMPC:HA (1:1), measured at 20 °C in ambient humidity. Spectra of the clean sample cell were used as reference spectra. An analysis of the spectra is shown in Table 6.1. on page 116.

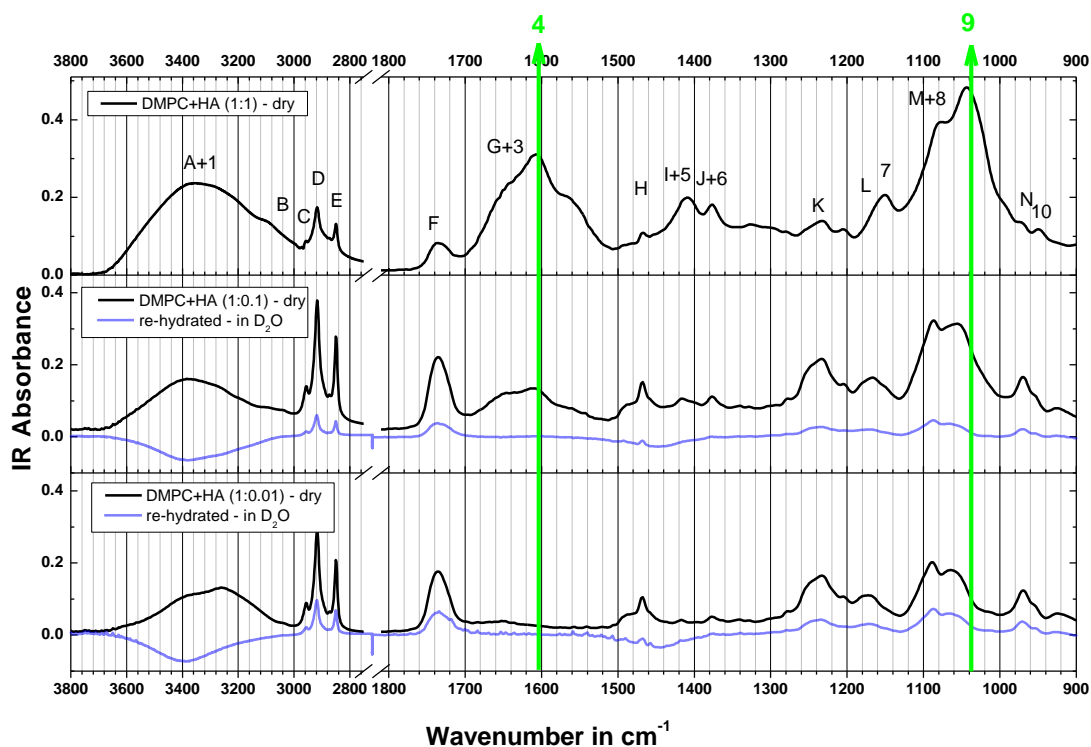


Figure 78: Infrared absorbance spectra of mixtures of DMPC and HA at different ratios. The black lines correspond to the absorption of the dried components, while the blue lines show the absorption, after the samples were hydrated with 20 μ l of pure D_2O . The labels of the absorption bands in the top plot correspond to lipid absorption bands (characters) and HA absorption bands (numbers). The decreasing absorption of HA with decreasing concentration can be best followed at the marked positions (green line).

From the performed measurements, one can estimate that a DMPC to HA mass ratio of around 1:0.1 is necessary in order to distinguish clearly between the infrared absorption of the two components. For lower HA concentrations, the absorption spectra are dominated by the DMPC infrared absorption bands. Furthermore, no molecular interaction could be detected.

DMPC label	$\tilde{\nu}_{\text{DMPC}}$ in cm^{-1}	$\tilde{\nu}_{\text{lit}}$ [48, 136]	vibrational modes	HA-label	$\tilde{\nu}_{\text{HA}}$ in cm^{-1}	$\tilde{\nu}_{\text{lit}}$ [134, 135]	vibrational modes
A	≈ 3363		$\nu(\text{H}_2\text{O})$	1	≈ 3300	≈ 3400	$\nu(\text{H}_2\text{O})$
B	3040	3028- 3050	$\nu_{\text{as}}(\text{CH}_3)$				
C	2955	2956	$\nu_{\text{as}}(\text{CH}_3)$				
D	2917	2920	$\nu_{\text{as}}(\text{CH}_2)$	2	2893	2889	$\nu_{\text{as}}(\text{CH}_3)$
	284	2850	$\nu_{\text{s}}(\text{CH}_2)$				
F	1736	1740	$\nu(\text{C}=\text{O})$				
G	1651	1650	$\nu(\text{C}=\text{C})$	3	1645	1639	$\nu(\text{C}=\text{O})$
				4	1604	1603- 1611	$\nu_{\text{as}}(\text{COO}^-)$
H	1468	1468	$\delta_{\text{s}}(\text{CH}_2)$				
I	1416	1418	$\delta_{\text{s}}(\text{CH}_2)$	5	1407	1411	$\nu(\text{C}-\text{N}), \delta(\text{N}-\text{H})$
J	1377	1378	$\delta(\text{CH}_3)$	6	1375	1377	$\nu(\text{C}=\text{O})$
K	1233	1250	$\nu_{\text{as}}(\text{PO}_2^-)$				
L	1172	1170	$\nu_{\text{as}}(\text{CO}-\text{O}-\text{C})$	7	1149	1150	$\nu(\text{CO}-\text{O}-\text{C})$
M	108	1092	$\nu_{\text{s}}(\text{PO}_2^-)$	8	1074	107	$\nu(\text{CO}-\text{O}-\text{C})$
				9	1035	1044	$\nu(\text{C}-\text{O})$
N	970	970	$\nu_{\text{as}}(\text{C}-\text{N}^+-\text{C})$	10	946	947	$\nu(\text{C}-\text{C})$

Table 6.1: Analysis of infrared absorption bands of DMPC ($\tilde{\nu}_{\text{DMPC}}$) and HA ($\tilde{\nu}_{\text{HA}}$), as seen in Figure 77 on page 115, shown in comparison with values from literature ($\tilde{\nu}_{\text{lit}}$), with the symmetric (s) and asymmetric (as) stretching ν , the deformation vibration δ , the scissoring vibration δ_{s}

6.2 Differential scanning calorimetry on multilamellar lipid vesicles

DSC measurements were conducted on fully hydrated DMPC multilayer vesicles diluted in pure D₂O or in a solution of 3 mg/mL HA in D₂O. DMPC was used in a concentration of 2.5 mg/mL. The temperature range between 15 °C and 45 °C was scanned (heated) several times with a rate of 1 °C per minute, until the system responded with reproducible line shapes (4. scan). Results for the first and fourth scan are shown in Figure 79. Upon heating both samples showed an endothermic pre-transition at (16.8 ± 0.1) °C and an endothermic main-transition at (24.38 ± 0.02) °C. As described in chapter 2.1 (on page 17), the pre-transition is the transition from the gel phase L_{β'} to the ripple phase P_{β'} of the multilamellar lipid system. In addition, the value for the main transition agrees well with the transition from the ripple phase P_{β'} to the fluid phase L_α of the multilamellar lipid system in D₂O [50]. Interestingly, for the HA in D₂O solution a shoulder at the positive side of the main transition appears with a maximum at (24.55 ± 0.02) °C, indicating a third transition. As this shoulder also appears with the system measured in pure D₂O (1. scan), the third transition is not provoked by the presence of HA. Reports about a third transition could not be found elsewhere. However, HA seems to stabilize the third transition of the DMPC multilayer system.

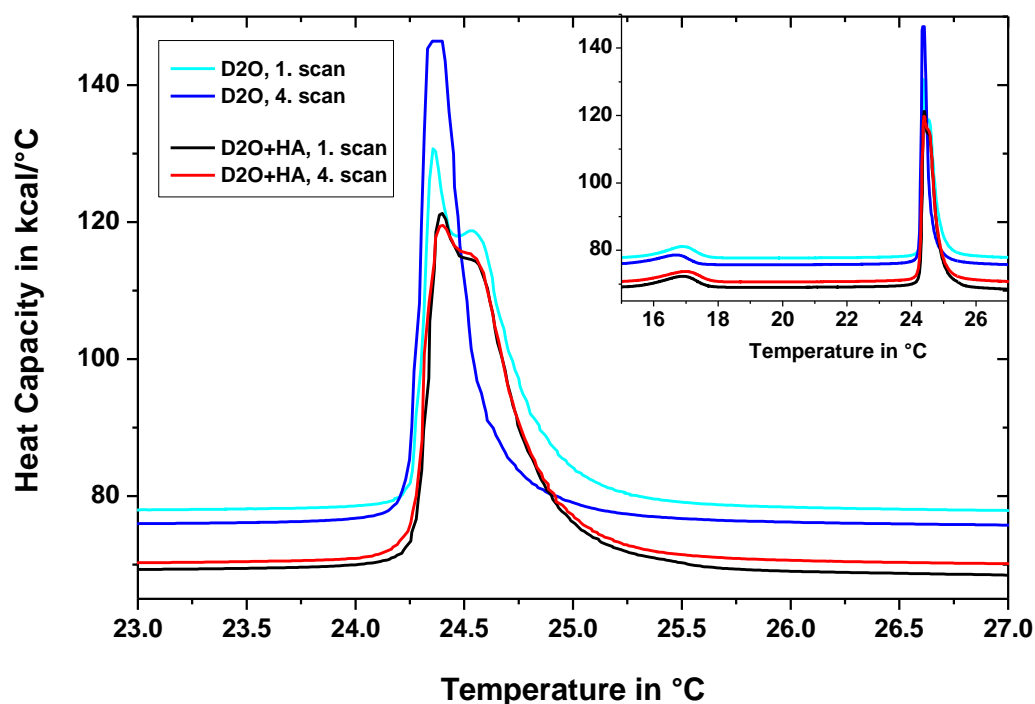


Figure 79: Differential scanning calorimetry data of 2.5 mg/mL DMPC dissolved in pure D₂O (light blue and dark blue line) or in a solution of 3 mg/mL HA in D₂O (black and red line). Shown are first and fourth scan of the measurements.

6.3 Effect of hyaluronic acid on the lamellar structure of surface bound lipid films

Introduction

A freshly prepared oligolamellar lipid coating on a disc-shaped silicon substrate (sample 1) was incubated in a solution of 3 mg/mL HA in D₂O and monitored over time at the BioRef neutron beam line. With a selected chopper frequency of 45 Hz the sample was measured at 5 different angular positions to cover the full Q-range from 0.0050 Å⁻¹ to 0.3563 Å⁻¹. The resolution was set to a constant value of 7%, resulting in a measurement time of 3 h over the probed Q-range. Certain parts of this chapter have already been published [109].

Bragg peak analysis

The first reflectivity curve shows a measurement conducted 6.7 h after incubating sample 1 in the HA solution at 20 °C (Figure 80). The Bragg peak at $Q_1=0.0949\text{Å}^{-1}$ reveals a repeat distance of $d_1 = (66.22 \pm 0.06) \text{Å}$. Subsequent reflectivity curves show a continuous decrease of the Bragg peak intensity at $Q_1 = 0.0949 \text{Å}^{-1}$ (Figure 81). For a more detailed look on the lamellar system the Bragg peak area, A , was analyzed. A is proportional to the number of layers contributing to the Bragg peak signal, as outlined in chapter 3.2.4 on page 39. In order to analyze the scattering curves independently from the influence of the reflectivity of the silicon substrate (Fresnel reflectivity) the curves were normalized by a simulated Fresnel reflectivity (R_{Fresnel}) curve from the bare silicon substrate (Figure 82). Afterwards, the Bragg peak area was integrated numerically. The integrated Bragg peak area A_1 from the peak at $Q_1 = 0.0949 \text{Å}^{-1}$ is shown as a function of time in Figure 84. The decreasing amplitude as well as the decreasing Bragg peak area indicates that the lipid film undergoes a structural change: lamellae with the lamellar spacing d_1 disappeared with time.

Two additional Bragg peaks appeared between 0.025 Å⁻¹ and 0.050 Å⁻¹ (Q_{P1}) and between 0.055 Å⁻¹ and 0.075 Å⁻¹ (Q_{P2}), respectively (Figure 80). They are the first ($n=1$) and second ($n=2$) order Bragg peaks of a new lamellar phase L_p with a repeat distance d_p . With evolving time these Bragg peaks became more and more pronounced, while their maximum positions shifted to smaller Q-values (Figure 83). The integrated Bragg peak area of the first and second order peak of the L_p phase, A_{P1+P2} , is shown in Figure 84. In addition to an increase in the Bragg peak area, the d-spacing increased with time (Figure 85). Starting with an already large repeat distance of $d_p = (137.12 \pm 0.80) \text{Å}$ after 6.7 h, a constant swelling rate was

observed after 19 h of incubation with a slope of $0.23 \pm 0.01 \text{ \AA}$ per h. A final measurement was performed after 89.5 h, showing a repeat distance of $d_p = (166.27 \pm 0.58) \text{ \AA}$.

Discussion

The presence of HA has a strong impact on the oligolamellar lipid coating. Upon incubation in a solution of 3 mg/mL HA in D_2O , the structure of the coating starts to change drastically: A new lamellar phase L_p appears. The d-spacing of the new phase L_p showed at first detection, after 6.7 h of incubation, a value twice that of the d-spacing of the original $P_{\beta'}$ phase. In addition, during the observation time, the lamellar $P_{\beta'}$ phase was still present. The comparison of the integrated Bragg peak areas of the L_p phase and the $P_{\beta'}$ phase reveals a reverse behaviour of the phases: While the scattering intensities for the L_p phase increases linearly with time, the scattering intensities for the $P_{\beta'}$ phase decreases linearly on the same time scale (Figure 84). This indicates a re-ordering of the lipid coating from $P_{\beta'}$ phase to the new L_p phase. Moreover, the constant sum of the peak areas $A_{tot} = A_1 + A_{p1} + A_{p2}$ over time shows that as many lamellae with lamellar spacing d_1 disappear as many lamellae with lamellar spacing d_p appear. Thus, no unbinding of lamellae is observed. From the fact that A_{tot} is constant with time and from the respective linear growth behaviour of $A_{p1} + A_{p2}$ one estimates completion of transition of the lipid layer from $P_{\beta'}$ to L_p phase at a constant temperature of 20°C after 328 h (~14 days).

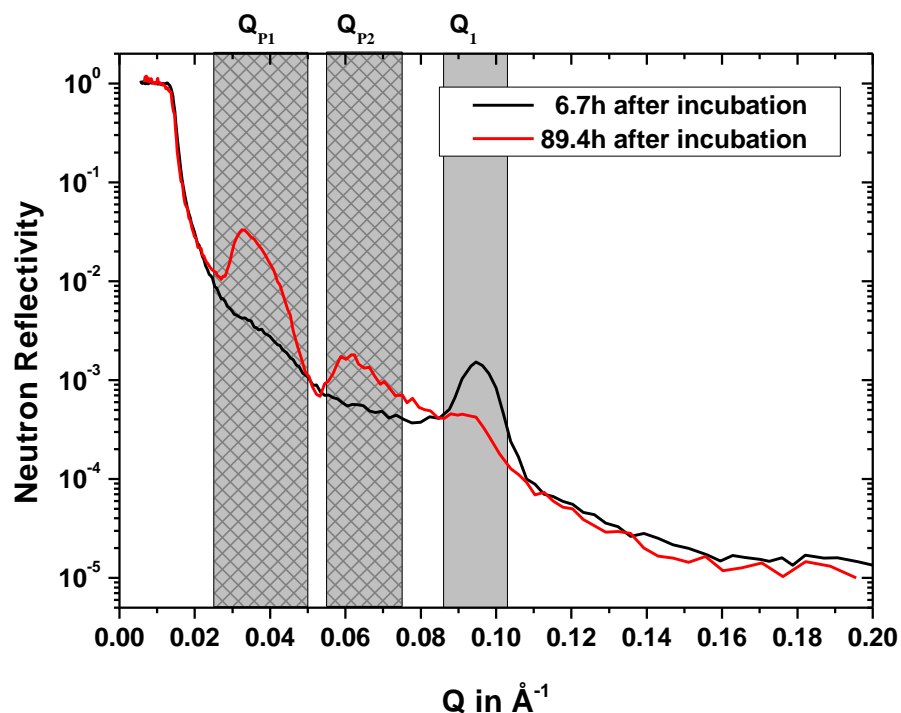


Figure 80: Neutron reflectivity curves of an oligolamellar lipid coating on silicon (sample 1) incubated in a solution of HA in D_2O . The figure shows the first (black) and the last (red) reflectivity curve of a series of measurements performed after the sample was incubated in the solution. The Bragg peak positions of the two different lamellar phases are highlighted in grey: Q_{P1} and Q_{P2} indicate the first and second order Bragg peak of the new lamellar phase L_p . The peak at Q_1 refers to the lamellar phase P_β of fully hydrated DMPC.

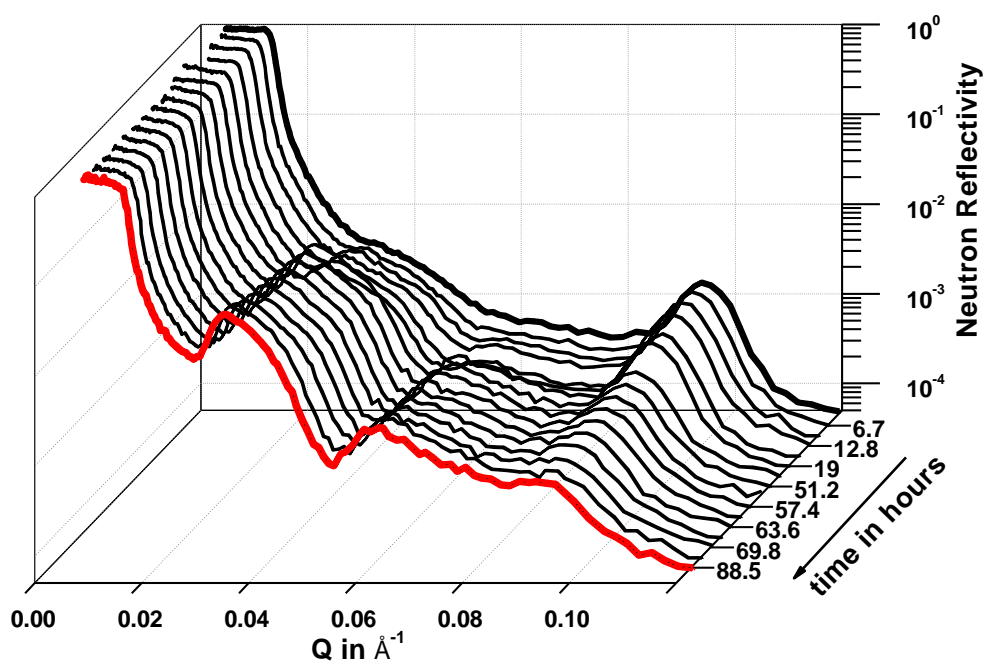


Figure 81: A series of neutron reflectivity curves of the oligolamellar lipid coating on silicon, sample 1, incubated in a solution of HA in D_2O as a function of incubation time. [109]

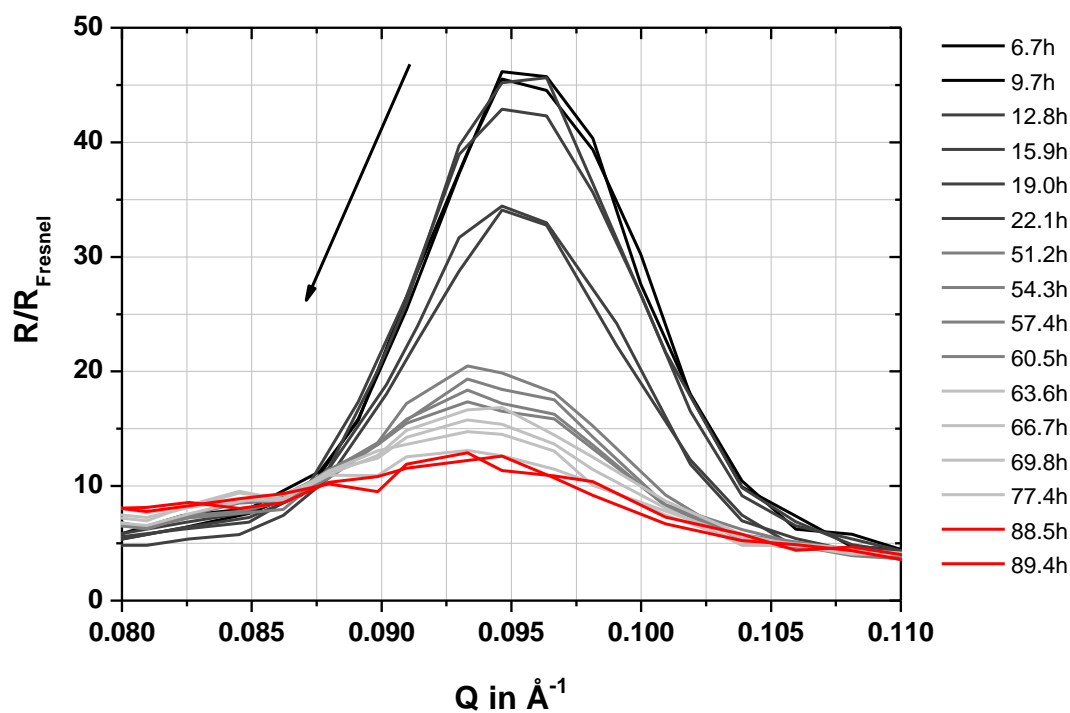


Figure 82: Neutron reflectivity (R) of the Bragg peak at Q_1 normalized to the Fresnel reflectivity (R_{Fresnel}) of the planar silicon substrate (sample 1). The peak vanishes with increasing time.

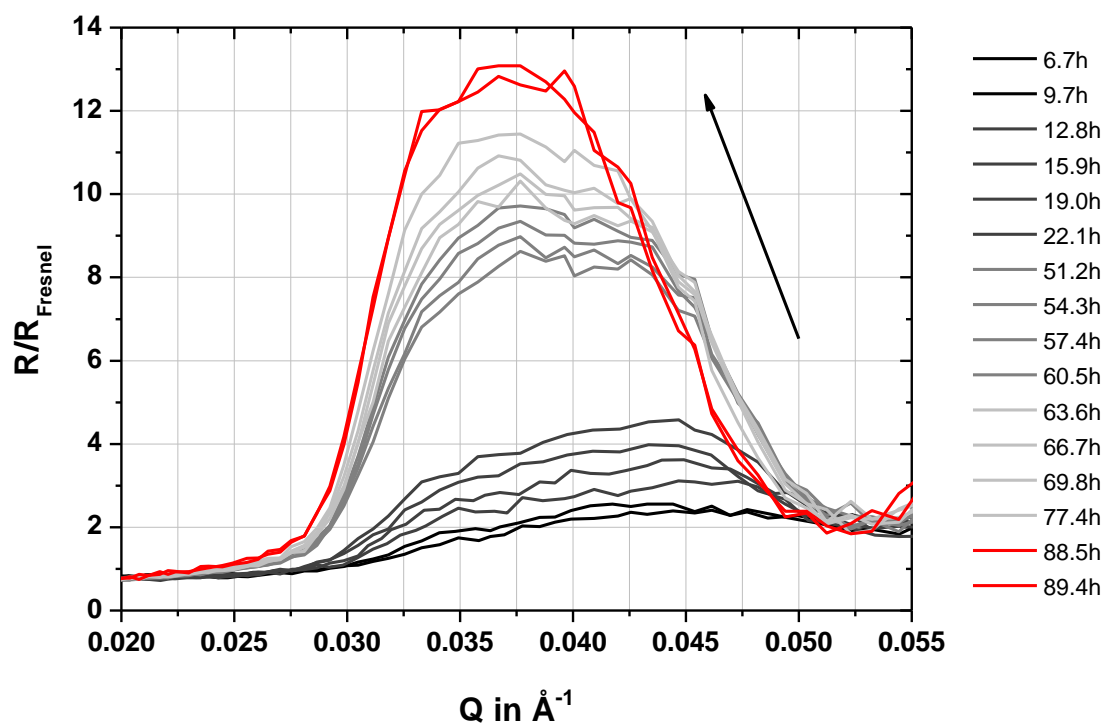


Figure 83: Neutron reflectivity (R) of the Bragg peak at Q_{p1} normalized to the Fresnel reflectivity (R_{Fresnel}) of the planar silicon substrate (sample 1). The peak becomes more and more pronounced with increasing time.

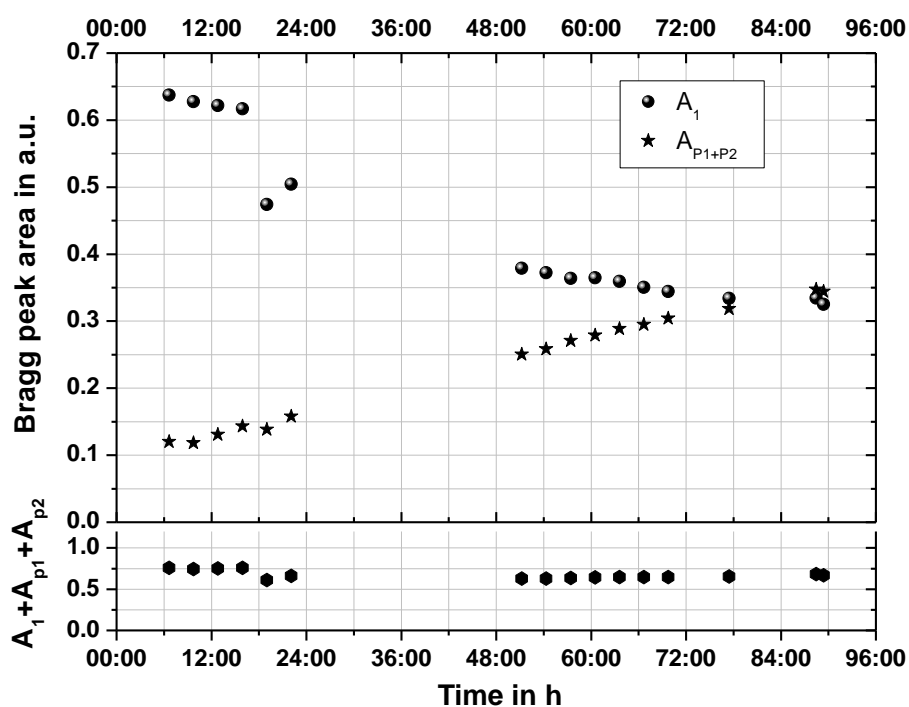


Figure 84: (top) Integrated Bragg peak area A_1 of the peak at Q_1 and the sum ($A_{P1} + A_{P2}$) of the Bragg peak areas of the peaks at Q_{P1} and Q_{P2} . (bottom) The total sum of A_1 , A_{P1} and A_{P2} is constant with time. [109]

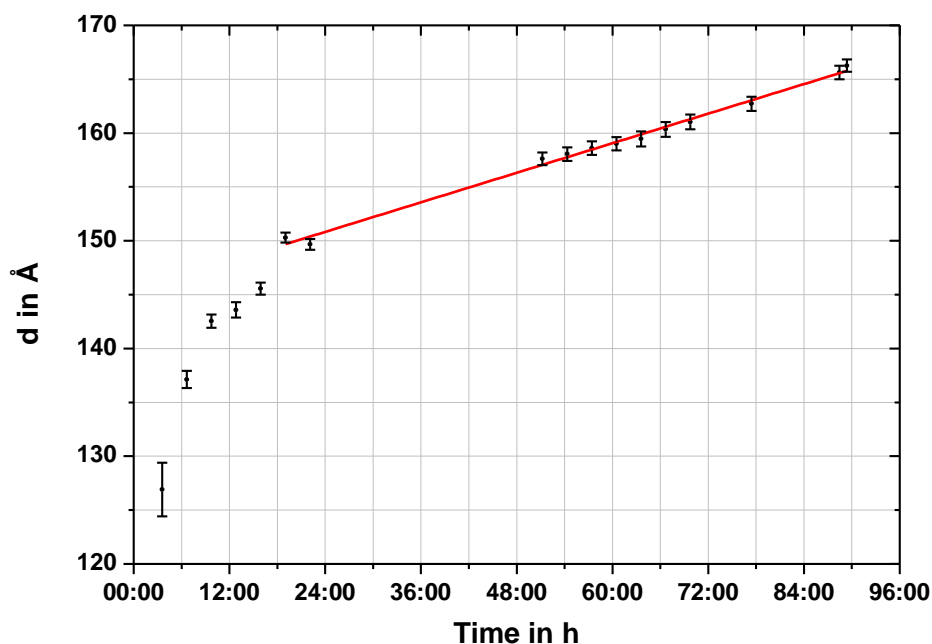


Figure 85: d -spacings resulting from Gaussian profiles fitted to the first order Bragg peaks of the L_p phase (black points). After 19 h a linear regime with a slope of 0.23 ± 0.01 Å/h is reached (red line).

6.4 Effect of time and temperature

Introduction

In order to investigate the structure of the lamella phase L_p found in supported DMPC coatings after incubation with HA at physiologically relevant temperatures, a freshly prepared oligolamellar lipid coating was prepared and measured. For this purpose, a block-shaped silicon substrate (sample 2) was spin-coated with a solution of 10 mg/mL DMPC in chloroform and incubated in a solution of 3 mg/mL HA in D_2O . Measurements were performed at 21°C and 39°C. Parts of this chapter have already been published [109]. A summary of the performed measurements is shown in Figure 86.

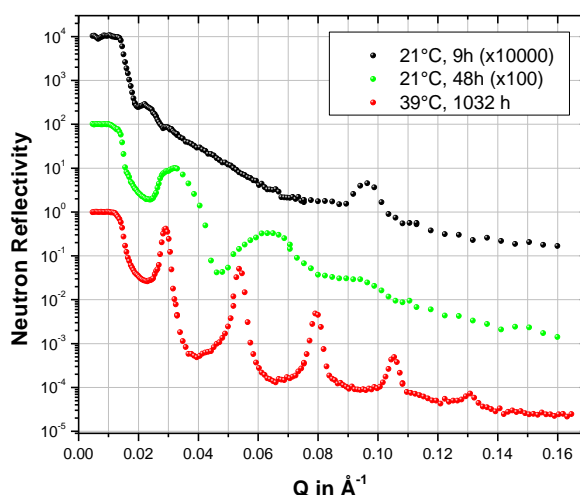


Figure 86: Neutron reflectivity of the oligolamellar lipid coating on a silicon substrate (sample 2), incubated in a solution of 3 mg/mL HA in D_2O as a function of incubation time and temperature. For clarity the plots are shifted vertically.

Bragg peak analysis

A first measurement, performed 9 h after incubation, showed a Bragg peak at $Q_1 = (0.0959 \pm 0.0002) \text{ \AA}^{-1}$, corresponding to a repeat distance of $d_1 = (65.52 \pm 0.14) \text{ \AA}$. The appearance of a Kiessig oscillation at $Q_K = 0.0217 \text{ \AA}^{-1}$ with $\Delta Q_K = 0.0085 \text{ \AA}^{-1}$ reveals a total layer thickness of $t = (739 \pm 40) \text{ \AA}$, built up by 11 lipid bilayers. An additional measurement after 48 h showed already the swelling of the lamellar system with Bragg peaks appearing at Q_{p1} and Q_{p2} , resulting a repeat distance of $d_p = (198.21 \pm 0.63) \text{ \AA}$. Finally, after 1032 h, 24 h after temperature increase to 39 °C, the reflectivity of the sample revealed five well-pronounced Bragg peaks. The series of Bragg peaks ($n = 1 \dots 5$) corresponds to the repeat distance d_p of the new lamellar phase L_p . An analysis of the Bragg peak positions corresponds to a repeat distance of $d_p = (247 \pm 1) \text{ \AA}$ at 39 °C.

Analysis by the optical matrix approach

The lipid bilayer model, described in chapter 5.1 on page 66, is used as a starting point for further analysis of the reflectivity curve measured at 39°C (Figure 86): Lipid bilayers are modelled by a layer of hydrophobic lipid chains, sandwiched between hydrophilic lipid head group layers. Two neighbouring bilayers are separated by solution interlayers. The total number of 11 bilayers, resulting from the analysis of Bragg peak position and Kiessig oscillations, taken from the first measurement at 21°C, was taken as a pre-condition for the model fit, assuming that no unbinding occurred. Due to the influence of the silicon substrate on the one hand, and the missing opposing layer on the other hand, the first and last bilayer of the oligolamellar stack of bilayers was fitted with values which are decoupled from the 9 core membranes. The model had to be re-adjusted, due to the drastic change in reflectivity upon incubation in the HA solution, compared to the reflectivity of an oligolamellar lipid coating incubated in pure D₂O: Two additional layers, close to the head groups of the lipids, have to be taken into account, in order to model the measured reflectivity curve (Figure 87). Each layer has a thickness of $d = 22 \text{ \AA}$ and a scattering length density of $SLD = 5.39 \times 10^{-6} \text{ \AA}^{-1}$ as determined from the model fit. The lower SLD, as compared to the pure solution with $SLD = 6.03 \times 10^{-6} \text{ \AA}^{-1}$, results from a higher proton density. Hence, this layer is composed of a binary mixture of HA and D₂O. For this reason the additional layer is labelled HA layer. By applying Equation 3.23 (on page 35) the volume fraction of HA can be extracted, using the experimentally determined scattering length density of the solution $SLD(D_2O) = 6.03 \cdot 10^{-6} \text{ \AA}^{-2}$ and the calculated value for HA by applying Equation 3.22 on page 34, presuming isotopic exchange of all displaceable H by D for HA in D₂O. Based on a mass density of 1 g/cm^3 and 11 potentially displaceable hydrogen atoms per HA monomer, the scattering length density shifts from $SLD(HA \text{ in } H_2O) = 1.46 \cdot 10^{-6} \text{ \AA}^{-2}$ to $SLD(HA \text{ in } D_2O) = 3.19 \cdot 10^{-6} \text{ \AA}^{-2}$. The volume fraction of HA in the HA layer could be determined to 23 % HA in 77 % D₂O.

The drastic increase in total d-spacing was taken care of by re-adjusting the water layer thickness (d_{solution}) in between two membranes from formerly 10 \AA to 142 \AA . The resulting theoretical curve, modelled by the optical matrix approach, fits well to the measured data points with $\chi^2 = 2.38 \times 10^{-2}$ (Figure 88). The adjusted model is sketched in Figure 87. The resulting scattering length density profile (Figure 89) shows the detailed coating profile along the z-direction, perpendicular to the sample surface. The figure shows alternate regions with a high SLD ($6.03 \cdot 10^{-6} \text{ \AA}^{-2}$) of the solution and low SLD ($2.88 \cdot 10^{-6} \text{ \AA}^{-2}$) of the lipid tail groups.

All fitting parameters are summarized in

Table 6.2 (on page 127).

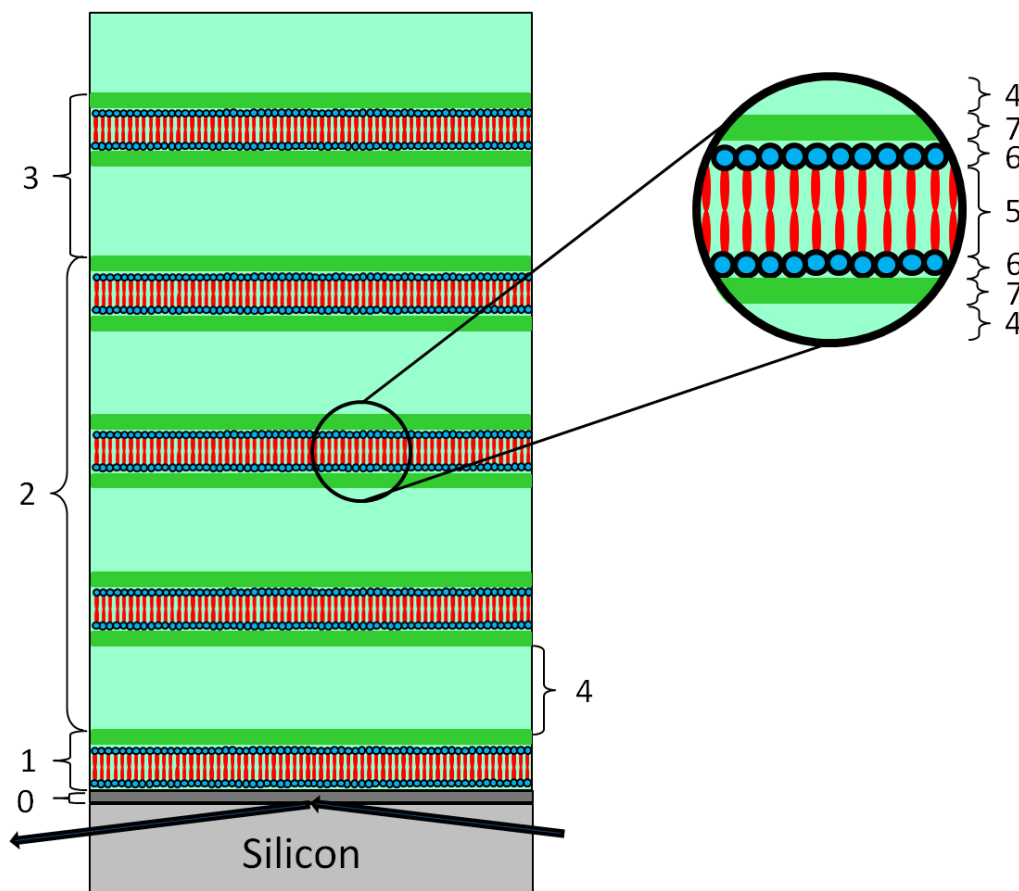


Figure 87: Model of a fully swollen, oligolamellar lipid coating on a silicon substrate, incubated in a solution of HA in D_2O . Silicon was used as a solid support, covered with a layer of silicon oxide (0). An oligolamellar lipid coating was modelled by subdividing the system into three parts: First, an inner lamella (1) is directly attached to the silicon oxide layer. The inner lamella is followed by several core lamellae (2), which have the same d and SLD. Finally, this stack of layers is covered by a terminal lamella, the outer lamella (3). Each lipid lamella is represented by a layer of hydrophobic lipid chains (5) with a hydrophilic head group layer at each side (6). Two neighbouring lamellae are separated by a solution interlayer (4). In addition, a HA layer (7) is attached to the outer surfaces of each membrane. Thickness and SLD of each layer were subject to fitting. [109]

For comparison of the extracted structural parameters with the reference system measured in pure D_2O , the neutron reflectivity curve of sample C (chapter 5.2.1 on page 77) was fitted with the more elaborated model: The combined interlayer was separated into two different layers, namely a head group layer (heads) and a solution interlayer (solution). As expected, the higher number of fit parameters resulted in a better fit: the χ^2 of the fit changed from 3.10×10^{-2} to 2.58×10^{-2} . The basic picture of the oligolamellar coating as shown in Figure 38 on page 66 is not affected by such procedure. The resulting values are in good agreement with earlier findings [110]. All parameters are listed in

Table 6.2 on page 127.

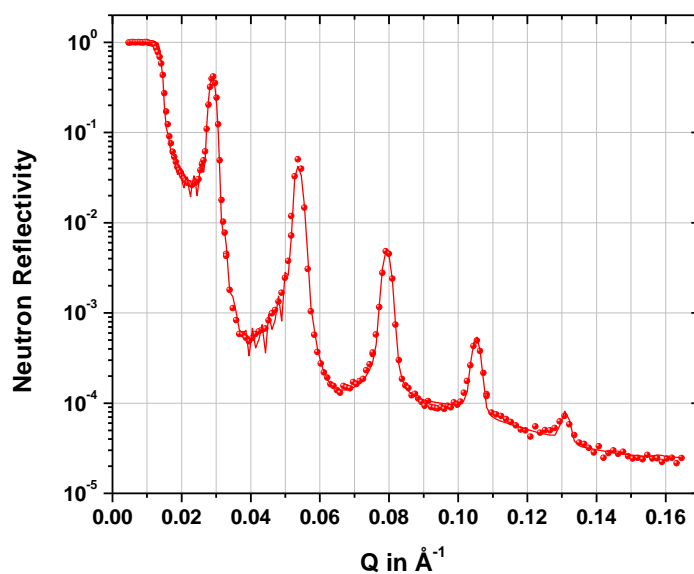


Figure 88: Neutron reflectivity of the oligolamellar lipid coating on a silicon substrate (sample 2) incubated for 43 days (1032 h) in a solution of 3 mg/mL HA in D_2O and measured at 39 °C. Bragg peaks are caused by a lamellar repeat distance of $d_p = (247 \pm 1) \text{ \AA}$. Solid line: Fit to the data. Parameters are listed in Table 6.2. [109]

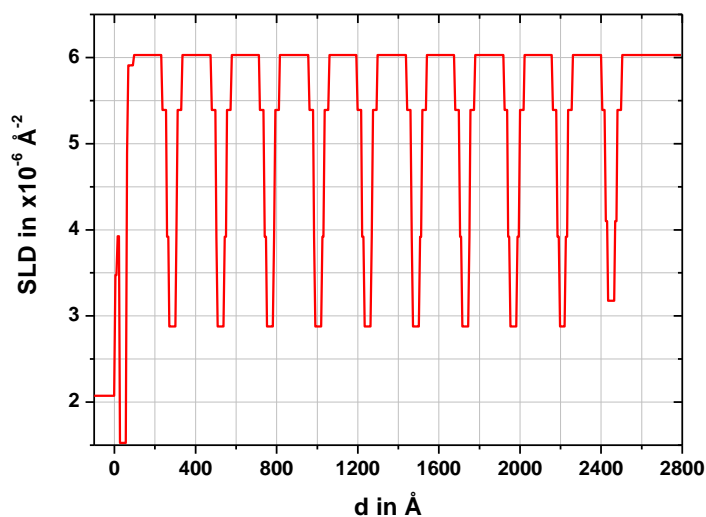


Figure 89: Scattering length density (SLD) plotted versus distance from the silicon substrate, z , of sample 2. The measurement was performed at 39 °C in a solution of 3 mg/mL HA in D_2O after 43 days (1032 h) of incubation. The plot is the real space representation of the fit in Figure 88. The parameters are listed in Table 6.2 [109]

		Sample C in D ₂ O @21 °C		Sample 2 1032 h in HA+D ₂ O @39 °C	
		d	SLD x 10 ⁻⁶ [Å] [Å ⁻²]	d	SLD x 10 ⁻⁶ [Å] [Å ⁻²]
substrate	silicon	N/A	2.07	N/A	2.07
	silicon oxide	18	3.48	10	3.48
inner lamella	heads	8	4.01	12	3.93
	tails	35	1.50	36	1.53
	heads	14	4.14	9	4.89
	HA layer	-	-	26	5.91
core lamellae	..				
	solution	10	6.25	142	6.03
	HA layer	-	-	22	5.39
	heads	10	3.64	10	3.92
	tails	34	1.79	33	2.88
	heads	10	3.64	10	3.92
	HA layer	-	-	22	5.39
..					
outer lamella	solution	16	6.25	142	6.03
	HA layer	-	-	19	5.39
	heads	11	3.75	12	4.10
	tails	34	2.07	34	3.18
	heads	8	5.89	12	4.10
	HA layer	-	-	19	5.39
solution	bulk solution	N/A	6.25	N/A	6.03
goodness of fit	χ^2	2.58 x10 ⁻²		2.38 x10 ⁻²	

Table 6.2: Fitting parameters for sample 2, incubated for 43 days (1032 h) in a solution of 3 mg/mL HA in D₂O, measured at 39°C (green column). For comparison the corresponding values for sample C, incubated in pure D₂O at 21°C (blue column) are also listed. The resulting scattering length density profile of sample 2 is shown in Figure 89. A detailed description of measurements on sample C is given in chapter 5.2.1 on page 71.

[109]

Fourier analysis

In addition to above analysis, a Fourier analysis of the measured Bragg peaks up to the fifth order ($n_{\max} = 5$) revealed a scattering length density profile $S_{\text{exp}}(z)$ of the 1D unit cell according to Equation 3.46 (on page 41), independent of the optical matrix approach. The result is shown in Figure 90 on page 129. For comparison with the optical matrix approach a theoretical scattering length density profile of a DMPC lipid membrane in pure D_2O was constructed, according the procure described by Wiener et al. in 1991 [137]. In brief [109], the unit cell is modelled as a lipid bilayer, sandwiched between two water layers (cf. Figure 4 on page 17) with the hydrophobic chain groups in the centre of the unit cell. The model bilayer is subdivided into a number of five quasi-molecular groups: methyl (CH_3), myristoyl ($2 \times C_{12}H_{24}$), glycerol ($C_5H_5O_4$), phosphate (O_4P) and choline ($C_5H_{13}N$). The water layers are represented by cylinders of pure D_2O molecules as conjunctions between two neighbouring membranes. The length of the cylinder is the difference between the total lamellar spacing $d_p = 247 \text{ \AA}$ resulting from the measurements and the thickness of the pure bilayer with $d_{\text{bilayer}} = 48 \text{ \AA}$ [138]. With an area A_{DMPC} of a DMPC molecule of 63 \AA^2 and a volume of a water molecule of 30 \AA^3 , 418 water molecules were calculated to be contained in a cylinder between two neighbouring membranes. For the centrosymmetric unit cell model, half of the water molecules are attributed to one lipid molecule and represented by 10 quasi-molecular groups, each with the SLD of 21 D_2O molecules. According to Wiener et al., each quasi-molecular group i at a position z_i can be represented by a Gaussian distribution and multiplied by its group neutron scattering length S_i . The sum over all distributions results in the theoretical scattering length profile $S_{\text{theo}}(z)$ of a single unit cell, taking the experimental resolution res into account:

$$S_{\text{theo}}(z) = \sum_{i=1}^x \frac{S_i}{res \sqrt{\pi}} \exp \left[- \left(\frac{z - z_i}{res} \right)^2 \right] \quad \text{Equation 6.1}$$

$$res = \frac{d_p}{2 n_{\max}} \quad \text{Equation 6.2.}$$

All values are summarized in Table 6.3. A comparison of $S_{\text{exp}}(z)$ and $S_{\text{theo}}(z)$, including the profile resulting from the difference between them, is shown in Figure 90 on page 129. All profiles are normalized by the area A_{DMPC} of one DMPC molecule, resulting in a SLD profile. The maximum difference between the two profiles arises at $z = \pm 44 \text{ \AA}$, indicating protonated

regions close to the head groups of the lipid molecules. With the resulting SLD at $z = 44 \text{ \AA}$ for SLD(theo) and SLD(exp) a volume fraction of 16% HA could be calculated for that position in the profile according to Equation 3.23 (on page 35).

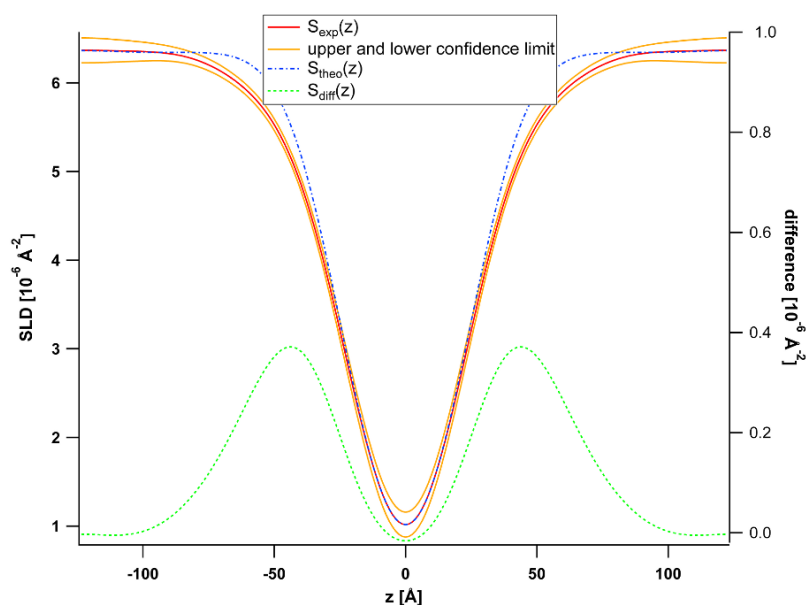


Figure 90: Scattering length density profiles resulting from a Fourier analysis of the measured Bragg peaks $S_{exp}(z)$ (red line, left abscissa) and from theoretical considerations $S_{theo}(z)$ (blue line, left abscissa), the later including only pure D_2O . The difference profile is shown in green (right abscissa).[109]

i	1	2	3	4	5	6	...	15
quasimolecular group	CH ₃	2xC ₁₂ H ₂₄	C ₅ H ₅ O ₄	O ₄ P	C ₅ H ₁₃ N	21xD ₂ O	...	21xD ₂ O
S_i in 10^{-5} \AA	-9.14	-19.97	37.70	28.34	-6	400	...	400
z_i in Å	0	7	15	20	23	30	...	120

Table 6.3: Parameters for SLD profile calculation by Fourier analysis. Values for scattering length S_i and position z_i are taken from literature [86, 137].[109]

Discussion

Even though a drastic change in reflectivity has been measured, the detailed analysis of the reflectivity data (

Table 6.2 on page 127) shows that lipid bilayer formation is not altered by the presence of HA in the incubating solution. The drastic increase in total repeat distance by 380 % did not destruct the lamellar order of the lipid molecules. In addition, the correlation between the individual membranes is high, resulting in five sharp Bragg peaks. Hence, with both incubating liquid phases, pure D₂O and the solution of HA in D₂O, the reflectivity of repeating lipid bilayers with a well-defined d-spacing appear clearly in the reflectivity data. The thickness of the hydrophobic core of one single DMPC bilayer membrane is 34 Å in pure D₂O and 33 Å in the solution of HA in D₂O. The values match theoretical predictions presuming a sequence of $2 \times 12 \times 1.27 \text{ \AA} + 2 \text{ \AA} = 32.48 \text{ \AA}$ for the (CH₂)₁₁-CH₃ H₃C-(CH₂)₁₁-acyl chain region in all-trans conformation and the van der Waals radii of the terminal H atoms within a confidence level of 95 %. The deviations of measured SLD from expectation are more pronounced. The extracted value of $1.79 \cdot 10^{-6} \text{ \AA}^{-2}$ in pure D₂O and $2.88 \cdot 10^{-6} \text{ \AA}^{-2}$ in the solution of HA in D₂O for the tail strata compares less favourable with the expected SLD of $-0.28 \cdot 10^{-6} \text{ \AA}^{-2}$ for a uniform condensed acyl chains layer [139]. The likely explanation for the observed increase in SLD in our case is the intrusion of pure water into the tails strata for the system measured against pure D₂O. Based on Equation 3.23 (on page 35) one calculates a volume fraction of D₂O of 32 % within the hydrophobic core of the lipid membranes in pure D₂O in line with observations reported from other solid-supported lipid membrane systems [140, 141]. For the system measured in the solution of HA in D₂O, the increase in SLD is potentially caused by the contribution of both, D₂O and HA to that volume fraction. In this case the description of the SLD of the respective layer contains the two unknown volume fractions $\phi_{\text{D}_2\text{O}}$ and ϕ_{HA} of D₂O and HA, respectively, within one equation. Hence, $\phi_{\text{D}_2\text{O}}$ and ϕ_{HA} cannot be further disentangled within the available set of data.

Although testified by computer simulation [142] the large amount of water (or aqueous HA solution) observed, is unlikely distributed homogenously within the alkane slabs. Formation of water channels across the individual lipid membranes seems more reasonable and has also been observed in other lipid and surfactant systems [143, 144]. Those water channels would fragment the oligolamellar lipid coating parallel to the substrate and generate a patchwork morphology of aligned lipid membrane platelets. The latter structure corresponds to a brick-and-mortar model as proposed for stratum corneum on a larger length scale [145, 146]. The

water channels must be smaller than the coherence length of the incoming neutrons, i.e., smaller than $\sim 1 \mu\text{m}$, as approaches of fitting the data by incoherent superposition of plain and lipid covered surface areas were out by a factor of 10, i.e., they yielded χ^2 values that were one order of magnitude larger than those of the best coherent (box model) fit. The thickness of the lipid head groups matches closely with the value of 9 \AA reported by Büldt and co-workers for hydrated DMPC membranes [147].

The additional HA layer, close to the outer head group region of the lipid membranes, is composed of a binary mixture of HA and D_2O . By applying Equation 3.23 (on page 35) the corresponding volume fraction of HA in that layer is 23 % HA in 77 % D_2O , using the extracted values from the box model fit (

Table 6.2 on page 127). The enrichment of HA in the boundary layer adjacent to the lipid head groups is also revealed by the Fourier analysis of the neutron reflectivity experiments. From the difference profile shown in Figure 90 (on page 129) HA concentration is highest in the interstitial water layer adjacent to the lipid membrane at $z = 43.8 \text{ \AA}$ (16 % HA) with decaying amounts of HA through the head group region into the tail strata ($z \rightarrow 0 \text{ \AA}$) and also decaying amounts of HA into the large aqueous interlayer ($z \rightarrow \pm 100 \text{ \AA}$). For comparison, the volume fraction of HA calculated from the box model is 7 % higher. In addition, the distance of the centre position of the HA layer from the centre of a bilayer membrane calculated from the box model fit is $33/2 + 10 + 22/2 = 37.5 \text{ \AA}$ (Table 6.3 on page 129). Hence, the positions of maximum HA concentration differ by $\Delta z = 6.3 \text{ \AA}$ dependent on type of analysis. We attribute the uncertainties in position and amount of HA to the limited experimental resolution.

It is relevant to ask how stability is achieved in the lipid coating in its L_p state, keeping in mind that the same oligolamellar lipid coating detaches from the substrate when heated above T_m in the absence of HA. The major counterpart of the van de Waals (vdW) force must be the electrostatic double layer repulsion generated by charging up opposing bilayer membranes (introduced in chapter 2.1 on page 17). This is achieved by the enrichment of the negatively charged HA in the opposing HA layers. In addition, long-ranged steric repulsion of the confined macromolecules might contribute in the same direction. Charging up and subsequent swelling of bulk lyotropic lipid phases was reported before. In the system dipalmitoylphosphatidylcholine (DPPC)/water a repeat distance of about 150 \AA was observed in the lamellar phase in the presence of 10 mM MgCl_2 by X-ray diffraction [26]. A modified

DLVO theory taking into account vdW-interaction of the membranes, hydration interaction of the membrane surfaces and electrostatic interactions caused by the Me^{2+} ions adsorbed to the membrane surfaces was able to reproduce the experimental results [24]. The theory predicted possible static repeat distances up to 250 Å [24, 27]. The lamellar repeat distance of our system of 247 Å at 39°C falls within that range and could be caused by such effect. The repeat distance of 247 Å was measured after 43 days of incubation time and hence is presumably the swelling limit of our system.

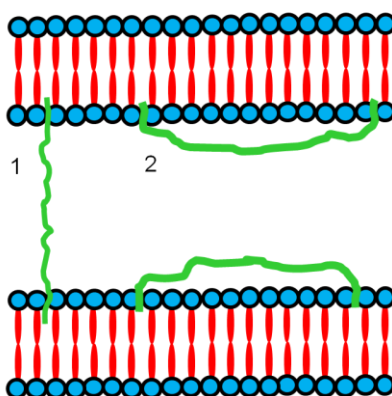


Figure 91: Bridging (1) and looping (2) conformation of a polymer chain, anchored in two opposing lipid membranes. The sketch is inspired by [148] and already published in [109].

HA, as other polymers, is expected to adopt looping and bridging conformations [57], which give rise to additional repulsive and steric (attractive) interactions. Figure 91 (above) illustrates possible configurations of the interfacial system DMPC + HA against excess water in its L_p state. Within that model, one side of the HA polymer anchors in the hydrophilic or hydrophobic slab of a lipid membrane and the other side either anchors in the same membrane (looping) or the adjacent membrane (bridging) [149, 150].

We observed high HA concentration, by a factor above 50 larger than the bulk concentration, in the boundary region of the lipid membranes (HA layer) and the respective interstitial water layers. That enrichment could be due to looped and/or anchored HA chains. Maximum swelling, on the other hand, was expected to be of the order of the end-to-end distance R_E of a free HA-chain in solution, which according to Kuhn [151] scales as

$$R_E = a \cdot (N - 1)^{\frac{3}{5}} \quad \text{Equation 6.3}$$

with the size a of a monomer unit and the degree of polymerization, N . From the measured mass density of 1 g/cm³ [152] and the molecular weight of a monomer unit of 378 Da we estimate a to be 10.6 Å presuming spherical shape. The hydrodynamic radii R_H of HA

reported from literature are $R_H = 116 \pm 10 \text{ \AA}$ for $M_w = 85.000 \text{ g/mol}$ and $R_H = 170 \pm 20 \text{ \AA}$ for $M_w = 160.000 \text{ g/mol}$, respectively. With $R_E = 2R_H$ the corresponding end-to-end distances R_E are $232 \pm 20 \text{ \AA}$ (85.000 Da) and $340 \pm 40 \text{ \AA}$ (160.000 Da) [153]. By applying Equation 6.3 with $a = 10.6 \text{ \AA}$ we calculate respective values R_E of 272 \AA (85.000 Da) and 398 \AA (160.000 Da) in reasonable agreement with the measured values. In our experiments we used HA with an average M_w of 769.000 Da. According to Equation 6.3 R_E is thus 1024 \AA in our case. That number is by a factor of 4 larger than the measured repeat distance of 247 \AA . Hence, the individual lipid lamellae are not simply separated by Gaussian coils of HA entering the interstitial water layers.

Whether HA anchors in the head group regions or the chain group region of the lipid membrane is not clear. Both options seem possible. Anchoring at and in the head group region of the lipid membrane is likely from the observed variations in SLD in the corresponding slabs and is also known from other di- and polysaccharides [22, 154, 155]. HA also forms hydrophobic patches [57], which could be anchored in the hydrophobic tail regions of lipid membranes. This way a single polymeric HA chain of about 2000 monomer units on average as in our case could easily span and thus crosslink several adjacent DMPC membranes in the heavily swollen state of the oligolamellar coating at the solid-liquid interface at temperatures above T_m . Different stretching of HA molecules in the hydrophobic lipid core and in the boundary region of lipid head groups and aqueous interlayers would then hold for the observed enrichment of HA in the latter boundary region. The intruding HA would transform the lipid coating into a spatially restricted lamellar hydrogel coating. Such network-like structures are reported for bulk lyotropic phases of DMPC in the presence of double-end anchored polymer-surfactants and aqueous suspensions of phospholipid vesicles in the presence of HA [10, 148]. The observed swelling limit is $\frac{1}{4}$ of the end-to-end distance of our high molecular weight HA. Thus it is rather likely that HA chains do bridge adjacent bilayers leaflets.

From the conducted experiment it is evident that high molecular weight HA stabilizes the oligolamellar DMPC coating on its solid support against the excess fluid phase at physiological temperature where – in absence of HA – detachment and irreversible loss of the lipid coating is observed. The HA-induced stabilization will be of importance wherever artificial solid implants are to be covered with lipid coatings for protection or biocompatibility reasons.

6.5 Effect of HA and salt

Introduction

The question remains open, what are the driving forces for the incorporation of HA molecules into an ordered lipid coating? In solution of neutral pH, HA is negatively charged [56]. Therefore, electrostatic interactions with the zwitterionic head groups of the DMPC molecules might take place. In order to screen the negative charges of HA, salt was added to the HA solution. Potential subsequent structural changes of a lipid coating were followed by performing neutron reflectivity measurements at V6 after incubation of a freshly prepared sample (sample 3) in a solution of 1 M NaCl and 3 mg/mL HA in D₂O. The sample consisted of a silicon disc that was spin-coated with a solution of 10 mg/mL DMPC in chloroform. Starting with incubation at 21°C for 9 h, temperature was increased to 38°C and the sample was measured again at 22 h (additional 11 h at 38 °C) and 37 h (additional 26 h at 38 °C).

Results

The neutron reflectivity of sample 3 at 21°C after 9 h revealed a well-ordered, oligolamellar lipid coating with a d-spacing of $d = (67.77 \pm 0.07) \text{ \AA}$ (Figure 92). From the Kiessig oscillations a total layer thickness of $t = (488 \pm 43) \text{ \AA}$ was extracted. With the d-spacing and Equation 3.36 (on page 39) it was calculated that the oligolamellar coating consisted of $N = 7.2 \pm 0.6$ lipid bilayers. A second measurement, performed after 11 h of incubation at 38°C, resulted in a reflectivity curve with the same characteristics. The Bragg peak amplitude revealed a d-spacing of $d = (66.02 \pm 0.10) \text{ \AA}$. The Kiessig oscillations maintained their frequency, indicating that the number N of substrate bound bilayers did not change. A final measurement (Figure 92) after 37 h of incubation, i.e. 26 h after temperature was increased to 38°C, showed identical results.

Discussion

In contrast to measurements with pure HA solutions, the lipid coating did not change its structure upon the addition of salt to the incubating solution. Even after 37 h of incubation time no swelling could be observed. Therefore, an interaction between the lipid coating and HA could not be observed. It is known that salt (NaCl) screens the electrostatic charges along polymer chains. This has two effects on a polymer: First, the charge density of a polymer–salt system is reduced and subsequently, a polymer transforms from a linear to a globular shape, because originally repulsive segments along the polymer chains vanish due to the screening of salt ions [156, 157]. The increase of the specific volume of HA upon increasing NaCl concentration could be proven by density measurements of HA in different media [152]. The

suppressed interaction of HA with the lipid coating could have on one hand its origins in reduced electrostatic interactions between HA and lipid coating. On the other hand, interactions between lipid coating and HA could have been prevented by the changed conformation of the HA molecules, hence, due to the coiled structure the HA molecules could not diffuse into the lipid coating, as their specific volume increased.

From the conducted experiments, as described in chapter 5.2, an unbinding transition in the L_α phase at 38 °C was expected. However, the addition of salt seems to stabilize the lipid coating in the L_α phase. This might be due to the fact, that the diffusion and mobility of lipid molecules within the bilayer is suppressed by the presence of NaCl [158] and therefore the unbinding process was not initiated.

The performed experiment shows clearly, that charges play an essential role for the characteristics of the lipid – HA system.

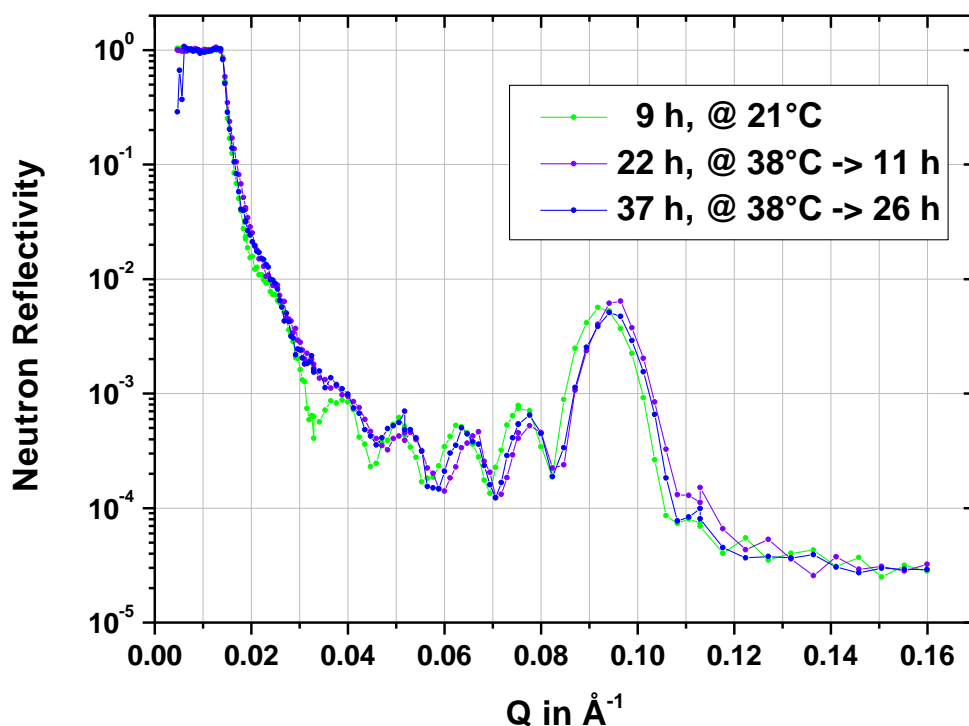


Figure 92: Neutron reflectivity curves of an oligolamellar lipid coating on silicon (sample 3), incubated in a solution of 3 mg/mL HA in D_2O , with 1 M NaCl added to the solution.

6.6 Effect of shear

Introduction

The stabilizing effect of HA on a DMPC lipid coating on silicon at 39°C has already been proven by experiments described above (chapter 6.4 on page 123). In order to mimic the forces acting on a lipid coating in joints, an external force was applied to oligolamellar lipid coatings, which were incubated in HA solutions by using the shear setup (described in chapter 3.2.6 on page 50). Structural changes of the coatings were followed by neutron reflectivity measurements accomplished with the AMOR instrument at PSI (Switzerland). Two different samples (sample 4 and 5), each coated with the spin-coating technique, using a solution of 10 mg/mL DMPC in chloroform, were prepared and measured under different shearing conditions. In order to mimic the shear force on a knee joint for a moderate load, a shear frequency of 1 to 2 Hz was estimated and applied to sample 4. For a more pronounced strain on a knee joint, for example resulting from a short distance sprint of a person, a frequency of 5 Hz was estimated and applied to sample 5.

Moderate load

A first sample (sample 4) was measured 0.5 h and 2.0 h after incubation at 21°C without shear force (Figure 93). Bragg peak analysis results in a d-spacing of $d = (64.92 \pm 0.07) \text{ \AA}$. In addition, the well-resolved Kiessig oscillations reveal a total layer thickness of $t = (640 \pm 74) \text{ \AA}$, built up by $N = 10 \pm 1$ bilayers. Until then, no swelling effect was observed. In order to catalyse the swelling process and the transformation of the lipid coating into the L_p phase, temperature was increased to 39 °C. A measurement 41.0 h after incubation showed the provoked effect: The transformation of the oligolamellar lipid coating, with the appearance of a Bragg peak in the lower Q-range, is clearly visible. A d-spacing of $d = (155.5 \pm 0.2) \text{ \AA}$ is calculated, which implies a swelling of the lipid coating by 240%. In addition, the second order Bragg peak is well-resolved. In the following, the coating was exposed to an external shear force in order to study the stability of the swollen membrane system. The first order Bragg peak amplitudes were used as a parameter for quantifying the number of substrate bound lipid membranes (compare to chapter 3.2.4 on page 33). Right after application of a shear force with a frequency of 1 Hz, the amplitude increased by a factor of 3 from 0.111 ± 0.005 to a value of 0.333 ± 0.012 , measured at 41 h and 43 h after incubation in the HA solution, respectively. However, a second measurement at 1 Hz after 47 h of incubation already showed a reduced Bragg peak amplitude of 0.210 ± 0.009 . An

increase of shear frequency to 2 Hz, induced a further decrease of the Bragg peak amplitude to a value of 0.169 ± 0.009 after 48 h and to a value of 0.054 ± 0.009 after 49 h. In order to verify, whether the reduction of amplitude is independent of the applied shear force, the shear force was interrupted for 3 h. Subsequent measurements showed that the downward trend of the peak amplitude was stopped. Within this time period, the Bragg peak gained intensity up to a value of 0.076 ± 0.008 after 52 h of incubation. However, the re-application of the external shear force with a frequency of 4 Hz resulted in a total loss of the Bragg peak, 55 h after incubation of the sample. The appearing Kiessig oscillations revealed the existence of a residual coating on the silicon substrate with a total layer thickness of $t = (175 \pm 6) \text{ \AA}$. Further measurements did not show any more changes in the reflectivity of the sample. Even an increase of shear frequency to 20 Hz did not alter the reflectivity curves anymore, measured 75 h after of incubation.

Pronounced load

Sample 5 already shows a transformation into the L_p phase at 21°C , 4 h after incubation in the solution (Figure 95). Two occurring Bragg peaks belong to a d-spacing of $d = (135.5 \pm 0.3) \text{ \AA}$. After 24 h of incubation time, the swelling proceeded further to a value $d = (163.9 \pm 0.3) \text{ \AA}$. Furthermore, 6 h after temperature was increased to 39°C , i.e. 34 h after incubation, a d-spacing of $d = (170.2 \pm 0.3) \text{ \AA}$ was measured. Application of a shear force with a frequency of 5 Hz immediately resulted in the loss of most of the lipid membranes as indicated by measurements performed 37 h after incubation. The fact that the remaining reflectivity of the silicon surface is still higher than the Fresnel reflectivity of the plain silicon substrate clearly indicates the presence of adsorbed material on the otherwise plain surface. A subsequent measurement without shear force did not show any further change in reflectivity of sample 5.

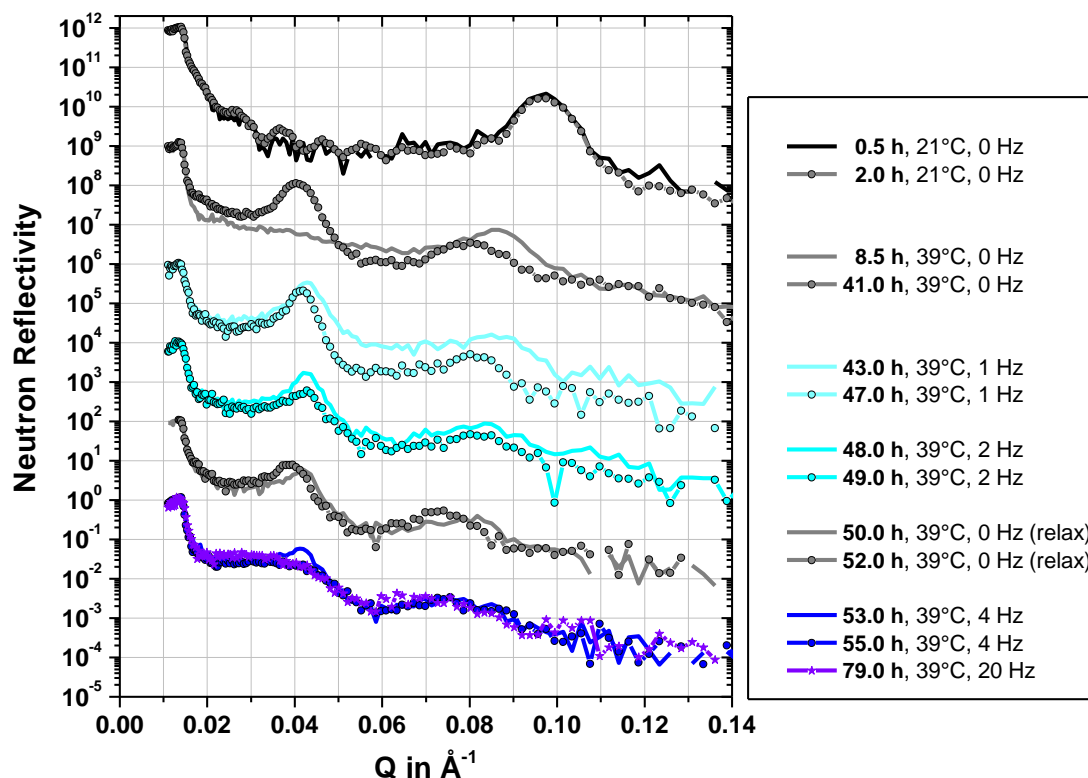


Figure 93: Neutron reflectivity measurements of sample 4 in the shear setup. A silicon substrate with an oligolamellar lipid coating was incubated in a solution of 3 mg/mL HA in D_2O . From top to bottom the curves are displayed with increasing incubation time. Temperature was increased from 21 °C to 39 °C after 8.5 h of incubation. In addition, after the transformation of the lipid coating in a HA rich L_p phase (43 h), an external shear was applied. For clarity, the reflectivity curves are shifted vertically.

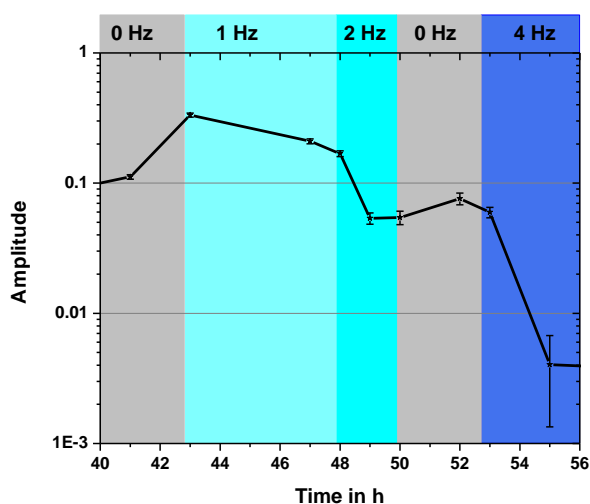


Figure 94: First order Bragg peak amplitudes of sample 4, measured after different times of incubation in a solution of 3 mg/mL HA in D_2O and at different shear rates. Upon application of a shear frequency of 4 Hz, the amplitude drops drastically. The corresponding reflectivity curves are shown in Figure 93.

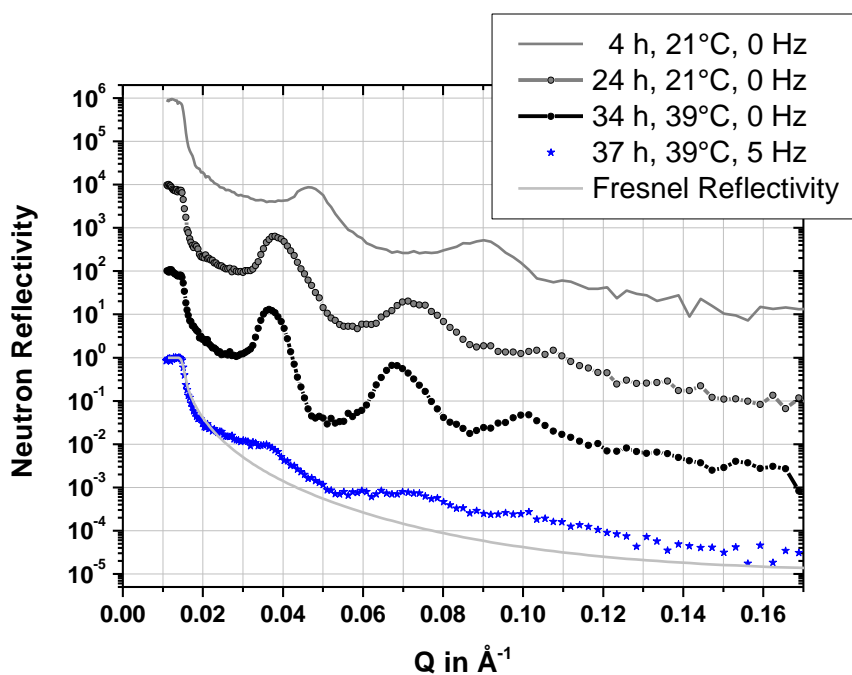


Figure 95: Neutron reflectivity curves of sample 5: An oligolamellar lipid coating on a silicon substrate, incubated in a solution of 3 mg/mL HA in D_2O as a function of incubation time, temperature and subsequent shear load.

Discussion

In independent experiments using the shear setup, the swelling process of oligolamellar lipid coatings upon incubation in solutions of 3 mg/mL HA on D_2O was followed. As expected, even below the main phase transition of bulk DMPC at 21°C an excessive swelling of the coating was observed without shear. Furthermore, the swelling of the lipid coating is accompanied with a stabilizing influence on the coating above the main phase transition of bulk DMPC at 39°C : A total unbinding of the lipid lamellae did not occur. In addition, the swollen coating resists a total unbinding upon a moderate applied shear force: Within 4 h of shear with a frequency of 1 Hz, the Bragg peak amplitude, resulting from the lipid coating, was always larger than the initial intensity, measured without shear. When sheared with 2 Hz for more than one hour, the Bragg peak amplitude decreased significantly. However, relaxing the system (0 Hz) stopped the decrease in amplitude and, therefore, the unbinding process.

Keeping the high viscosity of the used HA solution in mind, the stability of the highly swollen coating (by 240 %) upon a moderate shear rate is astonishing. However, the exertion of a more pronounced strain on the system, by applying 4 Hz or 5 Hz, resulted in immediate destruction of the coating with only film residues still bound to the surface.

6.7 Effect of pressure

Introduction

The influence of hydrostatic pressure on the HA-induced swelling behaviour of an oligolamellar lipid coating was studied. An experimental cycle was conducted on the basis of the pressure dependent experiment described in chapter 5.1.2 on page 77. The difference was in using a solution of 3 mg/mL HA in D₂O as the liquid phase, instead of pure D₂O. NR measurements were performed at the V6 instrument with the high pressure cell [96]. The aim of the experiment was to follow structural changes in the lipid coating when crossing the main phase transition from the high pressure region (90 MPa) to the low pressure region (45MPa) at 38°C. A freshly prepared oligolamellar lipid coating was prepared using the spin-coating technique with a solution of 10 mg/mL DMPC in chloroform (sample 6).

Results

Directly after exposing sample 6 to the liquid phase in the pressure cell a reflectivity curve was taken at 21°C and 0.1 MPa (Figure 96). The sample showed a Bragg peak at $Q_B = (0.0970 \pm 0.0005) \text{ \AA}^{-1}$, resulting in a d-spacing of $d = (64.77 \pm 0.33) \text{ \AA}$. Kiessig oscillations appeared, but are not pronounced enough to be resolved in order to determine the total film thickness within reasonable accuracy. Analysis by the optical matrix method produced a matching fit by assuming 12 lipid membranes making up the whole lipid film. In the fitting routine essentially the same parameters were used as for sample *E* described in chapter 5.1.2 (Table 5.3 on page 83). Differences occur in the number of layers and the SLD of the bulk solution, which was increased from 6.13 \AA^{-2} to 6.37 \AA^{-2} . Increasing the pressure to 90 MPa (at 21°C) resulted in a loss of Bragg peak amplitude by 75%. Here, only a Q-range around the Bragg peak from 0.078 \AA^{-1} to 0.108 \AA^{-1} was measured. Increase in temperature to 38°C (at 90 MPa) reversed the intensity loss almost completely: 83% of the initial value at 0.1 MPa was reached. In addition, a slight increase in reflectivity was observed between 0.04 \AA^{-1} and 0.05 \AA^{-1} . The subsequent pressure release changed the reflectivity of the lipid coating dramatically: the Bragg peak shifted to smaller Q values. This swelling of the lipid coating, as described in the previous chapter, was only seen after pressure release to 45 MPa at a constant temperature of 38°C (see Figure 96).

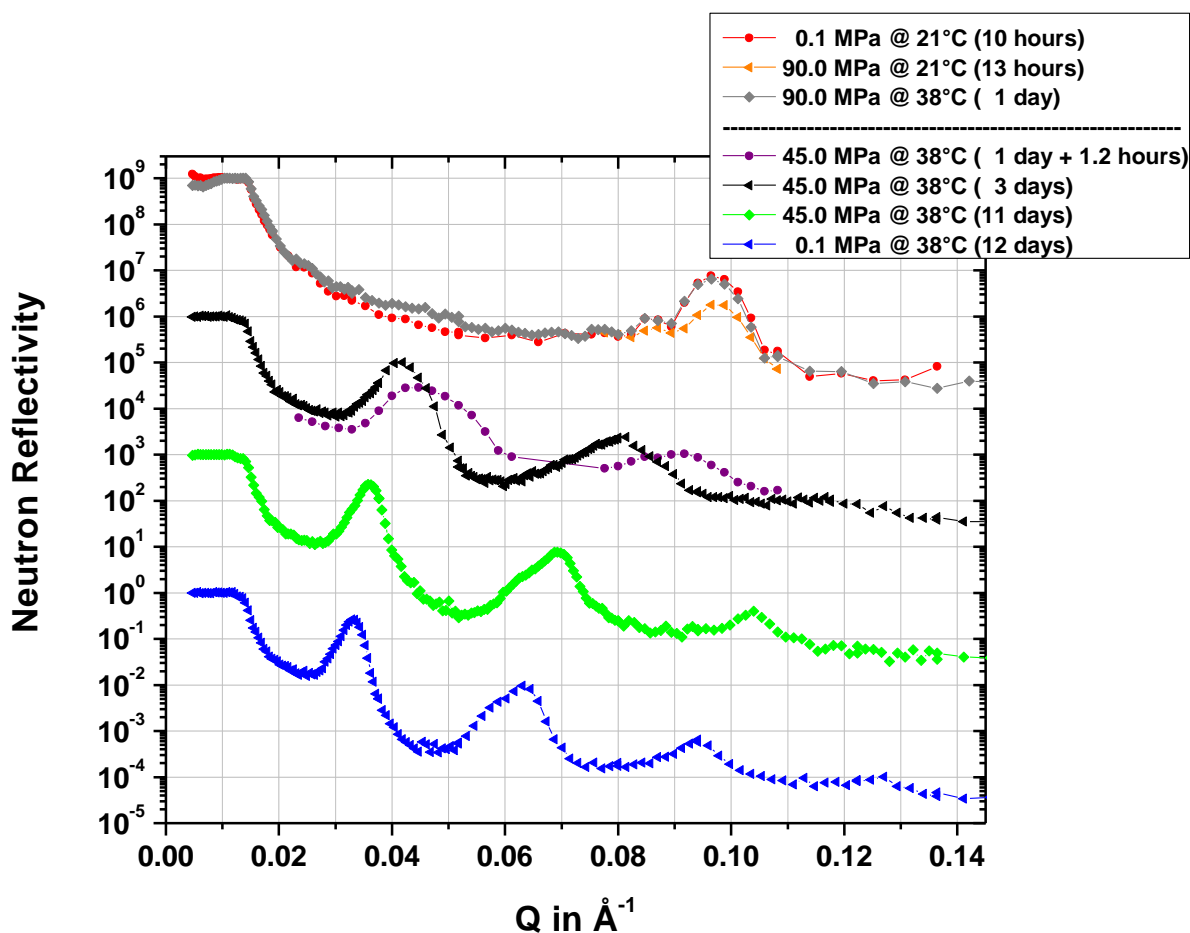


Figure 96: Neutron reflectivity curves of the oligolamellar lipid coating, sample 6, on silicon, measured against a solution of HA in D_2O . After crossing the phase transition by releasing the pressure from 90 MPa to 45 MPa at 38 °C a pronounced shift of the first Bragg peak to lower Q -values occurred. The incubation times are shown in brackets. For clarity the curves are shifted vertically.

In order to follow the swelling process of the lipid coating with time, the Q range between 0.024 \AA^{-1} and 0.104 \AA^{-1} was measured every 1.2 h over a total time interval of 46 h (Figure 97). A Bragg peak analysis of the first order Bragg peak is shown in Figure 98. The increasing area and decreasing FWHM indicate an ordering of the lipid lamellae with time. After 8 h the d-spacing increases almost linearly with a constant value of $0.390 \pm 0.003 \text{ \AA}/\text{h}$. After 46 h a d-spacing of $d = (152.06 \pm 0.32) \text{ \AA}$ was measured. A last reflectivity curve was measured under these conditions 10 days after the pressure was released from 90 MPa to 45 MPa (Figure 96). During these 10 days the pressure and temperature were kept constant (at 45 MPa and 38°C). Bragg peak analysis of the first order Bragg peak at $Q_B = 0.0359 \text{ \AA}^{-1}$ revealed a d-spacing of $d = (175.02 \pm 0.20) \text{ \AA}$. After the pressure was fully reduced to 0.1 MPa (at 38°C) the d-spacing increased further to $d = (190.34 \pm 0.30) \text{ \AA}$ and Bragg peaks up to the fourth order became visible. A summary of the finally measured d-spacings is given in Figure 99.

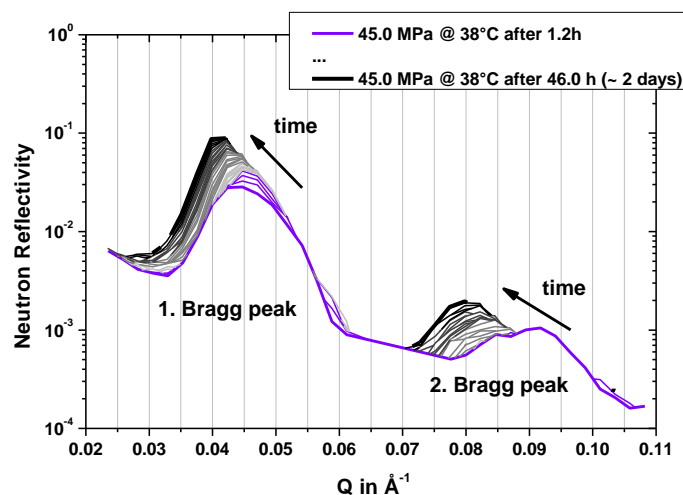


Figure 97: Time dependent neutron reflectivity curves of the oligolamellar lipid coating, sample 6, on silicon, measured against a solution of HA in D_2O at 45 MPa and 38 °C. A measurement of the displayed Q -range took 1.2 h and was repeated until 46 h after releasing the pressure from 90 MPa to 45 MPa. A pronounced shift of the first and second Bragg peak to lower Q -values occurred with time.

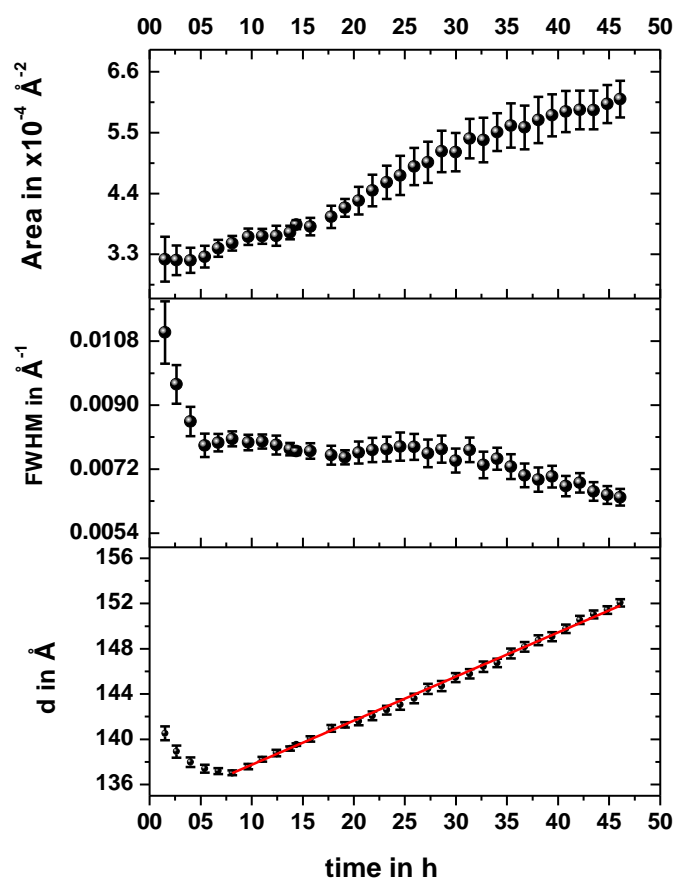


Figure 98: Bragg peak analysis of the first order Bragg peak after releasing the pressure to 45 MPa at 38 °C. The red line represents a linear fit with a slope of $0.390 \pm 0.003 \text{ \AA/h}$. The Bragg peaks are shown in Figure 97.

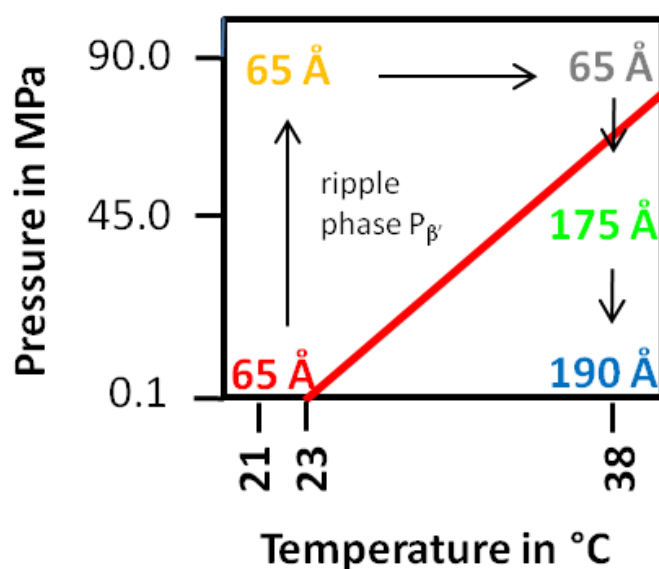


Figure 99: Phase diagram of bulk DMPC lyotropic phases with the performed experimental cycle. The repeat distances shown were measured against a solution of 3 mg/mL HA in D_2O . After crossing the phase boundary for fully hydrated DMPC bulk phases at 69 MPa and 38 °C (red line, from [111]) by pressure release, a pronounced swelling occurred from 65 Å to a final value of 190 Å.

Analysis of intermediate states

Many reflectivity curves displayed so far have been recorded for non-equilibrium states of the lipid systems (for example Figure 97 on page 142). Using the model of a fully swollen lipid coating in the HA rich L_p phase (Figure 87 on page 125), the reflectivity curve of a non-equilibrated lipid coating during swelling was fitted. Here, the reflectivity curve of sample 6, recorded at 38°C, 10 days after the pressure was released to 45 MPa, was taken as a representative example (Figure 100, bottom). The broad and non-symmetric Bragg peak shapes already reveal an incoherent superposition of reflectivity curves, resulting from a variety of d-spacings within the probed lipid coating at the time of the measurement. It is assumed that the lipid bilayers are still present at that stage of transformation. Therefore, for a model of a non-equilibrated lipid coating, a variety of reflectivity curves were simulated considering bilayers which were separated by of solution interlayers with different thickness d_{solution} (compare to Table 6.3 on page 129 and Figure 87 on page 125). Figure 100 (top) shows simulated reflectivity profiles, based on the model for a fully swollen lipid coating in the L_p phase as described in

Table 6.2 on page 127. The difference between the individual simulations is the thickness of the solution layers, d_{solution} , in between the bilayers. Here, eleven reflectivity curves with

d_{solution} varying from 100 Å to 150 Å were simulated. Otherwise the same fitting parameters as displayed in

Table 6.2 on page 127 were implemented for the simulations in the *Parratt32* software package. Subsequently, an incoherent superposition of the simulated reflectivity curves was calculated, using different weight factors for each simulated curve. The best congruency between the measured curve and the calculated superposition was achieved with the set of reflectivity data displayed in Figure 101 and Table 6.4. The resulting reflectivity curve is in good agreement with the measured reflectivity curve, indicating the validity of the above described approach.

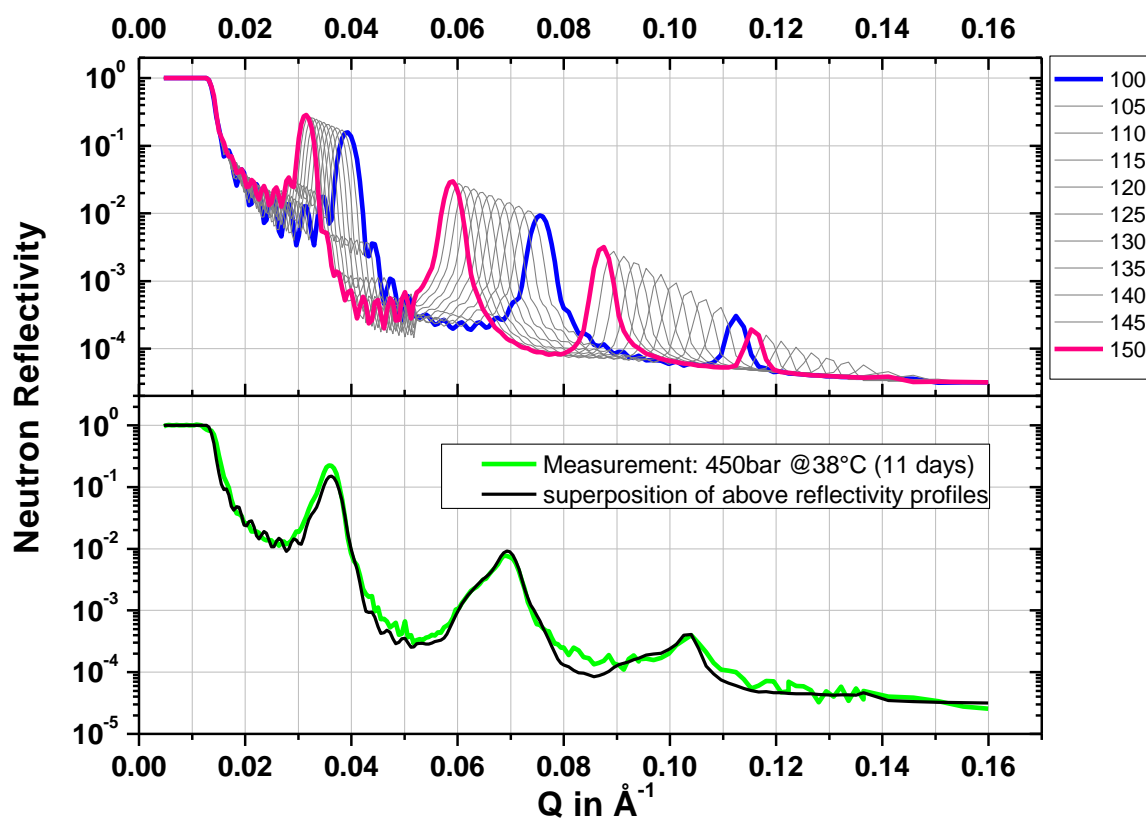


Figure 100: The reflectivity curve of sample 6 (bottom graph, green line), measured 11 days of incubation in a solution of 3 mg/mL HA in D_2O , was approximated by a superposition (bottom graph, black line) of 11 simulated reflectivity curves (top graph). For the simulated reflectivity curves solution interlayer thicknesses d_{solution} between 100 Å (top graph, blue line) and 150 Å (top graph, purple line) were used with different proportions in order to result in the best approximation.

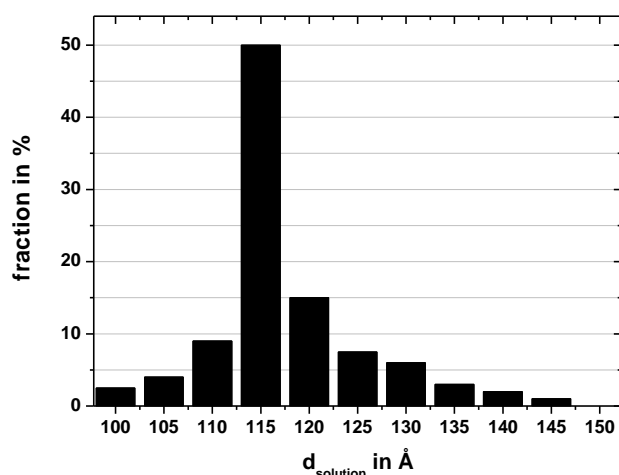


Figure 101: Used fractions for a superposition of simulated reflectivity curves with different solution interlayer thicknesses d_{solution} .

d_{solution} in Å	used fraction
100	2.5 %
105	4.0 %
110	9.0 %
115	50.0 %
120	15.0 %
125	7.5 %
130	6.0 %
135	3.0 %
140	2.0 %
145	1.0 %
150	0.0 %

Table 6.4: Corresponding values to the diagram of Figure 101.

Discussion

Even after 10 h of incubation in a solution of HA in D₂O at 0.1 MPa and 21°C, the lipid coating revealed a d-spacing of 65 Å, typical of DMPC in the ripple phase P_β. This result contradicts previous measurements showing that even at 20°C after 6.7 h the swelling process can be initiated. A pressure increase to 90.0 MPa may have stabilized the system further as still no swelling was observed (see Figure 99 on page 143). The loss in intensity of the Bragg peak amplitude is due to a loss in scattering contrast between the inter-layers and the tail group layers (compare to model in Figure 38 on page 66), initiated by additional D₂O molecules in the DMPC chain group region. Raising temperature to 38°C seemed to relocate D₂O molecules out of the tails group strata and the initial neutron contrast re-appears. This D₂O movement within the DMPC lamellae has been observed before [50, 96]. However, its origin is still unclear. The additional temperature increase to 38°C did not alter the Bragg peak position, and thus the d-spacing of the system. Only a pressure release to 45.0 MPa initiated swelling with 0.390 ± 0.003 Å/h, which is about twice as fast as the swelling behaviour observed earlier at 21°C and 0.1 MPa with 0.23 ± 0.01 Å/h (chapter 6.3 on page 122). A comparison is shown in Figure 102. Measurements made after 10 days show a strong deviation from a linear swelling behaviour, with a d-spacing of 175 Å. After an additional pressure drop to 0.1 MPa, the d-spacings of the coating increased further by 9%, to a repeat distance of 191 Å. It cannot be ruled out, that the swelling process would have continued, but

due to the end of the beam time it was not possible to perform further measurements. The broad Bragg peak of the final measurement at 0.1 MPa and 38°C (Figure 96 on page 141) indicates a coating with a distribution of d-spacings, typical of a non-equilibrium state.

The presumption of a distribution of d-spacings was validated by above analysis (Figure 100 on page 144). Unfortunately, the analysis does not reveal the special sequence of the d-spacing distribution. But it is assumed, that the swelling of the oligolamellar lipid coating progresses with the diffusion of HA molecules into the coating, starting at the outer membranes. The resulting gradient in HA concentration then provokes different stages of the swelling process. It shall be pointed out, that a d-spacing below 125 Å has not been measured for the described system. There could be two different reasons: First, the primary diffusion of HA molecules into the coating took place in a time interval too short to be resolved by the performed measurements, or second, the structure of the lipid coating changed instantly upon HA molecules entering the interlayer space between two neighbouring membranes.

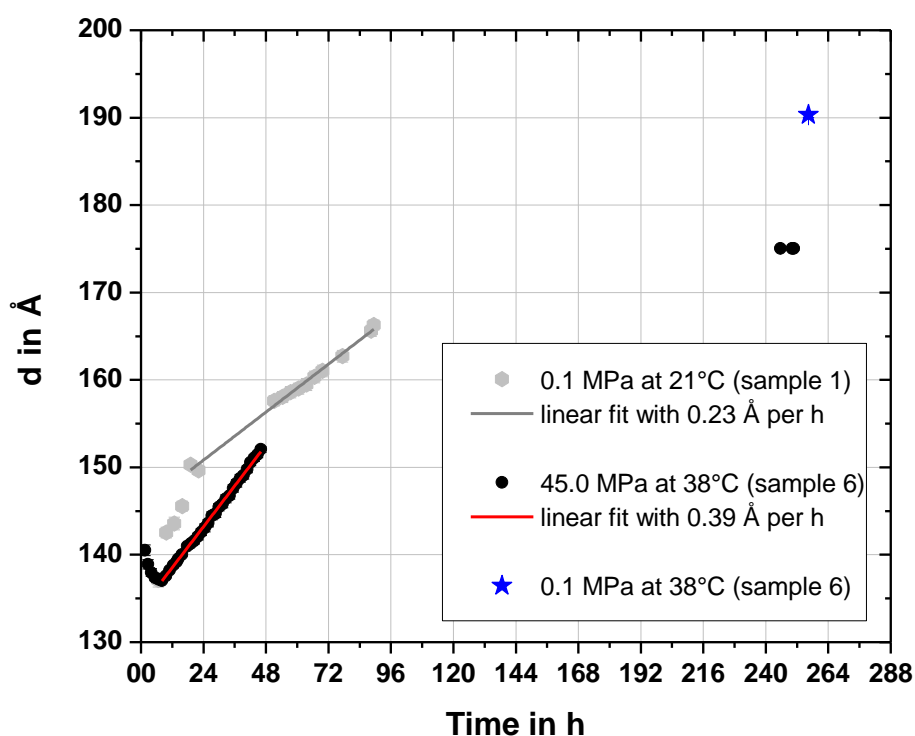
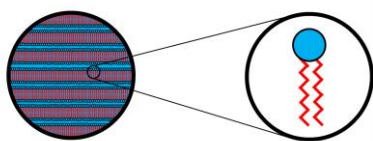


Figure 102: Comparison of d-spacings in HA solutions as a function of incubation time for sample 1, measured at 0.1 MPa and 21 °C (from chapter 6.3 on page 122), and sample 6, measured at 45 MPa and 38 °C. For comparison, the d-spacing for sample 6, measured at 38 °C after pressure reduction to 0.1 MPa is shown. The error bars are smaller than the symbols.

6.8 Phase transition of multilamellar lipid systems



The aim of this chapter is to correlate changes of a lipid multilayer system as seen by different techniques on different length scales. First, the question about intramolecular changes of lipid molecules is addressed. On that length scale, Fourier transform infrared spectroscopy (FTIR) was performed on the lipid system in an ATR setup. Secondly, structural changes of the lipid multilayer on the length scale of the lipid bilayer were addressed. The study of those structural changes was performed by neutron reflectometry (NR). With the tools of BioRef at hand we were able to perform ATR-FTIR and NR measurements simultaneously on the same multilayer system. A combined ATR-FTIR and NR experiment was conducted on a solid supported lipid multilayer system, incubated with a 3 mg/mL solution of HA in D₂O. The experiment was performed according to the measurements on the reference system, performed in pure D₂O (compare to chapter 5.3 on page 97): A silicon ATR crystal (ATR5) was used as integrative sample support, with a lipid multilayer coating, prepared with the air brush technique. In contrast to the reference system, the sample was incubated in a solution of 3 mg/mL HA in D₂O in the sample cell after evaporation of chloroform. In order to promote the interaction between HA and the DMPC multilayer, the system was tempered two times between 20°C and 30°C and set to 50°C six days before the measurements were started. The temperature range around the main phase transition between 20°C and 30°C of the DMPC multilayer system was probed. The experimental cycle covered two scans in the respective temperature interval from 20°C to 30 °C: First, the sample was heated from 20°C to 30° (heating); second, the sample was directly cooled again to 20°C (cooling). Temperature was changed every 100 minutes in 0.5°C steps. At each temperature two subsequent NR measurements were performed and 5-6 IR absorbance spectra recorded.

First, the infrared absorption signals are analyzed (chapter 6.8.1), followed by an analysis of the neutron reflectometry results (chapter 6.8.2). In the last part, the results of the two techniques are compared and discussed (chapter 6.8.3).

6.8.1 Infrared absorption of a multilamellar lipid coating

Conformational changes of lipid molecules were studied by ATR-FTIR using the setup described in chapter 4. A measurement consisting of 124 full scans was conducted every 20 minutes, resulting in 5-6 absorbance spectra per temperature step.

Results

The asymmetric $\nu_{as}(\text{CH}_2)$ and symmetric $\nu_s(\text{CH}_2)$ stretching bands show high peak amplitudes and sharp peak shapes, as shown in Figure 103 (below) for 20°C and 30°C of the heating cycle, and for 20°C of the cooling cycle. To follow the main phase transition of the DMPC lipid molecules, the analysis was focused on the $\nu_s(\text{CH}_2)$ absorbance bands.

For each temperature step, the absorption band was fitted by a Gaussian profile. The results are shown in Figure 104 (on page 150). Compared to the reference system measured against pure D_2O , the absorbance of the $\nu_s(\text{CH}_2)$ vibration shows the same temperature behaviour: A pronounced change in wavenumber, FWHM and amplitude between 24.0°C and 24.5°C. A main difference between the two measured systems was observed in the peak amplitudes: The amplitudes appear smaller by a factor of 2.4 for the system incubated in a 3mg/mL solution of HA in D_2O compared to the reference system, indicating that less material is within the penetration depth of the infrared beam, due to the swelling of the coating. A discussion is given on page 154.

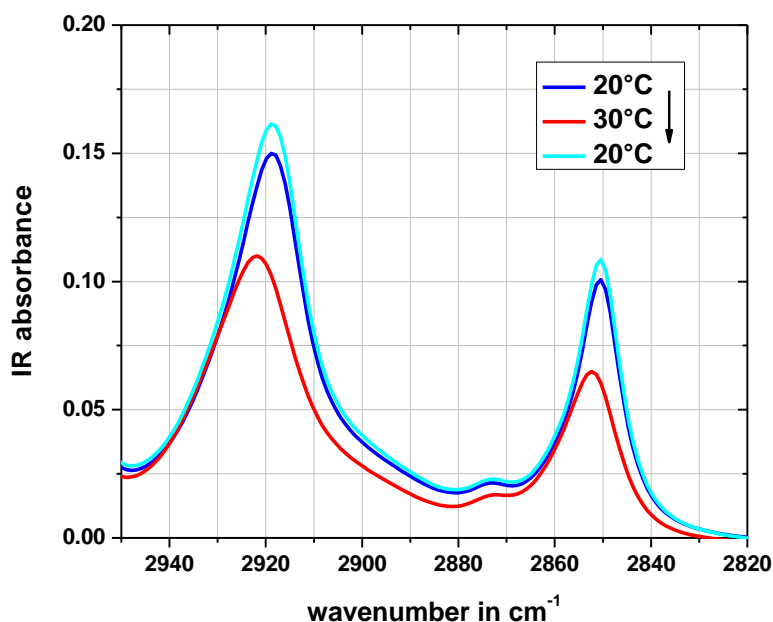


Figure 103: Infrared absorption of a multilamellar lipid coating on a silicon substrate (ATR5) incubated in a solution of 3 mg/mL HA in D_2O . Shown is the absorbance of the CH_2 groups at elevated temperatures, measured after 80 minutes of equilibration time. Temperature was cycled from 20 °C to 30 °C and back to 20 °C.

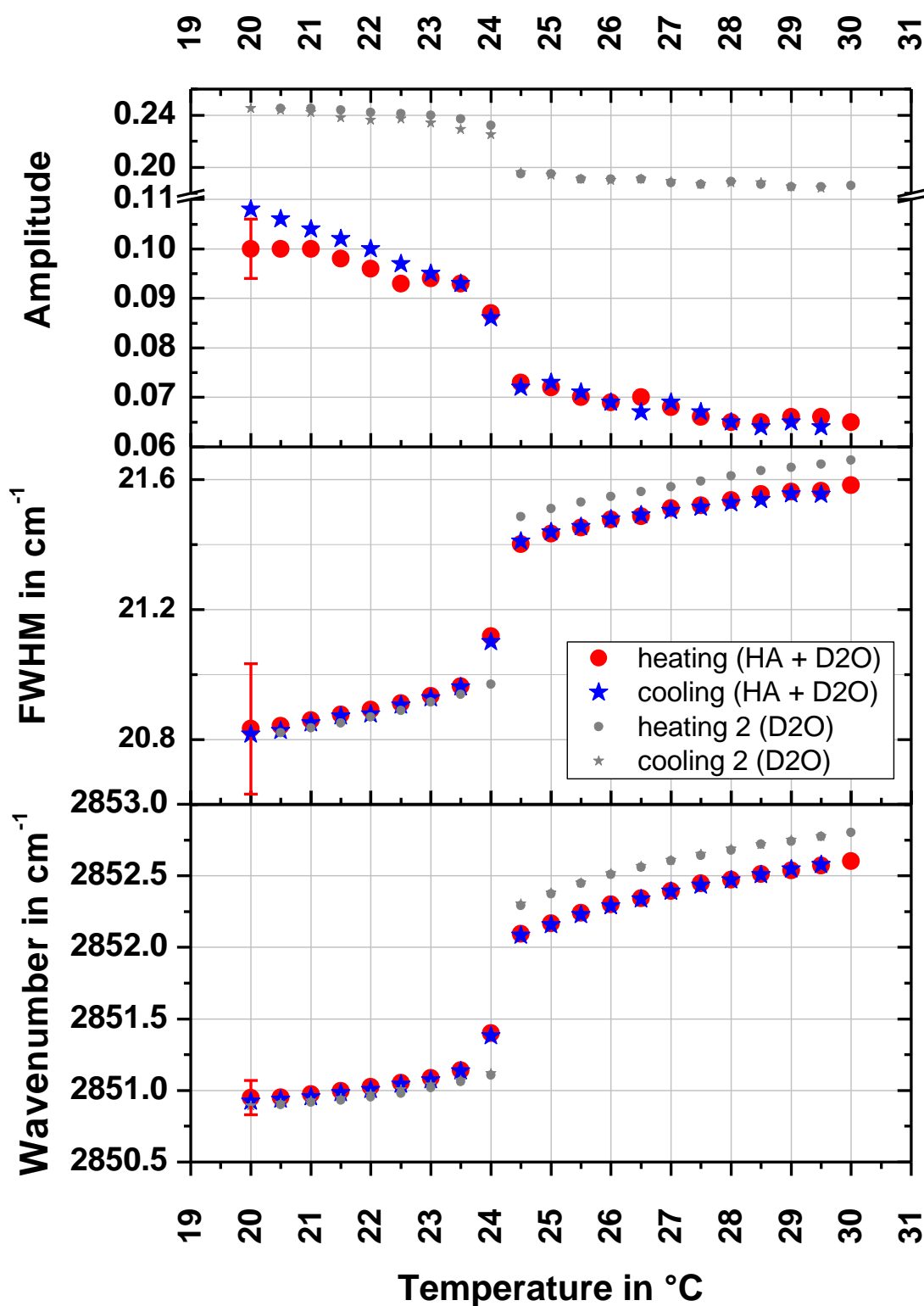


Figure 104: Infrared absorption band analysis by fitting Gaussian profiles to the $\nu_s(\text{CH}_2)$ absorption band of a multilamellar DMPC lipid coating on silicon (ATR5) in comparison against pure D₂O (grey symbols, from Figure 68 on page 100) or incubated in a solution of 3 mg/mL HA in D₂O (red and blue symbols). The shown results are measured after 80 minutes of equilibration time. For better legibility error bars ($\delta\text{wavenumber} = 0.12 \text{ cm}^{-1}$, $\delta\text{FWHM} = 0.2 \text{ cm}^{-1}$ and $\delta\text{amplitude} = 0.006$) are displayed only for the first data points taken at 20 $^{\circ}\text{C}$.

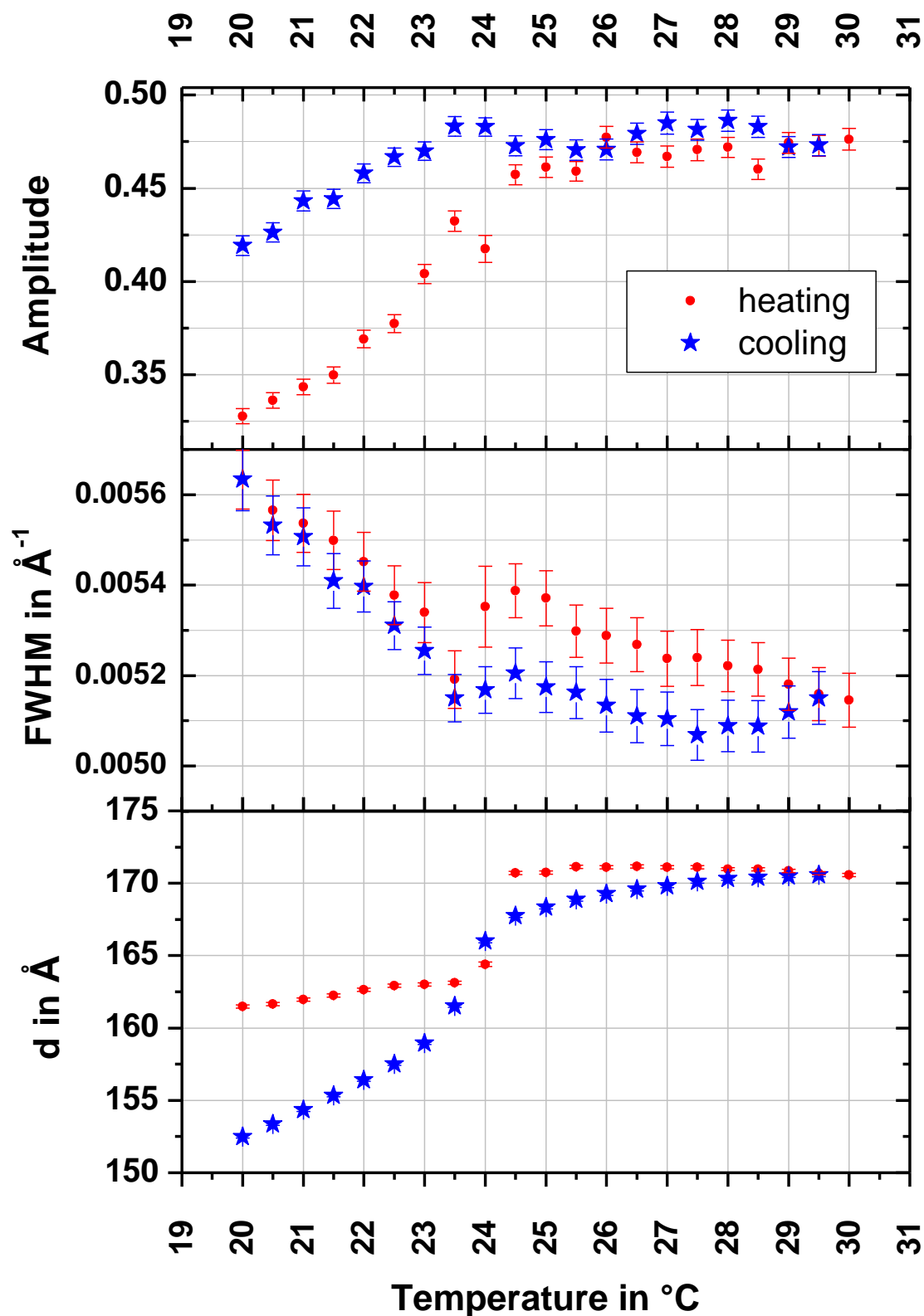


Figure 105: Neutron reflectivity results (meas. 2) of the heating and cooling cycle. Shown are results of Gaussian fits to the first order Bragg peak. Error bars are not shown, if smaller than the symbols.

6.8.2 Neutron reflectivity of a multilamellar lipid coating

In order to follow temperature-induced changes in structure and organization of the multilayer system, the neutron reflectivity of the solid-liquid interface was measured. With a selected chopper frequency of 45 Hz at BioRef, sample ATR5 was measured at 5 different angular positions θ to cover a Q-range from 0.005 \AA^{-1} to 0.200 \AA^{-1} in total. The resolution was set to a constant value of 7% over the Q-range probed. For each temperature step two complete reflectivity curves (meas. 1 and meas. 2) were recorded. The second measurement (meas. 2) was performed in order to distinguish between time dependent and temperature dependent effects. One measurement took 50 minutes of measurement time.

Results

In each reflectivity curve three Bragg peaks are clearly visible in the probed Q-range, which are the first, second and third order peak of the lamellar phase L_p (Figure 106). As in chapter 5.3.2, the analysis was focused on the first order Bragg peak, since position, height and width of the peak reveal the desired information about the lamellar structure of the multilayer system. Each peak was fitted by a Gaussian function. The resulting repeat distances, FWHM and amplitudes are displayed in Figure 105 on page 151.

The **heating** cycle shows three distinct regions: First, between 20.0°C and 23.5°C , the repeat distance d increases almost linearly from $(161.5 \pm 0.1) \text{ \AA}$ to $(163.1 \pm 0.1) \text{ \AA}$. In the same interval the FWHM decreases from $(0.0056 \pm 0.0001) \text{ \AA}^{-1}$ to $(0.0052 \pm 0.0001) \text{ \AA}^{-1}$ and the amplitude increases from 0.328 ± 0.004 to 0.432 ± 0.005 . Second, between 24.0°C and 24.5°C a *jump* in repeat distance occurs from $(164.4 \pm 0.2) \text{ \AA}$ to $(170.7 \pm 0.1) \text{ \AA}$. The FWHMs and amplitudes of the Bragg peaks do not show a similarly significant change in that temperature regime. In the third region, between 24.5°C and 30.0°C , the repeat distance is almost constant at a value of $(170.9 \pm 0.3) \text{ \AA}$. In addition, the FWHMs and amplitudes are almost constant within error.

Upon **cooling** the system from 30.0°C to 24.5°C the repeat distances fall below the corresponding repeat distances of the heating cycle for each temperature step. At 24°C the repeat distance is $(166.0 \pm 0.1) \text{ \AA}$. Again, the FWHMs and amplitudes are almost constant in this temperature region. However, the FWHMs are in general slightly smaller, as compared to the heating cycle. Between 23.5°C and 20°C the repeat distances decrease almost linear to a final value of $(152.5 \pm 0.1) \text{ \AA}$, which is 9 \AA smaller than the starting value. Also the FWHM

and amplitude show a linear behaviour: the FWHM increases to a final value of $(0.0056 \pm 0.007) \text{ \AA}^{-1}$ which is identical to the starting value. The amplitude decreases to a value of 0.419 ± 0.005 . In that temperature region the amplitudes are always higher, then the ones of the heating cycle. A discussion is given on page 154.

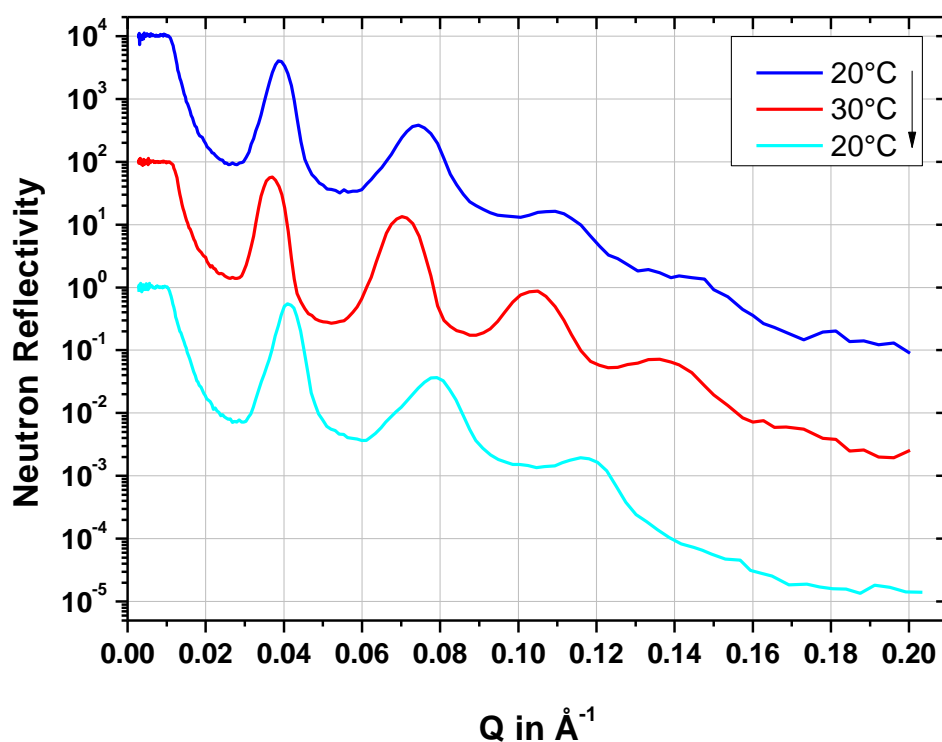


Figure 106: Neutron reflectivity (meas. 2) of a multilamellar lipid coating on a silicon substrate (ATR5) incubated in a solution of 3mg/mL HA in D_2O as a function of temperature and time.

6.8.3 Discussion

Already the first combined measurement at 20°C clearly shows the strong influence of HA on the DMPC lipid coating: Compared to the reference measurements (with $d \approx 65 \text{ \AA}$), conducted against pure D₂O, the repeat distance of $d = 161.5 \text{ \AA}$ is around 250 % higher (Figure 107). However, the broad peak shapes (Figure 106 on page 153) indicate that the system is not yet in its fully swollen and equilibrated state, despite the excessive temper protocol performed before the actual measurements. This might be due to the fact, that in contrast to an oligolamellar coating, the coating analyzed here is composed of a micrometer thick, multilamellar film. Therefore, more time might be needed, to swell the system to equilibrium and to transform all lipid lamellae into the L_p phase. However, higher order Bragg peaks are already clearly visible, indicating the presence of the L_p phase. Interestingly, non-swollen layers are no longer present or below the detection limit of the measurement, since no Bragg peak at $Q = 0.1 \text{ \AA}^{-1}$ appears.

Even though the structure of the coating is strongly affected by the presence of HA already at temperatures below T_m , the DMPC phase transition has a further impact on the temperature response of the system. In the reference system, the repeat distance of the multilamellar lipid coating against pure D₂O does not exhibit a drastic change between 24.0°C and 24.5°C, but started shrinking above 24.5°C (Figure 107, bottom). This decrease in d-spacing is due to chain melting of the lipid molecules in the L_α phase [36]. In contrast, the d-spacing of the system incubated in HA solution instantaneously increased by 4 % upon heating from 24.0°C to 24.5°C and stayed constant up to 30°C (Figure 107, top). This instantaneous change in d-spacing upon heating from 24.0°C to 24.5°C is directly correlated to the instantaneous change in wavenumber as measured by ATR-FTIR for the same temperature step (Figure 104 on page 150).

The performed measurements show that the phase transition temperature T_m between 24.0°C and 24.5°C does not change in the presence of HA, but structural changes upon crossing the phase transition are significantly different in the presence of HA. An increase in the partial specific volume of HA by of 4% in the temperature range from 25°C and 30°C was reported by Gómez-Alejandre et al. [152]. The origins of the additional swelling of the multilamellar lipid coating above T_m might be due to changes of the partial specific volume of HA. Here, the question remains open, how the main phase transition of the lipid molecules affects the conformation of HA.

Another reason for the additional swelling of the lipid coating might be due to a change in the electrostatic charge density of opposing membrane surfaces: Upon a better alignment of the lipid membranes in the L_α phase, as discussed in chapter 5.3.2 on page 102, the adsorbed and negatively charged HA molecules might follow this alignment and subsequently, the surface charge density might increase. This would result in an increase of repulsive electrostatic forces of opposing membranes and hence, an increase in d-spacing upon crossing the main phase transition.

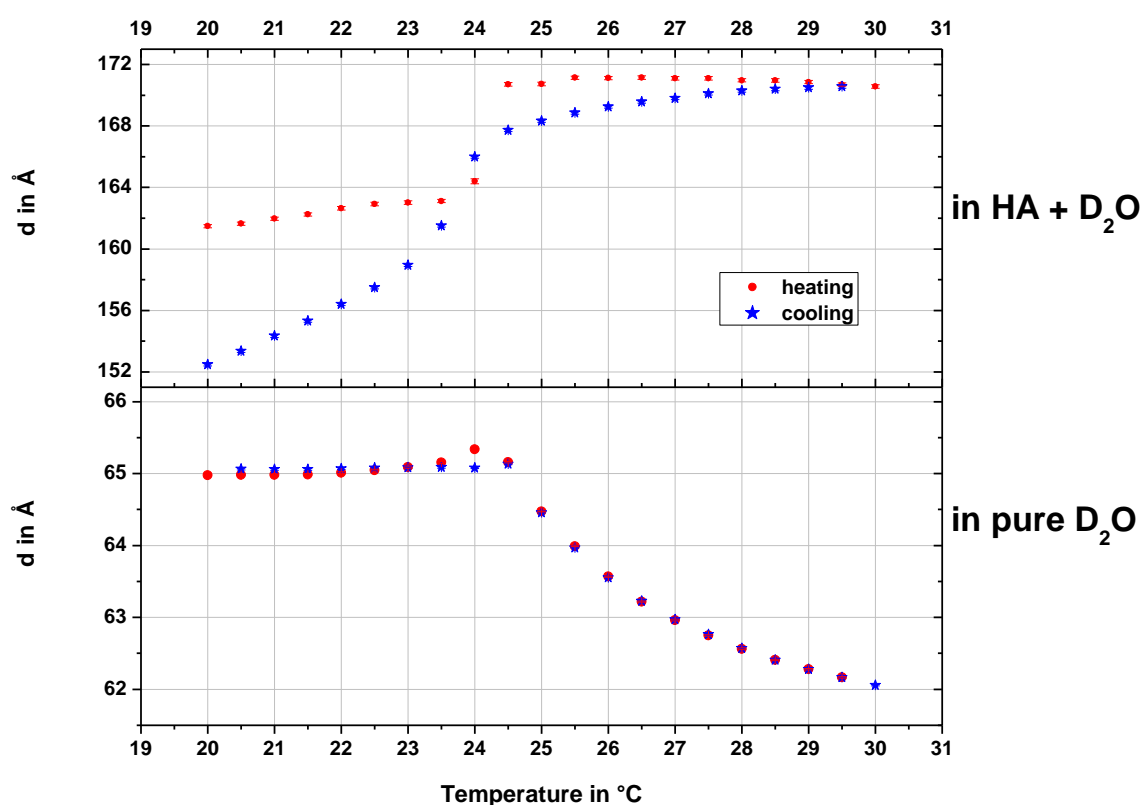


Figure 107: Neutron reflectivity results (meas. 2) for d-spacings as a function of temperature, calculated from the first order Bragg peak position. The Bragg peaks resulted from multilamellar lipid coatings on a silicon ATR substrate (ATR5) incubated in pure D₂O (bottom) or in a solution of 3 mg/ml HA in D₂O (top). Error bars are not shown, if smaller than the symbols.

6.9 Summary of chapter 6

Chapter 6 dealt with the investigation of solid-supported DMPC lipid membranes closer to physiological conditions i.e. incubated in solutions of hyaluronic acid (HA) in D₂O. The focus was on the interactions of DMPC with HA as probed by neutron reflectivity and ATR-FTIR as a function of the external control parameters temperature (T), pressure (p) and shear rate.

Reference infrared absorption spectra of DMPC, HA and mixtures of both were recorded in the ATR-FTIR mode and the absorption peaks were correlated to the vibrational modes of the molecules. An interaction between DMPC and HA was not detected with the experimental setup.

A pronounced impact of HA on the structure of DMPC layers was revealed by neutron reflectivity experiments. A tremendous swelling of the oligolamellar coatings took place with time over a period of several days. The final d-spacing of the lipid lamellae was about 4 times larger than the initial one. Besides the provoked swelling HA stabilized the lipid coating in its L_α phase so that no unbinding occurred in that case. The swollen lipid layer system was found to be stable against moderate applied shear (1 Hz). Increased shear load (4 Hz) induced unbinding of the lipid coating from support. Addition of NaCl to the incubating solution of HA in D₂O or application of elevated hydrostatic pressure suppressed swelling. The results were discussed in the context of classical DLVO theory including additional repulsive electrostatic contributions.

Combined NR and ATR-FTIR measurements on a DMPC multilayer coating revealed an additional and reversible increase in thickness of the coating upon crossing the main phase transition P_{β'}→L_α of the lipid system. Although the effect of HA on structure and stability of the interfacial lipid coatings was most pronounced, a direct interaction on the molecular scale of the molecules could not be traced. FTIR and DSC measurements documented undisturbed main phase transitions of the lipid assemblies with and without HA present.

7. Conclusions and Outlook

Oligolamellar lipid coatings were successfully prepared and structurally characterized by X-ray reflectometry in the dry state of the coating and by neutron reflectometry against different aqueous solutions for complementary *in-situ* measurements. The systems served as model lipid coatings for two purposes: 1) To study fundamental membrane principles and their structural organization and 2) to investigate more applied functionalities related to protection wear of artificial body implants and joint lubrication. The design and implementation of an external attenuated total reflection - Fourier transform infrared spectroscopy (ATR-FTIR) beam line in the BioRef neutron reflectometer, proved to be extremely supportive.

At first, the stability of solid-supported DMPC lipid membranes was investigated against pure D₂O (Figure 108). The coatings remained stable on their solid support in the ripple phase P_{β'} of the lipid molecules below the main phase transition. This could be shown for various environmental conditions such as increasing temperature, elevated hydrostatic pressure, application of external shear force, for silicon and titanium supports. By neutron reflectometry measurements on oligolamellar lipid stacks a profound reduction in stability for the liquid-like phase L_α of the lipid molecules was found. Upon heating above the main phase transition temperature all investigated oligolamellar lipid coatings unbound irreversibly from the solid support. In the vicinity of the main phase transition between the ripple phase P_{β'} and the liquid-like phase L_α drastic changes in neutron reflectivity and infrared absorption signals were also observed for multilamellar lipid coatings. The combined IR and neutron reflectivity measurements at BioRef revealed the appearance of an anomalous behaviour of the d-spacing upon approaching the main phase transition, independent of the lipid chain melting process. It is supposed, that a decrease in bending rigidity κ of the lipid membranes is the origin of the observed anomalous swelling.

At second, investigations of DMPC lipid membranes under physiological conditions close to that in knee joints have been performed. Here, the main interest was in the study of interactions between solid-supported lipid membranes and hyaluronic acid (HA), which is a main component of the synovial fluid in mammalian joints. A major impact of HA on the structure and stability of the lipid layers was observed (Figure 108). Their d-spacing

increased by a factor of four and the stability extended to physiological relevant temperatures. Furthermore, an increase in d-spacing was accompanied with a chain melting process upon crossing the main phase transition temperature ($P_{B^*} \rightarrow L_{\alpha}$).

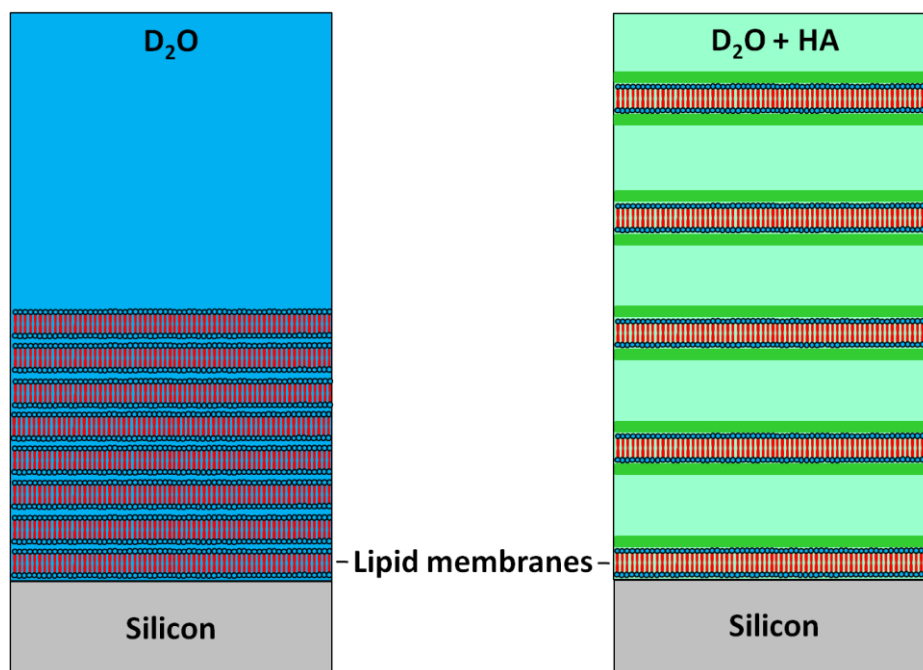


Figure 108: Model for oligolamellar lipid coatings on silicon in pure D_2O (left) and after incubation in a solution of HA in D_2O (right).

The impact of HA on DMPC lipid coatings could be suppressed by screening the electrostatic charges of HA with salt ions. The origin of the interactions between DMPC and HA was further elucidated by replacing HA with negatively or positively charged synthetic polyelectrolytes of different charge densities.

The observed stabilization of substrate-bound oligolamellar lipid layers by HA might contribute to lubrication in mammalian joints and the protection of cartilage by the formation of HA/DMPC hydrogel networks. A lamellar hydrogel phase in a system of polymers and lipid membranes has already been reported in literature [148], and it has also been shown that phospholipid vesicles in solutions containing HA build up network-like structures [10].

With the successful combination of ATR-FTIR and NR with BioRef at hand, further model systems for biological interfaces and processes, such as protein adsorption at model membranes, can now be investigated simultaneously with the two complementary methods.

Appendix A: Summary of the measured samples

Sample	coating type	instrument	d-spacing in Å		subject of investigation
@ 21 °C (P _β)					
(measured in pure D₂O, chapter 5)					
A	oligolamellar	V6	66.89	± 0.04	effect of temperature
B	oligolamellar	V6	73.36	± 0.11	effect of temperature
C	oligolamellar	V6	65.48	± 0.05	effect of temperature
D	multilamellar	V6	65.31	± 0.25	effect of temperature
E	oligolamellar	V6	65.20	± 0.30	effect of pressure
F	oligolamellar	AMOR	65.19	± 0.02	effect of shear
TiA	Ti + oligolamellar	V6	66.10	± 0.77	effect of substrate
TiB	Ti + oligolamellar	AMOR	68.03	± 0.13	effect of substrate/shear
ATR5	multilamellar	BioRef	64.10	± 0.01	combined IR and NR
(measured in a solution of 3 mg/mL HA in D₂O, chapter 6)					
1	oligolamellar	BioRef	66.22	± 0.06	effect of HA
2	oligolamellar	V6	65.52	± 0.14	effect of temperature
3	oligolamellar	V6	67.77	± 0.07	effect of NaCl
4	oligolamellar	AMOR	64.92	± 0.07	effect of shear
5	oligolamellar	AMOR	-	-	effect of shear
6	oligolamellar	V6	64.77	± 0.33	effect of pressure
ATR5	multilamellar	BioRef	-	-	combined IR and NR
			$\bar{d} = 66.35 \pm 2.31$		(± standard deviation)

Appendix B: Mechanical test of the pressure cell

The functional efficiency of the high pressure cell was verified in an independent experiment. The pressure cell for neutron reflectometry experiments was introduced in chapter 3.2.7 on page 51. The impact of external mechanical pressure was studied on a 60 mm needle of a syringe including its cover (Figure 109). During the experiment the needle was placed in the separation cell housing a steel piston on the side connected to the sample volume. When the pressure of 90 MPa was applied, the piston pressed against the needle. Strong deformations of the needle were observed after the experiment. The performed experiment demonstrated successfully the pressure build-up in the sample volume of the pressure cell.



Figure 109: Effect of pressure on a needle including its cover. The picture shows the needle before (A) and after (B) the exposure to 90 MPa along the longitudinal axis.

Appendix C: List of selected publications

Journals

Kreuzer, M., T. Kaltofen, R. Steitz, B.H. Zehnder, and R. Dahint, *Pressure cell for investigations of solid-liquid interfaces by neutron reflectivity*. Review of Scientific Instruments, 2011. 82(2): p. 023902-7 URL: <http://dx.doi.org/10.1063/1.3505797>.

Kreuzer, M., M. Strobl, M. Reinhardt, C. Hemmer, T. Hauß, R. Dahint, and R. Steitz, *Impact of a model synovial fluid on supported lipid membranes*. submitted to Biochimica et Biophysica Acta - Biomembranes, 2011.

Strobl, M., R. Steitz, M. Kreuzer, A. Nawara, F. Mezei, M. Rose, P. Amitesh, M. Grunze, and R. Dahint, *BioRef – a time-of-flight neutron reflectometer combined with in-situ infrared spectroscopy at the Helmholtz Centre Berlin*. Journal of Physics: Conference Series, 2010. 251(1): p. 012059 URL: <http://stacks.iop.org/1742-6596/251/i=1/a=012059>.

Strobl, M., R. Steitz, M. Kreuzer, M. Rose, H. Herrlich, F. Mezei, M. Grunze, and R. Dahint, *BioRef: A versatile time-of-flight reflectometer for soft matter applications at Helmholtz-Zentrum Berlin*. Review of Scientific Instruments, 2011. 82(5): p. 055101 URL: <http://dx.doi.org/10.1063/1.3581210>.

Paul, N., A. Paul, R. Steitz, M. Kreuzer, M. Lux-Steiner, *Selective Self Assembly of Neurotransmitter Molecules on Polyelectrolyte Multilayers*. submitted to Journal of Physical Chemistry, 2011.

Pictures

Kreuzer, M., *A fish-eye perspective of BioRef*. coverage of inside NMI3 by Integrated Infrastructure Initiative for Neutron Scattering and Muon Spectroscopy (NMI3), 2011(2) URL: www.nmi3.eu/news-and-media/newsletter-.html.

Conference contributions

Kreuzer, M., M. Strobl, M. Reinhardt, R. Dahint and R. Steitz

Stabilization of lipid multilayer systems by polysaccharides
at European Colloid and Interface Society (ECIS) in Berlin, Germany (2011)

Kreuzer, M., M. Strobl, M. Reinhardt, R. Dahint and R. Steitz

Incorporation of polysaccharides in lipid multilayer systems
at 5th European Conference on Neutron Scattering (ECNS) in Prague, Czech Republic (2011)

Kreuzer, M., M. Strobl, M. Reinhardt, R. Dahint and R. Steitz

The swelling/stability effect of hyaluron on a lipid multilayer system
at Deutsche Physikalische Gesellschaft (DPG) - Frühjahrstagung in Dresden, Germany
(2011)

Kreuzer, M., R. Dahint and R. Steitz

Oligolamellar Lipid Layers Under Load: A Model for Artificial Implants
at Deutsche Physikalische Gesellschaft (DPG) - Frühjahrstagung in Regensburg, Germany
(2010)

Kreuzer, M., R. Dahint and R. Steitz

Lubrication in model joints – a study on shear dependence
at Zsigmondy Kolloquium in Bayreuth, Germany (2009)

Kreuzer, M., T. Kaltofen, R. Dahint and R. Steitz

A Study of Shear Dependence on Lipid Layers
at Neutrons and X-rays meet biology workshop in Berlin, Germany (2009)

Kreuzer, M., T. Kaltofen, R. Dahint and R. Steitz

Lubrication in model joints – a study on shear dependence
at Deutsche Neutronenstreutagung in Munich, Germany (2008)

Table of Figures

Figure 1: Model for oligolamellar lipid coatings in pure D ₂ O (left) and after incubation in a solution of HA in D ₂ O (right).	7
Figure 2: Radiograph of a human knee joint (left) [14]. Schematic diagram (right), showing a close up of the opposing bones, covered with cartilage and lipid layers, separated by synovial fluid.....	14
Figure 3: Model systems: Lamellar lipid membranes as coatings on a silicon substrate, incubated in pure water as a reference (left) or incubated in a model synovial fluid, consisting of a solution of hyaluronic acid (HA) in water (right).	16
Figure 4: Sketch of a stack of lipid membranes (bilayers). A bilayer consists of hydrophobic lipid chains (d_{chains}) with hydrophilic lipid heads (d_{heads}) on either side. Neighbouring membranes are separated by an inter water layer (d_{solution}). The repeat distance (d) is measured by scattering experiments. The figure is inspired by [18].	17
Figure 5: Calorimetric melting profile of 1,2-dimyristoyl-sn-glycero-3-phosphocholine (DMPC) lipid vesicles in pure D ₂ O. The used calorimetric setup is described in chapter 3.2.1 (on page 24) and the measurement itself in chapter 6.2 on page 117. Inserted sketches, displaying the membrane structure, are from [34].	19
Figure 6: Schematic structure of 1,2-dimyristoyl-sn-glycero-3-phosphocholine (DMPC) taken from [51].	21
Figure 7: Schematic structure of hyaluronic acid (HA) from [62].	22
Figure 8: Schematic diagram of a differential scanning calorimetry (DSC) instrument.	25
Figure 9: Schematic diagram of a FTIR setup with a Michelson interferometer.....	28
Figure 10: Photograph of BioATR II setup for ATR-FTIR measurements.....	30
Figure 11: Scattering geometry at a smooth surface for $n_1 < n_2$	32
Figure 12: Theoretically calculated neutron reflectivity curves from a smooth interface between air (SLD = 0) and silicon (SLD = $2.07 \times 10^{-6} \text{ \AA}^{-1}$) as a function of Q (bottom abscissa) and in addition as a function of incident angle α_{in} with a neutron wavelength of $\lambda = 4.66 \text{ \AA}$ (top abscissa). The curve in black results from a scattering geometry where the neutron hit the surface from the air-side of the sample and in red from the silicon side. The green curve results from the reflectivity of a 150 Å thick polystyrene (SLD = $1.42 \times 10^{-6} \text{ \AA}^{-1}$) coating on a silicon substrate, illuminated from the silicon side. The scattering geometry is displayed in Figure 13.	37
Figure 13: Scattering geometry for thin films with $n_1 < n_2 < n_3$	38
Figure 14: Schematic diagram of the V6 instrument. A graphite monochromator is used to select a wavelength of $\lambda = 4.66 \text{ \AA}$. The angular resolution can be set by the slit system. The neutrons can be detected with several single counters or with a position sensitive detector (PSD).	43
Figure 15: Photograph with beam line scientists at the V6 instrument.	44
Figure 16: Schematic diagram of the V18 instrument (BioRef). A chopper system enables time-of-flight (TOF) measurements with variable wavelength resolutions. The slit system is set to corresponding values of	

angular resolutions. A wide range of angular sample positions can be obtained by using a goniometer, in order to cover a Q-range up to 0.4 \AA^{-1} in our case. Finally, the neutrons are detected with a position sensitive detector (PSD). [100]47

Figure 17: Top view of chopper SC2 at the V18 neutron beam line. On the left side is the chopper housing. The neutrons are incident from the right side through a neutron guide (dark green).47

Figure 18: Transmission of SC1: Wavelength dependent burst time $\tau(\lambda)$, normalized by the maximum burst time $\tau_0(\lambda_0)$, as a function of passing wavelength λ , normalized to λ_0 . Only for $\lambda \leq \lambda_0$ the wavelength resolution is constant (green line), while it is changing for $\lambda > \lambda_0$ (blue line). The third chopper, SC2, blocks wavelengths longer than λ_0 (black pattern) and in addition prevents overlapping of neutrons with very short and long wavelengths from neighbouring pulses (red pattern). The diagram is inspired by [95].48

Figure 19: Fisheye perspective of the V18 instrument in the neutron guide hall I of BER II at the Helmholtz-Zentrum Berlin with the sample position in the centre. The neutrons are incident through the chopper system from the right side and are recorded at the neutron detector on the left side. The IR setup is on the sample stage in the centre of the picture, with the IR spectrometer on top. [101]49

Figure 20: Schematic diagram of the shear setup for neutron reflectivity measurements.50

Figure 21: Photograph of the shear setup. [102]50

Figure 22: Schematic diagram of the pressure cell for neutron reflectivity measurements. A piston separates the sample solution from the hydraulic fluid.51

Figure 23: Schematic diagram of the spin-coating technique.52

Figure 24: X-ray (XR) reflectivity of spin-coated silicon wafers, measured in air. As a coating solution the lipid molecule DMPC was solved in chloroform in different concentrations $c(\text{DMPC})$53

Figure 25: Resulting number of lipid bilayers N_{BK} on a spin-coated silicon wafer. N_{BK} was calculated by using the values of the Bragg peak position (B) and the Kiessig oscillations (K). Solutions with different DMPC concentrations $c(\text{DMPC})$ in chloroform were used as coating solution. The red line represents a fit of a second order polynomial function to the data points.53

Figure 26: Schematic diagram of the air-brush technique.54

Figure 27: X-ray reflectivity of DMPC lipid coated silicon wafers. The coatings were achieved by two different techniques: Spin-coating a solution of 10 mg/mL DMPC in chloroform (green) or by the air-brush technique. The inset shows a magnification of the low Q-region.55

Figure 28: Scans around the first Bragg peak position with a fixed detector position (rocking scan). Both curves are normalized to measurement time (40 sec/point) and to incident intensity I_0 . The minor differences in maximum positions are probably due to differences in temperature and humidity during the measurements.55

Figure 29: Picture with an overview of the infrared setup: A spectrometer mounted to an item holder (item Industrietechnik GmbH, Germany) above the sample position.56

Figure 30: Sketches of the integrative silicon substrate ATR13 for combined infrared (IR) spectroscopy and neutron reflectivity measurements at BioRef. Left: ATR13 in the horizontal position with a sketched IR

beam in magenta. Right: ATR13 in a vertical position with the IR beam shown in the realistic position for a combined measurement, passing through the centre of the substrate. The neutron beam is sketched in green.57

Figure 31: Design drawing of the sample cell for combined infrared and neutron reflectivity measurements at a solid-liquid interface. The top aluminium plate is not shown. The silicon ATR substrate is marked transparent.59

Figure 32: Photograph of the sample cell connected to an external water bath.59

Figure 33: External beam pathway with sample cell (centre) on a translation table (right side) and a nitrogen cooled mercury cadmium telluride detector in dark red (left side) 60

Figure 34: Side view (left picture) and front view (right picture) of IR guide system, with the IR beam in violet. The lenses (green) are gold-coated and have focal lengths of $f_1 = f_2 = 400$ mm and $f_3 = 43$ mm, respectively. The lens f_1 focuses the beam on the sample and f_2 reconstitutes a parallel beam after being transmitted through the sample. The lens f_3 focuses the beam on the detector plate.61

Figure 35: Infrared (IR) setup on the neutron reflectivity (NR) sample stage at the V18 beam line at Helmholtz-Zentrum Berlin. The red spot marks the sample position.62

Figure 36: Schematic diagram of the used infrared beam geometry (red), with the two focusing lenses f_1 and f_2 , in order to measure an absorbance spectrum of the silicon ATR crystal (ATR8). For the reference signal I_0 , a polished silicon wafer was used to provoke a single “external” reflection, without ATR crystal in the beam path, followed by a measurement of the sample signal intensity I in ATR geometry. Here, all infrared light is guided through the ATR crystal, resulting in nine internal reflections..... 64

Figure 37: Infrared signals measured at the BioRef setup: First, by using a polished silicon wafer to provoke a single “external” reflection (blue line) yielding a reference signal I_0 , and second, by guiding the infrared beam through a silicon ATR crystal (black line), as a sample measurement I . The resulting absorbance spectrum of the silicon ATR crystal, calculated by Equation 3.8 (on page 28), is shown in the bottom graph (green line). The silicon crystal does not absorb between 6000 cm^{-1} and 1500 cm^{-1} . For wavenumbers smaller than 1500 cm^{-1} , the intensity drops drastically due to the high photon absorption cross section of silicon in this wavenumber range. The infrared beam geometries are illustrated in Figure 36 and described in the text..... 64

Figure 38: Model for an oligolamellar lipid coating in excess D_2O on a silicon substrate. The individual layers are described in the text on page 67. [109] 66

Figure 39: Simulated neutron reflectivity curves according to the model of a multi-layered lipid coating on a silicon substrate in excess D_2O . The first curve in the very front with a number of $N = 0$ bilayers represents the Fresnel reflectivity of the uncoated silicon substrate..... 68

Figure 40: Exemplary Gaussian fit (red line) to the Bragg peak (black squares) simulated with $N = 10$ bilayers at $Q_B = (0.0966 \pm 0.0001)\text{ \AA}^{-1}$ with $\text{FWHM} = (0.0080 \pm 0.0003)\text{ \AA}^{-1}$ and an area of $(0.60 \pm 0.03) \times 10^{-4}\text{ \AA}^{-1}$. 69

Figure 41: Blue points indicate the FWHM derived from a Gaussian fit to the Bragg peak at $Q = 0.1\text{ \AA}^{-1}$. The green line is guide to the eye calculated by $y = K*(Q/N)$ according to Equation 3.37. 70

Figure 42: Red points represent the area of a Gaussian fit to the Bragg peak at $Q = 0.1\text{ \AA}^{-1}$. The green line is

guide to the eye.70

Figure 43: Calculated number of bilayers N_{FWHM} according to Equation 3.37 for the blue points and according N_{area} according to Equation 3.39 for the red points with the constant $\sigma = 6.9 \times 10^{-5}$. The green line is guide to the eye with calculated $N =$ given N70

Figure 44: Neutron reflectivity of lipid-coated silicon substrates incubated in pure D_2O at 21 °C. The curves are shifted along the vertical axis for clarity.73

Figure 45: Neutron reflectivity after crossing the phase transition. The curves are shifted along the vertical axis for clarity.73

Figure 46: Number of bilayers (N_{FWHM}) as a function of temperature. For each temperature two measurements were performed. While for the oligolamellar coatings (sample A, B and C) an unbinding process starts for $T > 24$ °C, the number of coherent scattering domains increases for the multilamellar cast film (sample D).73

Figure 47: Neutron reflectivity profiles at different temperatures for sample A, B and D incubated in pure D_2O . At each temperature two measurements were performed.74

Figure 48: Neutron reflectivity profiles at different temperatures of Sample C, incubated in pure D_2O . At each temperature step two measurements were performed.75

Figure 49: Neutron reflectivity of a lipid coated silicon substrate (sample C) against excess D_2O . [109]76

Figure 50: Scattering length density profiles across the solid-liquid interface of a lipid coated silicon substrate (sample C) against excess D_2O corresponding to the fits in Figure 49. Upon increasing temperature the lipid bilayer unbind from the solid support. All values are listed in Table 5.2 on page 77.76

Figure 51: Bragg peak analysis for sample C. The red lines are guides to the eye, showing the average slope for the amplitude and the average values for FWHM and d , for the temperature range between 21°C and 23°C. At 25°C a drastic change in all three parameters is clearly visible.78

Figure 52: Calculated number of lipid bilayers N by using amplitude (blue points) or FWHM (green points) of Gaussian fits to the first Bragg peak. The red stars show values for a best fit by using the optical matrix approach and the Parratt software package79

Figure 53: Neutron reflectivity curves (symbols) of an oligolamellar lipid coating on silicon (sample E), measured against pure D_2O . Solid lines are Parratt fits to the data, with corresponding SLD profiles shown in Figure 54. [96]81

Figure 54: Scattering length density (SLD) profiles perpendicular to the solid-liquid interface, corresponding to the fits in Figure 53. [96]82

Figure 55: Phase diagram of DMPC with a summary of the experimental findings. The red line indicates the main phase transition for the bulk system, taken from [111]. One experimental cycle was performed along the arrows starting at 0.1 MPa and 20 °C. All three measurements in the ripple phase $P_{\beta'}$ revealed a repeat distance of 65 Å. After crossing the phase transition at 38 °C unbinding of lipids occurred (stars). [96]82

Figure 56: Close-up region of the critical momentum transfer Q_c on a linear scale. The total reflection edge

shifts to higher Q-values with increasing pressure. [96]84

Figure 57: Neutron reflectivity curves of an oligolamellar lipid coating on silicon (sample F) in excess D₂O. After the first two measurements at 21 °C a shear force was applied with a frequency of 5 Hz. Subsequently the temperature was increased up to 30 °C. At each temperature step two reflectivity measurements were made.....86

Figure 58: Results of the Bragg peak analysis of the first order Bragg peaks, displayed in Figure 57.87

Figure 59: X-ray reflectivity measurement of sample TiA, TiB and TiC, before lipid coating, in order to characterize the titanium layers on the silicon substrates. The Kiessig oscillations revealed a d-spacing of $t = (148 \pm 4) \text{ \AA}$. The Bragg peaks with unknown origin at $Q_B = (1.0241 \pm 0.0002) \text{ \AA}^{-1}$ appeared only for TiA and TiB, but not for TiC.....89

Figure 60: Neutron reflectivity of sample TiA in excess D₂O at elevated temperatures.89

Figure 61: Neutron reflectivity profiles of sample TiA in excess D₂O, measured in the temperature range between 20 °C and 30 °C. At each temperature step two measurements were performed.90

Figure 62: Neutron reflectivity of sample TiB at elevated temperatures, measured with the shear setup. As opposed to sample TiA, sample TiB was sheared at 5 Hz during the increase in temperature.91

Figure 63: Neutron reflectivity curves of sample TiB, measured in the shear setup at elevated temperatures. All plots illustrated with a blue border are measured under a constant shear force at a frequency of 5 Hz.91

Figure 64: Bragg peak analysis of sample TiB.92

Figure 65: Sketch of the unbinding process of a lipid coating from a silicon substrate in excess D₂O by vesicle formation.95

Figure 66: Comparison of all measured first order Bragg peak amplitudes as a function of temperature. Taking the amplitude as a measure for the number of solid-bound lipid layers, the graph shows clearly that all oligolamellar lipid coatings unbind from the substrate: Without shear between 24 °C and 26 °C (Sample A, B, C), with shear between 26 °C and 28 °C (Sample F and TiB). The oligolamellar coating of sample TiA was not stable, in strong contrast to sample D, for which the multilamellar coating remained bound to the substrate over the measured temperature and time range.....96

Figure 67: Infrared absorption of a multilamellar lipid coating on a silicon substrate (ATR5) against pure D₂O. Shown is the absorbance of the CH₂ groups, measured after 80 minutes of equilibration time. Temperature was cycled from 20 °C to 30 °C to 20 °C and back to 30 °C.99

Figure 68: Infrared absorption band analysis by fitting Gaussian profiles to the $\nu_s(\text{CH}_2)$ absorption band. Shown are the results of measurements, performed after 80 minutes of equilibration time. For legibility, error bars are displayed only for the first data point taken at 20 °C ($\delta\text{wavenumber} = 0.12 \text{ cm}^{-1}$, $\delta\text{FWHM} = 0.12 \text{ cm}^{-1}$ and $\delta\text{amplitude} = 0.011$).100

Figure 69: Neutron reflectivity results (meas. 2) of the Bragg peak analysis of the first order Bragg peak at $Q \approx 0.1 \text{ \AA}$. Error bars are not shown, if smaller than the symbols.101

Figure 70: Neutron reflectivity resulting from a multilamellar lipid coating in excess D₂O. Shown are the first order Bragg peaks of the second measurements of all four temperature cycles between 20 °C and 30 °C.

.....	102
Figure 71: Neutron reflectivity (meas.2) of a multilamellar lipid coating on a silicon substrate (ATR5) against pure D ₂ O. Temperature was cycled from 20 °C to 30 °C to 20 °C and back to 30 °C.....	103
Figure 72: Ratio between <i>amplitude</i> and <i>1FWHM</i> as a function of temperature.	105
Figure 73: The d-spacings for the cycle cooling1. Displayed are the values for both measurements (meas. 1 and meas. 2) measured with a time difference of 50 min.	106
Figure 74: Measurements at BioRef comprise structural orders on different length scales. While the lamellar lipid order on the mesoscopic scale is probed by neutron reflectivity, the lipid chain order on the molecular length scale is probed by infrared spectroscopy.	107
Figure 75: Comparison between neutron reflectivity (NR) and infrared absorption (IR) data. Shown are the Bragg peak amplitude from NR (green) and the absorption amplitude from IR (red). While the NR amplitude is proportional to the lipid bilayer order, the IR amplitude is proportional to the chain order of the individual lipid molecules. The signals show inverse behaviour. The values for the IR amplitude are within an uncertainty of ± 0.011 , as is illustrated for the first point only. The uncertainties of the NR amplitudes are smaller than the symbols.	109
Figure 76: Comparison between neutron reflectivity (bottom) and infrared spectroscopy (top) data. Shown are the d-spacings (bottom) of a multilamellar lipid coating on silicon support and the corresponding wavenumbers (top) of the $\nu_s(\text{CH}_2)$ absorption band. The temperature range between 20 °C and 30 °C was investigated in four successive temperature cycles. The values for the wavenumbers are within an uncertainty of $\pm 0.12 \text{ cm}^{-1}$, as is illustrated for the first point only. The uncertainties of the d-spacings are smaller than the symbols.	109
Figure 77: Infrared absorbance spectra of DMPC (top), HA (middle) and a mixture (bottom) of DMPC:HA (1:1), measured at 20 °C in ambient humidity. Spectra of the clean sample cell were used as reference spectra. An analysis of the spectra is shown in.....	115
Figure 78: Infrared absorbance spectra of mixtures of DMPC and HA at different ratios. The black lines correspond to the absorption of the dried components, while the blue lines show the absorption, after the samples were hydrated with 20 μl of pure D ₂ O. The labels of the absorption bands in the top plot correspond to lipid absorption bands (characters) and HA absorption bands (numbers).The decreasing absorption of HA with decreasing concentration can be best followed at the marked positions (green line).	115
Figure 79: Differential scanning calorimetry data of 2.5 mg/mL DMPC dissolved in pure D ₂ O (light blue and dark blue line) or in a solution of 3 mg/mL HA in D ₂ O (black and red line).Shown are first and fourth scan of the measurements.	117
Figure 80: Neutron reflectivity curves of an oligolamellar lipid coating on silicon (sample 1) incubated in a solution of HA in D ₂ O. The figure shows the first (black) and the last (red) reflectivity curve of a series of measurements performed after the sample was incubated in the solution. The Bragg peak positions of the two different lamellar phases are highlighted in grey: Q_{P1} and Q_{P2} indicate the first and second order Bragg peak of the new lamellar phase L_p . The peak at Q_1 refers to the lamellar phase P_β of fully	

hydrated DMPC 120

Figure 81: A series of neutron reflectivity curves of the oligolamellar lipid coating on silicon, sample 1, incubated in a solution of HA in D₂O as a function of incubation time. [109] 120

Figure 82: Neutron reflectivity (R) of the Bragg peak at Q₁ normalized to the Fresnel reflectivity (R_{Fresnel}) of the planar silicon substrate (sample 1). The peak vanishes with increasing time. 121

Figure 83: Neutron reflectivity (R) of the Bragg peak at Q_{p1} normalized to the Fresnel reflectivity (R_{Fresnel}) of the planar silicon substrate (sample 1). The peak becomes more and more pronounced with increasing time..... 121

Figure 84: (top) Integrated Bragg peak area A₁ of the peak at Q₁ and the sum (A_{p1}+A_{p2}) of the Bragg peak areas of the peaks at Q_{p1} and Q_{p2}. (bottom) The total sum of A₁, A_{p1} and A_{p2} is constant with time. [109] 122

Figure 85: d-spacings resulting from Gaussian profiles fitted to the first order Bragg peaks of the L_p phase (black points). After 19 h a linear regime with a slope of 0.23 ± 0.01 Å/h is reached (red line). 122

Figure 86: Neutron reflectivity of the oligolamellar lipid coating on a silicon substrate (sample 2), incubated in a solution of 3 mg/mL HA in D₂O as a function of incubation time and temperature. For clarity the plots are shifted vertically. 123

Figure 87: Model of a fully swollen, oligolamellar lipid coating on a silicon substrate, incubated in a solution of HA in D₂O. Silicon was used as a solid support, covered with a layer of silicon oxide (0). An oligolamellar lipid coating was modelled by subdividing the system into three parts: First, an inner lamella (1) is directly attached to the silicon oxide layer. The inner lamella is followed by several core lamellae (2), which have the same d and SLD. Finally, this stack of layers is covered by a terminal lamella, the outer lamella (3). Each lipid lamella is represented by a layer of hydrophobic lipid chains (5) with a hydrophilic head group layer at each side (6). Two neighbouring lamellae are separated by a solution interlayer (4). In addition, a HA layer (7) is attached to the outer surfaces of each membrane. Thickness and SLD of each layer were subject to fitting. [109]..... 125

Figure 88: Neutron reflectivity of the oligolamellar lipid coating on a silicon substrate (sample 2) incubated for 43 days (1032 h) in a solution of 3 mg/mL HA in D₂O and measured at 39 °C. Bragg peaks are caused by a lamellar repeat distance of d_p = (247 ± 1) Å. Solid line: Fit to the data. Parameters are listed in Table 6.2. [109]..... 126

Figure 89: Scattering length density (SLD) plotted versus distance from the silicon substrate, z, of sample 2. The measurement was performed at 39 °C in a solution of 3 mg/mL HA in D₂O after 43 days (1032 h) of incubation. The plot is the real space representation of the fit in Figure 88. The parameters are listed in Table 6.2 [109]..... 126

Figure 90: Scattering length density profiles resulting from a Fourier analysis of the measured Bragg peaks S_{exp}(z)(red line, left abscissa) and from theoretical considerations S_{theo}(z) (blue line, left abscissa), the later including only pure D₂O. The difference profile is shown in green (right abscissa).[109] 129

Figure 91: Bridging (1) and looping (2) conformation of a polymer chain, anchored in two opposing lipid membranes. The sketch is inspired by [148] and already published in [109]. 132

Figure 92: Neutron reflectivity curves of an oligolamellar lipid coating on silicon (sample 3), incubated in a solution of 3 mg/mL HA in D ₂ O, with 1 M NaCl added to the solution.	135
Figure 93: Neutron reflectivity measurements of sample 4 in the shear setup. A silicon substrate with an oligolamellar lipid coating was incubated in a solution of 3 mg/mL HA in D ₂ O. From top to bottom the curves are displayed with increasing incubation time. Temperature was increased from 21 °C to 39 °C after 8.5 h of incubation. In addition, after the transformation of the lipid coating in a HA rich L _p phase (43 h), an external shear was applied. For clarity, the reflectivity curves are shifted vertically.	138
Figure 94: First order Bragg peak amplitudes of sample 4, measured after different times of incubation in a solution of 3 mg/mL HA in D ₂ O and at different shear rates. Upon application of a shear frequency of 4 Hz, the amplitude drops drastically. The corresponding reflectivity curves are shown in Figure 93.	138
Figure 95: Neutron reflectivity curves of sample 5: An oligolamellar lipid coating on a silicon substrate, incubated in a solution of 3 mg/mL HA in D ₂ O as a function of incubation time, temperature and subsequent shear load.	139
Figure 96: Neutron reflectivity curves of the oligolamellar lipid coating, sample 6, on silicon, measured against a solution of HA in D ₂ O. After crossing the phase transition by releasing the pressure from 90 MPa to 45 MPa at 38 °C a pronounced shift of the first Bragg peak to lower Q-values occurred. The incubation times are shown in brackets. For clarity the curves are shifted vertically.	141
Figure 97: Time dependent neutron reflectivity curves of the oligolamellar lipid coating, sample 6, on silicon, measured against a solution of HA in D ₂ O at 45 MPa and 38 °C. A measurement of the displayed Q-range took 1.2 h and was repeated until 46 h after releasing the pressure from 90 MPa to 45 MPa. A pronounced shift of the first and second Bragg peak to lower Q-values occurred with time.	142
Figure 98: Bragg peak analysis of the first order Bragg peak after releasing the pressure to 45 MPa at 38 °C. The red line represents a linear fit with a slope of $0.390 \pm 0.003 \text{ \AA /h}$. The Bragg peaks are shown in Figure 97.	142
Figure 99: Phase diagram of bulk DMPC lyotropic phases with the performed experimental cycle. The repeat distances shown were measured against a solution of 3 mg/mL HA in D ₂ O. After crossing the phase boundary for fully hydrated DMPC bulk phases at 69 MPa and 38 °C (red line, from [111]) by pressure release, a pronounced swelling occurred from 65 Å to a final value of 190 Å.	143
Figure 100: The reflectivity curve of sample 6 (bottom graph, green line), measured 11 days of incubation in a solution of 3 mg/mL HA in D ₂ O, was approximated by a superposition (bottom graph, black line) of 11 simulated reflectivity curves (top graph). For the simulated reflectivity curves solution interlayer thicknesses d_{solution} between 100 Å (top graph, blue line) and 150 Å (top graph, purple line) were used with different proportions in order to result in the best approximation.	144
Figure 101: Used fractions for a superposition of simulated reflectivity curves with different solution interlayer thicknesses d_{solution}	145
Figure 102: Comparison of d-spacings in HA solutions as a function of incubation time for sample 1, measured at 0.1 MPa and 21 °C (from chapter 6.3 on page 122), and sample 6, measured at 45 MPa and 38 °C. For comparison, the d-spacing for sample 6, measured at 38 °C after pressure reduction to	

0.1 MPa is shown. The error bars are smaller than the symbols. 146

Figure 103: Infrared absorption of a multilamellar lipid coating on a silicon substrate (ATR5) incubated in a solution of 3 mg/mL HA in D₂O. Shown is the absorbance of the CH₂ groups at elevated temperatures, measured after 80 minutes of equilibration time. Temperature was cycled from 20 °C to 30 °C and back to 20 °C. 149

Figure 104: Infrared absorption band analysis by fitting Gaussian profiles to the $\nu_s(\text{CH}_2)$ absorption band of a multilamellar DMPC lipid coating on silicon (ATR5) in comparison against pure D₂O (grey symbols, from Figure 68 on page 100) or incubated in a solution of 3 mg/mL HA in D₂O (red and blue symbols). The shown results are measured after 80 minutes of equilibration time. For better legibility error bars ($\delta\text{wavenumber} = 0.12 \text{ cm}^{-1}$, $\delta\text{FWHM} = 0.2 \text{ cm}^{-1}$ and $\delta\text{amplitude} = 0.006$) are displayed only for the first data points taken at 20 °C. 150

Figure 105: Neutron reflectivity results (meas. 2) of the heating and cooling cycle. Shown are results of Gaussian fits to the first order Bragg peak. Error bars are not shown, if smaller than the symbols. 151

Figure 106: Neutron reflectivity (meas. 2) of a multilamellar lipid coating on a silicon substrate (ATR5) incubated in a solution of 3mg/mL HA in D₂O as a function of temperature and time. 153

Figure 107: Neutron reflectivity results (meas. 2) for d-spacings as a function of temperature, calculated from the first order Bragg peak position. The Bragg peaks resulted from multilamellar lipid coatings on a silicon ATR substrate (ATR5) incubated in pure D₂O (bottom) or in a solution of 3 mg/ml HA in D₂O (top). Error bars are not shown, if smaller than the symbols. 155

Figure 108: Model for oligolamellar lipid coatings on silicon in pure D₂O (left) and after incubation in a solution of HA in D₂O (right). 159

Figure 109: Effect of pressure on a needle including its cover. The picture shows the needle before (A) and after (B) the exposure to 90 MPa along the longitudinal axis. 161

References

1. **Roach, H.I., T. Aigner, S. Soder, J. Haaq, and H. Welkerling**, *Pathobiology of osteoarthritis: pathomechanisms and potential therapeutic targets*. Current Drug Targets, 2007. 8(2): p. 271-82 URL: <http://www.ncbi.nlm.nih.gov/pubmed/17305505>.
2. **Bronner, F. and M.C. Farach-Carson**, eds. *Bone and Osteoarthritis*. 1st ed. Topics in Bone Biology. Vol. 4. 2008, Springer: London. 218.URL: <http://dx.doi.org/10.1007/978-1-84628-701-5>.
3. **Aigner, T., A. Sachse, P.M. Gebhard, and H.I. Roach**, *Osteoarthritis: Pathobiology—targets and ways for therapeutic intervention*. Advanced Drug Delivery Reviews, 2006. 58(2): p. 128-149 URL: <http://dx.doi.org/10.1016/j.addr.2006.01.020>.
4. **Hills, B.A.**, *Graphite-like lubrication of mesothelium by oligolamellar pleural surfactant*. Journal of Applied Physiology, 1992. 73(3): p. 1034-9 URL: <http://jap.physiology.org/content/73/3/1034.long>.
5. **Hills, B.A.**, *Oligolamellar lubrication of joints by surface-active phospholipids*. Journal of Rheumatology, 1989. 16(1): p. 82-91 URL: <http://www.ncbi.nlm.nih.gov/pubmed/2716011>.
6. **Benz, M., N. Chen, and J. Israelachvili**, *Lubrication and wear properties of grafted polyelectrolytes, hyaluronan and hylan, measured in the surface forces apparatus*. Journal of Biomedical Materials Research Part A, 2004. 71A(1): p. 6-15 URL: <http://dx.doi.org/10.1002/jbm.a.30123>.
7. **Longaker, M.T., N. Scott Adzick, J.L. Hall, S.E. Stair, T.M. Crombleholme, B.W. Duncan, S.M. Bradley, M.R. Harrison, and R. Stern**, *Studies in fetal wound healing, VII. Fetal wound healing may be modulated by hyaluronic acid stimulating activity in amniotic fluid*. Journal of Pediatric Surgery, 1990. 25(4): p. 430-433 URL: [http://dx.doi.org/10.1016/0022-3468\(90\)90387-o](http://dx.doi.org/10.1016/0022-3468(90)90387-o).
8. **Toole, B.P.**, *Hyaluronan promotes the malignant phenotype*. Glycobiology, 2002. 12(3): p. 37R-42R URL: <http://glycob.oxfordjournals.org/content/12/3/37R.abstract>.
9. **Greene, G.W., X. Banquy, D.W. Lee, D.D. Lowrey, J. Yu, and J.N. Israelachvili**, *Adaptive mechanically controlled lubrication mechanism found in articular joints*. Proceedings of the National Academy of Sciences, 2011. 108(13): p. 5255-5259 URL: <http://dx.doi.org/10.1073/pnas.1101002108>.

10. **Pasquali-Ronchetti, I., D. Quaglino, G. Mori, B. Bacchelli, and P. Ghosh,** *Hyaluronan-Phospholipid Interactions*. Journal of Structural Biology, 1997. 120(1): p. 1-10 URL: <http://dx.doi.org/10.1006/jsbi.1997.3908>.
11. **Kawano, T., H. Miura, T. Mawatari, T. Moro-Oka, Y. Nakanishi, H. Higaki, and Y. Iwamoto,** *Mechanical effects of the intraarticular administration of high molecular weight hyaluronic acid plus phospholipid on synovial joint lubrication and prevention of articular cartilage degeneration in experimental osteoarthritis*. Arthritis & Rheumatism, 2003. 48(7): p. 1923-1929 URL: <http://dx.doi.org/10.1002/art.11172>.
12. **Hills, B.A.,** *Boundary lubrication in vivo*. Proceedings of the Institution of Mechanical Engineers, Part H: Journal of Engineering in Medicine, 2000. 214(1): p. 83-94 URL: <http://pih.sagepub.com/content/214/1/83.abstract>.
13. **Forsey, R.W., J. Fisher, J. Thompson, M.H. Stone, C. Bell, and E. Ingham,** *The effect of hyaluronic acid and phospholipid based lubricants on friction within a human cartilage damage model*. Biomaterials, 2006. 27(26): p. 4581-4590 URL: <http://dx.doi.org/10.1016/j.biomaterials.2006.04.018>.
14. **Konink, S.d.,** *Front side of the left knee*. 2011.
15. **Scholes, S.C., A. Unsworth, and E. Jones,** *Polyurethane unicondylar knee prostheses: simulator wear tests and lubrication studies*. Physics in Medicine and Biology, 2007. 52(1): p. 197 URL: <http://stacks.iop.org/0031-9155/52/i=1/a=013>.
16. **Willumeit, R., A. Schuster, P. Iliev, S. Linser, and F. Feyerabend,** *Phospholipids as implant coatings*. Journal of Materials Science: Materials in Medicine, 2007. 18(2): p. 367-380 URL: <http://dx.doi.org/10.1007/s10856-006-0702-9>.
17. **Chandler, D.,** *Interfaces and the driving force of hydrophobic assembly*. Nature, 2005. 437(7059): p. 640-647 URL: <http://dx.doi.org/10.1038/nature04162>.
18. **Nagle, J.F., H.I. Petrache, N. Gouliaev, S. Tristram-Nagle, Y. Liu, R.M. Suter, and K. Gawrisch,** *Multiple mechanisms for critical behavior in the biologically relevant phase of lecithin bilayers*. Physical Review E, 1998. 58(6): p. 7769 URL: <http://link.aps.org/doi/10.1103/PhysRevE.58.7769>.
19. **Gaines Jr, G.L.,** *On the history of Langmuir-Blodgett films*. Thin Solid Films, 1983. 99(1-3): p. ix-xiii URL: [http://dx.doi.org/10.1016/0040-6090\(83\)90351-6](http://dx.doi.org/10.1016/0040-6090(83)90351-6).
20. **Derjaguin, B.,** *On the repulsive forces between charged colloid particles and on the theory of slow coagulation and stability of lyophobic sols*. Transactions of the Faraday Society, 1940. 35: p. 203-215 URL: <http://dx.doi.org/10.1039/TF9403500203>.
21. **Verwey, E. and J. Overbeek,** *Theorie der Stabilität lyophober Kolloide*. Colloid and

- Polymer Science, 1955. 141(1): p. 44-45 URL: <http://dx.doi.org/10.1007/BF01511752>.
22. **Deme, B., M. Dubois, T. Zemb, and B. Cabane**, *Effect of carbohydrates on the swelling of a lyotropic lamellar phase*. Journal of Physical Chemistry, 1996. 100(9): p. 3828-3838 URL: <http://dx.doi.org/10.1021/jp952179j>.
 23. **Israelachvili, J.N. and H. Wennerstrom**, *Entropic forces between amphiphilic surfaces in liquids*. Journal of Physical Chemistry, 1992. 96(2): p. 520-531 URL: <http://dx.doi.org/10.1021/j100181a007>.
 24. **Ohshima, H. and T. Mitsui**, *A theory of the effects of calcium ions on the lamellar phase of dipalmitoyl lecithin*. Journal of Colloid and Interface Science, 1978. 63(3): p. 525-537 URL: [http://dx.doi.org/10.1016/s0021-9797\(78\)80012-5](http://dx.doi.org/10.1016/s0021-9797(78)80012-5).
 25. **Tanaka, M., E. Schneck, H.Y. Yoshikawa, and F.F. Rossetti**, *Physical Chemistry of Biological Interfaces: Generic and Specific Roles of Soft Interlayers*. Chemistry – An Asian Journal, 2011. 6(7): p. 1728-1738 URL: <http://dx.doi.org/10.1002/asia.201100112>.
 26. **Inoko, Y., T. Yamaguchi, K. Furuya, and T. Mitsui**, *Effects of cations on dipalmitoyl phosphatidylcholine/cholesterol/water systems*. Biochimica et Biophysica Acta (BBA) - Biomembranes, 1975. 413(1): p. 24-32 URL: [http://dx.doi.org/10.1016/0005-2736\(75\)90055-3](http://dx.doi.org/10.1016/0005-2736(75)90055-3).
 27. **Izumitani, Y.**, *A Theory of the Effects of the Field-Dependent Affinity of Calcium Ions on the Lamellar Phase of Dipalmitoyl Lecithin*. Journal of Colloid and Interface Science, 1996. 182(1): p. 6-16 URL: <http://dx.doi.org/10.1006/jcis.1996.0431>.
 28. **Armstrong, C., M. Kaye, M. Zamponi, E. Mamontov, M. Tyagi, T. Jenkins, and M. Rheinstadter**, *Diffusion in single supported lipid bilayers studied by quasi-elastic neutron scattering*. Soft Matter, 2010. 6(23): p. 5864-5867 URL: <http://dx.doi.org/10.1039/c0sm00637h>.
 29. **Harroun, T.A., M.P. Nieh, M.J. Watson, V.A. Raghunathan, G. Pabst, M.R. Morrow, and J. Katsaras**, *Relationship between the unbinding and main transition temperatures of phospholipid bilayers under pressure*. Physical Review E, 2004. 69(3): p. 031906 URL: <http://dx.doi.org/10.1103/PhysRevE.69.031906>.
 30. **Mannock, D.A., R.N.A.H. Lewis, and R.N. McElhaney**, *A calorimetric and spectroscopic comparison of the effects of ergosterol and cholesterol on the thermotropic phase behavior and organization of dipalmitoylphosphatidylcholine bilayer membranes*. Biochimica et Biophysica Acta (BBA) - Biomembranes, 2010.

- 1798(3): p. 376-388 URL: <http://dx.doi.org/10.1016/j.bbamem.2009.09.002>.
31. **Schubert, T., E. Schneck, and M. Tanaka**, *First order melting transitions of highly ordered dipalmitoyl phosphatidylcholine gel phase membranes in molecular dynamics simulations with atomistic detail*. The Journal of Chemical Physics, 2011. 135(5): p. 055105-11 URL: <http://link.aip.org/link/?JCP/135/055105/1>.
32. **Luzatti, V.**, ed. *Biological Membranes: X-Ray Diffraction Studies of Lipid-Water Systems*. ed. D. Chapman. Vol. 1. 1968, Academic Press London.URL.
33. **Hianik, T.**, *Biological Membranes and Membrane Mimics*. Bioelectrochemistry. Chapter 3. 2008: John Wiley & Sons. 87-156.URL: <http://dx.doi.org/10.1002/9780470753842.ch3>.
34. **Winter, R., J. Erbes, C. Czeslik, and A. Gabke**, *Effect of pressure on the stability, phase behaviour and transformation kinetics between structures of lyotropic lipid mesophases and model membrane systems*. Journal of Physics: Condensed Matter, 1998. 10(49): p. 11499 URL: <http://stacks.iop.org/0953-8984/10/i=49/a=036>.
35. **Heimburg, T.**, *Membrane Structure*, in *Thermal Biophysics of Membranes*. 2007, Wiley-VCH Verlag GmbH & Co. KGaA. p. 15-27.
36. **Nagle, J.F.**, *Theory of the Main Lipid Bilayer Phase Transition*. Annual Review of Physical Chemistry, 1980. 31: p. 157-195 URL: <http://dx.doi.org/10.1146/annurev.pc.31.100180.001105>.
37. **Lemmich, J., K. Mortensen, J.H. Ipsen, T. Hønger, R. Bauer, and O.G. Mouritsen**, *Small-angle neutron scattering from multilamellar lipid bilayers: Theory, model, and experiment*. Physical Review E, 1996. 53(5): p. 5169 URL: <http://dx.doi.org/10.1103/PhysRevE.53.5169>.
38. **Mason, P.C., J.F. Nagle, R.M. Epand, and J. Katsaras**, *Anomalous swelling in phospholipid bilayers is not coupled to the formation of a ripple phase*. Physical Review E, 2001. 63(3): p. 1-4 URL: <http://link.aps.org/doi/10.1103/PhysRevE.63.030902>.
39. **Hønger, T., K. Mortensen, J.H. Ipsen, J. Lemmich, R. Bauer, and O.G. Mouritsen**, *Anomalous swelling of multilamellar lipid bilayers in the transition region by renormalization of curvature elasticity*. Physical Review Letters, 1994. 72(24): p. 3911 URL: <http://dx.doi.org/10.1103/PhysRevLett.72.3911>.
40. **Pabst, G., H. Amenitsch, D.P. Kharakoz, P. Laggner, and M. Rappolt**, *Structure and fluctuations of phosphatidylcholines in the vicinity of the main phase transition*. Physical Review E, 2004. 70(2): p. 021908 URL:

- <http://link.aps.org/doi/10.1103/PhysRevE.70.021908>.
41. **Chen, F.Y., W.C. Hung, and H.W. Huang**, *Critical Swelling of Phospholipid Bilayers*. Physical Review Letters, 1997. 79(20): p. 4026 URL: <http://dx.doi.org/10.1103/PhysRevLett.79.4026>.
 42. **Korreman, S.S. and D. Posselt**, *Chain length dependence of anomalous swelling in multilamellar lipid vesicles*. The European Physical Journal E: Soft Matter and Biological Physics, 2000. 1(1): p. 87-91 URL: <http://dx.doi.org/10.1007/s101890050010>.
 43. **Chu, N., N. Kucaronerka, Y. Liu, S. Tristram-Nagle, and J.F. Nagle**, *Anomalous swelling of lipid bilayer stacks is caused by softening of the bending modulus*. Physical Review E, 2005. 71(4): p. 041904_1-8 URL: <http://dx.doi.org/10.1103/PhysRevE.71.041904>.
 44. **Pabst, G., J. Katsaras, V.A. Raghunathan, and M. Rappolt**, *Structure and Interactions in the Anomalous Swelling Regime of Phospholipid Bilayers*. Langmuir, 2003. 19(5): p. 1716-1722 URL: <http://dx.doi.org/10.1021/la026052e>.
 45. **Fragneto, G., T. Charitat, E. Bellet-Amalric, R. Cubitt, and F. Graner**, *Swelling of Phospholipid Floating Bilayers: The Effect of Chain Length†*. Langmuir, 2003. 19(19): p. 7695-7702 URL: <http://dx.doi.org/10.1021/la026972x>.
 46. **Zhang, R., W. Sun, S. Tristram-Nagle, R.L. Headrick, R.M. Suter, and J.F. Nagle**, *Critical Fluctuations in Membranes*. Physical Review Letters, 1995. 74(14): p. 2832-2835 URL: <http://link.aps.org/doi/10.1103/PhysRevLett.74.2832>.
 47. **Lipowsky, R. and S. Leibler**, *Unbinding Transitions of Interacting Membranes*. Physical Review Letters, 1986. 56(23): p. 2541-2544 URL: <http://dx.doi.org/10.1103/PhysRevLett.56.2541>.
 48. **Hübner, W. and H.H. Mantsch**, *Orientation of specifically $^{13}\text{C}=\text{O}$ labeled phosphatidylcholine multilayers from polarized attenuated total reflection FT-IR spectroscopy*. Biophysical Journal, 1991. 59(6): p. 1261-1272 URL: [http://dx.doi.org/10.1016/s0006-3495\(91\)82341-4](http://dx.doi.org/10.1016/s0006-3495(91)82341-4).
 49. **Sillerud, L.O. and R.E. Barnett**, *Lack of transbilayer coupling in phase transitions of phosphatidylcholine vesicles*. Biochemistry, 1982. 21(8): p. 1756-1760 URL: <http://dx.doi.org/10.1021/bi00537a009>.
 50. **Chen, C.H.**, *Interactions of lipid vesicles with solvent in heavy and light water*. The Journal of Physical Chemistry, 1982. 86(18): p. 3559-3562 URL: <http://dx.doi.org/10.1021/j100215a014>.

51. **Avanti Polar Lipids Incorporation.** *DMPC*; CAS-Number 18194-24-6. Available from:
http://www.avantilipids.com/index.php?option=com_content&view=article&id=214&Itemid=206&catnumber=850345.
52. **Meyer, K. and J.W. Palmer,** *The polysaccharide of the virteous humor.* Journal of Biological Chemistry, 1934. 107(3): p. 629-634 URL:
<http://www.jbc.org/content/107/3/629.short>.
53. **Weissmann, B. and K. Meyer,** *The Structure of Hyalobiuronic Acid and of Hyaluronic Acid from Umbilical Cord1,2.* Journal of the American Chemical Society, 1954. 76(7): p. 1753-1757 URL: <http://dx.doi.org/10.1021/ja01636a010>.
54. **Lee, H.G. and M.K. Cowman,** *An Agarose Gel Electrophoretic Method for Analysis of Hyaluronan Molecular Weight Distribution.* Analytical Biochemistry, 1994. 219(2): p. 278-287 URL: <http://dx.doi.org/10.1006/abio.1994.1267>.
55. **Cowman, M.K. and S. Matsuoka,** *Experimental approaches to hyaluronan structure.* Carbohydrate Research, 2005. 340(5): p. 791-809 URL: <http://dx.doi.org/10.1016/j.carres.2005.01.022>.
56. **Quemeneur, F., M. Rinaudo, and B. Pépin-Donat,** *Influence of Polyelectrolyte Chemical Structure on their Interaction with Lipid Membrane of Zwitterionic Liposomes.* Biomacromolecules, 2008. 9(8): p. 2237-2243 URL: <http://dx.doi.org/10.1021/bm800400y>.
57. **Mikelsaar, R.-H. and J.E. Scott,** *Molecular modelling of secondary and tertiary structures of hyaluronan, compared with electron microscopy and NMR data. Possible sheets and tubular structures in aqueous solution.* Glycoconjugate Journal, 1994. 11(2): p. 65-71 URL: <http://dx.doi.org/10.1007/BF00731145>.
58. **Scott, J.E. and F. Heatley,** *Hyaluronan forms specific stable tertiary structures in aqueous solution: A ¹³C NMR study.* Proceedings of the National Academy of Sciences, 1999. 96(9): p. 4850-4855 URL: <http://dx.doi.org/10.1073/pnas.96.9.4850>.
59. **Balazs, E.A., D. Watson, I.F. Duff, and S. Roseman,** *Hyaluronic acid in synovial fluid. I. Molecular parameters of hyaluronic acid in normal and arthritic human fluids.* Arthritis & Rheumatism, 1967. 10(4): p. 357-376 URL: <http://dx.doi.org/10.1002/art.1780100407>.
60. **Adams, M.E., A.J. Lussier, and J.G. Peyron,** *A Risk-Benefit Assessment of Injections of Hyaluronan and its Derivatives in the Treatment of Osteoarthritis of the Knee.* Drug Safety, 2000. 23(2): p. 115-130 URL:

- <http://www.ncbi.nlm.nih.gov/pubmed/10945374>.
61. **Marjorie J, R.**, *A review of hyaluronan and its ophthalmic applications*. Optometry - Journal of the American Optometric Association, 2011. 82(1): p. 38-43 URL: <http://dx.doi.org/10.1016/j.optm.2010.08.003>.
62. **Edgar181**. *Chemical structure of hyaluronan*. Available from: <http://en.wikipedia.org/wiki/Hyaluronan>.
63. **Merck KGaA**. *Hyaluronic Acid; CAS-Number 9067-32-7* Available from: http://www.merck-chemicals.com/germany/life-science-research/hyaluronic-acid-sodium-salt-streptococcus-pyrogenes/EMD_BIO-385908/p_zzmb.s1L_wAAAEWhmEfVhTm?WFSimpleSearch_NameOrID=hyaluro nic+acid&BackButtonText=search+results.
64. **Millipore**. Available from: <http://www.millipore.com/>.
65. **Sigma-Aldrich**. Available from: <http://www.sigmaaldrich.com/>.
66. **Merck KGaA**. *Chloroform; CAS-Nummer 67-66-3*. Available from: http://www.merck-chemicals.com/germany/chloroform/MDA_CHEM-102447/p_Wmub.s1L3dcAAAEW8eEfVhTl?WFSimpleSearch_NameOrID=%0967-66-3&BackButtonText=search+results.
67. **Siliziumbearbeitung Andrea Holm**. Available from: <http://www.holm-silicon.de/>.
68. **Lewis, R.N.A.H., D.A. Mannoek, and R.N. McElhaney**, *Differential Scanning Calorimetry in the Study of Lipid Phase Transitions in Model and Biological Membranes*. Methods in Molecular Biology. Vol:400, Methods in Membrane Lipids. , ed. A. Dopico. 2008: WILEY-VCH Verlag.URL: <http://dx.doi.org/10.1002/cbic.200800067>.
69. **Dittrich, M., M. Heinze, C. Wölk, S.S. Funari, B. Dobner, H. Möhwald, and G. Brezesinski**, *Structure–Function Relationships of New Lipids Designed for DNA Transfection*. ChemPhysChem, 2011. 12(12): p. 2328-2337 URL: <http://dx.doi.org/10.1002/cphc.201100065>.
70. **Hesse, M., H. Meier, and B. Zeeh**, *Spectroscopic Methods in Organic Chemistry*. 2. ed. 2007, Stuttgart, Germany: Georg Thieme Verlag.URL: <http://webshop.thieme.de/webshop/product/thieme/9783131060426/detail.jsf;jsessionid=F307086513600FF056475BFA655D9162>.
71. **Griffiths, P.R. and J.A. de Haseth**, *Fourier Transform Infrared Spectrometry*. Chemical Analysis—A Series of Monographs of Analytical Chemistry and Its Applications. Vol. 83. 1986, Chichester, New York, Brisbane, Toronto, Singapore:

- John Wiley + Sons.URL: <http://dx.doi.org/10.1002/bbpc.19860901224>.
72. **Tiago Becerra Paolini.** *Infrared spectroscopy.* 2011; Available from: http://en.wikipedia.org/wiki/Infrared_spectroscopy.
73. **Michelson, A.A. and E.W. Morley,** *On the relative motion of the earth and the luminiferous aether.* American Journal of Science, 1887. 203: p. 333-345 URL: <http://www.aip.org/history/gap/Michelson/Michelson.html>.
74. **Fourier, J.B.J.,** *Théorie analytique de la chaleur ("The Analytic Theory of heat").* 1822, Paris: F. Didot.URL: <http://www.archive.org/details/thorieanalytiqu00fourgoog>.
75. **Gerthsen, C.,** *Gerthsen Physik.* 24 ed, ed. D. Meschede. 2010: Springer Berlin.URL: <http://dx.doi.org/10.1007/978-3-642-12894-3>.
76. **Staat, H., H. Heise, and E. Korte,** *Fehleranalyse für die Bestimmung der Extinktionskoeffizienten von Flüssigkeiten im infraroten Spektralbereich.* Fresenius' Journal of Analytical Chemistry, 1983. 316(2): p. 170-179 URL: <http://dx.doi.org/10.1007/BF00488182>.
77. **Harrick, N.J.,** *Study of physics and chemistry of surfaces from frustrated total internal reflections.* Physical Review Letters, 1960. 4(5): p. 224 - 226 URL: <http://dx.doi.org/10.1103/PhysRevLett.4.224>.
78. **Daillant, J. and A. Gibaud,** eds. *X-ray and Neutron Reflectivity.* Lecture Notes in Physics. Vol. 770. 2009, Springer: Berlin Heidelberg.URL: <http://dx.doi.org/10.1007/978-3-540-88588-7>.
79. **Röntgen, W.C.,** *Über eine neue Art von Strahlen (Vorläufige Mitteilung).* Aus den Sitzungsberichten der Würzburger Physik.-medic. Gesellschaft, 1895: p. 1-10.
80. **Röntgen, W.C.,** *On a new kind of rays.* Journal of the Franklin Institute, 1896. 141(3): p. 183-191 URL: [http://dx.doi.org/10.1016/s0016-0032\(96\)90066-6](http://dx.doi.org/10.1016/s0016-0032(96)90066-6).
81. **Compton, A.H.,** *The scattering of X-rays.* Journal of the Franklin Institute, 1924. 198(1): p. 57-72 URL: [http://dx.doi.org/10.1016/s0016-0032\(24\)90007-x](http://dx.doi.org/10.1016/s0016-0032(24)90007-x).
82. **Prins, J.A.,** *The Total Reflection of X-Rays.* Nature, 1927. 120: p. 188-189 URL: <http://dx.doi.org/10.1038/120188a0>.
83. **Lekner, J.,** *Reflection theory and the analysis of neutron reflection data.* Physica B, 1991. 173(1-2): p. 99-111 URL: [http://dx.doi.org/10.1016/0921-4526\(91\)90040-L](http://dx.doi.org/10.1016/0921-4526(91)90040-L).
84. **Trapp, M., T. Gutberlet, F. Juranyi, T. Unruh, B. Demé, M. Tehei, and J. Peters,** *Hydration dependent studies of highly aligned multilayer lipid membranes by neutron scattering.* Vol. 133. 2010: AIP. 164505.URL: <http://dx.doi.org/doi/10.1063/1.3495973>.

85. **NIST.** *Scattering Length Density Calculator.* 2010 [cited 2011; Available from: <http://www.ncnr.nist.gov/resources/sldcalc.html>].
86. **Sears, V.F.,** *Neutron scattering lengths and cross sections.* Neutron News, 1992. 3(3): p. 26 - 37 URL: <http://www.informaworld.com/10.1080/10448639208218770>.
87. **Schrödinger, E.,** *Quantisierung als Eigenwertproblem.* Annalen der Physik, 1926. 79: p. 361 URL: <http://gallica.bnf.fr/ark:/12148/bpt6k153811/f1>.
88. **Mezei, F., R. Golub, F. Klose, and H. Toews,** *Focussed beam reflectometer for solid and liquid surfaces.* Physica B: Condensed Matter, 1995. 213-214: p. 898-900 URL: [http://dx.doi.org/10.1016/0921-4526\(95\)00317-3](http://dx.doi.org/10.1016/0921-4526(95)00317-3).
89. **Weinbach, S.P., I. Weissbuch, M. Lahav, L. Leiserowitz, K. Kjaer, W.G. Bouwman, and J. Als Nielsen,** *Self-assembled crystalline monolayers and multilayers of n-alkanes on the water surface.* Advanced Materials, 1995. 7(10): p. 857-862 URL: <http://dx.doi.org/10.1002/adma.19950071009>.
90. **Jensen, T.R., K. Balashev, T. Bjørnholm, and K. Kjaer,** *Novel methods for studying lipids and lipases and their mutual interaction at interfaces. Part II. Surface sensitive synchrotron X-ray scattering.* Biochimie, 2001. 83(5): p. 399-408 URL: [http://dx.doi.org/10.1016/s0300-9084\(01\)01265-2](http://dx.doi.org/10.1016/s0300-9084(01)01265-2).
91. **Pabst, G., R. Koschuch, B. Pozo-Navas, M. Rappolt, K. Lohner, and P. Lagner,** *Structural analysis of weakly ordered membrane stacks.* Journal of Applied Crystallography, 2003. 36(6): p. 1378-1388 URL: <http://dx.doi.org/10.1107/S0021889803017527>.
92. **Parratt, L.G.,** *Surface Studies of Solids by Total Reflection of X-Rays.* Physical Review, 1954. 95(2): p. 359 URL: <http://link.aps.org/doi/10.1103/PhysRev.95.359>.
93. **Braun, C.,** *Grenzflächenstruktur und Grenzflächeneffekte von Phasenübergängen in Lyotropen Systemen: Röntgen- und Neutronenreflektivitätsuntersuchungen an wässrigen Systemen von Alkylpolyglykolethern (C10E4, C12E4, C12E5).* Thesis. 1999. Institut für Chemie at Technische Universität Berlin. Herdecke : GCA-Verl. URL: <http://worldcat.org/oclc/76026063>.
94. **Hauß, T., S. Dante, T.H. Haines, and N.A. Dencher,** *Localization of coenzyme Q10 in the center of a deuterated lipid membrane by neutron diffraction.* Biochimica et Biophysica Acta (BBA) - Bioenergetics, 2005. 1710(1): p. 57-62 URL: <http://dx.doi.org/10.1016/j.bbabbio.2005.08.007>.
95. **van Well, A.A.,** *Double-disk chopper for neutron time-of-flight experiments.* Physica

- B: Condensed Matter, 1992. 180-181(Part 2): p. 959-961 URL: [http://dx.doi.org/10.1016/0921-4526\(92\)90521-s](http://dx.doi.org/10.1016/0921-4526(92)90521-s).
96. **Kreuzer, M., T. Kaltofen, R. Steitz, B.H. Zehnder, and R. Dahint**, *Pressure cell for investigations of solid-liquid interfaces by neutron reflectivity*. Review of Scientific Instruments, 2011. 82(2): p. 023902-7 URL: <http://dx.doi.org/10.1063/1.3505797>.
97. **Voets, I.K., W.M. de Vos, B. Hofs, A. de Keizer, M.A. Conhen Stuart, R. Steitz, and D. Lott**, *Internal Structure of a Thin Film of Mixed Polymeric Micelles on a Solid/Liquid Interface*. The Journal of Physical Chemistry B, 2008. 112(23): p. 6937-6945 URL: <http://dx.doi.org/10.1021/jp709758p>.
98. **Strobl, M., R. Steitz, M. Kreuzer, A. Nawara, F. Mezei, M. Rose, P. Amitesh, M. Grunze, and R. Dahint**, *BioRef – a time-of-flight neutron reflectometer combined with in-situ infrared spectroscopy at the Helmholtz Centre Berlin*. Journal of Physics: Conference Series, 2010. 251(1): p. 012059 URL: <http://stacks.iop.org/1742-6596/251/i=1/a=012059>.
99. **Strobl, M., R. Steitz, M. Kreuzer, M. Rose, H. Herrlich, F. Mezei, M. Grunze, and R. Dahint**, *BioRef: A versatile time-of-flight reflectometer for soft matter applications at Helmholtz-Zentrum Berlin*. Review of Scientific Instruments, 2011. 82(5): p. 055101 URL: <http://dx.doi.org/10.1063/1.3581210>.
100. **Strickert, E.**, *BioRef Infografik*. on behalf of Helmholtz-Zentrum Berlin - Department Communication, 2011 URL: https://www.helmholtz-berlin.de/aktuell/pr/bildarchiv/forschung/neutronen_en.html.
101. **Kreuzer, M.**, *A fish-eye perspective of BioRef*. inside NMI3 by Integrated Infrastructure Initiative for Neutron Scattering and Muon Spectroscopy (NMI3), 2011(2) URL: www.nmi3.eu/news-and-media/newsletter.html.
102. **Kaltofen, T.**, *Biophysikalische Aspekte der Schmierung natürlicher Gelenke*. Thesis. 2008. Physikalisch Chemisches Institut at Ruprecht-Karls-Universität Heidelberg. URL: <http://www.ub.uni-heidelberg.de/archiv/8822>.
103. **Clemens, D., P. Gross, P. Keller, N. Schlumpf, and M. Könnecke**, *AMOR – the versatile reflectometer at SINQ*. Physica B: Condensed Matter, 2000. 276-278(0): p. 140-141 URL: [http://dx.doi.org/10.1016/s0921-4526\(99\)01386-1](http://dx.doi.org/10.1016/s0921-4526(99)01386-1).
104. **Gupta, M., T. Gutberlet, J. Stahn, P. Keller, and D. Clemens**, *AMOR — the time-of-flight neutron reflectometer at SINQ/PSI*. Pramana, 2004. 63(1): p. 57-63 URL: <http://dx.doi.org/10.1007/BF02704051>.

105. **Rehfeldt, F., R. Steitz, S.P. Armes, R. von Klitzing, A.P. Gast, and M. Tanaka**, *Reversible Activation of Diblock Copolymer Monolayers at the Interface by pH Modulation, 1: Lateral Chain Density and Conformation*. The Journal of Physical Chemistry B, 2006. 110(18): p. 9171-9176 URL: <http://dx.doi.org/10.1021/jp054532j>.
106. **Mennicke, U. and T. Salditt**, *Preparation of Solid-Supported Lipid Bilayers by Spin-Coating*. Langmuir, 2002. 18(21): p. 8172-8177 URL: <http://dx.doi.org/10.1021/la025863f>.
107. **Salditt, T., C. Münster, J. Lu, M. Vogel, W. Fenzl, and A. Souvorov**, *Specular and diffuse scattering of highly aligned phospholipid membranes*. Physical Review E, 1999. 60(6): p. 7285-7289 URL: <http://link.aps.org/doi/10.1103/PhysRevE.60.7285>.
108. **Raghunathan, V., R. Shori, O.M. Stafsudd, and B. Jalali**, *Nonlinear absorption in silicon and the prospects of mid-infrared silicon Raman lasers*. physica status solidi (a), 2006. 203(5): p. R38-R40 URL: <http://dx.doi.org/10.1002/pssa.200622062>.
109. **Kreuzer, M., M. Strobl, M. Reinhardt, C. Hemmer, T. Hauß, R. Dahint, and R. Steitz**, *Impact of a model synovial fluid on supported lipid membranes*. submitted to Biochimica et Biophysica Acta - Biomembranes, 2011.
110. **Haas, H., R. Steitz, A. Fasano, G.M. Liuzzi, E. Polverini, P. Cavatorta, and P. Riccio**, *Laminar Order within Langmuir–Blodgett Multilayers from Phospholipid and Myelin Basic Protein: A Neutron Reflectivity Study*. Langmuir, 2007. 23(16): p. 8491-8496 URL: <http://dx.doi.org/10.1021/la700733y>.
111. **Smeller, L.**, *Pressure-temperature phase diagrams of biomolecules*. Biochimica et Biophysica Acta (BBA) - Protein Structure and Molecular Enzymology, 2002. 1595(1-2): p. 11-29 URL: [http://dx.doi.org/10.1016/s0167-4838\(01\)00332-6](http://dx.doi.org/10.1016/s0167-4838(01)00332-6).
112. **Eisenblätter, J. and R. Winter**, *Pressure Effects on the Structure and Phase Behavior of DMPC-Gramicidin Lipid Bilayers: A Synchrotron SAXS and 2H-NMR Spectroscopy Study*. Biophysical Journal, 2006. 90(3): p. 956-966 URL: <http://dx.doi.org/10.1529/biophysj.105.069799>.
113. **Winter, R.**, *Effects of hydrostatic pressure on lipid and surfactant phases*. Current Opinion in Colloid and Interface Science, 2001. 6(3): p. 303-312 URL: <http://www.ingentaconnect.com/content/els/13590294/2001/00000006/00000003/art00092>
[http://dx.doi.org/10.1016/S1359-0294\(01\)00092-9](http://dx.doi.org/10.1016/S1359-0294(01)00092-9).
114. **Braganza, L.F. and D.L. Worcester**, *Hydrostatic pressure induces hydrocarbon chain interdigitation in single-component phospholipid bilayers*. Biochemistry, 1986.

- 25(9): p. 2591-2596 URL: <http://dx.doi.org/10.1021/bi00357a047>.
115. **Winter, R. and C. Czeslik**, *Pressure effects on the structure of lyotropic lipid mesophases and model biomembrane systems*. *Zeitschrift für Kristallographie*, 2000. 215(8): p. 454 URL: <http://dx.doi.org/10.1524/zkri.2000.215.8.454>.
116. **Heremans, K.**, *High Pressure Effects on Proteins and other Biomolecules*. Annual Review of Biophysics and Bioengineering, 1982. 11(1): p. 1-21 URL: <http://dx.doi.org/10.1146/annurev.bb.11.060182.000245>.
117. **Emmet, R.T. and F.J. Millero**, *Specific volume of deuterium oxide from 2.deg. to 40.deg. and 0 to 1000 bars applied pressure*. *Journal of Chemical & Engineering Data*, 1975. 20(4): p. 351-356 URL: <http://dx.doi.org/10.1021/je60067a006>.
118. **Wang, Y., J. Zhang, J. Wu, J.L. Coffey, Z. Lin, S.V. Sinogeikin, W. Yang, and Y. Zhao**, *Phase Transition and Compressibility in Silicon Nanowires*. *Nano Letters*, 2008. 8(9): p. 2891-2895 URL: <http://dx.doi.org/10.1021/nl8016576>.
119. **Wooley, P.H. and E.M. Schwarz**, *Aseptic loosening*. *Gene Therapy*, 2004. 11(4): p. 402-407 URL: <http://dx.doi.org/10.1038/sj.gt.3302202>.
120. **Khan, M.A., R.L. Williams, and D.F. Williams**, *In-vitro corrosion and wear of titanium alloys in the biological environment*. *Biomaterials*, 1996. 17(22): p. 2117-2126 URL: [http://dx.doi.org/10.1016/0142-9612\(96\)00029-4](http://dx.doi.org/10.1016/0142-9612(96)00029-4).
121. **Cho, S.J., T. Krist, and F. Mezei**, *Dependence of interface layer thickness in FeCo-Si multilayers on sputtering parameters*. *Thin Solid Films*, 2003. 444(1-2): p. 158-164 URL: [http://dx.doi.org/10.1016/s0040-6090\(03\)01095-2](http://dx.doi.org/10.1016/s0040-6090(03)01095-2).
122. **Sant, C., M.B. Daia, P. Aubert, S. Labdi, and P. Houdy**, *Interface effect on tribological properties of titanium-titanium nitride nanolaminated structures*. *Surface and Coatings Technology*, 2000. 127(2-3): p. 167-173 URL: [http://dx.doi.org/10.1016/s0257-8972\(00\)00663-0](http://dx.doi.org/10.1016/s0257-8972(00)00663-0).
123. **Mills, T.T., G.E.S. Toombes, S. Tristram-Nagle, D.-M. Smilgies, G.W. Feigenson, and J.F. Nagle**, *Order Parameters and Areas in Fluid-Phase Oriented Lipid Membranes Using Wide Angle X-Ray Scattering*. *Biophysical Journal*, 2008. 95(2): p. 669-681 URL: <http://dx.doi.org/10.1529/biophysj.107.127845>.
124. **Nagle, J.F. and S. Tristram-Nagle**, *Structure of lipid bilayers*. *Biochimica et Biophysica Acta (BBA) - Reviews on Biomembranes*, 2000. 1469(3): p. 159-195 URL: [http://dx.doi.org/10.1016/s0304-4157\(00\)00016-2](http://dx.doi.org/10.1016/s0304-4157(00)00016-2).
125. **Pabst, G., H. Amenitsch, D.P. Kharakoz, P. Laggner, and M. Rappolt**, *Structure and fluctuations of phosphatidylcholines in the vicinity of the main phase transition*.

- Physical review. E, Statistical, nonlinear, and soft matter physics, 2004. 70(2 Pt 1): p. 021908 URL: <http://ukpmc.ac.uk/abstract/MED/15447516>.
126. **Vogel, M., C. Münster, W. Fenzl, D. Thiaudière, and T. Salditt**, *Fully hydrated and highly oriented membranes: an experimental setup amenable to specular and diffuse X-ray scattering*. Physica B: Condensed Matter, 2000. 283(1-3): p. 32-36 URL: [http://dx.doi.org/10.1016/s0921-4526\(99\)01886-4](http://dx.doi.org/10.1016/s0921-4526(99)01886-4).
127. **Lecuyer, S. and T. Charitat**, *From supported membranes to tethered vesicles: Lipid bilayers destabilisation at the main transition*. Europhysics Letters, 2006. 75(4): p. 652 URL: <http://dx.doi.org/10.1209/epl/i2006-10145-2>.
128. **Caffrey, M. and J. Hogan**, *LIPIDAT: A database of lipid phase transition temperatures and enthalpy changes. DMPC data subset analysis*. Chemistry and Physics of Lipids, 1992. 61(1): p. 1-109 URL: [http://dx.doi.org/0.1016/0009-3084\(92\)90002-7](http://dx.doi.org/0.1016/0009-3084(92)90002-7).
129. **Lewis, R.N.A.H. and R.N. McElhaney**, *The structure and organization of phospholipid bilayers as revealed by infrared spectroscopy*. Chemistry and Physics of Lipids, 1998. 96(1-2): p. 9-21 URL: [http://dx.doi.org/10.1016/s0009-3084\(98\)00077-2](http://dx.doi.org/10.1016/s0009-3084(98)00077-2).
130. **Kóta, Z., M. Debreczeny, and B. Szalontai**, *Separable contributions of ordered and disordered lipid fatty acyl chain segments to νCH_2 bands in model and biological membranes: A Fourier transform infrared spectroscopic study*. Biospectroscopy, 1999. 5(3): p. 169-178 URL: [http://dx.doi.org/10.1002/\(SICI\)1520-6343\(1999\)5:3<169::AID-BSPY6>3.0.CO;2-#](http://dx.doi.org/10.1002/(SICI)1520-6343(1999)5:3<169::AID-BSPY6>3.0.CO;2-#).
131. **Pabst, G.**, *Global properties of biomimetic membranes: perspectives on molecular features*. Biophysical Reviews and Letters, 2006. 1(1): p. 57-84 URL: www.worldscinet.com/brl/01/0101/S1793048006000069.html.
132. **Guard-Friar, D., C.H. Chen, and A.S. Engle**, *Deuterium isotope effect on the stability of molecules: phospholipids*. The Journal of Physical Chemistry, 1985. 89(9): p. 1810-1813 URL: <http://dx.doi.org/10.1021/j100255a054>.
133. **Laurent, T. and J. Fraser**, *Hyaluronan*. The FASEB Journal, 1992. 6(7): p. 2397-2404 URL: <http://www.fasebj.org/content/6/7/2397.abstract>.
134. **Donghui, F., W. Beibei, X. Zheng, and G. Qisheng**, *Determination of hyaluronan by spectroscopic methods*. Journal of Wuhan University of Technology-Materials Science Edition, 2006. 21(3): p. 32-34 URL: <http://dx.doi.org/10.1007/BF02840874>.
135. **Cho, K.Y., T.W. Chung, B.C. Kim, M.K. Kim, J.H. Lee, W.R. Wee, and C.S.**

- Cho**, *Release of ciprofloxacin from poloxamer-graft-hyaluronic acid hydrogels in vitro*. International Journal of Pharmaceutics, 2003. 260(1): p. 83-91 URL: [http://dx.doi.org/10.1016/s0378-5173\(03\)00259-x](http://dx.doi.org/10.1016/s0378-5173(03)00259-x).
136. **Winter, R. and F. Noll**, *Methoden der Biophysikalischen Chemie*. 1998: Teubner Studienbücher Chemie.URL: <http://www.viewegteubner.de/Buch/978-3-8348-1316-9/Methoden-der-Biophysikalischen-Chemie.html>.
137. **Wiener, M.C., G.I. King, and S.H. White**, *Structure of a fluid dioleoylphosphatidylcholine bilayer determined by joint refinement of x-ray and neutron diffraction data. I. Scaling of neutron data and the distributions of double bonds and water*. Biophysical Journal, 1991. 60(3): p. 568-576 URL: [http://dx.doi.org/10.1016/s0006-3495\(91\)82086-0](http://dx.doi.org/10.1016/s0006-3495(91)82086-0).
138. **Nagle, J.F. and S. Tristram-Nagle**, *Structure of lipid bilayers*. Biochimica et Biophysica Acta - Reviews on Biomembranes, 2000. 1469(3): p. 159-195 URL: <http://www.sciencedirect.com/science/article/B6T22-41J60H2-3/2/81789ddf702d8032191290e3d1e19b8d>.
139. **Haas, H., R. Steitz, A. Fasano, G.M. Liuzzi, E. Polverini, P. Cavatorta, and P. Riccio**, *Laminar order within Langmuir-Blodgett multilayers from phospholipid and myelin basic protein: A neutron reflectivity study*. Langmuir, 2007. 23(16): p. 8491-8496 URL: <http://dx.doi.org/10.1021/la700733y>.
140. **Koenig, B.W., S. Kruger, W.J. Orts, C.F. Majkrzak, N.F. Berk, J.V. Silverton, and K. Gawrisch**, *Neutron Reflectivity and Atomic Force Microscopy Studies of a Lipid Bilayer in Water Adsorbed to the Surface of a Silicon Single Crystal*. Langmuir, 1996. 12(5): p. 1343-1350 URL: <http://dx.doi.org/10.1021/la950580r>.
141. **Kugler, R. and W. Knoll**, *Polyelectrolyte-supported lipid membranes*. Bioelectrochemistry, 2002. 56(1-2): p. 175-178 URL: [http://dx.doi.org/10.1016/S1567-5394\(02\)00031-2](http://dx.doi.org/10.1016/S1567-5394(02)00031-2).
142. **Grunze, M., I. Fedyanin, and A. Pertsin**, *Mechanism of short-range interfacial repulsion between hydrated phosphatidylcholine bilayers: Comparison with phosphatidylethanolamine*. Surface Science, 2009. 603(10-12): p. 1937-1944 URL: <http://dx.doi.org/10.1016/j.susc.2008.09.059>.
143. **McDermott, D.C., J.R. Lu, E.M. Lee, R.K. Thomas, and A.R. Rennie**, *Study of the adsorption from aqueous-solution of hexaethylene glycol monododecyl ether on silica substrates using the technique of neutron reflection*. Langmuir, 1992. 8(4): p. 1204-1210 URL: <http://dx.doi.org/10.1021/la00040a031>.

144. **Smith, H.L., M.C. Howland, A.W. Szmodis, Q.J. Li, L.L. Daemen, A.N. Parikh, and J. Majewski**, *Early Stages of Oxidative Stress-Induced Membrane Permeabilization: A Neutron Reflectometry Study*. *Journal of the American Chemical Society*, 2009. 131(10): p. 3631-3638 URL: <http://dx.doi.org/10.1021/ja807680m>.
145. **Heisig, M., R. Lieckfeldt, G. Wittum, G. Mazurkevich, and G. Lee**, *Non steady-state descriptions of drug permeation through stratum corneum .I. The biphasic brick-and-mortar model*. *Pharmaceutical Research*, 1996. 13(3): p. 421-426 URL: <http://dx.doi.org/10.1023/A:1016048710880>
146. **Charalambopoulou, G.C., P. Karamertzanis, E.S. Kikkinides, A.K. Stubos, N.K. Kanellopoulos, and A.T. Papaioannou**, *A study on structural and diffusion properties of porcine stratum corneum based on very small angle neutron scattering data*. *Pharmaceutical Research*, 2000. 17(9): p. 1085-1091 URL: <http://dx.doi.org/10.1023/A:1026453628800>.
147. **Büldt, G., H.U. Gally, J. Seelig, and G. Zaccai**, *Neutron-diffraction studies on phosphatidylcholine model membranes. I. Head group conformtaion*. *Journal of Molecular Biology*, 1979. 134(4): p. 673-691 URL: [http://dx.doi.org/10.1016/0022-2836\(79\)90479-0](http://dx.doi.org/10.1016/0022-2836(79)90479-0).
148. **Slack, N.L., P. Davidson, M.A. Chibbaro, C. Jeppesen, P. Eiselt, H.E. Warriner, H.W. Schmidt, P. Pincus, and C.R. Safinya**, *The bridging conformations of double-end anchored polymer-surfactants destabilize a hydrogel of lipid membranes*. *The Journal of Chemical Physics*, 2001. 115(13): p. 6252-6257 URL: <http://link.aip.org/link/?JCP/115/6252/1>.
149. **Lipowsky, R.**, *Adhesion of Membranes via Anchored Stickers*. *Physical Review Letters*, 1996. 77(8): p. 1652 URL: <http://dx.doi.org/10.1103/PhysRevLett.77.1652>.
150. **Lee, J.H., J.P. Gustin, T.H. Chen, G.F. Payne, and S.R. Raghavan**, *Vesicle-biopolymer gels: Networks of surfactant vesicles connected by associating biopolymers*. *Langmuir*, 2005. 21(1): p. 26-33 URL: <Go to ISI>://000226232700006.
151. **Kuhn, P.S.**, *A simple model for the collapse of polyelectrolyte macromolecules*. *Physica A*, 2002. 311(1-2): p. 50-58 URL: <Go to ISI>://000177222900005.
152. **Gómez-Alejandre, S., E. Sánchez de la Blanca, C. Abradelo de Usera, M.F. Rey-Stolle, and I. Hernández-Fuentes**, *Partial specific volume of hyaluronic acid in different media and conditions*. *International Journal of Biological Macromolecules*, 2000. 27(4): p. 287-290 URL: [http://dx.doi.org/10.1016/S0141-8130\(00\)00130-6](http://dx.doi.org/10.1016/S0141-8130(00)00130-6).

153. **Buhler, E. and F. Boué**, *Chain Persistence Length and Structure in Hyaluronan Solutions: Ionic Strength Dependence for a Model Semirigid Polyelectrolyte*. *Macromolecules*, 2004. 37(4): p. 1600-1610 URL: <http://dx.doi.org/10.1021/ma0215520>.
154. **Luzardo, M.d.C., F. Amalfa, A.M. Nuñez, S. Díaz, A.C. Biondi de Lopez, and E.A. Disalvo**, *Effect of Trehalose and Sucrose on the Hydration and Dipole Potential of Lipid Bilayers*. *Biophysical Journal*, 2000. 78(5): p. 2452-2458 URL: [http://dx.doi.org/10.1016/s0006-3495\(00\)76789-0](http://dx.doi.org/10.1016/s0006-3495(00)76789-0).
155. **Lambruschini, C., A. Relini, A. Ridi, L. Cordone, and A. Gliozzi**, *Trehalose Interacts with Phospholipid Polar Heads in Langmuir Monolayers*. *Langmuir*, 2000. 16(12): p. 5467-5470 URL: <http://dx.doi.org/10.1021/la991641e>.
156. **Dodoo, S., R. Steitz, A. Laschewsky, and R. von Klitzing**, *Effect of ionic strength and type of ions on the structure of water swollen polyelectrolyte multilayers*. *Physical Chemistry Chemical Physics*, 2011. 13(21): p. 10318-10325 URL: <http://dx.doi.org/10.1039/C0CP01357A>.
157. **Van der Schee, H.A. and J. Lyklema**, *A lattice theory of polyelectrolyte adsorption*. *The Journal of Physical Chemistry*, 1984. 88(26): p. 6661-6667 URL: <http://dx.doi.org/10.1021/j150670a031>.
158. **Böckmann, R.A., A. Hac, T. Heimburg, and H. Grubmüller**, *Effect of Sodium Chloride on a Lipid Bilayer*. *Biophysical Journal*, 2003. 85(3): p. 1647-1655 URL: [http://dx.doi.org/10.1016/S0006-3495\(03\)74594-9](http://dx.doi.org/10.1016/S0006-3495(03)74594-9).

Abbreviations

	description	introduced...
absorbance	infrared absorbance	on page 28
AMOR	neutron reflectometer at PSI	on page 50
ATR	attenuated total reflectance	on page 29
B	Bragg peak	on page 38
BioRef	neutron reflectometer at HZB	on page 44
DLVO	theory named after Derjaguin, Landau, Verwey and Overbeek	on page 18
DMPC	lipid: 1,2-dimyristoyl-sn-glycero-3-phosphocholine	on page 21
DSC	differential scanning calorimetry	on page 24
c	speed of light	on page 28, on page 33
d	repeat-distance or d-spacing	on page 17, on page 38
d_p	penetration depth	on page 29
ν	frequency	on page 26
FTIR	Fourier transform infrared spectroscopy	on page 27
FWHM	full width at half maximum	on page 28, on page 69
h	Planck constant	on page 26, on page 33
HZB	Helmholtz-Zentrum Berlin	
I_0	initial intensity	on page 28
I	resulting intensity	on page 28
IR	infrared spectroscopy	on page 26
κ	bending rigidity	on page 18
K	Kiessig fringe or Kiessig oscillation	on page 38
L_α	liquid like phase	on page 19
M	number of internal reflections at the sample surface	on page 57
N	number of lipid lamellae	on page 38
N_{BK}	N calculated according to Equation 3.38	on page 38
N_{amp}	N calculated according to Equation 3.40	on page 39
N_{area}	N calculated according to Equation 3.41	on page 39
N_{FWHM}	N calculated according to Equation 3.39	on page 39

ABBREVIATIONS

NR	neutron reflectometry	on page 33
Q	momentum transfer	on page 35
Q _c	critical momentum transfer	on page 36
P _β	ripple phase	on page 19
PSI	Paul-Scherrer Institute in Switzerland	on page 50
R	reflectivity	on page 32
γ	heat rate	on page 24
SINQ	Swiss spallation neutron source	on page 50
SLD	scattering length density	on page 34
t	total coating thickness	on page 38
T _m	main phase transition temperature	on page 20
$\tilde{\nu}$	wavenumber	on page 28
V6	neutron reflectometer at HZB	
V18	alternative for BioRef	on page 44
XR	X-ray reflectometry	on page 33

Ich erkläre hiermit, dass ich die vorgelegte Dissertation selbst verfasst und mich keiner anderen als der von mir ausdrücklich bezeichneten Quellen und Hilfen bedient habe. An keiner anderen Stelle habe ich ein Prüfungsverfahren beantragt und die Dissertation nicht in dieser oder anderer Form bereits anderweitig als Prüfungsarbeit verwendet oder einer anderen Fakultät als Dissertation vorgelegt.

Berlin, den Dezember 2011

.....

Martin Kreuzer